

Using Lattice Engineering and Porous Materials Gating to Control Activity and Stability in Heterogeneous Catalysis

A dissertation by

Allison Patricia Young

submitted to the Faculty of the Department of Chemistry
in partial fulfillment of the requirements for the degree of
Doctor of Philosophy

Boston College
Morrissey College of Arts and Sciences
Graduate School
September 2018

Using Lattice Engineering and Porous Materials Gating to Control Activity and Stability in Heterogeneous Catalysis

Allison Patricia Young

Advisor: Chia-Kuang Tsung, Ph.D.

Heterogeneous catalysis is a critical field for chemical industry processes, energy applications, and transportation, to name a few. In all avenues, control over the activity and selectivity towards specific products are of extreme importance. Generally, two separate methods can be utilized for controlling the active surface areas; a below and above the surface approach. In this dissertation, both approaches will be addressed, first starting with controlling the active sites from a below approach and moving towards control through sieving and gating effects above the surface.

For the first part half, the control of the product selectivity is controlled by finely tuning the atomic structures of nanoparticle catalysts, mainly Au-Pd, Pd-Ni-Pt, and Pd-Ni₃Pt octahedral and cubic nanoparticle catalysts. Through these shaped core-shell, occasionally referred to as core@shell, particles the shape is maintained in order to expose and study certain crystal facets in order to obtain a more open or closed series of active sites. With the core shell particles, the interior core particle (Au and Pd) is used for the overall shape but also to expansively/compressively strain the outer shell layer. By straining the surface, the surface electronic structure is altered, by raising or lowering the d-band structure, allowing for reactants to adsorb more or less strongly as well as adsorb on different surface sites. For the below the surface projects, the synthesized nanoparticle catalyst are used for electrochemical oxidation reactions, such as ethanol and methanol oxidation, in order to study the effect of the core and shell layers on initial activity, metal

migration during cycling, as well as particle stability and activity using different crystal structures. In particular, the use of core shell, alloyed, and intermetallic (ordered alloys) particles are studied in more detail.

In the second half of this dissertation, control of the selectivity will be explored from the top down approach; in particular the use of metal organic framework (MOF) will be utilized. MOF, with its inherent size selective properties due to caging effects from the chosen linkers and nodes, is used to coat the surface of catalysts for gas, liquid, and electrochemical catalysis. By using nanoparticle catalyst, the use of MOF, more explicitly the robust zirconium based UiO-66, as a crystalline capping agent is first explored. By incorporating both the nanoparticle and UiO-66 amino functionalized precursors in the synthesis, the nanoparticles are formed first and followed by coating in UiO-66-NH₂, where the amino group acts as an anchor, completely coating the particles. The full coating is tested through size selective alkene hydrogenations with the NP surface further tested by liquid phase selective aldehyde hydrogenations; the UiO-66-NH₂ pores help to guide the reactant molecule in a particular orientation for the carbonyl to interact rather than the unsaturated C=C bond. This approach is taken for more complex hybrid structures for electrochemical proton exchange membrane fuel cell (PEMFC) conditions. Through the gating effects, the UiO-66 blocks the Pt surface active sites from poisonous sulfonate groups off of the ionomer membrane while simultaneously preventing aggregation and leaching of Pt atoms during electrochemical working conditions.

To my family, for all their love and support.

“There is a tide in the affairs of men. Which, taken at the flood, leads on to fortune.”
- *Julius Caesar*
Act –IV, Scene III

Table of Contents

Table of Contents	i
Acknowledgement	v
List of Figures	vii
List of Tables	xii
Project Description	1
1.0 Introduction	5
1.1 Metal Nanoparticles for Heterogeneous Catalysis	6
1.1.1 Synthesis Methods for Metal Nanoparticles	7
1.1.2 Metal Nanoparticle Motifs for Electrochemical Reactions	11
1.2 Metal Organic Framework for Heterogeneous Catalysis	14
1.2.1 Synthesis Methods for Nanoparticles Encapsulated in Metal Organic Framework	14
1.2.2 Metal Oorganic Frameworks for Heterogeneous Catalysis	18
1.3 References	21
2.0 Electrochemically Induced Surface Metal Migration in Well-Defined Core-Shell Nanoparticles and Its General Influence on Electrocatalytic Reactions	27
2.1 Abstract	27
2.2 Introduction	28
2.3 Experimental Methods	32
2.3.1 Chemicals	32
2.3.2 Synthesis of 30 nm Au Nanooctahedra	32
2.3.3 Synthesis of ~35 nm Au-Pd Core-Shell Nanooctahedra	33
2.3.4 Characterization	33
2.3.5 Electrochemical Measurements.....	34
2.4 Results and Discussion	35
2.4.1 Synthesis of Au-Pd Core-Shell Nanooctahedra Electrocatalysts	35
2.4.2 Au Migration through Electrochemical Blank Scans.....	36
2.4.3 TEM/STEM-EDX Characterization of Au-Pd Nanooctahedra after Electrochemical Blank Scans	41
2.4.4 Electrolyte Effect on Au Migration During Electrochemical Blank Scans...	45
2.4.5 Au Migration During Electrochemical Ethanol Oxidation (EOR).....	48

2.4.6	Au-Pd Ethanol Oxidation Reaction Activiy Trends.....	52
2.5	Conclusion	54
2.6	References.....	55
3.0	Shaped Pd-Ni-Pt Core-Sandwich-Shell Nanoparticles: Influence of Ni Sandwich Layers on Catalytic Electrooxidations.....	60
3.1	Abstract	60
3.2	Introduction.....	61
3.3	Experimental Methods	65
3.3.1	Chemicals	65
3.3.2	Synthesis of Cubic Pd-Ni-Pt Nanoparticles	65
3.3.3	Synthesis of Cubic Pd-Pt Nanoparticles.....	66
3.3.4	Synthesis of Cubic Au-Pd-Ni-Pt Nanoparticles	67
3.3.5	Synthesis of Octahedral Pd-Ni-Pt Nanoparticles	67
3.3.6	Characterization	67
3.3.7	STEM/EDX.....	68
3.3.8	Electrochemical Measurements.....	68
3.4	Results and Discussion	70
3.4.1	Synthesis of Pd-Ni-Pt Sandwich Nanoparticles	70
3.4.2	Characterization of Pd-Ni-Pt Sandwich Nanoparticles by TEM	72
3.4.3	Analysis of Structure, Composition, and Strain in Pd-Ni-Pt Sandwich Nanoparticles by STEM/EDX, HAADF, HRTEM Imaging, and XRD.	74
3.4.4	Electrocatalysis by Pd-Ni-Pt Sandwich Nanoparticles	79
3.4.5	Electrocatalytic Oxidation of Methanol in Alkaline Electrolyte.....	84
3.4.6	Electrocatalytic Oxidation of Formic Acid and Methanol in Acidic Electrolyte	85
3.4.7	Re-Examination of Pd-Ni-Pt Sandwich Nanoparticles After Electrocatalysis Experiments.....	87
3.4.8	Synthesis of Quaternary, Multi-Shelled Au-Pd-Ni-Pt Nanoparticles and Pd-Ni-Pt Sandwich Nanooctahedra	90
3.5	Conclusion	92
3.6	References.....	93
4.0	Synthesis of Shaped Ni₃Pt Nanoframes through the Low-Temperature Annealing of Pd-Ni-Pt Core-Sandwich-Shell Nanoparticles.....	99
4.1	Abstract	99
4.2	Introduction.....	100
4.3	Experimental Methods	102
4.3.1	Chemicals	102
4.3.2	Synthesis of Cubic Two Layered Pd-Ni-Pt Core-Sandwich-Shell Nanoparticles.....	103
4.3.3	Synthesis of Cubic Four Layered Pd-Ni-Pt Core-Sandwich-Shell Nanoparticles.....	103
4.3.4	Deposition of Nanoparticle Catalysts on Vulcan Carbon Support and Thermal Annealing.....	104
4.3.5	Characterization	104
4.3.6	ICP-OES.....	105

4.3.7	Electrochemical Measurements.....	106
4.4	Results and Discussion	107
4.4.1	Pd-Ni-Pt Layer Number and Thickness Control Study of Precursor Nanoparticle Catalysts.....	107
4.4.2	Nanoframe Synthesis Through Thermal Annealing of Precursor Pd-Ni-Pt Nanoparticles.....	109
4.4.3	Electrochemical Alkaline Methanol Oxidation Before and After Thermal Annealing	111
4.4.4	Electrochemical Alkaline Methanol Oxidation After Thermal Annealing Held for Differing Time Periods	114
4.4.5	Pd-Ni ₃ Pt Formation and TEM Study After Thermal Annealing.....	116
4.4.6	X-ray Diffraction Characterization of Pd-Ni-Pt Nanoparticle Catalysts Before and After Thermal Annealing.....	119
4.5	Conclusion	121
4.6	References.....	122
5.0	One-Pot Nanoparticle Encapsulation Utilizing Metal-Organic Framework as Crystalline Capping Agent for Selective Catalysis.....	125
5.1	Abstract	125
5.2	Introduction.....	126
5.3	Experimental Methods	129
5.3.1	Chemicals	129
5.3.2	Synthesis of UiO-66 and UiO-66-NH ₂	130
5.3.3	Synthesis of NP@UiO-66-NH ₂ and NP/UiO-66 Composites.....	131
5.3.4	Synthesis of Size Controlled Pd@UiO-66-NH ₂ and Pt@UiO-66-NH ₂ Composites	131
5.3.5	Synthesis of PVP Capped 5 nm Pt and Pd Nanocrystals and Corresponding PVP Coated 5 nm Pt NPs@UiO-66-NH ₂ Pt NPs/UiO-66-NH ₂ Composites	132
5.3.6	Synthesis of Pt@UiO-66-NH ₂ Through Wetness Impregnation.....	133
5.3.7	Catalyst Preparation and Gas Phase Hydrogenation Study.....	133
5.3.8	¹ H NMR Characterization of Crotonaldehyde Hydrogenation Products	135
5.3.9	Characterization	135
5.4	Results and Discussion	136
5.4.1	One-pot Synthesis of Pd and Pt Nanoparticles in UiO-66-NH ₂	136
5.4.2	Probing the NP@UiO-66-NH ₂ Surface Through Fourier-transform Infrared Spectroscopy (FTIR)	142
5.4.3	Composition and Size Control of the NP@UiO-66-NH ₂ Composites using a One-pot and Two-pot Method	144
5.4.4	Size Selective Alkene Hydrogenations over Encapsulated NP@UiO-66-NH ₂	149
5.4.5	Composition Effect on Ethylene Hydrogenation Activity	153
5.4.6	Liquid Phase Hydrogenation of Crotonaldehyde	155
5.5	Conclusion	157
5.6	References.....	158

6.0	Hybrid Pt/CNT@UiO-66 Electrocatalysts for Increased Stability in the Oxygen Reduction Reaction	163
6.1	Abstract	163
6.2	Introduction.....	164
6.3	Experimental Methods	167
6.3.1	Chemicals	167
6.3.2	Synthesis of Pt/CNT <i>via</i> Pt Deposition.....	168
6.3.3	Synthesis of Pt/CNT@UiO-66: Traditional Method.....	168
6.3.4	Synthesis of Pt/CNT@UiO-66: Pre-hydrolysis Method.....	169
6.3.5	Synthesis of Pt/CNT@UiO-66-4F: Aqueous Method.....	170
6.3.6	Characterization	171
6.3.7	Size Selective Alkene Hydrogenation.....	172
6.3.8	ICP-OES.....	173
6.3.9	Electrochemical Measurements.....	174
6.4	Results and Discussion	176
6.4.1	Synthesis and TEM Characterization of Pt Nanoparticles Deposited on Carbon Nanotubes	176
6.4.2	Synthesis and Characterization of UiO-66 Coated Pt Nanoparticles Deposited on Carbon Nanotubes	178
6.4.3	Size Selective Alkene Hydrogenations of Ethylene and Cyclooctene	186
6.4.4	Electrochemically Active Surface Area Measurement for Pt Detachment	188
6.4.5	Electrochemical Oxygen Reduction Reaction on a Rotating Ring Electrode System	189
6.5	Conclusion	195
6.6	References.....	196
7.0	Conclusion.....	200

Acknowledgement

First, I would like to thank my advisor, Frank Tsung. He has been an invaluable resource and guide along this journey. Thank you to Professors Wang, Waegele, and Mohanty for giving me the opportunity to share my research and taking time out of their busy days to read and listen to this dissertation. To the Boston College chemistry department staff, thank you for all you do to make everything run as smoothly as possible. Thank you to all of the collaborators across the globe for their many contributions; Prof. Wenyu Huang, Prof. Franklin Tao, Prof. James Evans, Prof. Paolo Scardi, Prof. SonBinh Nguyen as well as their many graduate students who contributed as well. To the Tsung group members past and present, your support through this time has truly helped get me to this point. In particular, Ben Williams has been incredibly helpful to me; Brian Sneed, my original mentor, taught me so much during my first year in the group; and Joe Morabito, thank you for the insightful discussion as well as your friendship outside of lab. Throughout the years, I had the pleasure of working with and mentoring incredible undergraduate students, Jane Yang, Ilektra Andoni, Matthew Golden, and Nima Boluriaan, thank you for your hard work and dedication. I thank the Wang Lab and the Waegele Lab as well as the BC Physics Department, for discussions and collaborations. Thank you to Boston College, Toyota, and the National Science Foundation for funding the research presented. To my undergraduate advisor at the National Institute of Standards and Technology, Edwin Chan, thank you for encouraging me to pursue my Ph.D. and helping nurture my love of research. To my friends from home, college, and Boston, thank you for always being there. In particular, thank you to

Jackie Kubala for listening and helping me keep my motivation. Finally, a very special thank you to my family, both immediate and extended. To my sister in law, Kaitlind, thank you for being so understanding and one of my biggest cheerleaders. To my brother, Brad, thank you for being an incredible academic, role model, and most of all, for being one of my best friends. To my parents, I wouldn't be where I am today if not for you. Your endless love, support, and encouragement through it all meant so much. I always knew I had someone fighting in my corner. Finally, to Josh Cohen, thank you for being my rock. I thank you all for your endless support.

List of Figures

Figure 1.1: Types of strain in nanoparticle metals that induces electronic band structure changes.....	9
Figure 1.2: Metal organic framework (MOF) building units.....	15
Figure 1.3: Selectivity capabilities imparted by MOF on a nanoparticle surface.....	16
Figure 1.4: Representative cartoon of nanoparticle and MOF surface and the tunability.....	19
Scheme 2.1: Schematic representation of surface metal migration of core-shell nanoparticles.....	30
Figure 2.1: Representative transmission electron microscopy (TEM) images of Au, Au-Pd thin shell, Au-Pd thick shell nanooctahedra and high resolution transmission electron microscopy (HRTEM) images of the Au-Pd interface.....	36
Figure 2.2: Voltammetric profiles of the Au-Pd nanooctahedra in 0.5 M H ₂ SO ₄ and corresponding Au/Pd surface areas.....	37
Figure 2.3: Voltammetric profile showing the method of quantifying the Au/Pd surface areas.....	38
Figure 2.4: TEM images of Au-Pd core-shell nanooctahedra before and after cycling in 0.5 M H ₂ SO ₄	42
Figure 2.5: Energy-dispersive X-ray spectroscopy (EDX) line scans and crystallographic representation of the thin shell Au-Pd nanooctahedra before and after cycling in 0.5 M H ₂ SO ₄	44
Figure 2.6: Scanning Transmission Electron Microscopy (STEM)/EDX elemental mapping and quantification mapping of the thin Au-Pd nanooctahedra before and after cycling in 0.5 M H ₂ SO ₄	45
Figure 2.7: Voltammetric profile of thin Au-Pd nanooctahedra and the effect of electrolyte on migration.....	47
Figure 2.8: Voltammetric profile of thin Au-Pd nanooctahedra and the effect of pH on migration.....	48
Figure 2.9: “Half” Voltammetric blank scans of thin Au-Pd nanooctahedra.....	50

Figure 2.10: Ethanol Oxidation Reaction (EOR) profiles performed on the thick and thin Au-Pd nanooctahedra.....	51
Figure 2.11: EOR profile performed on pure Au nanooctahedra.....	52
Scheme 3.1: Schematic representation for the synthesis of the Pd-Ni-Pt core-sandwich-shell nanoparticles.....	64
Figure 3.1: TEM images of cubic Pd-Ni-Pt electrocatalysts and Pd-Pt control with recolored insets to show the defined layers.....	73
Figure 3.2: High-angle annular dark-field imaging (HAADF), STEM/EDX elemental maps and HRTEM of Pd-Ni-Pt nanoparticles with measured atomic spacing.....	75
Figure 3.3: TEM and HRTEM of the Pd-Ni-Pt morphology and lattice distortion due to lattice mismatch.....	77
Figure 3.4: Powder X-ray diffraction (pXRD) spectra of the different Pd-Ni-Pt nanoparticles.....	79
Figure 3.5: Cyclic voltammetry (CV) blank scans in acidic, H ₂ SO ₄ , and alkaline, KOH, electrolyte used to determine the electrochemically active surface area (ECSA) of Pd-Ni-Pt nanoparticles.....	80
Figure 3.6: CV and Chronoamperometry (CA) curves for Pd-Ni-Pt in KOH methanol oxidation (MOR).....	81
Figure 3.7: CV and CA curves for Pd-Ni-Pt in H ₂ SO ₄ MOR and formic acid oxidation (FOR).....	82
Figure 3.8: Acidic transient current density plots of Pd-Ni-Pt catalysts.....	86
Figure 3.9: TEM images of Pd-Ni-Pt electrocatalysts after CV scans in H ₂ SO ₄ and KOH showing compositional changes.....	88
Figure 3.10: TEM/HRTEM of cubic Au-Pd-Ni-Pt and octahedral Pd-Ni-Pt nanoparticles.....	91
Figure 3.11: TEM with colored overlay of cubic Au-Pd-Ni-Pt particles with corresponding EDX data.....	92
Figure 4.1: TEM characterization of the two and four layered precursor nanoparticles as synthesized.....	108

Scheme 4.1: Schematic representation of the formation of mixed Pd-Ni ₃ Pt nanoparticles through metal migration.....	109
Figure 4.2: Electrochemical alkaline methanol oxidation (MOR) after thermal annealing at different temperatures.....	113
Figure 4.3: Lattice spacing measurements from TEM after thermal annealing at different temperatures.....	113
Figure 4.4: Electrochemical alkaline MOR after thermal annealing held for differing times.....	115
Figure 4.5: Low magnification TEM images of the nanoparticle catalysts after thermal annealing at different temperatures.....	118
Figure 4.6: HRTEM images of the nanoparticle catalysts after thermal annealing at different temperatures.....	118
Figure 4.7: Powder x-ray diffraction of the as synthesized and final nanoframe catalysts.....	120
Scheme 5.1: Schematic representation of the formation of the NP@UiO-66-NH ₂ in a one pot method.....	136
Figure 5.1: TEM image time study of the NP@UiO-66-NH ₂ growth process.....	137
Figure 5.2: TEM images of the Pd/Pt one pot encapsulated NPs within UiO-66-NH ₂ with corresponding alloyed Pd/Pt EDX line map.....	138
Figure 5.3: TEM and FTIR study for NP surface and linker interaction.....	140
Figure 5.4: TEM images of the one pot method with terephthalic acid (BDC) and amino-terephthalic acid (BDC-NH ₂) linker and the effect on encapsulation.....	141
Figure 5.5: FTIR data showing the surface interaction of the BDC-NH ₂ with the encapsulated NP.....	142
Figure 5.6: STEM/EDX line mapping of differently alloyed Pd/Pt NPs within UiO-66-NH ₂ using the one pot method.....	146
Figure 5.7: Powder XRD patterns of pure UiO-66-NH ₂ and NP@UiO-66-NH ₂ utilizing the one pot encapsulation method.....	147
Figure 5.8: TEM images indicating no metal leaching from the NPs during synthesis conditions.....	148

Figure 5.9: TEM images and corresponding nanoparticle size count through a two pot encapsulation method.....	149
Figure 5.10: SEM images of Pd@UiO-66-NH ₂ and pure UiO-66-NH ₂ indicating the maintained structure.....	151
Figure 5.11: Size exclusion alkene hydrogenation catalysis and composition effect on hydrogenation activities.....	152
Figure 5.12: Size exclusion alkene hydrogenation catalysis of Pd@UiO-66-NH ₂ and Pd/UiO-66-NH ₂	153
Figure 5.13: Ethylene hydrogenation catalysis over a mixture of Pd and Pt NPs showing no synergistic effect on activities.....	154
Figure 5.14: Ethylene hydrogenation catalysis of Pt@UiO-66-NH ₂ and Pt(PVP)@UiO-66-NH ₂	155
Scheme 6.1: General schematic representation of the formation of Pt/CNT.....	177
Figure 6.1: TEM images and corresponding particle size count of Pt/CNT.....	177
Scheme 6.2: General schematic representation of the formation of Pt/CNT@UiO-66.....	178
Figure 6.2: TEM of the Pt/CNT@UiO-66 samples obtained <i>via</i> the pre-hydrolysis coating method.....	179
Figure 6.3: TEM and grain size determination of the Pt/CNT@UiO-66-4F using the aqueous synthesis method at differing acetic acid concentrations.....	181
Figure 6.4: TEM and XRD of Pt/CNT@UiO-66 from the traditional method.....	183
Figure 6.5: Representative image of Pt leaching and Pt detachment concerns.....	185
Figure 6.6: Size-selective hydrogenation of ethylene and cyclooctene.....	187
Figure 6.7: Electrochemically active surface area (ECSA) measurements from H ₂ adsorption to determine Pt NP detachment from the CNT after coating.....	189
Figure 6.8: Model of the final ORR Pt/CNT@UiO-66 catalyst and corresponding roles.....	190
Figure 6.9: Photograph of the working electrochemical cell for ORR.....	191

Figure 6.10: Summary of ORR data for initial and end of life (EOL) value after an accelerated aging process.....192

Figure 6.11: TEM images after EOL studies for Pt/CNT and Pt/CNT@UiO-66 samples.....194

List of Tables

Table 1.1: Reducing agents and their corresponding reduction potentials.....	10
Table 4.1: Summary of ICP-OES data for precursor nanoparticles.....	110
Table 5.1: Summary of ICP-OES data for various compositions of Pd/Pt@UiO-66-NH ₂	145
Table 5.2: Summary of the crotonaldehyde hydrogenation catalysis results.....	157
Table 6.1: ICP-OES values for the Pt loss percentage after the different coating methods.....	185
Table 6.2: Size-selective hydrogenation results for the conversion percent of ethylene and cyclooctene.....	188
Table 6.3: Summary of initial and EOL ORR data with percentage of lost capabilities.....	193

Project Description

Heterogeneous catalysis has been a rising field for several years. By incorporating catalysts of different phase than the adsorbed reactant species, reaction transformations are able to take place with easier end catalyst/product separation and potential for catalyst recyclability when compared to traditional homogenous catalysts. In this work, heterogeneous catalysis is studied in the gas and liquid phase using batch reactors as well as electrochemical cells.

First, the use of nanoparticle catalysts is studied. In chapter 2, the exploration of Au core with Pd shell nanooctahedra catalysts through electrochemical means is probed. Ethanol oxidation, a small molecule oxidation reaction, is used to follow catalyst transformation throughout cycling as well as studying the stability of catalyst with different thicknesses of the exterior shell. By synthesizing core-shell particles, the effects of strain is studied. The Au core has a larger lattice parameter than that of the Pd shell and by obtaining epitaxial overgrowth through a slow reduction, the Pd and Au interface will align, compressively and expansively straining their crystal lattices, thus altering the d-band and surface electronics of the Pd surface. By utilizing well define nanooctahedra, migration effects for the [111] facet and the diffusion of Au to the surface are also probed.

From the Au-Pd structure, more complex Pd-Ni-Pt core-sandwich-shell nanoparticles are synthesized and studied in chapter 3. From the previous results, as well as those presented in literature, strained Pt surfaces have increased catalytic performance with a higher degree of stability due to less strongly binding adsorbates. The Pd core

serves as a nanoparticle substrate to influence and maintain the overall shape, the Ni sandwich layer is added to influence the Pt surface through a high degree of strain from the large lattice mismatch, and the Pt shell is the strained catalytic surface. During this process, the degree of strain is tested by changing the overall particle size (i.e. smaller particles are inherently more strained than larger) as well as the Ni layer thickness. Finally, electrochemical atom migration is also touched upon by using both acid and basic electrolyte during the methanol oxidation reaction.

Having synthesized and studied the strain effects on core-shell and core-sandwich-shell particles and the degree of alloying that occurs due to working conditions in the electrochemical cell, chapter 4 focuses on metal migration from external heating to induce the formation of more stable intermetallic structures. Intermetallic structures are ordered alloys which generally require high synthesis temperatures to achieve. As a result, very little shape control has been found when forming these intermetallic catalyst, however, due to their very ordered structure, catalyst selectivity and stability is increased. For this system, two samples are synthesized using the same Pd-Ni-Pt system, maintaining a 3:1 ration of Ni:Pt, one with thick Ni and Pt layers and the other a four layer system with two thin Ni layers sandwiched by two thin Pt layers (annotated as Pd-(Ni-Pt)₂). Several annealing temperatures are tested to induce full Ni/Pt mixing, where the Pd core only serves as a template due to the inability to mix with Ni except for at temperatures much high than we are testing. The atom migration of the two samples annealed at differing temperatures is probed through transmission electron microscopy, x-ray diffraction, and electrochemical methanol oxidation. The diffusion

kinetics of the two samples, the thicker with one interface and the thinner with multiple interfaces to allow for easier mixing, are also briefly investigated.

Chapter 5 and 6 focus on changing the selectivity and stability of heterogeneous nanoparticle catalyst by using the “from above” approach. First, the use of metal organic framework (MOF), a porous coordination material formed from metal nodes and organic linkers, is studied as a crystalline capping agent. MOF materials have inherent size selective sieving properties due to their porous coordinative nature. By changing the metal nodes or organic linkers, the pore sizes and apertures can also be tuned. UiO-66, a robust, zirconium based MOF is chosen due to its chemical and thermal stability as well as linker tenability. For chapter 5, the amino functionalized linker, aminoterephthalic acid, is chosen. The dangling amino group allows for the linker that anchor the *in situ* forming nanoparticle catalyst and cap them, maintaining a separation of particles and a cleaner surface when compared to more traditional approaches of synthesizing the nanoparticle first with a capping agent to then be encapsulated or forming the MOF first and using wetness impregnation approach which damages the MOF structure, potentially causing fractures, decreasing the selectivity. The as synthesized nanoparticle within UiO-66-NH₂ samples can have different composition and sized nanoparticles. They are also tested for full encapsulation by size selective alkene hydrogenations and for product selectivity by liquid phase aldehyde hydrogenation.

With the ability to coat nanoparticles with MOF, the system is expanded for use in electrochemical reactions. For use in fuel cell type reactions, a conductive polymer is typically incorporated to enhance the proton conduction from anode to cathode. Due to this, the Pt surface found in both reactions can easily become poisoned from the dangling

sulfonate groups in the ionomer; Nafion. UiO-66 is not particularly conductive, therefore a conductive support for the Pt particles is used, carbon nanotubes (CNTs). Pt decorated CNTs are coated in UiO-66 through three methods; a pre-hydrolysis of the nodes, an aqueous phase, and a traditional organic phase method. From these methods, the traditional method yields the best coverage of the Pt surface to ensure protection from poisoning as well as a decreased incidence of Pt leaching and particle detachment from the CNT support. The Pt/CNT@UiO-66 samples are then used to perform electrochemical oxygen reduction under proton exchange membrane fuel cell (PEMFC) conditions. Accelerated aging studies are performed to view catalyst stability when compared to the traditional Pt/C system.

1.0 Introduction

Heterogeneous catalysis is the process by which a reaction, typical of needing a catalyst, occurs using reactants of different phases than the catalyst itself. Generally speaking, the vast majority of these reactions occur using solid catalysts with either gas or liquid phase reactants.¹ Heterogeneous catalysis is critical for the growth of civilization in a vast number of areas²; industrial applications and reactions³, clean energy applications^{1,4}, and biomedical and pharmaceutical transformations^{5,6}, to name a few. In particular, there has recently been a larger focus towards using heterogeneous catalysis in the energy related space^{1,4,7}. By utilizing a catalyst of a different phase from the reactant species, the ability to more easily recycle the catalyst is key; similarly, the stability is also increased by using supports⁸⁻¹⁰.

In typical heterogeneous catalysis, an essential step is the process of adsorption and desorption¹. For the reaction to occur, the reactant must first interact with the catalyst surface and adsorb, or bind, to the active sites. During this process of adsorption, the reactant molecules binding strength is based on the electronic structure of the active material; stronger adsorption meaning reactants bind more strongly whereas weaker adsorption causes less reactant interaction. If molecules chemisorb too strongly, the active surface can become poisoned and ultimately deactivated¹¹. For example, a main deactivation pathway for Pt catalysts is strongly bound CO adsorbed on the surface. The

adsorbed CO is unable to desorb and eventually adheres to all active sites, making the catalyst useless^{12,13}. To change the adsorption and desorption behavior and maintain an active surface, two general approaches can be taken; changing the electronic structure (through strain, composition, and shape) of the catalyst thereby altering the reactant binding strength^{2,14}, or by using caging effect¹⁵, in this instance, metal organic framework, for an above the surface approach, to avoid the catalyst coming into contact with poisoning species all together.

1.1 Metal Nanoparticles for Heterogeneous Catalysis

The field of heterogeneous is constantly growing as new catalysts and hybrid catalyst materials are synthesized. In recent years, there has been a large growth in the field through the incorporation of metal nanoparticles in these reactions. With the small size and large surface area, the content of precious metals needed for reactions to reach similar activity of bulk catalyst is further reduced. As the field has grown in the last several years, nanoparticle catalysts have developed from monometallic species with no defined shape, to complex multi-metallic materials utilizing high index facets to complete complex catalysis achieving record high activities. As the field progresses, the activity and selectivity will continue to grow with price reduction by incorporating lesser expensive transition metals or metal-oxides and supports as well as forming better defined structures with precisely tuned electronic band structures for the needed reaction.

1.1.1 Synthesis Methods for Metal Nanoparticles

In a general sense, metal nanoparticles are synthesized due to the burst nucleation and subsequent growth in a solution through the reduction of metal ions. The production of the particles is best described by the LaMer approach¹⁶ in which the metal ion precursors are reduced, forming clusters which overcome the energetic barrier for forming a new interface. After producing the burst of nucleation, a growth stage will take place, using the remaining monomer ion concentration. This growth process can also occur if a seed particle is placed within the growth solution, at which point, the ions will reduce onto, or around the seed.

Due to the high degree of surface energy, the formed nanoparticles will aggregate to micro-sized particles, ultimately precipitating out, unless the surface energy is stabilized through external capping agents. Generally, these stabilizing agents will interact with the particle surface creating a buffer between one particle and another. By maintaining a distance of separation and electrostatic repulsion, they refrain from aggregating and crashing out of solution, keeping them viable for further use. Additionally, the use of capping agents, such as cetyltrimethylammonium halide salts, incorporates halide groups which bind to the nanoparticle surface more or less strongly depending on the exposed facet. By incorporating halides, growth of different facets is induced or shut down, culminating in particles with differently exposed facets. Although the initial reports of shape controlled nanoparticles were few and far between, the production of shape-controlled nanocrystals has been growing after early advances, particularly by El-Sayed *et al*, the Huang group, and Niu *et al*, with their works on Pt, Au,

and Pd¹⁷⁻¹⁹. Currently, a wide variety of capping agents and shape controlling agents have been used to form a library of shaped nanoparticles of different faceting and metal compositions. Although nanoparticles show high activity towards catalytic reactions, the desire for more robust, less expensive, and even more active nanoparticle catalysts led to the design and realization of more complex nanoparticle motifs.

With the advent of shape controlled mono-metallic nanoparticles in the mid 1990's¹⁷, the field of nanoparticle synthesis and research saw a huge degree of growth and influx of new, more complex nanostructures. The newly implemented nanostructures displayed novel reactivity and stability, opening a new realm of multi-metallic alloyed, core-shell, and intermetallic catalysts, helping to propel the use of nanoparticles in more heterogeneous reactions.

The trend in recent years has been to develop and improve these heterogeneous nanoparticle catalysts by implementing an atomic level of control in the production of nanoparticles in order to fine-tune the surface electronic structures available. In order to obtain the level of tunability and control needed, several key mechanisms have been proposed; the overarching goal of each is to shift the d-band center of the metal surface in order to tune the binding strength and active sites reactant molecules interact with. These methods include altering the electronic structures through ligand effect, by causing the metal surface to be altered through direct electronic interactions of the surface metal to underlying or adjacent, different metal atoms^{20,21}. Similarly, incorporating more than one metal causes synergetic, or ensemble effects, in which specific active sites become available due to the secondary metal²². Finally, the use of lattice strain, or geometric effects, in which the surface electronic structure is altered by the shifting of lattice

parameters. Due to the difference in the lattice parameter of different atoms, or from under coordinated sites, each will compress or expand in order to accommodate the strain. There are several types of strain; due to size, shape, grain boundaries, core-shell interactions, and alloys or intermetallic structures (Figure 1.1)²³. The catalytic surface that is experiencing the lattice strain also has a shift in its d-band center due to the change in the overlap²⁴⁻²⁶. With the ability to shift the d-band center, the surface electronic structure of the synthesized particles, whether they be alloys (disordered crystal structures of two or more metal types), core-shell (an interior core of one metal with a deposited shell of a secondary metal), or intermetallic (ordered alloys of two or more metal types) as seen in Figure 1.2, the catalyst can be tuned for the particular reaction.

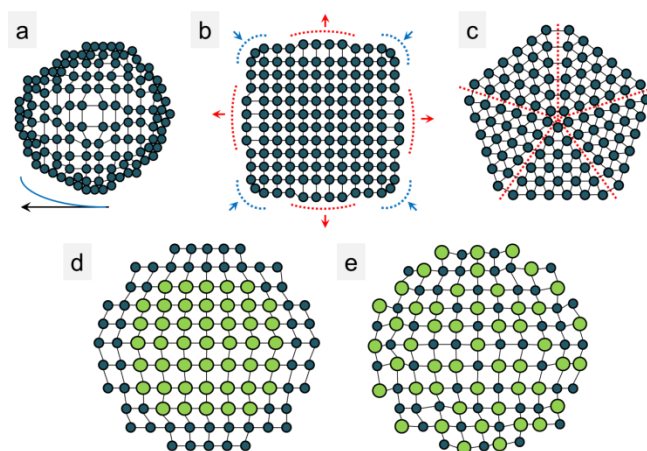


Figure 1.1: Typical forms of strain found in metal nanoparticles that cause a shift in the electronic band structure (adapted from ref. 23) a. size, b. shape, c. twin boundaries, d. core-shell, e. alloy or intermetallic

For each type of nanoparticle catalyst mentioned, certain complications arise from the synthesis methods available. For alloyed particles, the reduction of the metal precursors must be considered. In order to create alloys from wet chemical methods and

produce shaped samples, the reduction rate of the chosen metals must match. Alloys in particular have been chosen due to the ability to incorporate non-precious metals with Pt, thus decreasing the overall amount of Pt needed while increasing the activity due to the ensemble and synergistic effects mentioned previously.

Other methods include the formation of core-shell and core-sandwich shell nanoparticles. First the core particle is synthesized using traditional colloidal nanoparticle syntheses and then the shell layer is reduced on the surface. In certain cases, a third or fourth layer may also be deposited. Similarly, the production of core shell particles can occur if the two metal precursors that are mixed together have vastly different reduction potentials where one is reduced, followed by the second. The core and shell interact through epitaxial growth of each metal atom on the other. When the lattices are mismatched, a degree of strain is imparted altering the catalyst initial abilities. Similar to alloyed particles, the reduction rate of each must be considered. Luckily, with the growth of nanoparticle synthesis, an array of reducing agents can be used individually or in combination to produce the desired reducing power (Table 1.1)

Reducing Agent	Structure	Standard Redox Potential
sodium borohydride		~ -1.2 V (stronger in base)
ammonia borane		~ -1.2 V (stronger in acid)
Hydrazine		~ -1.2 V (stronger in base)
ascorbic acid		~ -0.13 V (stronger in acid)
citric acid		~ -0.30 V

Table 1.1: Standard reducing potentials of commonly used reducing agents in nanoparticle synthesis

Finally, intermetallic compounds (IMC), are crystalline ordered alloys with very specific stoichiometry and long range atomic ordering, have started to garner a lot of attention. Bulk IMC materials have been more extensively studied due to their unique properties and active surface. Because of the unique properties, research into IMC nanomaterials is gaining attention, particularly by the Schaak group²⁷⁻²⁹. For these particles, three traditional synthesis methods are used 1) a top down approach using bulk phase IMC synthesized through heating of mixed metallic powders followed by milling, crushing or etching into nanoparticles^{30,31} ; 2) direct synthesis using wet chemistry at elevated temperatures³² ; and 3) using nanoparticle alloys or core shell structures are precursor particles to then undergo annealing²⁸. In each of these instances, the morphology of the nanoparticle may not be retained.

1.1.2 Metal Nanoparticle Motifs for Electrochemical Reactions

With the push towards “green chemistry” it is widely accepted that catalytic processes and fuel processes need to be environmentally friendly. As the need for alternative fuels rises, heterogeneous catalysis is available to step in. With the common goal to decrease CO₂ emissions, fuel cell reactions are of particular interest. In these reactions, the general catalyst at both the anode and cathode is Pt. Unfortunately, Pt can easily be poisoned from the surface coming into contact with contaminants in the feed gas, the polymer membranes used (proton exchange membrane (PEM) for PEM fuel cells), as well as byproducts produced throughout the course of the reaction. Due to this, the d-

band structure of the Pt needs to be altered for the poisonous species to bind less strongly, so the Pt does not deactivate.

Using the synthetic strategies from above; alloys, core-shell, and intermetallic particles, a new degree of stability can be brought to the Pt catalyst through the “below the surface approach”. It is worth mentioning, for electrochemistry, the reactions are very dependent on the facet exposed. In 2014, Chen *et al*, synthesized Pt₃Ni nanoframes that showed superior activity and stability compared to the traditional Pt/C catalysts. Through the incorporation of non-precious Ni, a synergetic effect was realized on the Pt surface and the stability was increased. With the use of nanoframes, the surface area was also drastically increased³³. Indeed, several attempts have been made at utilizing these non-precious alloys in PEMFC reactions. Unfortunately, although the initial activity and mass activity is higher than traditional Pt/C catalysts, due to the nature of the alloys and the harsh acidic environments of PEMFC, the non-precious metal within the alloy can leach out dropping the stability and life time of the catalysts. Chen *et al* recently published a paper in ACS Nano³⁴ studying the effects of alloyed nanoframes and their stability by using different etching methods. With the leaching from alloyed samples, the use of core-shell nanoparticles for fuel cell electrocatalysis became more prominent.

With the use of core-shell particles, the strain from the lower layer would alter the electronic structure of the Pt shell layer in a similar fashion as the alloyed samples; in this case though, the stability would be increased due to the shell around the non-precious metal or less stable core. Strasser *et al*, showed that the lattice strain imparted on the Pt outer shell of a core-shell Pt-PtCu catalyst enhanced the activity in the cathodic oxygen reduction reaction (ORR) for many fuel cells. By intentionally creating Pt skin layer, the

Cu was protected throughout cycling from further etching and the lattice strain enhanced the Pt catalytic activity³⁵. Similar results have been seen in other heterogeneous reactions such as the oxidation of CO using Ru-Pt core shell particles as well³⁶. Although lattice strain does increase the activity, similar problems over long cycling times occur with core-shell particles. Under running conditions, surface rearrangement is a concern³⁷, and due to this, pin-prick holes in the Pt arrangement can have detrimental effects on the interior core and leaching effects.

As synthesis capabilities increased, the use of intermetallic particles became more prevalent. Due to their crystal structure, the nanoparticles are inherently more stable and less likely to undergo restructuring during working conditions. In a Nature Materials paper in 2013, intermetallic Pt-Co core-shell structures for ORR were presented with enhanced activity and stability showing that the incorporation of the non-precious metal into a stable crystal lattice ensured less leaching. Meanwhile a Pt skin was used as the catalyst surface. From the strain imparted below the surface as well as the enhanced stability, less surface poisoning occurred³⁸.

Although by changing altering the d-band structure from below, the stability and activity can be increased, the de-alloying is still a concern. For core-shell particles, the strain imparted is ideal, but with fractures in the surface, the particles can still undergo metal migration and changes in the faceting of the nanoparticles, whereas for intermetallic particles, there is still less knowledge and synthetic strategy on shaped IMC particles. Additionally, the characterization of such particles can be difficult. Although the below the surface approach enhances the activity and in certain instances the stability,

it is worth noting, a second method for catalyst stability and selectivity is possible; using an “above the surface” approach through porous materials and selective sieving effects.

1.2 Metal Organic Frameworks for Heterogeneous Catalysis

Although metal nanoparticles have been explored as a possible solution towards green energy and industrial processes, their propensity to deactivate due to surface poisoning and aggregation is still a concern; even with below the surface electronic band structure manipulations. As a result, core shell materials utilizing a nanoparticle core encapsulated within a porous shell have gained attention. The porous shell material allows for reactants to have accessibility to the particle surface while increasing its durability and recyclability. Among common crystalline porous materials, metal organic frames, in particular is a promising class of encapsulation material.

1.2.1 Synthesis Methods for Nanoparticles Encapsulated in Metal Organic Framework

Metal-organic frameworks (MOFs) are porous, crystalline solids formed from the three dimensional coordination of metal nodes and bridging organic ligands which feature permanent microporosity upon solvent removal³⁹. MOFs have record surface areas up to few thousand m^2/g and high molecular selectivity, which make MOFs attractive and promising materials for molecular storage and particularly separation⁴⁰. The highly selective behavior of a MOF is a function of its pore aperture structure and the chemical groups exposed on its inner surface. MOF, formed through metal secondary

building units or nodes, and organic linkers coordinate and self-assemble as porous coordination polymers, containing pores and apertures depending on the metal node and linker used. The various choices of metal node allow for metal binding sites with near infinite tunability of organic linkers provided by synthetic organic chemistry.⁴¹ This explosion in the number of degrees of freedom available to the synthetic chemist when designing a MOF for a given application – thousands even across a MOF series of the same underlying topology – is the material’s main attraction over other porous materials, Figure 1.2.⁴²

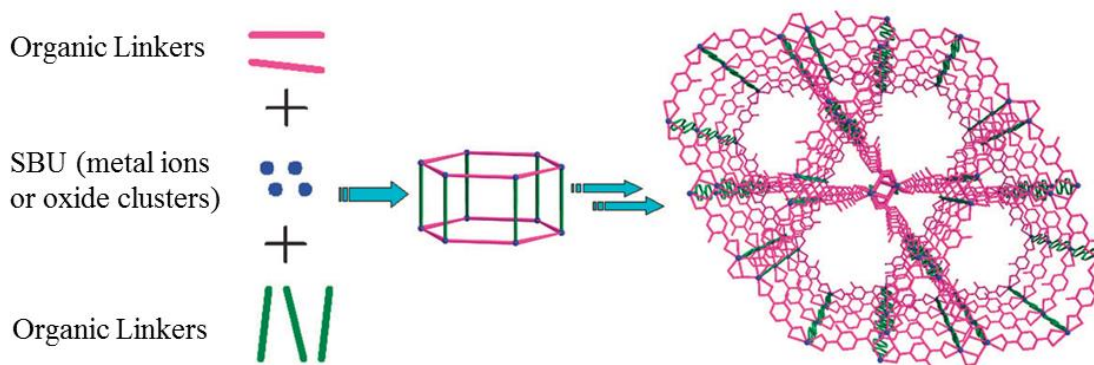


Figure 1.2: MOF Synthesis building blocks to form the porous coordination polymers. Secondary building units creating the metal ion or cluster nodes and the organic linkers.⁴²

MOF have proven the ability to regulate molecular diffusion through their apertures and pores, the sorption properties, and the orientation and conformation through which molecules pass through and interact with interior cages.⁴² Although MOF have several unique properties, ie. gas storage⁴³, separation⁴³, and drug delivery^{44,45}, a major role is heterogeneous catalysis⁴⁶. Due to their porous nature, the incorporation of metal nanoparticles within the interior pores of the MOF allows for new functionality,

selectivity, and stability to the nanoparticle catalyst where the nanopores offer confinement effects and enforce reactant selectivity based on size and adsorption properties (Figure 1.3).

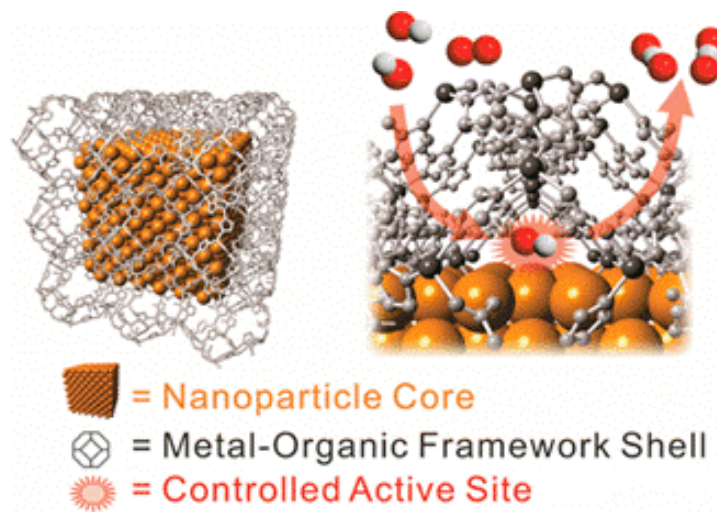


Figure 1.3: Heterogeneous catalysis approach by protecting catalyst surface through caging effects of MOF to act as molecular sieves for reactants to protect the nanoparticle surface

For most MOF syntheses, the metal nodes are created from metal salts dissolved within organic solvent. By incorporating the needed linker, the MOF coordinates to form the 3D structure at high temperatures. With the very tunable nature of metal organic frameworks, huge libraries of these materials have been created. Furukawa *et al* published an extensive table of the many nodes and linkers currently employed in MOF synthesis.⁴⁷

To generate hybrid nanoparticle within metal organic framework, several methods can be used. The most traditional and wide spread method is post-synthetic wetness impregnation⁴⁸⁻⁵⁰ where the as synthesized porous material is soaked in a solution of metal salt precursors to allow the metal ions to diffuse into the pores; the metal salts are

confined to the pores, using the MOF as a template. The ions are then reduced to form the nanoparticle catalysts encapsulated within the pores. This method was used to create hybrid Au nanoparticles within zeolitic imidazole framework (Au@ZIF-8), a zinc based MOF with imidazole linkers⁴⁸. Similarly, this method has been utilized to deposit highly active Pt nanoparticles within MIL-101; a Cr based MOF that uses terephthalic acid linkers⁴⁹. With this method, several different metal salts can be used to produce a wide assortment of hybrid composites, however there are several key disadvantages. Because the formation of the particles is dependent on the diffusion of metal ions into the MOF, the control over the particle dispersity, composition, and morphology are lacking. By soaking the MOF template, the particles also have a tendency to form on the exterior surface and can fracture the MOF coating during the reduction step.⁵¹

In order to tackle the drawbacks that arise from the wetness impregnation process new methodologies have been developed to produce fully encapsulated particles. By utilizing pre-formed colloidal nanoparticles with traditional capping agents, they can be incorporated during the MOF synthesis steps.⁵²⁻⁵⁵ The pre-synthesized nanoparticles are introduced in the MOF precursor solutions and the coating is able to form around them completely encapsulating their surfaces. By first synthesizing the nanoparticles, several disadvantages from wetness impregnation can be combated; the size, composition, and shape can all be controlled prior to use. Xu *et al* used polyvinyl pyrrolidone (PVP) capped Pt nanoparticles and encapsulated them in UiO-66, a very robust Zr MOF with terephthalic acid linkers, to show enhanced H₂O₂ oxidation⁵⁶. There have even been reports of using colloidal nanoparticle surfactants as structure directing agents in Pd and Au nanoparticles within ZIF-8⁵³. As with wetness impregnation, there are a few

drawbacks that must be considered, mainly the use of colloidal nanoparticle capping agents are adhered to the nanoparticle surface, which can then block active sites for catalysis.

A final approach is using MOF itself as the nanoparticle capping agent. This method allows for a cleaner nanoparticle surface while still imparting the selectivity inherent to the MOF, therefore controlling the catalytic selectivity. In order for this method to work, the linkers or metal nodes need to coordinate with the dissolved nanoparticle metal ions to act as a capping agent to avoid particle aggregation. As shown by the Li group⁵⁷, capping agent free Pt nanoparticles were encapsulated in MOF through *in situ* reduction of the Pt salt by the organic solvent and “capped” by the linker. This chelating effect of the linker and forming metal nanoparticle lowers the particle surface energy like a traditional colloidal capping agent would. In recent years, this method has become more widely used to form these hybrid nanoparticle within MOF composites and has opened the doors for new nanoparticle within MOF motifs with cleaner nanoparticle surfaces for heterogeneous catalysis with enhanced selectivity and stability⁵⁸.

1.2.2 Metal Organic Frameworks for Heterogeneous Catalysis

Metal organic frameworks have been utilized in a variety of ways, with a focus towards catalysis. With the incorporation of metal nanoparticles in MOF, the particles inherit the selectivity from the MOF coating and its selective properties as well as enhanced stability from aggregation and leaching during working conditions, and enhanced chemical environments from functionalized linkers (Figure 1.4).

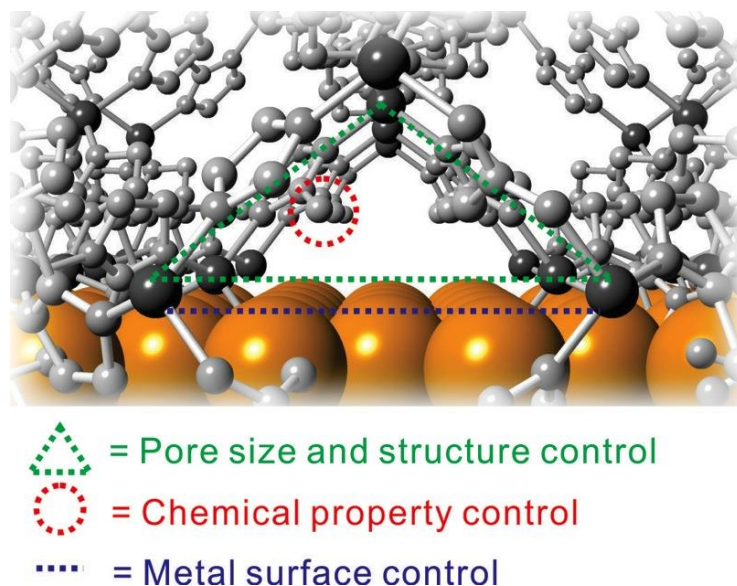


Figure 1.4: Illustration of the nanoparticle with and MOF interface with the tunable properties highlighted. The pore size (green) by changing the linker length, the chemical property (red) by functionalizing the linkers and the metal surface (blue) by incorporating different metal nanoparticles

These hybrid catalyst systems are applicable to a wide variety of chemical transformations in the gas and liquid phase as well as through electrochemical means. In 2014, Zhang *et al*, displayed the size selective hydrogenations of alkenes in liquid phase reactions as well as the reduction of CO₂ in the gas phase using Pt nanoparticles encapsulated within the very chemically and thermally stable UiO-66⁵⁹. UiO-66, with an aperture size of 5 Å, only allowed for the smaller reactant molecules to pass through to interact with the nanoparticle catalyst inside. The larger molecules were excluded from interacting with the nanoparticle. With the ability to tune the pore sizes and the aperture size of MOF, the ability to use them toward selective molecular sieving has advanced.

As with the ability to selectively exclude molecules, MOF coatings can also be used to confine reactants into certain orientations to only allow particular parts of

molecules to come in contact with the encapsulated catalyst. As mentioned previously, heterogeneous catalysis is an immensely important field for pharmaceutical and fine chemicals. As presented in Nature in 2016, Pt nanoparticles incorporated under a layer of MIL-101 was used to perform selective hydrogenation on aldehydes to form the desired unsaturated alcohol products. Due to the nature of MIL-101 and the interaction the reactant molecules had, not only with the confinement from the pores, but also with the nodes, the desired product was produced. In comparison, for the same reaction run where the particles were not encapsulated, an array of the hydrogenation products were formed.⁶⁰ Similar results were seen in an Au@ZIF-8 material used by Stephenson *et al*⁶¹. Additionally, MOF have shown the ability to selectively uptake certain gases over others due to the chemical environments within the pores⁶².

Although MOFs play a role in size selective catalysis, they can also be used in electrochemical reactions to provide stability to the electrochemical catalyst by reducing aggregation and leaching during electrochemical cycling. In addition, MOF is able to provide enhance proton conductivity when the linkers are functionalized. UiO-66, with the composition $Zr_6O_4(OH)_4(1,4\text{-benzenedicarboxylate})_6$,⁶³ has been shown to have proton conductivity when linkers are functionalized.⁶⁴

The goal of this research is to utilize both methods to increase the activity, selectivity, and stability of nanoscale heterogeneous catalyst. First, the use of lattice strain to induce changes in the electronic band structure of nanoparticles will be discussed in order to reduce the poisoning effect during electrochemical oxidations and change the activity of the reaction. Beginning with simple core-shell structures and moving to more complex core-sandwich-shell structures, the degree of lattice strain and

incorporation of a non-precious metal are explored. Using the core-sandwich-shell motif, intermetallic nanoparticles are then synthesized for increased activity in electrochemical methanol oxidation. Finally, in the later part, the top down approach to increased selectivity and stability is discussed. Through use of metal organic framework, mainly UiO-66, nanoparticles are capped to show selective alkene and aldehyde hydrogenation reactions. Lastly, a complex hybrid nanoparticle and MOF composite is used for increase stability for electrochemical oxygen reduction.

1.3 References

- [1.] Schlogl, R., Heterogeneous Catalysis, *Angew. Chem. Int. Ed.*, **2015**, *54*, 3465-3520
- [2.] Bell, A., The Impact of Nanoscience on Heterogeneous Catalysis, *Science*, **2003**, *299*, 1688-1691
- [3.] Satterfield, C.N., Heterogeneous Catalysis in Industrial Practice, *2nd Edition*, United States: N. p., **1991**
- [4.] Somorjai, G.A.; Li, Y., Nanoscale Advances in Catalysis and Energy Applications, *Nano. Lett.*, **2010**, *10*, 2289-2295
- [5.] Zhao, M.; Ou, S.; Wu, C.D., Porous Metal-Organic Frameworks for Heterogeneous Biomimetic Catalysis, *Acc. Chem. Res.*, **2014**, *47*, 1199-1207
- [6.] Khan, J.H.; Schue, F.; George, G.A., Heterogeneous Ring-Opening Polymerization of Lactones for Biomedical Applications, *Polym. Int.* **2009**, *58*, 296-301
- [7.] Friend, C.M.; Xu, B., Heterogeneous Catalysis: A Central Science for a Sustainable Future, *Acc. Chem. Res.*, **2017**, *50*, 517-521
- [8.] Rodriguez-Reinoso, F., The Role of Carbon Materials in Heterogeneous Catalysis, *Carbon*, **1998**, *36*, 159-175
- [9.] Astruc, D.; Lu, F.; Aranzaes, J.R., Nanoparticles as Recyclable Catalysts: The Frontier Between Homogeneous and Heterogeneous Catalysis, *Angew. Chem. Int. Ed.*, **2005**, *44*, 7852-7872

- [10.] Yang, X.F.; Wang, A.; Qiao, B.; Li, J.; Liu, J.; Zhang, T., Single-Atom Catalysts: A New Frontier in Heterogeneous Catalysis, *Acc. Chem. Res.*, **2013**, *46*, 1740-1748
- [11.] Bligaard, T.; Norskov, J.K.; Dahl, S.; Matthiesen, J.; Christensen, C.H.; Sehested, J., The Bronste-Evans-Polanyi Relation and the Volcano Curve in Heterogeneous Catalysis, *J. Catal.*, **2004**, *224*, 206-217
- [12.] Akhade, A.A.; Luo, W.; Nie, X.; Bernstein, N.J.; Asthagiri, A.; Janki, M.J., Poisoning Effect of Adsorbed CO During CO₂ Electroreduction on Late Transition Metals, *Phys. Chem. Chem. Phys.*, **2014**, *16*, 20429-20435
- [13.] Friedrich, K.A.; Geyxers, K.P.; Linke, U.; Stimming, U.; Stumper, J., CO Adsorption and Oxidation on a Pt(111) Electrode Modified by Ruthenium Deposition: An IR Spectroscopic Study, *J. Electroanal. Chem.*, **1996**, 123-128
- [14.] Stamenkovic, V.; Mun, B.S.; Mayrhofer, K.J.J.; Ross, P.N.; Markovic, N.M.; Rossmeisl, J.; Greeley, J.; Norskov, J.K., Changing the Activity of Electrocatalysts for Oxygen Reduction by Tuning the Surface Electronic Structure, *Angew. Chem.*, **2006**, *118*, 2963-2967
- [15.] Thomas, J.M.; Raja, R.; Lewis, D.W., Single-Site Heterogeneous Catalysts, *Angew. Chem. Int. Ed.*, **2005**, *44*, 6456-6482
- [16.] LaMer, V.K.; Dinegar, R.H., Theory, Production and Mechanism of Formation of Monodispersed Hydrosols, *J. Am. Chem. Soc.*, **1950**, *72*, 4847-4854
- [17.] Ahmadi, T.S.; Wang, Z.L.; Green, T.C.; Henglein, A.; El-Sayed, M.A., Shape-Controlled Synthesis of Colloidal Platinum Nanoparticles, *Science*, **1996**, *272*, 1924-1926
- [18.] Wu, H.L.; Kuo, C.H.; Huang, M.H., Seed-Mediated Synthesis of Gold Nanocrystals with Systematic Shape Evolution from Cubic to Trisoctahedral and Rhombic Dodecahedral Structures, *Langmuir*, **2010**, *26*, 12307-12313
- [19.] Niu, W.; Zhang, L.; Xu, G., Shape-Controlled Synthesis of Single-Crystalline Palladium Nanocrystals, *ACS Nano*, **2010**, *4*, 1987-1996
- [20.] Kitchin, J.; Norskov, J.; Barteau, M.; Chen, J., Role of Strain and Ligand Effects in the Modification of the Electronic and Chemical Properties of Bimetallic Surfaces, *Phys. Rev. Lett.*, **2004**, *93*, 156801
- [21.] Tang, W.; Henkelman, G., Charge Redistribution in Core-Shell Nanoparticles to Promote Oxygen Reduction, *J. Chem. Phys.*, **2009**, *130*, 194504
- [22.] Burda, C.; Chen, X. B.; Narayanan, R.; El-Sayed, M. A. Chemistry and Properties of Nanocrystals of Different Shapes, *Chem. Rev.*, **2005**, *105*, 1025-1102

- [23.] Sneed, B.; Young, A.; Tsung, C.K., Building Up Strain in Colloidal Metal Nanoparticle Catalysts, *Nanoscale*, **2015**, 7, 12248-12265
- [24.] Mavrikakis, M.; Hammer, B.; Norskov, J. K., Effect of Strain on the Reactivity of Metal Surfaces, *Phys. Rev. Lett.*, **1998**, 81, 2819-2822
- [25.] Kibler, L. A.; El-Aziz, A. M.; Hoyer, R.; Kolb, D. M., Tuning Reaction Rates by Lateral Strain in a Palladium Monolayer, *Angew. Chem. Int. Ed.*, **2005**, 44, 2080-2084
- [26.] Wang, J. X.; Inada, H.; Wu, L.; Zhu, Y.; Choi, Y.; Liu, P.; Zhou, W.P.; Adzic, R.R., Oxygen Reduction on Well-Defined Core-Shell Nanocatalysts: Particle Size, Facet, and Pt Shell Thickness Effects, *J. Am. Chem. Soc.*, **2009**, 131, 17298- 17302
- [27.] Sra, A. K.; Ewers, T. D.; Schaak, R. E., Direct Solution Synthesis of Intermetallic AuCu and AuCu₃ Nanocrystals and Nanowire Networks, *Chem. Mater.*, **2005**, 17, 758-766
- [28.] Sra, A. K.; Schaak, R. E., Synthesis of Atomically Ordered AuCu and AuCu₃ Nanocrystals from Bimetallic Nanoparticle Precursors, *J. Am. Chem. Soc.*, **2004**, 126, 6667-6672
- [29.] Cable, R. E.; Schaak, R. E., Low-Temperature Solution Synthesis of Nanocrystalline Binary Intermetallic Compounds using the Polyol Process, *Chem. Mater.*, **2005**, 17, 6835-6841
- [30.] Enayati, M. H.; Salehi, M., Formation Mechanism of Fe₃Al and FeAl Intermetallic Compounds During Mechanical Alloying, *J. Mater. Sci.* **2005**, 40, 3933-3938
- [31.] Kovnir, K.; Osswald, J.; Armbruster, M.; Teschner, D.; Weinberg, G.; Wild, U.; Knop-Gericke, A.; Ressler, T.; Grin, Y.; Schloegl, R., Etching of the Intermetallic Compounds PdGa and Pd(3)Ga(7): An Effective Way to Increase Catalytic Activity?, *J. Catal.*, **2009**, 264, 93-103
- [32.] Schaefer, Z. L.; Vaughn II, D. D.; Schaak, R. E., Solution Chemistry Synthesis, Morphology Studies and Optical Properties of Distinct Nanocrystalline Au-Zn Intermetallic Compounds, *J. Alloys and Comp.*, **2010**, 490, 98-102
- [33.] Chen, C.; Kang, Y.; Huo, Z.; Zhu, Z.; Huang, W.; Xin, H. L.; Snyder, J. D.; Li, D.; Herron, J. A.; Mavrikakis, M.; Chi, M.; More, K. L.; Li, Y.; Markovic, N. M.; Somorjai, G. A.; Yang, P.; Stamenkovic, V. R., Highly Crystalline Multimetallic Nanoframes with Three-Dimensional Electrocatalytic Surfaces, *Science*, **2014**, 343, 1339- 1343

- [34.] Chen, S.; Niu, Z.; Xie, C.; Gao, M.; Lai, M. Li, M.; Yang, P., Effects of Catalyst Processing on the Activity and Stability of Pt-Ni Nanoframe Electrocatalysts, *ACS Nano*, **2018**, *Article ASAP*
- [35.] Strasser, P.; Koh, S.; Anniyev, T.; Greeley, J.; More, K.; Yu, C.; Liu, Z.; Kaya, S.; Nordlund, D.; Ogasawara, H.; Toney, M.F.; Nilsson, A., Lattice-strain Control of the Activity in Dealloyed Core-shell Fuel Cell Catalysts, *Nat. Chem.*, **2010**, *2*, 454-460
- [36.] Alayoglu, S.; Nilekar, A. U.; Mavrikakis, M.; Eichhorn, B., Ru-Pt Core-shell Nanoparticles for Preferential Oxidation of Carbon Monoxide in Hydrogen, *Nat. Mater.*, **2008**, *7*, 333-338
- [37.] Tao, F.; Grass, M. E.; Zhang, Y.; Butcher, D. R.; Renzas, J. R.; Liu, Z.; Chung, J.Y.; Mun, B.S.; Salmeron, M.; Somorjai, G. A., Reaction-Driven Restructuring of Rh-Pd and Pt-Pd Core-Shell Nanoparticles, *Science*, **2008**, *322*, 932-934
- [38.] Wang, D.; Xin, H.L.; Hovden, R.; Wang, H.; Yu, Y.; Muller, D. A.; DiSalvo, F. J.; Abruna, H. D., Structurally Ordered Intermetallic Platinum-Cobalt Core-Shell Nanoparticles with Enhanced Activity and Stability as Oxygen Reduction Electrocatalysts, *Nat. Mater.*, **2012**, *12*, 81-87
- [39.] James, S.L., Metal-organic Frameworks, *Chem. Soc. Rev.*, **2003**, *5*, 276-288
- [40.] Lee, J.; Farha, O. K.; Roberts, J.; Scheidt, K.A.; Nguyen, S. T.; Hupp, J. T., Metal-Organic Framework Materials as Catalysts, *Chem. Soc. Rev.*, **2009**, *38*, 1450
- [41.] Zhou, H. C.; Kitagawa, S., Metal-Organic Frameworks (MOFs), *Chem. Soc. Rev.*, **2014**, *43*, 5415-5418
- [42.] Jiang, H. L.; Xu, Q., Porous Metal-Organic Frameworks as Platforms for Functional Applications, *Chem. Commun.*, **2011**, *47*, 3351-3370
- [43.] Li, J. R.; Kuppler, R. J.; Zhou, H. C., Selective Gas Adsorption and Separation in Metal-Organic Frameworks, *Chem. Soc. Rev.*, **2009**, *38*, 1477-1504
- [44.] Horcajada, P.; Gref, R.; Baati, T.; Allan, P. K.; Maurin, G.; Couvreur, P.; Ferey, G.; Morris, R. E.; Serre, C., Metal-Organic Frameworks in Biomedicine, *Chem. Rev.*, **2012**, *112*, 1232-1268
- [45.] Zhuang, J.; Kuo, C. H.; Chou, L. Y.; Liu, D. Y.; Weerapana, E.; Tsung, C. K., Optimized Metal-Organic Framework Nanospheres for Drug Delivery: Evaluation of Small-Molecule Encapsulation *ACS Nano*, **2014**, *8*, 2812-2819

- [46.] Phan, N. T. S.; Le, K. K. A.; Phan, T. D., MOF-5 as an Efficient Heterogeneous Catalyst for Friedel-Crafts Alkylation Reactions, *Appl. Catal. A. Gen.*, **2010**, *383*, 246-253
- [47.] Furukawa, H.; Cordova, K. E.; O'Keefe, M.; Yaghi, O., The Chemistry and Applications of Metal-Organic Frameworks, *Science*, **2013**, *341*, 974
- [48.] Jiang, H. L.; Liu, B.; Akita, T.; Haruta, M.; Sakurai, H.; Xu, Q., Au@ZIF-8: CO Oxidation over Gold Nanoparticles Deposited to Metal-Organic Framework, *J. Am. Chem. Soc.*, **2009**, *131*, 11302-11303
- [49.] Gu, X.; Lu, Z. H.; Jiang, H. L.; Akita, T.; Xu, Q., Synergistic Catalysis of Metal-Organic Framework-Immobilized Au-Pd Nanoparticles in Dehydrogenation of Formic Acid for Chemical Hydrogen Storage, *J. Am. Chem. Soc.*, **2011**, *133*, 11822-11825
- [50.] Aijaz, A.; Karkamkar, A.; Choi, Y. J.; Tsumori, N.; Ronnebro, E.; Autrey, T.; Shioyama, H.; Xu, Q., Immobilizing Highly Catalytically Active Pt Nanoparticles Inside the Pores of Metal-Organic Framework: A Double Solvents Approach, *J. Am. Chem. Soc.*, **2012**, *134*, 13926-13929
- [51.] Zhu, Q. L.; Li, J.; Xu, Q., Immobilizing Metal Nanoparticles to Metal-Organic Frameworks with Size and Location Control for Optimizing Catalytic Performance, *J. Am. Chem. Soc.*, **2013**, *135*, 10210-10213
- [52.] Sugikawa, K.; Furukawa, Y.; Sada, K., SERS-Active Metal-Organic Frameworks Embedding Gold Nanorods, *Chem. Mater.*, **2011**, *23*, 3132-3134
- [53.] Hu, P.; Zhuang, J.; Chou, L.Y.; Lee, H. K.; Ling, X.Y.; Chuang, Y.C.; Tsung, C. K., Surfactant-directed Atomic to Mesoscale Alignment: Metal Nanocrystals Encased Individually in Single-Crystalline Porous Nanostructures, *J. Am. Chem. Soc.*, **2014**, *136*, 10561-10564
- [54.] Zhao, M.; Deng, K.; He, L.; Liu, Y.; Li, G.; Zhao, H.; Tang, Z., Core-Shell Palladium Nanoparticle@Metal-organic Frameworks as Multifunctional Catalysts for Cascade Reactions, *J. Am. Chem. Soc.*, **2014**, *136*, 1738-1741
- [55.] He, L.; Liu, Y.; Liu, J.; Xiong, Y.; Zheng, J.; Tang, Z., Core-Shell Noble-metal@Metal-organic-framework Nanoparticles with Highly Selective Sensing Properties, *Angew. Chem. Int. Ed. Engl.*, **2013**, *52*, 3741-3745
- [56.] Xu, Z.; Yang, L.; Xu, C., Pt@Ui-66 Heterostructures for Highly Selective Detection of Hydrogen Peroxide with an Extended Linear Range, *Anal. Chem.*, **2015**, *87*, 3438-3444

- [57.] Wang, P.; Zhao, J.; Li, X.; Yang, Y.; Yang, Q.; Li, C., Assembly of ZIF Nanostructures around Free Pt Nanoparticles: Efficient Size-Selective Catalysts for Hydrogenation of Alkenes Under Mild Conditions, *Chem. Commun. (Camb)*, **2013**, *49*, 3330-3332
- [58.] Liu, H.; Chang, L.; Chen, L.; Li, Y., *In Situ* One-Step Synthesis of Metal-Organic Framework Encapsulated Naked Pt Nanoparticles without Additional Reductants, *J. Mater. Chem. A*, **2015**, *3*, 8028-8033
- [59.] Zhang, W.; Lu, G.; Cui, C.; Liu, Y.; Li, S.; Yan, W.; Xing, C.; Chi, Y. R.; Yang, Y.; Huo, F., A Family of Metal-Organic Frameworks Exhibiting Size-Selective Catalysis with Encapsulated Noble-Metal Nanoparticles, *Adv. Mater.*, **2014**, *26*, 4056-4060
- [60.] Zhao, M.; Yuan, K.; Wang, Y.; Li, G.; Guo, J.; Gu, L.; Hu, W.; Zhao, H.; Tang, Z., Metal-Organic Frameworks as Selectivity Regulators for Hydrogenation Reactions, *Nature*, **2016**, 76-80
- [61.] Stephenson, C. J.; Whitford, C. L.; Stair, P. C.; Farha, O. K.; Hupp, J. T., Chemoselective Hydrogenation of Crotonaldehyde Catalyzed by an Au@ZIF-8 Composite, *ChemCatChem*, **2016**, *8*, 855-860
- [62.] Chen, B.; Ma, S.; Zapata, F.; Fronczek, F. R.; Lobkovsky, E. B.; Zhou, H.C., Rationally Designed Micropores within a Metal-Organic Framework for Selective Sorption of Gas Molecules, *Inorg. Chem.*, **2007**, *46*, 1233-1236
- [63.] Cavka, J. H.; Jakobsen, S.; Olsbye, U.; Guillou, N.; Lamberti, C.; Bordiga, S.; Lillerud, K. P. A New Zirconium Inorganic Building Brick Forming Metal Organic Frameworks with Exceptional Stability. *J. Am. Chem. Soc.* **2008**, *130*, 13850–13851
- [64.] Piscopo, C. G.; Polyzoidis, A.; Schwarzer, M.; Loebbecke, S. Stability of UiO-66 under acidic treatment: Opportunities and limitations for post-synthetic modifications. *Micro. Meso. Mater.* **2015**, *208*, 30–35

2.0 Electrochemically Induced Surface Metal Migration in Well-Defined Core-Shell Nanoparticles and Its General Influence on Electrocatalytic Reactions

Note: This chapter was published as: Casey N. Brodsky, Allison P. Young, Ka Chon Ng, Chun-Hong Kuo, Chia-Kuang Tsung, "Electrochemically Induced Surface Metal Migration in Well-Defined Core-Shell Nanoparticles and Its General Influence on Electrocatalytic Reactions," ACS Nano, 2014, 8(9), 9368-9378.

Reprinted with permission from Casey N. Brodsky, Allison P. Young, Ka Chon Ng, Chun-Hong Kuo, Chia-Kuang Tsung, Electrochemically Induced Surface Metal Migration in Well-Defined Core-Shell Nanoparticles and Its General Influence on Electrocatalytic Reactions, *ACS Nano*, **2014**, 8(9), 9368-9378. Copyright © 2014 American Chemical Society

URL Link: <https://pubs.acs.org/doi/abs/10.1021/nn503379w>

DOI: 10.1021/nn503379w

2.1 Abstract

Bimetallic nanoparticle catalysts provide enhanced activity, as combining metals allows tuning of electronic and geometric structure, but the enhancement may vary during the reaction because the nanoparticles can undergo metal migration under catalytic reaction conditions. Using cyclic voltammetry to track the surface composition over time, we carried out a detailed study of metal migration in a well-defined model Au-Pd core-shell nanocatalyst. When subjected to electrochemical conditions, Au migration from the

core to the shell was observed. The effect of Pd shell thickness and electrolyte identity on the extent of migration was studied. Migration of metals during catalytic ethanol oxidation was found to alter the particle's surface composition and electronic structure, enhancing the core-shell particles' activity. We show that metal migration in core-shell nanoparticles is a phenomenon common to numerous electrochemical systems and must be considered when studying electrochemical catalysis.

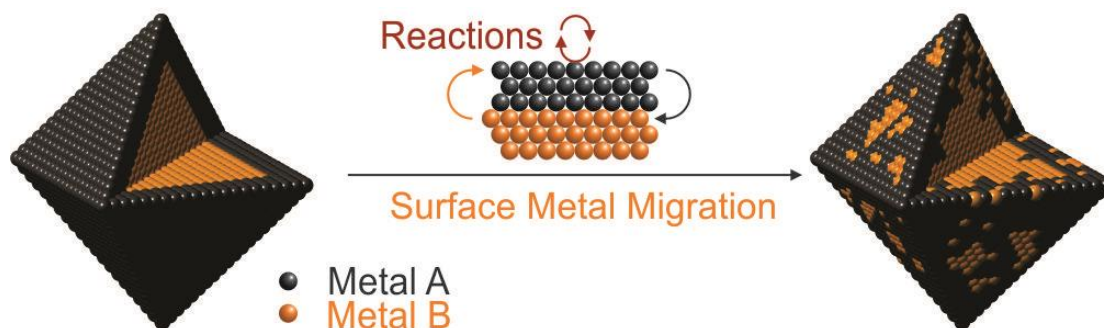
2.2 Introduction

Bimetallic nanoparticles (NPs) often exhibit activity superior to their monometallic counterparts, due to a combination of metal-metal interactions. Many examples of increased catalytic activity on bimetallic core-shell or alloy NPs have been published in the literature.¹⁻⁸ Electronic effects, also called ligand effects or charge redistribution, alter the electronic structure of the metal surface through direct electron interaction between the two metals. The resulting increase in activity can be explained by the position of the surface metal's d-band center in relation to the Fermi level, affecting how strongly reactive adsorbate molecules can bind to the metal surface.⁹⁻¹¹ The geometric effect, or lattice strain, also alters catalytic activity by changing the position of the d-band center. When two metals with different lattice sizes are brought into contact, the crystal lattice near the boundary needs to restructure a small amount to reduce the lattice mismatch. Expansive strain reduces orbital overlap, narrowing the d-band and raising the d-band center, while compressive strain increases overlap, widening the d-band and lowering the d-band center.^{9,12-14} Synergy, or ensemble effects, involves the

availability of specific metal active sites. Many catalytic reactions that take place on a metal surface require a specific type of binding site to achieve the correct orientation, for example, a 3-fold Pd site or a monomer Pt site, while the wrong site can lead to poisoning of the surface or unwanted byproducts. Adding a second metal to an NP catalyst can alter activity by preferentially tuning the types of active sites available to adsorbates.¹⁵⁻¹⁷

While bimetallic and multi-metallic NPs often exhibit improved activity compared to their monometallic counterparts, it is difficult to optimize activity by simply manipulating composition and structure, because metal migration causes the influence of electronic, geometric, and ensemble effects to change over time. Bimetallic nanoparticles undergo metal migration when subjected to reaction conditions, caused by surface energy differences and oxidizing or reducing agents in the system (Scheme 2.1). This has attracted great attention in recent catalysis research.¹⁸ Using the popular core-shell structure as an example, the core metal may have lower surface energy than the shell metal, so when given enough energy, the core metal will migrate to the particle surface in order to lower the overall surface energy. Experimental and computational work has been done to study heat-induced metal migration. Computational studies modeled the high-temperature melting of Au-Pt core-shell NPs, finding the migration of Au from core to shell to be inhomogeneous and dependent on shell thickness.¹⁹ A recent experimental study used various calcination temperatures and gas environments to migrate Au in Au-Pt core-shell NPs and manipulate the ratio of Pt to Au in the alloyed shell, finding that the migration of Au from core to shell increased catalytic activity in electro-oxidations. They attributed this result to electronic and synergetic effects: the Au in the shell both altered Pt's electronic structure and manipulated the types of active sites available.²⁰ It has also

been found that metal migration can occur under catalytic reaction conditions. In gas phase heterogeneous catalysis, both the reaction temperature and the gases present in the reaction mixture affect metal migration. It was shown that in Rh-Pt and Rh-Pd NPs, Rh and Pd or Pt alternately and reversibly migrate to the surface as the gas environment is changed. Metallic Pd and Pt have lower surface energies than Rh, so they move to the surface under reducing conditions, but Rh forms more stable oxides, so it moves to the surface under oxidizing conditions.²¹ A similar finding was achieved with Au-Pd NPs under a CO/O₂ atmosphere, in which the ratio of gases present determined the surface composition of the particles.²² Migration has also been seen *in situ* in electrocatalytic reaction conditions, in the cases of Pt-Ni²³ and Pt-Cu.²⁴ In many cases, the compositional and structural changes resulting from metal migration can lead to higher activity, but may also decrease durability.



Scheme 2.1: Surface metal migration of core-shell nanoparticles. In the case of this chapter, metal “A” is Pd while metal “B” is Au, where the migration occurs during electrochemical cycling.

While the impact on catalysis of electrochemically induced metal migration has been shown, such study is less extensive compared to work on synthetic routes and catalysis for metal core-shell nanoparticles. Here, we study metal migration induced by

reaction conditions in a well-defined model Au-Pd core-shell nanocatalyst; a system that has been well studied synthetically.²⁵⁻²⁸ Pd is an important catalytic metal for a number of energy- and industrially relevant reactions,²⁹⁻³³ and Au has been shown to increase Pd's activity in many cases,^{34,35} so this an important bimetallic system in which to study migration. Au has a lower surface energy than Pd and is prone to outward migration from core to shell.³⁶ The structural and compositional changes resulting from metal migration need to be studied in order to understand the stability of Au-Pd bimetallic catalysts, as well as to elucidate the real active surface of the catalyst, which may be different from that of the as-synthesized NPs. Migration in Au-Pd NPs has been studied theoretically *via* high-temperature simulations³⁶ and in gas phase heterogeneous catalysis,³⁷ but to our knowledge it has not been studied under electrocatalytic conditions. In this work, well-defined Au-Pd core-shell octahedral NPs were synthesized as a model catalyst and tested under a number of different electrochemical conditions to understand the mechanism and catalytic consequences of *in situ* metal migration. Octahedral particles were chosen because the {111} crystal facet is the most stable and close-packed low-index facet, and a 30 nm particle size was chosen because the relatively large size allows good control over shape and shell thickness. Different morphologies and sizes will be studied in the future; for an initial study, the good stability and well-controlled structure of the 30 nm octahedra provide an excellent model catalyst platform. We show that electrochemical cycling during both voltammetric profiles and catalytic ethanol oxidation induces surface composition changes, that the mechanism of change likely involves both Au migration and Pd oxidative dissolution, and that the compositional changes affect catalytic activity through a combination of bimetallic interactions.

2.3 Experimental Methods

2.3.1 Chemicals

L-Ascorbic acid ($C_6H_8O_6$, 99 %), hydrochloric acid (HCl, 37 %), palladium(II) chloride ($PdCl_2$, 99 %), gold(III) chloride trihydrate ($AuCl_3 \cdot 3H_2O$, ~50 % Au by wt), sodium citrate tribasic dihydrate ($Na_3C_6H_5O_7 \cdot 2H_2O$, 99.5 %), and perchloric acid ($HClO_4$, 70 %) were all obtained from Sigma-Aldrich. Cetyltrimethylammonium bromide (CTAB, 98 %) was obtained from Calbiochem. Cetyltrimethylammonium chloride (CTAC, 99 %) was obtained from Fluka. Sulfuric acid (H_2SO_4 , 95 %) and sodium hydroxide (NaOH, 95 %) were obtained from BDH. Nitrogen gas (N_2 , 99 %) was obtained from Airgas. Ethanol (CH_3OH , 99.8 %) was obtained from Acros. Deionized water (DI Water, 18.2 M Ω) was used in all procedures. Hydrochloric acid was used to prepare the acidic precursors for gold and palladium. Concentrated HCl was diluted, added to a beaker containing the metal chloride salt, and stirred under gentle heating to produce the 0.01 M stock solutions.

2.3.2 Synthesis of 30 nm Au Nanooctahedra

First, deionized water (97 mL) was added to a glass hydrothermal vessel that contained CTAB (550 mg), and sonication was applied to dissolve the CTAB. Next, a 0.01 M solution of $HAuCl_4$ (2.500 mL) was added, along with a 0.1 M solution of sodium citrate (0.500 mL). The hydrothermal vessel was placed in an oven at 110 °C for 24 hours. The final solution was centrifuged at 6000 rpm for 20 min. This process was

repeated two more times to ensure that any excess surfactant was removed. Lastly, the resulting clear supernatant was discarded, and the particles were redispersed in deionized water (10 mL).

2.3.3 Synthesis of ~35 nm Au-Pd Core-Shell Nanooctahedra

First, deionized water (10 mL) was added to a 20 mL vial containing CTAB (50 mg), and sonication was applied to dissolve the CTAB. Then, a portion of 30 nm Au octahedral seeds (0.500 mL) was added to the solution. Next, a portion of 0.01 M solution of H_2PdCl_4 (15 or 50 μL) was added, along with a 0.04 M solution of ascorbic acid (0.100 mL). A stir bar was added, and the capped vial was placed in a water bath at 40 °C for 24 hours with gentle stirring. These particles were washed by centrifugation at 6000 rpm for 10 minutes. This process was repeated two more times. The final clear supernatant was discarded, and the particles were redispersed in deionized water (1 mL). Synthesis with 15 μL of 0.01 M H_2PdCl_4 gave core-shell nanooctahedra with a ~1.5 nm shell, while synthesis with 50 μL of 0.01 M H_2PdCl_4 gave core-shell nanooctahedra with a ~4.5 nm shell.

2.3.4 Characterization

Samples were prepared for TEM by washing several times with DI water and placing 1.0 μL droplets of particle solutions on carbon-coated copper grids, which were then allowed to dry in air. The instrument used for TEM was a JEOL JEM2010F operated at 200 kV. High-resolution STEM and EDX mapping experiments were performed on a

FEI Probe Cs corrected Titan operating at 200 kV. The high-angle annular dark field (HAADF) images were acquired by a Fischione HAADF detector, and the EDX maps were acquired by ChemiSTEM technology with four windowless SDD detectors. This instrument incorporates the condenser spherical aberration corrector and X-FEG with probe current 0.4 nA in a 0.31 nm spot and can achieve a resolution of 0.08 nm as well as efficient X-ray collection rate.

2.3.5 Electrochemical Measurements

A concentrated particle solution (5 μ L) was deposited onto the previously alumina-polished surface of a glassy carbon working electrode (CH Instruments). A typical three-electrode system was used to perform the electrochemical experiments: a glassy carbon working electrode with deposited particles, a saturated calomel electrode (SCE) reference electrode, and a platinum auxiliary electrode (both CH Instruments) were connected to a potentiostat system (BioLogic VSP). The electrodes were put into a three-neck flask containing aqueous electrolyte solutions that had been previously bubbled with nitrogen gas. Voltammetric profiles were carried out in 0.5 M H₂SO₄ scanning from -0.19 to 1.46 V at 50 mV/s; in 0.5 M HClO₄ from -0.19 to 1.46 V at 50 mV/s; and in 0.5 M KOH from -1.0 to 0.6 V at 50 mV/s. Ethanol oxidation was performed in a 1 M KOH + 1 M ethanol solution, scanning from -0.8 to 0.3 V at a scan rate of 50 mV/s. The current was normalized by Pd area, determined by measuring the hydrogen adsorption/desorption charge in a sulfuric acid blank scan.

2.4 Results and Discussion

2.4.1 Synthesis of Au-Pd Core-Shell Nanooctahedra Electrocatalysts

An aqueous phase, cetyltrimethylammonium bromide (CTAB)-capped synthetic method similar to that employed in our recent work³⁸ was used to create 30-35 nm Au-Pd core-shell nanooctahedra. As an ionic capping agent, CTAB is relatively loosely associated with the NP surface and can be removed by a combination of centrifugation in water and potential cycling, so it is a suitable capping agent with which to study surface structure and catalysis. Large, well-defined NPs with tunable shell thicknesses are suitable model catalysts for the study of metal migration, so hydrothermally synthesized Au octahedral NPs with a corner-to-corner length of 30 nm were chosen as seeds, as reported in the literature.³⁹ Pd was grown epitaxially over the Au seeds, and by varying the amount of Pd precursor in the growth solution, Pd shells of tunable thicknesses were obtained. Adding 15 μL of 0.01 M H_2PdCl_4 to the growth solution yielded Pd shells approximately 1.5 nm thick (thin shell), while adding 50 μL of 0.01 M H_2PdCl_4 to the growth solution yielded Pd shells approximately 4.5 nm thick (thick shell). Transmission electron microscopy (TEM) images of the Au seeds and thin and thick shell Au-Pd octahedra are shown in Figure 2.1. Figure 2.1d shows the continual lattice fringes from the Au core to Pd shell phases, indicating epitaxial growth. Both particle types have well-defined structures and good monodispersity, which allows us to perform the thorough electrochemical study discussed below.

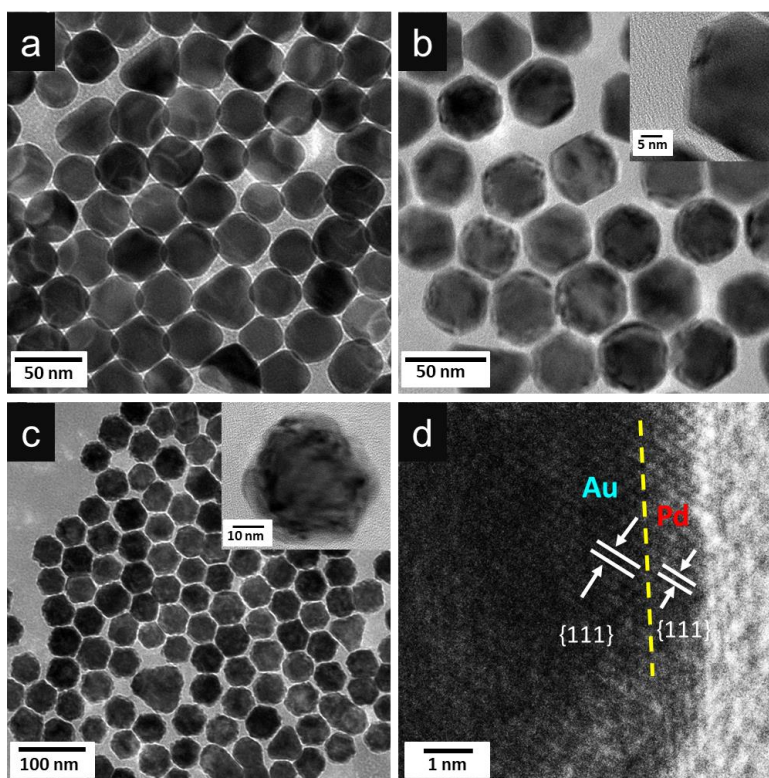


Figure 2.1: TEM images of (a) Au nanooctahedra, (b) thin shell Au-Pd nanooctahedra, and (c) thick shell Au-Pd nanooctahedra and (d) HR-TEM image of a thin shell octahedron's Au-Pd interface, showing epitaxial growth. Insets in (b) and (c) show magnified images of a single Au-Pd particle.

2.4.2 Au Migration through Electrochemical Blank Scans

Voltammetric profiles of the thin shell octahedra were performed in 0.5 M H₂SO₄ to characterize the surface composition of the particles over time. The charges associated with characteristic peaks in the profile are proportional to Au and Pd surface areas: the peaks for hydrogen adsorption and desorption on Pd (Pd-H) occur between -0.19 and 0.06 V, and the peak for oxide reduction on Au (Au-ox) occurs on the cathodic scan

between 1.0 and 0.8 V.²⁰ Cycles 3, 10, and 20 of thin shell octahedra profiles are shown in Figure 2.2a. The Pd-H peaks decrease and the Au-ox peaks increase in magnitude over time, indicating increasing amounts of Au exposed on the surface. Quantitative surface areas can be obtained by averaging the Pd-H adsorption and desorption peak charges and dividing by $212 \mu\text{C}/\text{cm}^2$, 40 and dividing the Au-ox peak charge by $340 \mu\text{C}/\text{cm}^2$ to give surface area in cm^2 (Figure 2.3 and in equation 2.1 and 2.2).²⁰

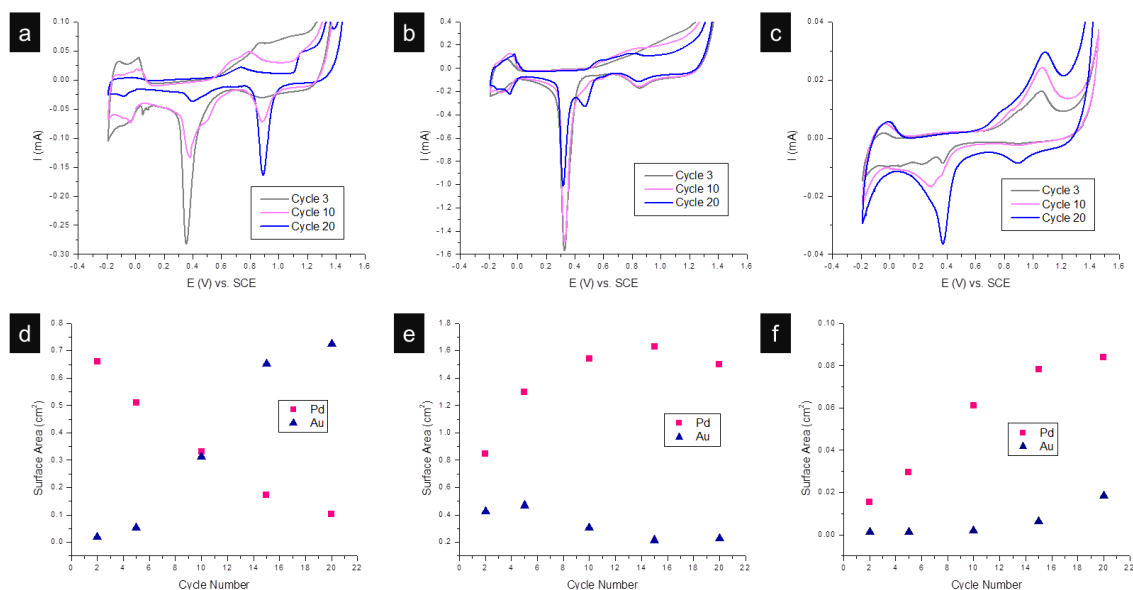


Figure 2.2: Voltammetric profiles of NPs in 0.5 M H_2SO_4 of (a) thin shell Au-Pd core-shell octahedra, (b) a mixture of pure Pd and Au NPs, and (c) thick shell Au-Pd core-shell octahedra. (d-f) Plots of Pd and Au surface areas calculated from voltammetric profile charges versus cycle number for thin shell Au-Pd core-shell octahedra, the Pd/Au mixture, and thick shell Au-Pd core-shell octahedra, respectively.

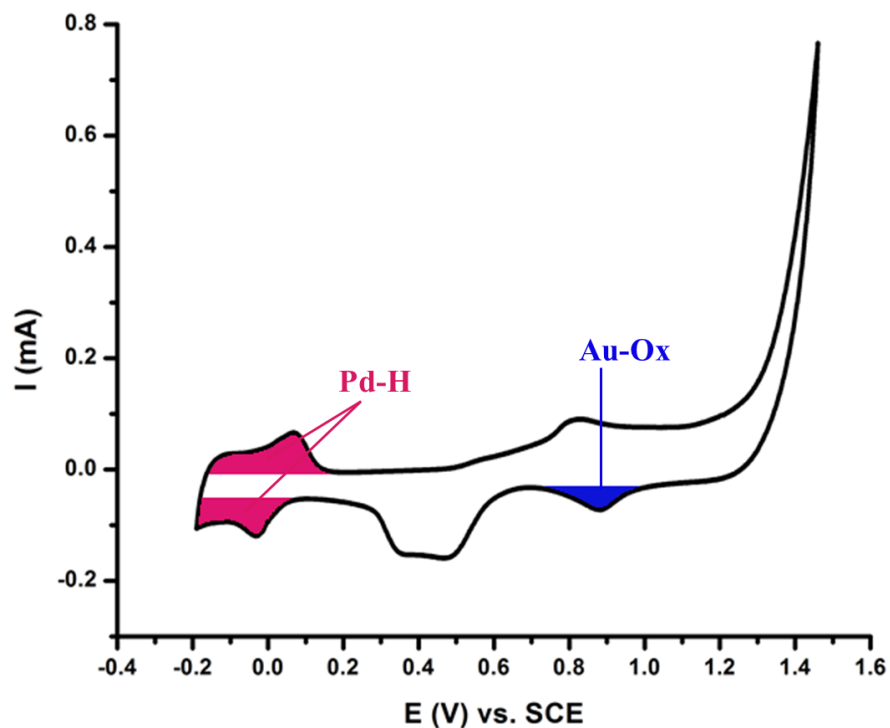


Figure 2.3: Method of quantifying Pd and Au surface areas, shown on a voltammetric profile of Au-Pd thin shell core-shell octahedra.

$$(2.1) A_{Pd}(cm^2) = \frac{(Q_{Pd-H(+)} + Q_{Pd-H(-)})\mu C}{2.212\mu C/cm^2}$$

$$(2.2) A_{Au}(cm^2) = \frac{(Q_{Au-Ox})\mu C}{340\mu C/cm^2}$$

These surface areas were calculated every five cycles and are plotted against cycle number in Figure 2.2d. This plot shows that the Pd surface area steadily decreases while the Au surface area steadily increases. This change in surface composition could occur either by outward migration of Au from the core to the shell or by dissolution of Pd from the particle surface into the electrolyte, or by a combination of both. As a control experiment, a mixture of pure Au and Pd NPs was synthesized and tested under the same

voltammetric profile conditions, shown in Figure 2.2b,e. After 20 cycles, little change in the shape or magnitude of the Pd-H and Au-ox peaks can be seen, and accordingly, the plot of surface area versus cycle number shows little change over time. The Pd surface area actually increases slightly at first, likely due to the surface becoming cleaner: while centrifugation removes excess solution CTAB, some CTAB molecules still remain associated with the surface after centrifugation,⁴¹ and this portion is stripped away by potential cycling. This CTAB cleaning effect is likely also present in the case of the thin shell octahedra, but the Au migration is so rapid in this case that it dwarfs the cleaning effect and Pd surface area immediately decreases. In addition, the same test was performed on the thick shell octahedra, shown in Figure 2.2c,f. The results are more similar to that of the Au/Pd mix than that of the thin shell octahedra: the Pd area increases slightly over the span of 20 cycles, likely due to surface cleaning. The near steady Pd areas in Figure 2.2e,f indicate that Pd dissolves relatively slowly into solution under these conditions; it takes 15 cycles to initiate a slow surface area decrease of pure Pd NPs, as compared with the immediate Pd surface area decrease in the case of the thin Pd shell, which provides evidence that the observed thin shell surface changes are not solely caused by Pd dissolution. The outward migration of the Au core atoms plays a more important role here. The rapid decrease in Pd surface area observed in Figure 2.2d could be due to Au atoms overtaking the surface, or that Au migration destabilizes Pd surface atoms and thus initiates Pd dissolution. The Pd shell must be thin to facilitate these changes; in Figure 2.2c,f the Pd shell is too thick to allow Au to migrate to the surface and/or cause Pd to dissolve.

The evolution in shape and peak placement of the voltammetric profiles in Figure 2.2 provides more information about the structural changes occurring during the electrochemical cycling. The {100} and {111} facet dominant surfaces of Pd NPs have unique peak potentials, as the two facets adsorb hydrogen and form oxides at different energies.⁴² In the hydrogen adsorption/desorption region (-0.19 to 0 V), {100} facets exhibit peaks to the right of {111}; in the oxidized Pd formation region (0.6 to 0.9 V anodic), {100} facets exhibit peaks to the left of {111}; and in the reduction of the oxidized Pd region (0.2 to 0.6 V cathodic), {100} facets exhibit peaks to the right of {111}. It can be seen in Figure 2.2a,b that with increased cycling a new peak grows in at 0.5 V on the cathodic scan. This peak corresponds to the reduction of oxidized Pd on a {100} facet and grows in next to the peak at 0.35 V corresponding to the reduction of oxidized Pd on a {111} facet. In addition, the Pd-H region peaks shift to the right with increased cycling, and the oxidized Pd formation peaks shift to the left. Each of these changes indicates that the fraction of exposed {111} facets decreases while the fraction of exposed {100} facets increases. This structural change makes sense when considering Pd dissolution under these electrochemical conditions. In an octahedral NP, the corners are the most under coordinated, and thus of highest energy, and are likely to change more easily than the more stable {111} faces, creating truncated cuboctahedral morphologies. The change of corners exposes {100} facets and gives rise to the above-mentioned {100} characteristic CV peaks. These changes in peak placement are seen to a lesser extent, however, in the case of thick shell octahedra in Figure 2.2c, corroborating the results of surface area measurements in Figure 2.2d,e,f that the lowest amount of Pd dissolution is seen in the case of the thick shell octahedra.

It is likely that the migration of Au from core to shell results from differences in surface and cohesive energies. Pd has a larger cohesive energy than Au; it is more favorable for Pd to be highly coordinated in the volume of a solid rather than under coordinated on the edge, and this effect is stronger for Pd than for Au. In addition, Au has a lower surface energy than Pd, which combined with the cohesive energy effect is a strong driving force for Au atoms to diffuse preferentially to the NP surface and displace Pd atoms.²² In one study, this energetic effect was found to induce irreversible Au migration only in Au-Pd NPs with a sufficiently thin shell, which correlates with the results in this work.⁴³ In a gas phase environment, the metal with lower surface energy tends to migrate outward under reducing conditions, while the more easily oxidized metal migrates outward under oxidative conditions.²¹ In an electrochemical environment, the condition switches from oxidative to reducing between every scan, but the same principles may apply; on the cathodic scans the lower surface energy Au migrates outward, and on the anodic scans Pd would be expected to oxidize and migrate outward. However, it has been found that the alloying of Au with Pd reduces the number of unoccupied electronic states in Pd's d-band, inhibiting Pd oxidation.^{43,44} It is possible that as Au migrates outward and the NP shell becomes alloyed, Pd can resist oxidation on the anodic scans and Au is able to remain on the surface.

2.4.3 TEM/STEM-EDX Characterization of Au-Pd Nanooctahedra after Electrochemical Blank Scans

TEM images were taken of the thin shell Au-Pd octahedra before and after 20 voltammetric profile cycles in 0.5 M H₂SO₄, shown in Figure 2.4. In order to have a

tangible amount of material to collect off of the electrode after cycling, it was necessary to load the NPs onto a conductive carbon Vulcan XC-72 support before deposition onto the electrode. Figure 2.4b,c shows that the octahedral shape of the NPs is largely maintained during cycling, although there may be some rounding of the corners into a cuboctahedral shape due to dissolution at the corners as discussed above, and Figure 2.4c may indicate the retention of a core-shell structure. TEM provides little contrast between Au and Pd atoms, however, so the existence of a core-shell structure or alloyed shell cannot be determined conclusively, and due to varied orientation on the three dimensional carbon support, it is difficult to ascertain the exact NP shape.

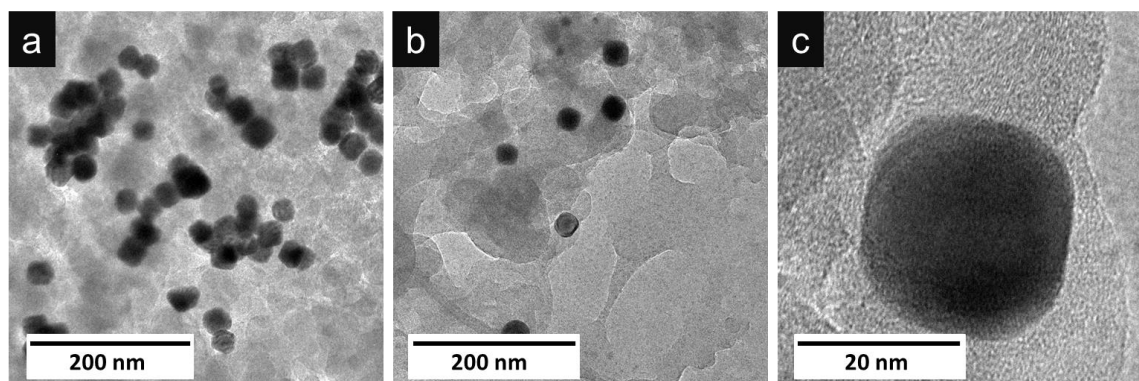


Figure 2.4: TEM images of thin shell Au-Pd core-shell octahedra on a Vulcan XC-72 support (a) before and (b, c) after 20 voltammetric profile cycles in 0.5 M H₂SO₄.

Scanning transmission electron microscopy (STEM) equipped with energy-dispersive X-ray spectroscopy (EDX) was used to study the Au-Pd thin shell core-shell octahedra before and after 20 cycles of voltammetric profile scanning in 0.5 M H₂SO₄. The resulting line scans are shown in Figure 2.5, along with crystal models depicting what we believe to be the Au-Pd structures before and after voltammetric profile scanning. The Pd line scan (red) before cycling has a sharp peak at each end, indicative of

a well-defined core-shell structure; the as-synthesized octahedra have a clear boundary between the Au core and Pd shell. The Pd line scan after cycling, on the other hand, lacks this characteristic feature and rather has a smooth bell curve shape similar to that of Au (blue), indicating the presence of both metals in the shell due to Au migration. The presence of both Au and Pd in the particle shell is corroborated by the presence of both Au and Pd peaks in the voltammetric profiles. STEM elemental mapping was also obtained of the Au-Pd octahedra, shown in Figure 2.6. The before and after maps appear similar, but it is important to note that even after cycling there remains virtually no Pd in the interior of the particle. This indicates that while Au migrates to the shell, there is little to no migration of Pd toward the core. Therefore, one possible mechanism of compositional change is that Au atoms migrate to the shell and displace Pd atoms, which then dissolve into solution instead of dissolving back into the interior of the NP. Or, Pd atoms first dissolve from the shell surface into solution, and Au atoms migrate into the shell to fill the vacancies left behind. The latter may be more likely, because when Pd atoms dissolve out of the shell, they leave high-energy, under coordinated sites and it becomes energetically favorable for Au atoms to fill these sites. The results of voltammetric profiles and surface area quantification (Figure 2.1) indicate that Pd does not dissolve into the solution on its own, as little decrease in Pd area was seen for pure Pd particles or a thick Pd shell. This implies that some modification or influence by the Au core may be needed to induce Pd dissolution and that the processes of Au migration and Pd dissolution are closely related.

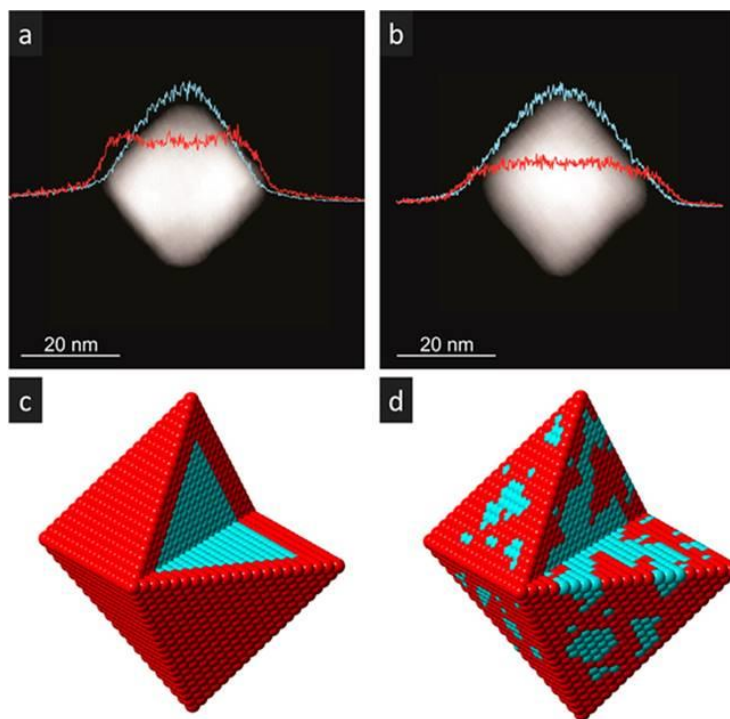


Figure 2.5: EDX line scans of Au-Pd thin shell core-shell octahedra on a Vulcan XC-72 support (a) as synthesized and (b) after 20 voltammetric profile cycles in 0.5 M H₂SO₄. (c, d) Crystal models of what we believe the NPs look like before cycling (core-shell) and after cycling (core-alloyed-shell). Pd is shown in red; Au in blue.

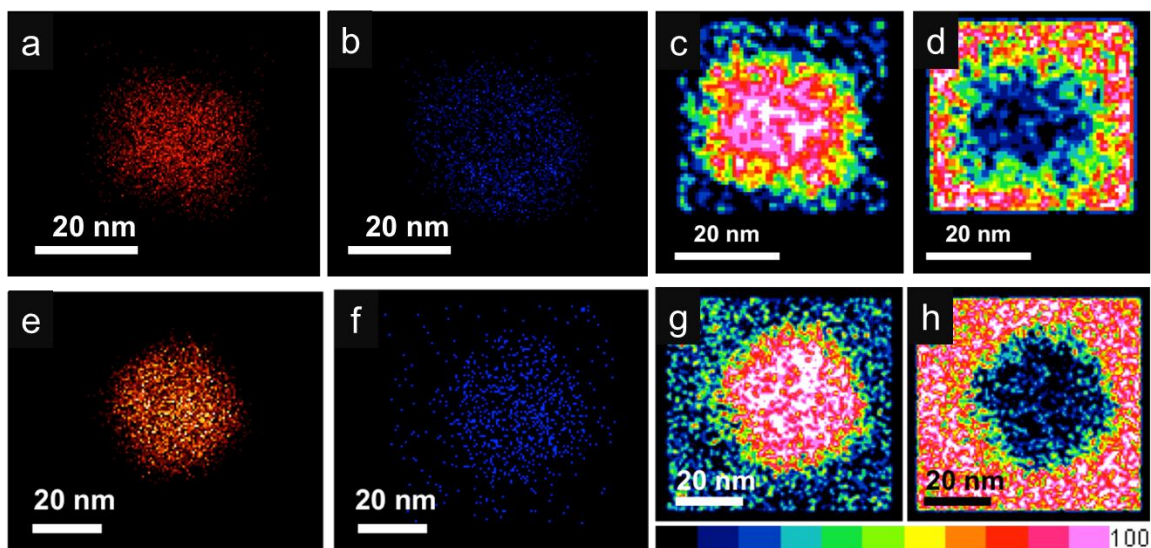


Figure 2.6: STEM/EDX of elemental mapping and quantification mapping of Au-Pd thin shell core-shell octahedra on Vulcan XC-72 support (a-d) as synthesized and (e-h) after 20 voltammetric profile cycles in 0.5 M H₂SO₄. Au is shown in red; Pd in blue. In the quantification maps pink indicates a high concentration of the element while black indicates a low concentration.

2.4.4 Electrolyte Effect on Au Migration during Electrochemical Blank Scans

Next, the effect of electrolyte on Au migration was studied by comparing voltammetric profiles of thin shell Au-Pd octahedra in 0.5 M sulfuric acid, perchloric acid, and potassium hydroxide, shown in Figure 2.7. These three electrolytes are the most commonly used in electrochemical NP characterization and were thus tested in order to gain a general understanding of metal migration behavior in voltammetric profiles, in both acidic and alkaline solutions. In sulfuric acid, a drastic change in Pd-H and Au-ox peaks can be seen between cycles 3 and 20; by cycle 20 the Pd-H peaks have diminished to almost nothing and the Au-ox peak has grown large. In perchloric acid, on the other

hand, the Pd-H and Au-ox peaks in cycles 3 and 20 differ minimally, and a drastic change as seen in sulfuric acid is not seen until cycle 50. In KOH, no change is seen even after 50 cycles. A different voltage range is needed for the KOH scans, but it has been shown that the characteristic peaks fall in the same relative positions;⁴⁵ thus the lack of change in the Pd-H and Au-ox peaks still indicates little to no migration/ dissolution. In addition, the changes in peak placement with repeated cycling discussed above are seen in Figure 2.7a,b but not c, again indicating little to no Pd dissolution in the KOH electrolyte. These results indicate that Au is able to migrate the fastest, and/or Pd dissolves the fastest, in sulfuric acid, slowly in perchloric acid, and not at all in an alkaline environment. The difference in migration/dissolution between acid electrolytes likely results from the different anions in solution. It has been reported that Pd's anodic oxidation and dissolution occurs to a different extent depending on the electrolyte.⁴⁶ The presence of anions in solution may facilitate the formation of dissolution intermediates or products by forming complexes with Pd cations, so the anion identity can affect the rate of dissolution. ClO_4^- anions are known to promote Pd dissolution to a lesser extent,⁴⁷ and to adsorb to Pd surfaces to a lesser extent,⁴⁸ than $\text{HSO}_4^-/\text{SO}_4^{2-}$. Thus, the HClO_4 electrolyte interacts less with the Pd surface and does not induce migration/dissolution as fast as H_2SO_4 .

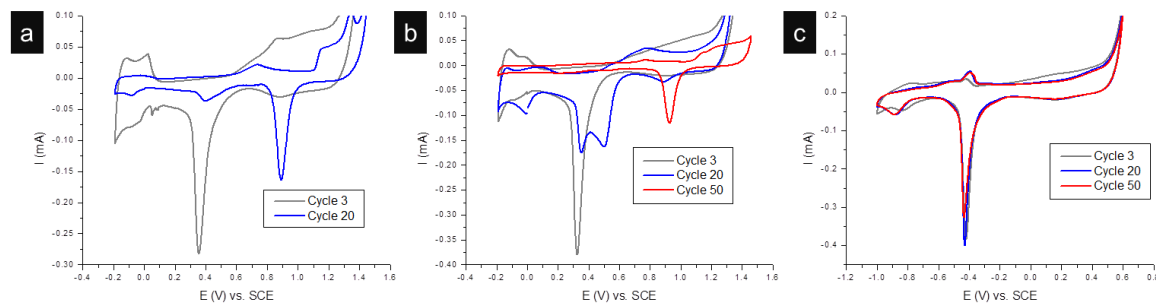


Figure 2.7: Voltammetric profiles of thin shell Au-Pd core-shell octahedra in (a) 0.5 M H_2SO_4 , (b) 0.5 M HClO_4 , and (c) 0.5 M KOH . A drastic change in surface composition is seen in H_2SO_4 , while less change is seen in HClO_4 and no change is seen in KOH .

As noted above, the potential range for the KOH profiles is different than that of the acidic electrolytes, only scanning to 0.6 V, so it is possible that a higher anodic potential is needed to induce Au migration and Pd dissolution, resulting in no compositional change in the KOH profile. We also note that there is no sulfate anion present in the KOH experiment, so the anion effect may also be at play in this system; OH^- anions may not facilitate Pd dissolution to the same extent as ClO_4^- and $\text{HSO}_4^-/\text{SO}_4^{2-}$. To further study the effect of pH on metal migration, voltammetric profiles of thin shell Au-Pd octahedra were obtained in pH 4, 7, and 10 0.5 M SO_4^{2-} electrolyte solutions, shown in Figure 2.8. Migration is observed in the pH 4 profile, as evidenced by the disappearance of the Pd-H peaks and the appearance of the Au-ox peak, while little to no migration is observed in the profiles at pH 7 and 10. In addition, the migration at pH 4 is observed to a lesser extent than that at pH 0 (0.5 M H_2SO_4 in Figure 2.5a). Because the characteristic Pd-H and Au-ox peaks occur at different potentials depending on the electrolyte pH, slightly different potential windows were necessary for each experiment (pH 0: -0.19 to 1.49 V, pH 4: -0.5 to 1.26 V, pH 7 and 10: -1.0 to 1.2 V). However, the

anodic potentials are sufficiently high in each case to fully oxidize both Pd and Au, so the trend observed is due to differences in pH rather than potential. It is known that Pd dissolution occurs to a greater extent at lower pH,⁴⁷ and it is likely that a sufficiently acidic electrolyte is necessary in this system to induce Pd dissolution and Au migration. To limit unwanted metal migration in bimetallic catalyst systems, therefore, it may be beneficial to perform reactions in an alkaline environment when possible.

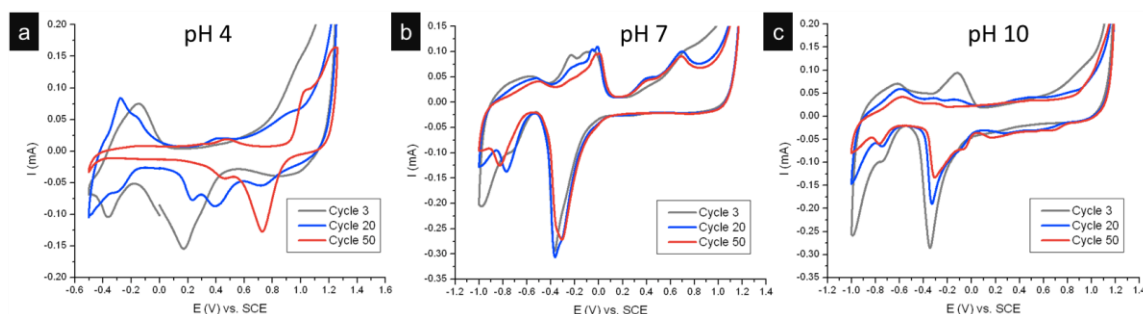


Figure 2.8: Voltammetric profiles of thin shell Au-Pd core-shell octahedra in 0.5 M SO_4^{2-} solutions at (a) pH 4, (b) pH 7, and (c) pH 10. Metal migration is observed in (a) by the disappearance of the Pd-H peaks and the appearance of the Au-ox peak, while little to no migration is observed in (b, c).

2.4.5 Au Migration During Electrochemical Ethanol Oxidation (EOR)

Next, the migration of Au was studied under catalytic conditions. Ethanol electro-oxidation is an important fuel cell reaction and, as such, has become a popular characterization method with which to test the activity of metal nanoparticles. While it is a widely utilized reaction, the effect of metal migration on ethanol oxidation activity in such a well-defined system is unstudied, making it a perfect model reaction for this work. The ethanol oxidation reaction (EOR) in an alkaline electrolyte was performed on the

thin and thick shell Au-Pd octahedral NPs to study both the effect of migration on electrocatalysis and the effect of shell thickness on migration. In order to compare activity of the two NP types, an electrochemically active surface area (ECSA) measurement with which to normalize current is needed. CO stripping is generally the best method for ECSA quantification, but did not give readable currents for these NPs. Voltammetric profiles can also be used to calculate ECSA, but as discussed above, these scans alter the NP surface. Instead, “half” blank scans, cycling from 0.19 to 0.3 V, were performed, thus avoiding the highly anodic region that causes Au migration and/or Pd dissolution. After 20 cycles of “half” blank scans, no change was seen, indicating no surface modification (Figure 2.9). Pd ECSA was determined by averaging the Pd-H peaks and dividing by $212 \mu\text{C}/\text{cm}^2$ as above. Two thousand cycles of ethanol oxidation were performed, and cycles 2, 500, and 2000 for thin and thick shell Au-Pd octahedra are shown in Figure 2.10. In the case of thin shell octahedra, two main peaks are present until about cycle 400, at which point two new peaks appear. These peaks are labeled I-IV in Figure 2.10a. Forward peak I and backward peak IV are in positions characteristic of ethanol oxidation on Pd,⁴⁹ while forward peak II and backward peak III are characteristic of ethanol oxidation on Au (Figure 2.11).⁵⁰ The presence of Au peaks indicates again that during electrochemical cycling Au migrates from the NP core to the shell. The normalized current densities of these peaks were measured every one hundred cycles and are plotted against cycle number in Figure 2.10c,d. For the thin shell octahedra, Pd's current density peaks around cycle 400, near $80 \text{ mA}/\text{cm}^2$, and begins to decrease steadily as Au peaks appear. The Au peaks hit a maximum at about 800 cycles before beginning to steadily decrease. The activity of all four peaks eventually flattens out near 10

mA/cm². The presence of Au peaks indicates migration of Au from core to shell, which interestingly does not occur until cycle 400, while occurring in the first 10 cycles in sulfuric acid voltammetric profiles. This may be due to the alkaline electrolyte or the low anodic voltage (the scans cycle from -0.8 to 0.3 V). The case of thick shell Au-Pd octahedra is strikingly different; Au peaks II and III never appear, indicating no migration of Au from core to shell, and the Pd activity reaches a maximum at cycle 100 near 14 mA/cm² and decreases rapidly, flattening out near 1 mA/cm². Thus, the thick Pd shell prevents Au migration, but the thin Pd shell provides a much higher overall current density of 80 versus 14 mA/cm² at peak and 10 versus 1 mA/cm² after 2000 cycles. It is also important to note that the thin shell octahedra increase in activity for the first 400 cycles; as Au moves toward the surface, it promotes Pd EOR activity, but when the Au surface coverage is too high, activity decreases.

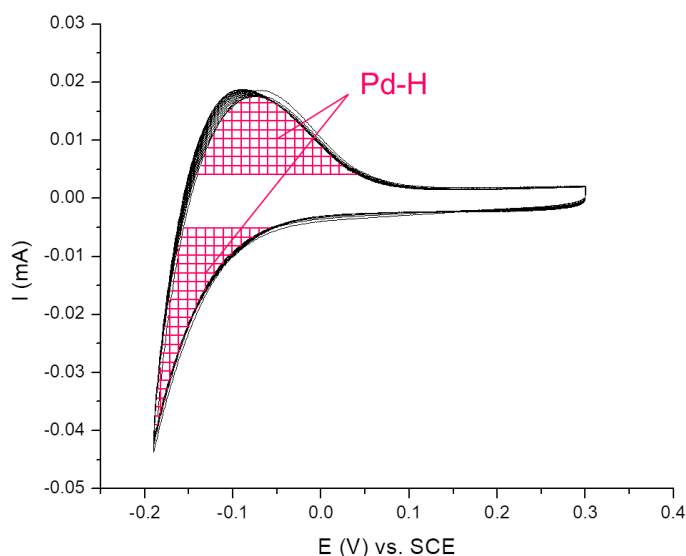


Figure 2.9: “Half” voltammetric profile blank scans of Au-Pd thin shell core-shell octahedra, scanning from -0.19 V to 0.3 V at a scan rate of 50 mV/s.

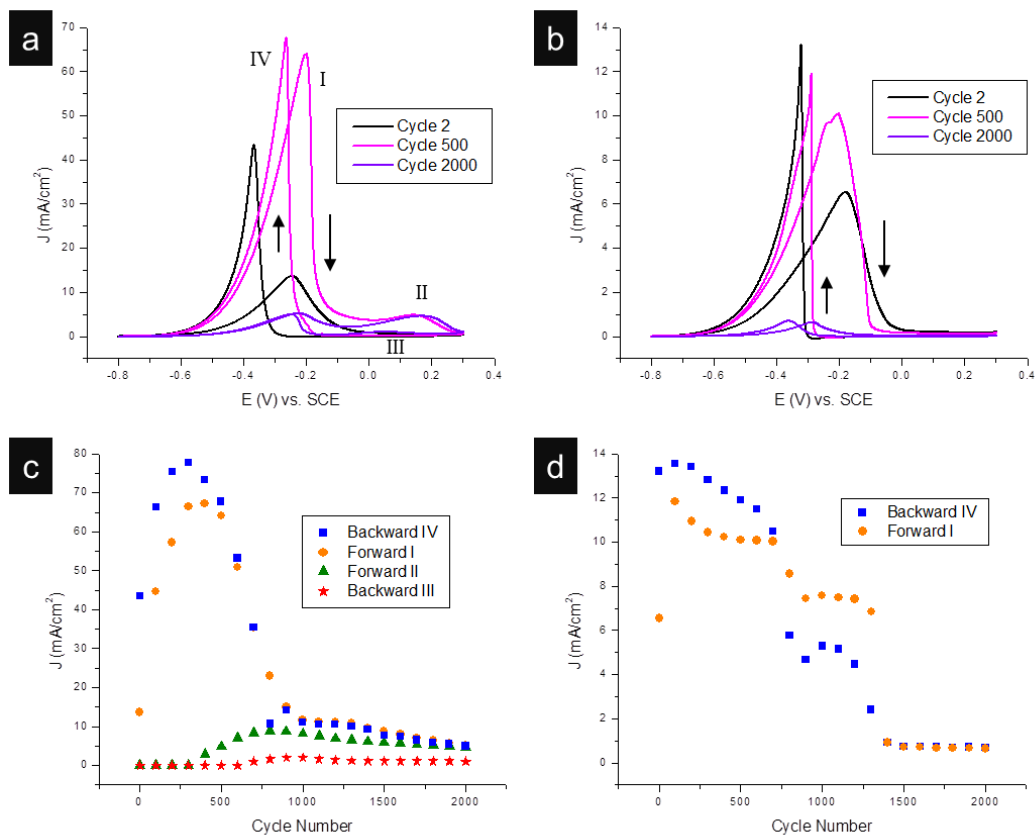


Figure 2.10: (a, b) Ethanol oxidation reaction (EOR) performed on thin and thick shell Au-Pd core-shell octahedra, respectively, in 1 M KOH + 1 M ethanol. (c, d) Plots of EOR current density versus cycle number for thin and thick shell octahedra, respectively, for peaks I-IV as labeled in (a).

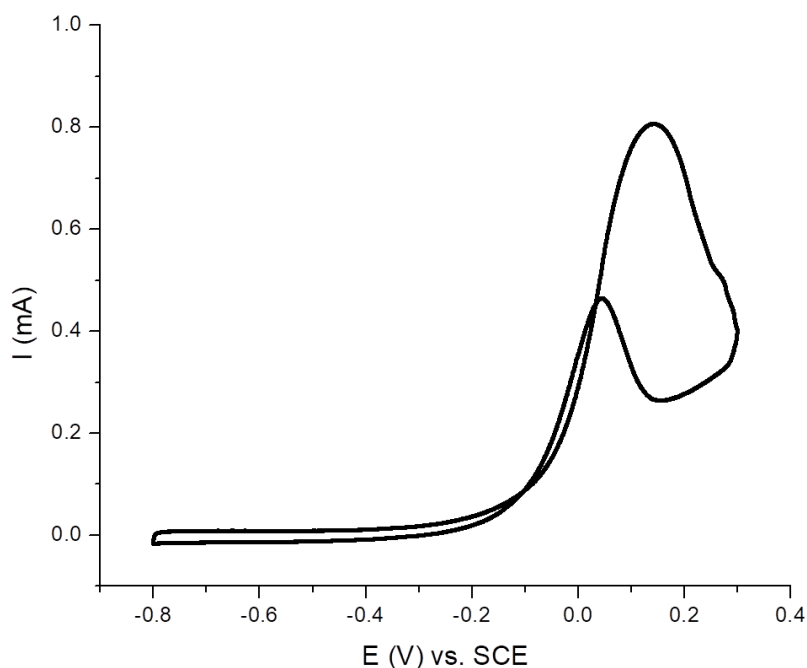


Figure 2.11: Ethanol oxidation on pure Au octahedral NPs. To confirm that peaks II and III observed in ethanol oxidation on Au-Pd thin shell core-shell octahedra was ethanol oxidation on an Au surface, ethanol oxidation was performed on pure Au octahedral particles as a control, shown here. The peaks observed on pure Au, near 0.1 V, correspond to the position of peaks II and III in the thin shell octahedra case. This confirms that those peaks belong to ethanol oxidation on Au and thus confirms that after repeated cycling, Au is present in the particle shell.

2.4.6 Au-Pd Ethanol Oxidation Reaction Activity Trends

These trends in activity can be explained by a combination of lattice strain, ligand, and ensemble effects. Au has a larger lattice size than Pd and expands Pd's lattice, raising its d-band center and increasing adsorbate bonding strength.³⁸ This effect can only

be seen for sufficiently thin Pd shells and thus increases EOR activity for thin shell but not thick shell octahedra.^{25,51} Ligand effects are likely also at play in this system. In general, electron density transfers from the metal with the higher Fermi level (Pd in this case) to the metal with the lower Fermi level (Au). However, in the special case of AuPd alloys, the opposite occurs, and even though s and p orbital electron density is transferred from Pd to Au, the catalytically important d orbital electron density is transferred from Au to Pd, lowering Pd's d-band center and decreasing the bonding strength of adsorbates.⁵² Thus, strain and ligand effects work in opposition here. In the thin shell core shell system, ligand effects are not yet present, and strain effects promote EOR activity by increasing chemisorption of ethanol. It is likely that in the first 400 cycles Au moves closer toward the shell and strain effects increase, hence the increase in EOR activity. After 400 cycles, however, Au is exposed on the surface; as evidenced by the appearance of peaks II and III; and the surface becomes a AuPd alloy. Once the alloy is present, ligand effects play a more important role and begin to weaken ethanol chemisorption, decreasing EOR activity. One study notes that the AuPd alloy ligand effect is not seen in Pd monolayers or thick shells, but requires Pd monomers surrounded by Au atoms,⁵² and becomes present once Au migrates to the shell in this case. In addition, as Au displaces surface Pd atoms, the number of ensemble Pd active sites on which ethanol oxidation takes place decreases, contributing along with ligand effects to the decrease in Pd EOR activity. In the thick shell octahedra, on the other hand, neither strain nor ligand nor ensemble effects are present, and the Pd shell acts much like a pure Pd catalyst. There is no Au-induced lattice expansion to promote activity and activity remains low. Activity

decreases with repeated cycling, possibly due to poisoning or oxidation of the Pd surface, which is not protected by Au alloying as in the thin shell case.^{43,44}

2.5 Conclusion

In this study, Au-Pd core-shell octahedral NPs with tunable thicknesses were synthesized and tested electrochemically. It was found that under electrochemical conditions Au migrates outward from the core to the shell, and the extent of migration depends on the identity and pH of the electrolyte, as well as the potential range used. STEM/EDX imaging and mapping of the octahedra post-electrochemical cycling and voltammetric profiles of an Au/Pd mixture provide evidence for the compositional and structural changes occurring by a combination of both Au migration and Pd dissolution mechanisms. Lastly, thin and thick shell Au-Pd core-shell octahedra were compared as EOR catalysts. It was found that migration was more prevalent in the thin shell particles, at first promoting EOR activity by strain effects but then inhibiting activity by ligand and ensemble effects. The thick octahedral shell prevented migration but also inhibited Au-induced strain effects, resulting in overall low catalytic activity. These results are interesting and instructive: in many reported bimetallic NP studies, scientists have focused on the activity of the first few electrocatalytic cycles, which has contributed a great understanding of ligand, strain, and ensemble effects. Yet, this study shows that structure and composition, and therefore activity, change over time during electrocatalysis. In addition, these results indicate that metal migration could be used to our advantage, by subjecting particles to electrochemical conditions to achieve a specific amount of migration, before using the particles as catalysts. Ligand, strain, and ensemble

effects play different roles in tuning catalytic activity at different stages of migration; thus, by selecting a number of electrochemical cycles we could manipulate migration to optimize these bimetallic effects and achieve enhanced catalytic activity.

2.6 References

- [1.] Tedsree, K.; Li, T.; Jones, S.; Chan, C.W.A.; Yu, K.M.K.; Bagot, P. A. J.; Marquis, E. A.; Smith, G. D. W.; Tsang, S. C. E. Hydrogen Production from Formic Acid Decomposition at Room Temperature Using a Ag-Pd Core-Shell Nanocatalyst. *Nat. Nanotechnol.* **2011**, *6*, 302–307.
- [2.] Deng, Y.-J.; Tian, N.; Zhou, Z.-Y.; Huang, R.; Liu, Z.-L.; Xiao, J.; Sun, S.-G. Alloy Tetrahedral Pd-Pt Catalysts: Enhancing Significantly the Catalytic Activity by Synergy Effect of High-Index Facets and Electronic Structure. *Chem. Sci.* **2012**, *3*, 1157–1161.
- [3.] Hong, J.; Kang, S.; Choi, B.; Kim, D.; Lee, S.; Han, S. Controlled Synthesis of Pd-Pt Alloy Hollow Nanostructures with Enhanced Catalytic Activities for Oxygen Reduction. *ACS Nano* **2012**, *6*, 2410–2419.
- [4.] Taufany, F.; Pan, C.; Rick, J.; Chou, H.; Tsai, M.; Hwang, B.; Liu, D.; Lee, J.; Tang, M.; Lee, Y.; *et al.* Kinetically Controlled Autocatalytic Chemical Process for Bulk Production of Bimetallic Core-Shell Structured Nanoparticles. *ACS Nano* **2011**, *5*, 9370–9381.
- [5.] Tsiakaras, P. PtM/C (M=Sn,Ru,Pd,W) Based Anode Direct Ethanol-PEMFCs: Structural Characteristics and Cell Performance. *J. Power Sources* **2007**, *171*, 107–112.
- [6.] Xiao, C. X.; Wang, L. L.; Maligal-Ganesh, R. V.; Smetana, V.; Walen, H.; Thiel, P. A.; Miller, G. J.; Johnson, D. D.; Huang, W. Y. Intermetallic NaAu₂ as a Heterogeneous Catalyst for Low-Temperature CO Oxidation. *J. Am. Chem. Soc.* **2013**, *135*, 9592–9595.
- [7.] Li, Q.; Jiang, R.B.; Ming, T.; Fang, C.H.; Wang, J.F. Crystalline Structure-Dependent Growth of Bimetallic Nanostructures. *Nanoscale* **2012**, *4*, 7070–7077.
- [8.] Zhu, Y.; Zhang, S.R.; Ye, Y.C.; Zhang, X.Q.; Wang, L.; Zhu, W.; Cheng, F.; Tao, F. Catalytic Conversion of Carbon Dioxide to Methane on Ruthenium-Cobalt Bimetallic Nanocatalysts and Correlation between Surface Chemistry of Catalysts under Reaction Conditions and Catalytic Performances. *ACS Catal.* **2012**, *2*, 2403–2408.

- [9.] Kitchin, J.; Norskov, J.; Barteau, M.; Chen, J. Role of Strain and Ligand Effects in the Modification of the Electronic and Chemical Properties of Bimetallic Surfaces. *Phys. Rev. Lett.* **2004**, *93*, 156801–156804.
- [10.] Tang, W.; Henkelman, G. Charge Redistribution in Core-Shell Nanoparticles to Promote Oxygen Reduction. *J. Chem. Phys.* **2009**, *130*, 194504–194504.
- [11.] Hu, S.; Scudiero, L.; Ha, S. Electronic Effect on Oxidation of Formic Acid on Supported Pd-Cu Bimetallic Surface. *Electrochim. Acta* **2012**, *83*, 354–358.
- [12.] Mavrikakis, M.; Hammer, B.; Norskov, J.K. Effect of Strain on the Reactivity of Metal Surfaces. *Phys. Rev. Lett.* **1998**, *81*, 2819–2822.
- [13.] Kibler, L.; El-Aziz, A.; Hoyer, R.; Kolb, D. Tuning Reaction Rates by Lateral Strain in a Palladium Monolayer. *Angew. Chem., Int. Ed.* **2005**, *44*, 2080–2084.
- [14.] Wang, X.; Orikasa, Y.; Takesue, Y.; Inoue, H.; Nakamura, M.; Minato, T.; Hoshi, N.; Uchimoto, Y. Quantitating the Lattice Strain Dependence of Monolayer Pt Shell Activity toward Oxygen Reduction. *J. Am. Chem. Soc.* **2013**, *135*, 5938–5941.
- [15.] Burda, C.; Chen, X. B.; Narayanan, R.; El-Sayed, M. A. Chemistry and Properties of Nanocrystals of Different Shapes. *Chem. Rev.* **2005**, *105*, 1025–1102.
- [16.] Cui, C.; Li, H.; Cong, H.; Yu, S.; Tao, F. Direct Evidence for Active Site-Dependent Formic Acid Electro-Oxidation by Topmost-Surface Atomic Redistribution in a Ternary PtPdCu Electrocatalyst. *Chem. Chem.* **2012**, *48*, 12062–12064.
- [17.] Wang, X.; Wang, M.; Zhou, D.; Xia, Y. Structural Design and Facile Synthesis of a Highly Efficient Catalyst for Formic Acid Electrooxidation. *Phys. Chem. Chem. Phys.* **2011**, *13*, 13594–13597.
- [18.] Tao, F.; Grass, M. E.; Zhang, Y.; Butcher, D. R.; Renzas, J. R.; Liu, Z.; Chung, J.Y.; Mun, B.S.; Salmeron, M.; Somorjai, G.A. Reaction-Driven Restructuring of Rh-Pd and Pt-Pd Core-Shell Nanoparticles. *Science* **2008**, *322*, 932–934.
- [19.] Huang, R.; Wen, Y.-H.; Shao, G.-F.; Sun, S.-G. Insight into the Melting Behavior of Au-Pt Core-Shell Nanoparticles from Atomistic Simulations. *J. Phys. Chem. C* **2013**, *117*, 4278–4286.
- [20.] Suntivich, J.; Xu, Z.; Carlton, C.E.; Kim, J.; Han, B.; Lee, S.W.; Bonnet, N.; Marzari, N.; Allard, L. F.; Gasteiger, H. A.; *et al.* Surface Composition Tuning of Au-Pt Bimetallic Nanoparticles for Enhanced Carbon Monoxide and Methanol Electro-oxidation. *J. Am. Chem. Soc.* **2013**, *135*, 7985–7991.

- [21.] Tao, F.; Grass, M.E.; Zhang, Y.; Butcher, D.R.; Aksoy, F.; Aloni, S.; Altoe, V.; Alayoglu, S.; Renzas, J. R.; Tsung, C.-K.; *et al.* Evolution of Structure and Chemistry of Bimetallic Nanoparticle Catalysts under Reaction Conditions. *J. Am. Chem. Soc.* **2010**, *132*, 8697–8703.
- [22.] Alayoglu, S.; Tao, F.; Altoe, V.; Specht, C.; Zhu, Z.; Aksoy, F.; Butcher, D. R.; Renzas, R. J.; Liu, Z.; Somorjai, G. A. Surface Composition and Catalytic Evolution of Au (x) Pd_{1-x} (x=0.25, 0.50 and 0.75) Nanoparticles under CO/O₂ Reaction in Torr Pressure Regime and at 200 °C. *Catal. Lett.* **2011**, *141*, 633–640.
- [23.] Tuae, X.; Rudi, S.; Petkov, V.; Hoell, A.; Strasser, P. *In-Situ* Study of Atomic Structure Transformations of Pt-Ni Nanoparticle Catalysts during Electrochemical Potential Cycling. *ACS Nano* **2013**, *1*, 5666–5674.
- [24.] Mani, P.; Srivastava, R.; Strasser, P. Dealloyed Pt-Cu Core-Shell Nanoparticle Electrocatalysts for Use in PEM Fuel Cell Cathodes. *J. Phys. Chem. C* **2008**, *112*, 2770–2778.
- [25.] Bhattarai, N.; Casillas, G.; Khanal, S.; Salazar, J.; Ponce, A.; Jose-Yacaman, M. Origin and Shape Evolution of Core-Shell Nanoparticles in Au-Pd: From Few Atoms to High Miller Index Facets. *J. Nanopart. Res.* **2013**, *15*, 1–13.
- [26.] Lu, C.; Prasad, K.; Wu, H.; Ho, J.; Huang, M. Au Nanocube Directed Fabrication of Au-Pd Core-Shell Nanocrystals with Tetrahedral, Concave Octahedral, and Octahedral Structures and Their Electrocatalytic Activity. *J. Am. Chem. Soc.* **2010**, *132*, 14546–14553.
- [27.] Yang, C.; Chanda, K.; Lin, P.; Wang, Y.; Liao, C.; Huang, M. Fabrication of Au-Pd Core-Shell Heterostructures with Systematic Shape Evolution Using Octahedral Nanocrystal Cores and Their Catalytic Activity. *J. Am. Chem. Soc.* **2011**, *133*, 19993–20000.
- [28.] DeSantis, C. J.; Skrabalak, S.E. Size-Controlled Synthesis of Au/Pd Octopods with High Refractive Index Sensitivity. *Langmuir* **2012**, *28*, 9055–9062.
- [29.] Jin, M.; Liu, H.; Zhang, H.; Xie, Z.; Liu, J.; Xia, Y. Synthesis of Pd Nanocrystals Enclosed by {100} Facets and with Sizes < 10 nm for Application in CO Oxidation. *Nano Res.* **2011**, *4*, 83–91.
- [30.] Tedsree, K.; Li, T.; Jones, S.; Chan, C.; Yu, K.; Bagot, P.; Marquis, E.; Smith, G.; Tsang, S. Hydrogen Production from Formic Acid Decomposition at Room Temperature Using a Ag-Pd Core-Shell Nanocatalyst. *Nat. Nanotechnol.* **2011**, *6*, 302–307.
- [31.] Meng, H.; Wang, C.; Shen, P.; Wu, G. Palladium Thorn Clusters as Catalysts for Electrooxidation of Formic Acid. *Energy Environ. Sci.* **2011**, *4*, 1522–1526.

- [32.] Hokenek, S.; Kuhn, J. N. Methanol Decomposition over Palladium Particles Supported on Silica: Role of Particle Size and Co-Feeding Carbon Dioxide on the Catalytic Properties. *ACS Catal.* **2012**, *2*, 1013–1019.
- [33.] Jin, T.; Guo, S.J.; Zuo, J.L.; Sun, S.H. Synthesis and Assembly of Pd Nanoparticles on Graphene for Enhanced Electrooxidation of Formic Acid. *Nanoscale* **2013**, *5*, 160–163.
- [34.] Feng, Y.; Liu, Z.; Xu, Y.; Wang, P.; Wang, W.; Kong, D. Highly Active PdAu Alloy Catalysts for Ethanol Electro-Oxidation. *J. Power Sources* **2013**, *232*, 99–105.
- [35.] Srejac, I.; Smiljanic, M.; Grgur, B.; Rakocevic, Z.; Strbac, S. Catalysis of Oxygen Reduction on Au Modified by Pd Nanoislands in Perchloric Acid Solution. *Electrochim. Acta* **2012**, *64*, 140–146.
- [36.] Huang, R.; Wen, Y.; Shao, G.; Zhu, Z.; Sun, S. Thermal Stability and Shape Evolution of Tetrahedral Au-Pd Core-Shell Nanoparticles with High-Index Facets. *J. Phys. Chem. C* **2013**, *117*, 6896–6903.
- [37.] Delannoy, L.; Giorgio, S.; Mattei, J.; Henry, C.; El Kolli, N.; Methivier, C.; Louis, C. Surface Segregation of Pd from TiO₂-Supported AuPd Nanoalloys under CO Oxidation Conditions Observed *in-Situ* by ETEM and DRIFTS. *ChemCatChem* **2013**, *5*, 2707–2716.
- [38.] Kuo, C.-H.; Lamontagne, L. K.; Brodsky, C. N.; Chou, L.-Y.; Zhuang, J.; Sneed, B. T.; Sheehan, M. K.; Tsung, C.-K. The Effect of Lattice Strain on the Catalytic Properties of Pd Nanocrystals. *ChemSusChem* **2013**, *6*, 1993–2000.
- [39.] Chang, C.; Wu, H.; Kuo, C.; Huang, M. Hydrothermal Synthesis of Monodispersed Octahedral Gold Nanocrystals with Five Different Size Ranges and Their Self-Assembled Structures. *Chem. Mater.* **2008**, *20*, 7570–7574.
- [40.] Jukk, K.; Alexeyeva, N.; Johans, C.; Kontturi, K.; Tammeveski, K. Oxygen Reduction on Pd Nanoparticle/Multi-Walled Carbon Nanotube Composites. *J. Electroanal. Chem.* **2012**, *666*, 67–75.
- [41.] Sau, T. K.; Murphy, C. J. Self-Assembly Patterns Formed Upon Solvent Evaporation of Aqueous Cetyltrimethylammonium Bromide-Coated Gold Nanoparticles of Various Shapes. *Langmuir* **2005**, *21*, 2923–2929.
- [42.] Zalineeve, A.; Coutanceau, C.; Jerkiewicz, G. Electrochemical Behavior of Unsupported Shaped Palladium Nanoparticles. *Langmuir* **2015**, *31*, 1605–1609.

- [43.] Wilson, A.; Sun, K.; Chi, M.; White, R.; LeBeau, J.; Lamb, H.; Wiley, B. From Core-Shell to Alloys: The Preparation and Characterization of Solution-Synthesized AuPd Nanoparticle Catalysts. *J. Phys. Chem. C* **2013**, *117*, 17557–17566.
- [44.] Sasaki, K.; Naohara, H.; Choi, Y.; Cai, Y.; Chen, W.; Liu, P.; Adzic, R. Highly Stable Pt Monolayer on PdAu Nanoparticle Electrocatalysts for the Oxygen Reduction Reaction. *Nat. Commun.* **2012**, *3*, 2–9.
- [45.] Tripkovic, A.; Popovic, K.; Grgur, B.; Blizanac, B.; Ross, P.; Markovic, N. Methanol Electrooxidation on Supported Pt and PtRu Catalysts in Acid and Alkaline Solutions. *Electrochim. Acta* **2002**, *47*, 3707–3714.
- [46.] Harrison, J.; Whitfield, T. The Dissolution of Palladium in Various Electrolytes. *Electrochim. Acta* **1983**, *28*, 1229–1236.
- [47.] Grden, M.; Lukaszewski, M.; Jerkiewicz, G.; Czerwinski, A. Electrochemical Behavior of Palladium Electrode: Oxidation, Electrodissolution, and Ionic Adsorption. *Electrochim. Acta* **2008**, *53*, 7583–7598.
- [48.] Bolzan, A. E.; Arvia, A. J. Effect of the Electrolyte Composition on the Electroreduction of Palladium Oxide Films. *J. Electroanal. Chem.* **1993**, *354*, 243–253.
- [49.] Zhou, Z.; Wang, Q.; Lin, J.; Tian, N.; Sun, S. *In-Situ* FTIR Spectroscopic Studies of Electrooxidation of Ethanol on Pd Electrode in Alkaline Media. *Electrochim. Acta* **2010**, *55*, 7995–7999.
- [50.] Cherevko, S.; Kulyk, N.; Chung, C. Utilization of Surface Active Sites on Gold in Preparation of Highly Reactive Interfaces for Alcohols Electrooxidation in Alkaline Media. *Electrochim. Acta* **2012**, *69*, 190–196.
- [51.] Ding, Y.; Fan, F.; Tian, Z.; Wang, Z. Atomic Structure of Au-Pd Bimetallic Alloyed Nanoparticles. *J. Am. Chem. Soc.* **2010**, *132*, 12480–12486.
- [52.] Gao, F.; Goodman, D. Pd-Au Bimetallic Catalysts: Understanding Alloy Effects from Planar Models and (Supported) Nanoparticles. *Chem. Soc. Rev.* **2012**, *41*, 8009–8020.

3.0 Shaped Pd-Ni-Pt Core-Sandwich-Shell Nanoparticles: Influence of Ni Sandwich Layers on Catalytic Electrooxidations

Note: This chapter was published as: Brian T. Sneed, Allison P. Young, Daniel Jalalpoor, Matthew C. Golden, Shunjia Mao, Ying Jiang, Yong Wang, Chia-Kuang Tsung, "Shaped Pd-Ni-Pt Core-Sandwich-Shell Nanoparticles: Influence of Ni Sandwich Layers on Catalytic Electrooxidation," ACS Nano, 2014, 8(7), 7239-7250. Portions of this chapter may be seen in Brian T. Sneed's 2015 dissertation titled, "Design of Strained Metal Nanocrystal Architectures for Energy Conversion Electrocatalysis". I thank him for the use of this material as a co-author of the above mentioned manuscript.

Reprinted with permission from Brian T. Sneed, Allison P. Young, Daniel Jalalpoor, Matthew C. Golden, Shunjia Mao, Ying Jiang, Yong Wang, Chia-Kuang Tsung, Shaped Pd-Ni-Pt Core-Sandwich-Shell Nanoparticles: Influence of Ni Sandwich Layers on Catalytic Electrooxidation, *ACS Nano*, **2014**, 8(7), 7239-7250. Copyright © 2014 American Chemical Society

URL Link: <https://pubs.acs.org/doi/abs/10.1021/nn502259g>

DOI: 10.1021/nn502259g

3.1 Abstract

Shape-controlled metal nanoparticles (NPs) interfacing Pt and nonprecious metals (M) are highly active energy conversion electrocatalysts; however, there are still few

routes to shaped M-Pt core-shell NPs and fewer studies on the geometric effects of shape and strain on catalysis by such structures. Here, well-defined cubic multilayered Pd-Ni-Pt sandwich NPs are synthesized as a model platform to study the effects of the nonprecious metal below the shaped Pt surface. The combination of shaped Pd substrates and mild reduction conditions directs the Ni and Pt overgrowth in an oriented, layer-by-layer fashion. Exposing a majority of Pt (100) facets, the catalytic performance in formic acid and methanol electro-oxidations (FOR and MOR) is assessed for two different Ni layer thicknesses and two different particle sizes of the ternary sandwich NPs. The strain imparted to the Pt shell layer by the introduction of the Ni sandwich layer (Ni-Pt lattice mismatch of $\sim 11\%$) results in higher specific initial activities compared to core-shell Pd-Pt bimetallic NPs in alkaline MOR. The trends in activity are the same for FOR and MOR electrocatalysis in acidic electrolyte. However, restructuring due to metal migration in acidic conditions suggests a more complex catalytic behavior from changes in composition. Notably, we also show that cubic quaternary Au-Pd-Ni-Pt multi-shelled NPs, and Pd-Ni-Pt nanooctahedra can be generated by the method, the latter of which hold promise as potentially highly active oxygen reduction catalysts.

3.2 Introduction

There has been a growing interest in the preparation of shaped binary and ternary metal nanoparticles (NPs) comprising nonprecious metals (M) as they achieve better activity, stability, and efficiency as electrocatalysts for energy conversion chemistry.¹⁻⁹ In particular, such shaped M-Pt NP oxygen reduction (ORR) electrocatalysts could advance the commercial viability of automotive hydrogen fuel cells.¹⁰ The superior performance

of shaped M-Pt NPs merits their study, but the many factors that influence catalytic behavior in these complex systems (ligand, ensemble, geometric, and strain effects) are difficult to parse out.¹¹ Often it remains that the most active and stable structures for these catalysts are composed of layers of Pt atoms above an M-Pt core, and so the target structure is re-envisioned as a core-shell NP architecture.^{10,12} In addition, it is shown that thin M-sandwich layers can exist due to restructuring during the reactions,¹³ and indeed there is experimental and theoretical work which discusses the stability of various Pt-M-Pt sandwich and multilayered Pt-skin structures.^{12,14-16} The aforementioned M-Pt NP surfaces reconstruct to the Pt-skin motif due to dealloying (leaching) of the nonprecious component from the surface during potential cycling in acidic conditions.^{17,18} Recent work predicts M-Pt NPs comprising a Pd-Ni core and Pt-shell to be more stable and highly active electrocatalysts for oxygen reduction.¹² All of this information suggests the investigation of core-shell and multi-shelled M-Pt nanoarchitectures to be a promising direction for fundamental catalysis research.

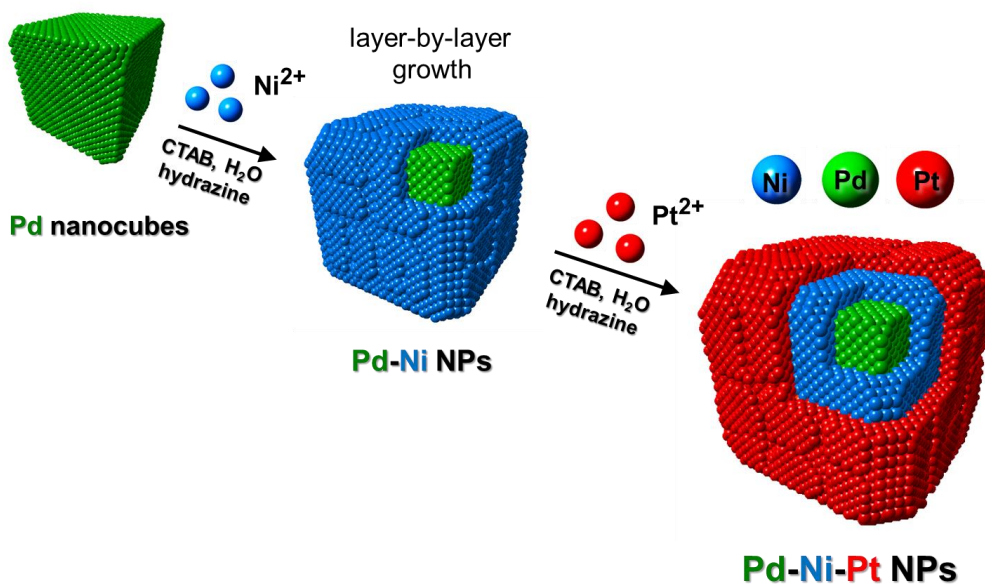
Despite the advancement of M-Pt NP electrocatalysts, such as Ni, there are few established methods for creating core-shell M-Pt NPs with well-defined shape control. Current strategies for producing Ni-Pt alloy NPs with shape control require Ni and Pt ions to be co-reduced.¹⁹ Usually, this is accompanied by a variety of capping/shaping agents.²⁰⁻²² Wu et al. have recently contributed a shape-controlled synthesis for Ni octahedra,²³ and others have demonstrated control of shape for bimetallic systems with core-shell Pd-Cu and Ag-Ni nanocubes.^{24,25} While these works are excellent examples of the power in colloidal synthesis, the synthesis with rational structural control remains a

challenge. Also, various cleaning methods are required due to the strong bonding capping agents used in these organic phase syntheses.

An aqueous,²⁶ layer-by-layer epitaxial overgrowth approach^{24,27-32} to shape-controlled M-Pt core-shell NPs would be desirable for the exploration of strained nanoarchitectures, as well as for the opportunity to study strain effects on catalysis by multi-shelled structures. Direct control of the size, overall shape, and the thickness of each layer in a core-sandwich-shell nanostructure would provide a platform to gain better understanding of lattice strain effects on catalytic activity and perhaps elucidate the limits for these effects experimentally. Previous works show tuning the shell thickness and NP size as a way to increase catalytic activity.^{12,33} The activity changes observed with expansive or compressive lattice strain (from the lattice mismatch at metal-metal interfaces) have been attributed to subtle altering of the binding energies of adsorbates, by way of perturbation of the surface d-band.^{18,34} The d-band model offers a straightforward design principle to fine-tune Pt-based electrocatalysts,¹¹ yet there is still much debate over its validity as a general descriptor and predictor of catalytic activity.^{35,36}

Herein, we present an aqueous, low temperature route to shape-controlled Pd-Ni-Pt core-sandwich-shell NPs using cetyltrimethylammonium bromide (CTAB) as the capping agent and hydrazine as the reducing agent. Scheme 3.1 demonstrates how Pd cubes function as shaped crystal substrates which catalyze and direct the oriented overgrowth of Ni. Pt ions are added after the Ni overgrowth to “trap” the metallic Ni phase and complete the layer-by-layer synthesis of the shaped ternary metal NPs. This

method allows for control of the overall size, shape, and layer thickness by the choice of substrate and amount of precursor salts added in the growth solution.



Scheme 3.1: Synthesis of cubic Pd-Ni-Pt core-sandwich-shell nanoparticles for use in catalytic electrooxidation of small molecules, such as methanol and formic acid

The strategy presented here is attractive toward the end-goal of understanding the impact of lattice strain on the catalytic performance of core-shell NPs. The cubic Pd-Ni-Pt structures are investigated as formic acid oxidation (FOR) and methanol oxidation (MOR) electrocatalysts, for which the Pt (100) facets are expected to have higher activity.³⁷ We discuss the findings of increased specific activity of the catalysts with a Ni-sandwich layer as being due to strain on Pt by the Ni layers beneath the surface. The durability of the different catalysts is assessed, and the smaller trimetallic Pd-Ni-Pt nanoparticles retain the highest activity over time over both the larger ternary NPs and the Pd-Pt control NPs for MOR in alkaline solutions. The trends in activity are similar in acidic conditions; however, because of dealloying and restructuring from potential

cycling in acid, their behavior may be more a result of a composition change at the surface, rather than from strain. We further show that an octahedral morphology can be produced by substituting Pd octahedra for the Pd nanocubes in the synthesis. These NPs could be the subject of future studies in oxygen reduction catalysis. Finally, we use the strategy to create quaternary, core-triple-shelled Au-Pd-Ni-Pt NPs with a cubic shape at a size of ~20 nm. To our knowledge, the novel, shaped multi-shelled nanoparticles shown here are unprecedented in the literature.

3.3 Experimental Methods

3.3.1 Chemicals

Nickel (II) chloride hexahydrate ($\text{NiCl}_2 \cdot 6\text{H}_2\text{O}$), potassium tetrachloroplatinate (II) (K_2PtCl_4), L-ascorbic acid (AA ($\text{C}_6\text{H}_8\text{O}_6$), 99 %), potassium hydroxide (KOH), and formic acid (HCOOH , 88%) were obtained from Sigma-Aldrich. Hydrazine monohydrate ($\text{N}_2\text{H}_4 \cdot \text{H}_2\text{O}$, 98 %) and perchloric acid (HClO_4 , 70 %) were obtained from Alfa Aesar. Cetyltrimethylammonium bromide (CTAB, 99 %) was obtained from Calbiochem, and sulfuric acid (H_2SO_4 , 95 %) was obtained from BDH. Methanol (CH_3OH , 99.8 %) was obtained from Acros. Deionized water (DI water, 18.2 $\text{M}\Omega$) was utilized in all experiments. Nitrogen gas (N_2 , 99 %) was obtained from Airgas.

3.3.2 Synthesis of Cubic Pd-Ni-Pt Nanoparticles

Cubic Pd substrates of two sizes (~10 and ~30 nm) were first prepared according to references.²⁷⁻²⁹ A solution containing 0.05 g of CTAB in 10 mL of DI water was then

prepared by sonication in a 20 mL glass vial. Then, 500 μL of the concentrated Pd nanocube solution (containing Pd cubes from eight reactions, redispersed in 10 mL DI water) was added to the vial, which was gently mixed. Next, 100 μL of 0.01 M NiCl_2 was added as the source of Ni^{2+} ions followed by 500 μL of 1.0 M hydrazine solution. Finally, the vial was vortexed, capped, and left unstirred for ~ 2 hours in a water bath set to 50 $^\circ\text{C}$. A color change from brown to gray/black occurred indicating the completed overgrowth. At this time, the vial was removed from the bath, briefly sonicated, uncapped, and 50 μL of 0.01 M K_2PtCl_4 was injected followed by capping, gentle mixing, and brief sonication (1-2 seconds). The solution was then returned to the water bath for ~ 1 hour at the same temperature and the Pd-Ni-Pt core-sandwich-shell NPs were then collected *via* centrifugation at 4000 rpm. The thickness of Ni and Pt could be changed by varying the amount of precursor in the growth solution; however, larger amounts of Ni precursor (in excess of 200 μL) led to precipitation of the particles before Pt ions were added.

3.3.3 Synthesis of Cubic Pd-Pt Nanoparticles

The Pd-Pt core-shell NPs were synthesized under the same conditions as the Pd-Ni-Pt NPs, excepting that Ni ions were not added, and ascorbic acid was used as the reducing agent, instead of hydrazine. Briefly, 250 μL of 0.01 M K_2PtCl_4 was added to an aqueous CTAB solution containing the ~ 30 nm Pd nanocubes in a 20 mL scintillation vial. The solution was mixed and heated for ~ 5 minutes at 50 $^\circ\text{C}$ with stirring, after which 200 μL of 0.04 M ascorbic acid was added. The vial was left open, heating at this temperature with stirring for ~ 2 hours. Finally, the vial was removed from heat and the NPs were collected by centrifugation at 5000 rpm for 10 min.

3.3.4 Synthesis of Cubic Au-Pd-Ni-Pt Nanoparticles

The ~10-12 nm cubic Au-Pd core-shell substrates were synthesized according to a procedure from a ref 27 with modifications; mainly, the overgrowth of Pd on Au cuboctahedral seeds was scaled up. Typically, the reagent amounts were increased by a factor of 10 without a loss in quality of the cubic shape. A 250 mL beaker was used instead of a scintillation vial, and this was sealed with a paraffin film for the duration of the reaction. These were then collected as before for use in the Ni-Pt overgrowth.

3.3.5 Synthesis of Octahedral Pd-Ni-Pt Nanoparticles

The ~30 nm Pd-Ni-Pt octahedra were synthesized under the same conditions as the cubic Pd-Ni-Pt NPs, except that 500 μ L of concentrated ~30 nm Pd octahedra solution, prepared according to ref 27, was used in place of the ~30 nm nanocubes

3.3.6 Characterization

For analysis by transmission electron microscopy (TEM), energy dispersive X-ray spectroscopy (EDX) and powder X-ray diffraction (XRD), samples were cleaned by three cycles of centrifugation, removal of the supernatant, and redispersion in DI water. After this, the final collection of particles was dispersed in ~50-100 μ L of DI water. For TEM characterization, 2 μ L of the concentrated nanoparticle solution was placed directly on a carbon-coated copper grid and allowed to dry. Alternatively, particles could be dropcast in 20 μ L aliquots on the copper grids. The instrument used was a JEOL JEM2010F accompanied by an EDX attachment operated at 200 kV. For XRD, particles were

concentrated in 20 μL of solution which was placed as a droplet on a thin glass slide and allowed to dry. A Bruker AXS D2 Phaser diffractometer was used for the XRD characterization.

3.3.7 STEM/EDX

High-resolution STEM and EDX mapping experiments were performed on a FEI Probe Cs corrected Titan operating at 200 kV. The high angle annular dark field (HAADF) images were obtained using a Fischione HAADF detector, and the EDX maps were acquired with ChemiSTEM technology with four windowless SDD detectors. The instrument incorporates the condenser spherical aberration corrector and X-FEG with probe current 0.4 nA in 0.31 nm spot and can achieve the resolution 0.08 nm as well as efficient X-ray collection rate.

3.3.8 Electrochemical Measurements

The Pd-Ni-Pt NP catalysts were loaded directly onto a glassy carbon working electrode (CH Instruments) without the use of a support for cyclic voltammetry. Typically, 2 μL droplets were placed on the electrode surface and allowed to dry. The cyclic voltammetry (CV) and chronoamperometry (CA) was done using a BioLogic VSP potentiostat in a three electrode system. A saturated calomel electrode was used as the reference electrode and a platinum wire as the counter electrode (both also obtained from CH Instruments). The acidic blank scans were carried out in 0.5 M sulfuric acid solution purged with nitrogen and cycled from -0.2 to 1.0 V at a scan rate of 100 mV/s. These

cycles were typically continued until stable voltammograms were obtained (~30-50 cycles). The alkaline blank scans were carried out in 0.1 M potassium hydroxide solution purged with nitrogen and cycled from -0.8 to 0.4 V at a scan rate of 100 mV/s. Approximately 20-30 cycles were run in this way until stable curves were reached. The electrochemically active surface area was determined by integration of the total charge collected from the hydrogen desorption peak and dividing this value by the charge per area required to remove the layer of hydrogen from the Pt surface ($210 \mu\text{C}/\text{cm}^2$). The alkaline electrooxidation of methanol was done in 0.05 M methanol and 0.1 M KOH solution. The scan rate was 100 mV/s and the cycles were run from -0.8 to 0.4 V. The highest initial activity usually occurred within the first 20 cycles and the reaction was stopped. The electrooxidation of formic acid was done in a solution which was 0.5 M in HCOOH and 0.5 M in HClO₄. The scan rate was 100 mV/s and the range was -0.2 to 1.2 V. The highest initial activity usually occurred within the first ~20 cycles and the reaction was stopped. Methanol oxidation reactions in acid were carried out in a solution, which was 0.5 M in CH₃OH and 0.5 M in H₂SO₄. The scan rate was 100 mV/s and the range was 0-1.0 V. The highest initial activity was usually obtained within ~20 cycles and the experiment was stopped. The CA curves for MOR in base and for FOR were obtained under identical conditions as previously described, except that the voltage was held constant at -0.1 and 0.4 V, respectively, and the current was measured over time. These potentials were chosen because of good overlap with the potential where peak current was obtained for each of the catalysts. The NP catalysts were put onto a Vulcan carbon support for the CA studies. A 20% by weight catalyst/carbon loading was used. For example, ~2 mg of the Vulcan XC-72 was added directly to a solution containing

~0.5 mg of dispersed NPs. This was then briefly sonicated, and the freshly prepared catalyst/carbon dispersion was then loaded onto the working electrode in 2-3 μL droplets and allowed to dry for the transient current density experiments. The catalysts were cycled in the blank solution and until initial activity was reached prior to the CA run. A blank scan was carried out just prior to the CA experiment in order to obtain a more accurate surface area determination for normalization of the catalytic activity

3.4 Results and Discussion

3.4.1 Synthesis of Pd-Ni-Pt Sandwich Nanoparticles

In attempting to synthesize shaped Pd-Ni-Pt multi-layered NPs by a wet chemical route, insights were gained from earlier works that successfully demonstrated control of Ni at this size scale. Grzelczak et al. were able to produce Ni NPs of different sizes by adjusting the Ni^{2+} to reducing agent ratio in the growth solution and observed size-dependent magnetic properties.³⁸ Their synthesis was accomplished in water at low temperatures using hydrazine as the reducing agent and CTAB surfactant. The authors confirmed metallic Ni in their work using X-ray structural analysis; however, it was speculated that the surface remained passivated by several oxide layers. Moreover, no control of faceting was reported. This general strategy was utilized to make Ni nanostructures in several of their works,³⁹⁻⁴¹ while others have since published variations of the Ni-reduction method.⁴²⁻⁴⁴ Recent syntheses yield more complex Ni nanostructures^{45,46} and theoretical work proposes and describes the faceting of Ni crystals.⁴⁷

Liz-Marzán's group showed that the Ni NPs could only be formed in this synthesis system under certain conditions: (1) catalytic Pt nanoparticle seeds must be introduced for the overgrowth of Ni; (2) the growth solution must be sealed to trap the H₂ gas evolved during the synthesis, which promotes Ni reduction and limits surface oxidation; and (3) the growth must occur without magnetic perturbations, such as a stir bar in the growth solution, otherwise the particles may collect and precipitate prematurely, or fuse into chains or wires. We hypothesized that we could make use of this approach, by reducing Ni on shaped Pd substrates instead of small Pt seeds. Their use of mild conditions with ionic surfactants resembled the conditions used for seed-mediated growth^{31,48,49} of other metal NPs from our previous work with Au, Pd, and Rh.^{27-29,50} It was feasible that combining the strategies would lead to a greater control of Ni faceting in the overgrowth, which has not been attempted before.

In a typical synthesis of Pd-Ni-Pt nanoparticles, shaped Pd substrates (nanocubes) were prepared following procedures in the literature,²⁷⁻²⁹ and dispersed into an aqueous solution of CTAB in a small glass vial. Nickel ions were then added in the form of nickel(II)-chloride hexahydrate (NiCl₂ · 6H₂O), and an amount of hydrazine monohydrate solution was added last. The vial was sealed and maintained in a water bath at 50 °C for ~2 hours (without stirring) until a color change occurred indicating the Ni overgrowth. Pt ions were then injected in the form of K₂PtCl₄, and heating continued in the water bath for ~1 hour. The ternary metal particles were then removed from heat and collected by centrifugation at 4000 rpm, redispersed, and washed for characterization. In other works, the problem of surface oxidation was avoided by alloying (co-reduction) or by working in organic solvent; however, it is shown that oxides can still form on the

surface of such structures in these conditions, especially in aqueous solutions.^{24,51} Accordingly, we attempted to prevent oxide formation by “capping” of the Ni layer with overgrowth of Pt in the same “pot”. This simultaneously addresses the issue of surface oxidation and creates the desired shaped M-Pt core-shell motif desired for catalysis.

3.4.2 Characterization of Pd-Ni-Pt Sandwich Nanoparticles by TEM

The “trapped” metallic Ni phase in the Pd-Ni-Pt NPs can be observed by contrast in transmission electron microscope (TEM) images shown in Figure 3.1. Three types of NPs with different sizes and Ni layer thicknesses were synthesized. The NPs in Figure 3.1a-c were synthesized by introducing 100 and 50 μL of the Ni and Pt precursors, respectively, to growth solutions containing ~ 30 nm Pd nanocubes. This resulted in ~ 2.5 nm of Ni and 1.6 nm of Pt layers. Particles in Figure 3.1d-f were synthesized similarly, excepting for a doubling of the amounts of the Ni and Pt metal precursors. This led to 4.1 nm of Ni and 1.6 nm of Pt overgrowth. The NPs shown in Figure 3.1g-i were created using smaller, ~ 12 nm Pd nanocubes in place of the larger substrates, resulting in NPs approximately ~ 20 nm in size. Nickel is observed in the TEM images as a lighter phase “sandwiched” between a dark Pd core and a darker Pt surface layer. The difference in contrast (z-contrast) is due to the increased electron scattering of the heavier 4d and 5d metals. Recolored TEM images in Figure 3.1 highlight the different metal phases in the structure. The final truncated cubic morphology is a result of the well-defined cubic shape of the Pd substrates and the layer-by-layer overgrowth. The roughened appearance of the surface is likely due to the lattice mismatch ($\sim 10\text{-}11\%$ for these metals) and high degree of strain and defects imparted by having the Ni “sandwiched” between the Pd and

Pt layers. Core shell Pd-Pt NPs also shown in Figure 3.1 j-l lack the Ni layer and are used for comparison as a control in X-ray diffraction and electrochemical catalysis studies presented later in this work; such structures have also shown enhanced performance in the literature as electrocatalysts.^{28,52}

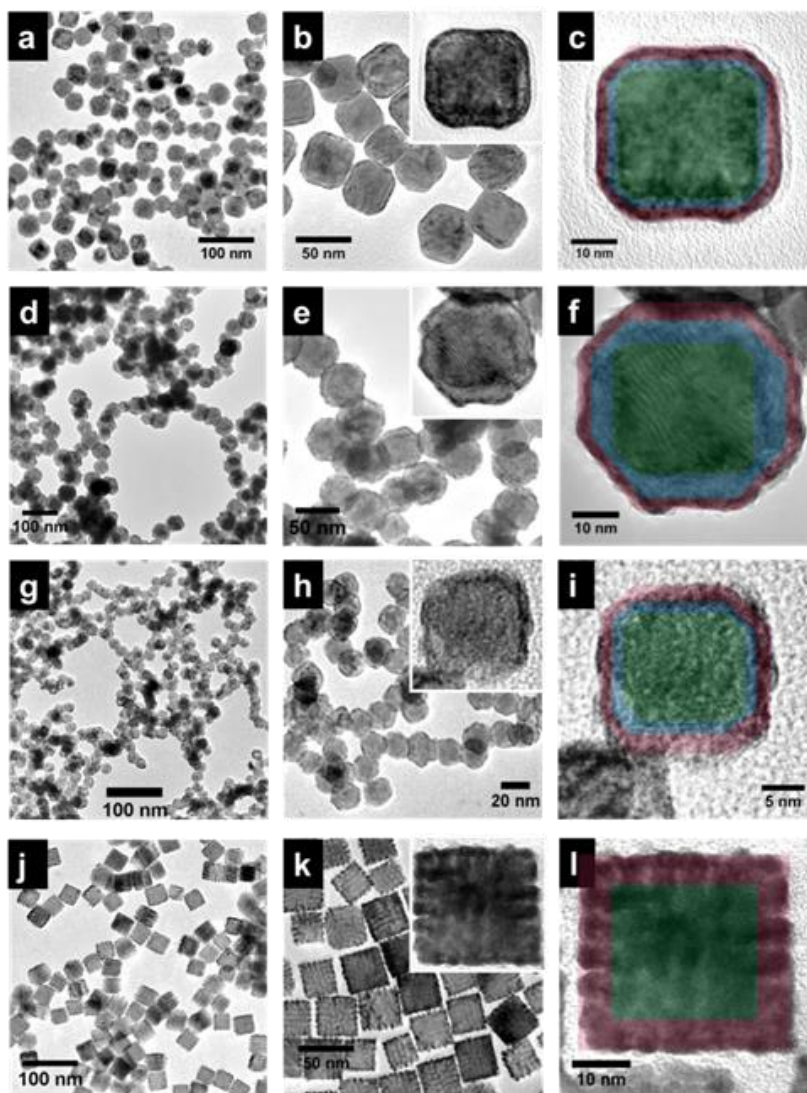


Figure 3.1: TEM and recolored TEM images of cubic Pd-Ni-Pt and Pd-Pt NPs. (a-c) Pd-Ni-Pt NPs synthesized with ~ 2.5 nm Ni sandwich; (d-f) NPs synthesized with ~ 4.1 nm Ni sandwich; (g-i) smaller ~ 20 nm Pd-Ni-Pt NPs; and (j-l) Pd-Pt core-shell NPs. The original TEM images that were recolored are shown as insets in the upper right of images

in the middle column. The Pd, Ni, and Pt regions are shown under green, blue, and red transparencies, respectively, in the recolored images.

3.4.3 Analysis of Structure, Composition, and Strain in Pd-Ni-Pt Sandwich Nanoparticles by STEM/EDX, HAADF, HRTEM Imaging, and XRD

To investigate the composition, conformal overgrowth, and to confirm the core-sandwich-shell structure of the Pd-Ni-Pt NPs, X-ray elemental analysis was carried out. Element maps from scanning transmission electron microscopy with energy dispersive X-ray spectroscopy (STEM/EDX) and high angle annular dark field images (HAADF) are given for the NPs in Figure 3.2a-f. There is a clear distinction between the lower mass Ni phase and heavier Pd and Pt phases in the HAADF images in Figure 3.2a,b as was observed in TEM. Here the Ni appears as a dark band between bright Pt and Pd regions. The STEM/EDX maps for each metal are given in Figure 3.2c-e with the overlaid map in Figure 3.2f confirming the double-shelled structure of the Pd-Ni-Pt NPs. The HRTEM image in Figure 3.2g shows continuous epitaxy from the Pd core through the Ni phase to the Pt shell. The size of the Ni-Pt shells is around ~ 4 nm, and this is composed by a ~ 2.5 nm layer of Ni. Measurements of the d-spacings in the HRTEM image in Figure 3.2g agree with the proposed core-sandwich-shell structure in that the (200) d-spacing becomes smaller traveling away from the Pd core from ~ 0.199 to ~ 0.193 nm in the Ni layer, but then increases near the Pt surface back to ~ 0.200 nm. This suggests the Pt atoms at the surface experience compression, and we speculate that thicker Ni layers could impart more strain to the Pt surface, by increasing influence of Ni's smaller lattice parameters. We also note that none of the measured d-spacings approach the larger bulk

NiO (200) d-spacing of 0.208 nm, which indicates a metallic Ni layer. This is discussed in more detail following the surface characterization by TEM.

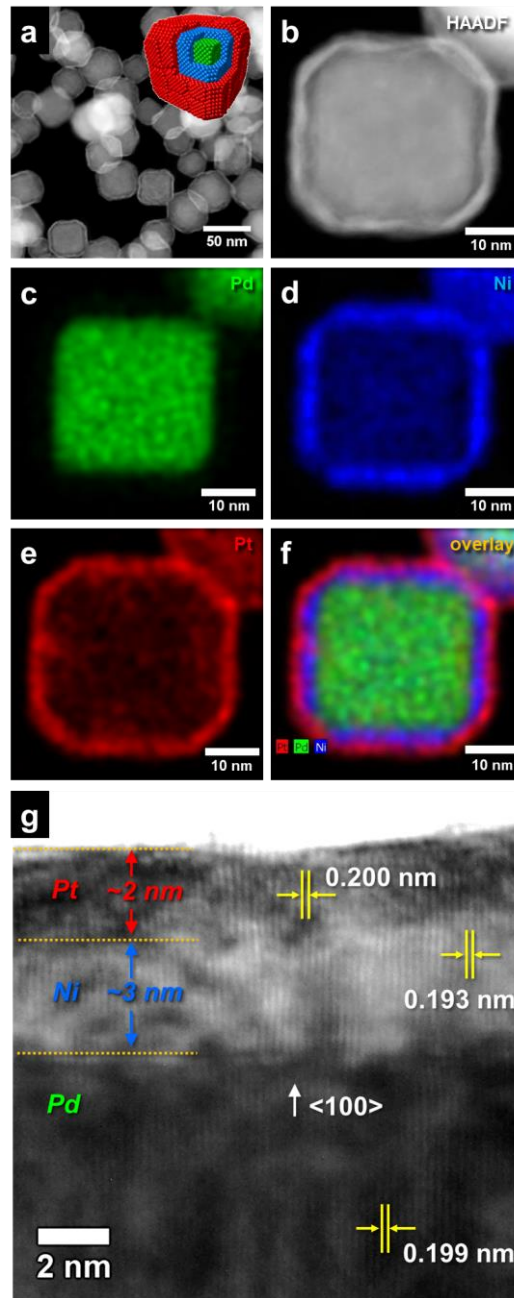


Figure 3.2: HAADF images, STEM/EDX elemental maps, and an HRTEM image of Pd-Ni-Pt NPs with a ~ 2.5 nm Ni layer. (a and b) HAADF images; (c-e) STEM/EDX element maps for Pd, Ni, and Pt, respectively, taken for the NP in (b); (f) the image containing the

overlaid maps; and (g) HRTEM cross section of a NP showing the layer thickness and measured 200 d-spacings. A structural model is given in the inset of (a).

The surface structure was probed by high resolution TEM (HRTEM) for individual particles and orientations shown in Figure 3.3. The overall truncated cubic morphology is apparent in Figure 3.3a,b with a model of the double-shelled particles inset of (a). In Figure 3.3c, square lattice patterns can be observed for NPs lying on the cube face ([100] zone axis). Figure 3.3d shows the rhombic (distorted hexagonal) lattice images for NPs lying on the cube edge ([110] zone axis). Both sets of images allow for examination of the proposed Pt(100) surface planes and epitaxy through the Ni and Pt shells. From these images and observation of several other NPs we can conclude they are primarily (100)-dominant in faceting, and that the Ni and Pt overgrowth occurs epitaxially, with some “lifted” terraces and steps at the surface, and edge dislocations in the shell produced by defects from the lattice misfit. In a lattice image of the corner of a Pd-Ni-Pt NP on edge in Figure 3.3e, an approximately $\sim 25^\circ$ curvature is observed in the atomic planes extending at different angles toward the surface, which we believe is also a result of the highly strained interfaces meeting at the vertex of the cubes. A similar observation of strain in Ni nanostructures has been described by Wang et al.²⁹ They show a nearly $\sim 40^\circ$ reversible “flip” in the unit cell of Ni nanowires induced by bending of the nanostructure.

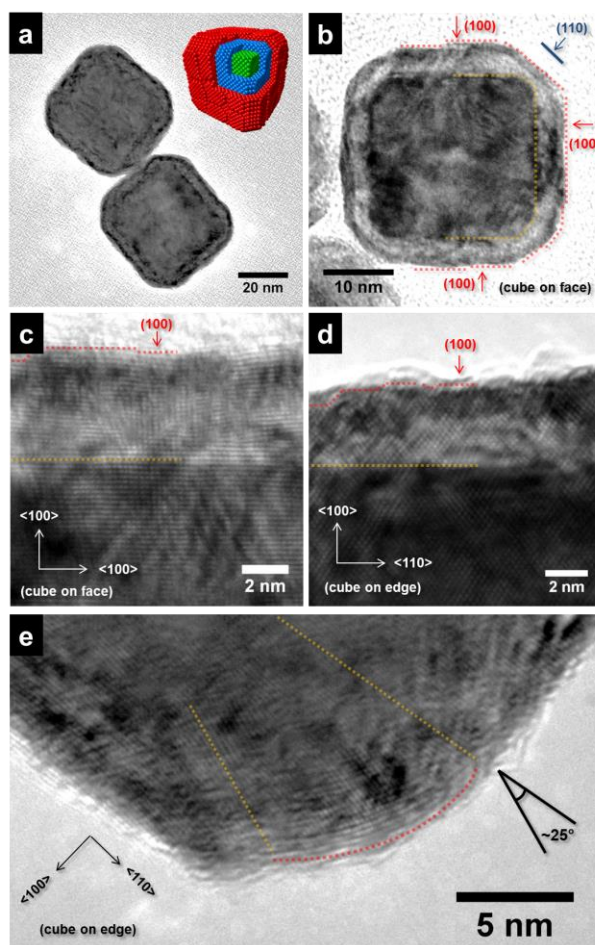


Figure 3.3: TEM and HRTEM images of Pd-Ni-Pt NPs. (a and b) TEM images showing the truncated cubic morphology with crystal model inset in (a). (c-e) HRTEM lattice images showing the epitaxy and surface structure. For the image in (c), square 2D lattices are obtained from viewing a NP down the 100 axis (cube lying on face), and for (d and e), the lattices come from viewing in the 110 direction (cube lying on edge). The image in (e) shows the lattice distortion in the shell brought about by the high interfacial mismatch for the metal layers (~10-11%) meeting at a corner.

The questions of oxide content and strain within the Ni phase are addressed by analysis of powder X-ray diffraction (XRD) of the Pd-Ni-Pt NPs and this is shown in Figure 3.4a,b. It is first noted that no diffraction peaks corresponding to the bulk NiO

positions can be observed for the samples. The spectrum for NPs with a ~ 2.5 nm Ni sandwich layer shows a single fcc diffraction pattern similar to the bulk Pd reference. Peaks were observed for the thicker NPs with a ~ 4.1 nm Ni sandwich layer close to the metallic Ni position. This global information shows that little to no oxide is forming during or after the synthesis and that metallic Ni resides within the sandwich layer. The pattern also suggests that the Ni lattice parameters may come closer to the bulk values with increasing thickness of the Ni sandwich layer (with decreasing influence of core and shell lattices)

XRD data is a good qualitative tool to indicate the existence of lattice strain. Both XRD spectra for the different shell thicknesses of Pd-Ni-Pt have peak “tails” in the direction of higher 2θ degrees. The magnification of the 111 region is displayed in Figure 3.4b. The tailing is a result of strain in the Ni layer, whereby the Ni lattice expands and Pd and Pt lattices compress. This tailing feature does not appear in the Pd-Pt control, and so corroborates with strain emanating from the introduction of the Ni sandwich layer. There is a lack of the tailing feature in the smaller Pd-Ni-Pt NPs because of the smaller domain size and broadening in the distribution. The maximum peak positions of all of the Pd-Ni-Pt NPs are shifted to the right of the bulk Pd $2\theta^\circ$ and little area under the peaks lie at the bulk Pt diffraction lines, especially for the higher angle 200 and 220 peaks. The exact amount of strain is not straightforward to assess from these shifts because of the differences between the spectra regarding the presence of broadening, the tailing feature, and the appearance of the “Ni” peak in the larger-sized, thicker-shelled NPs.

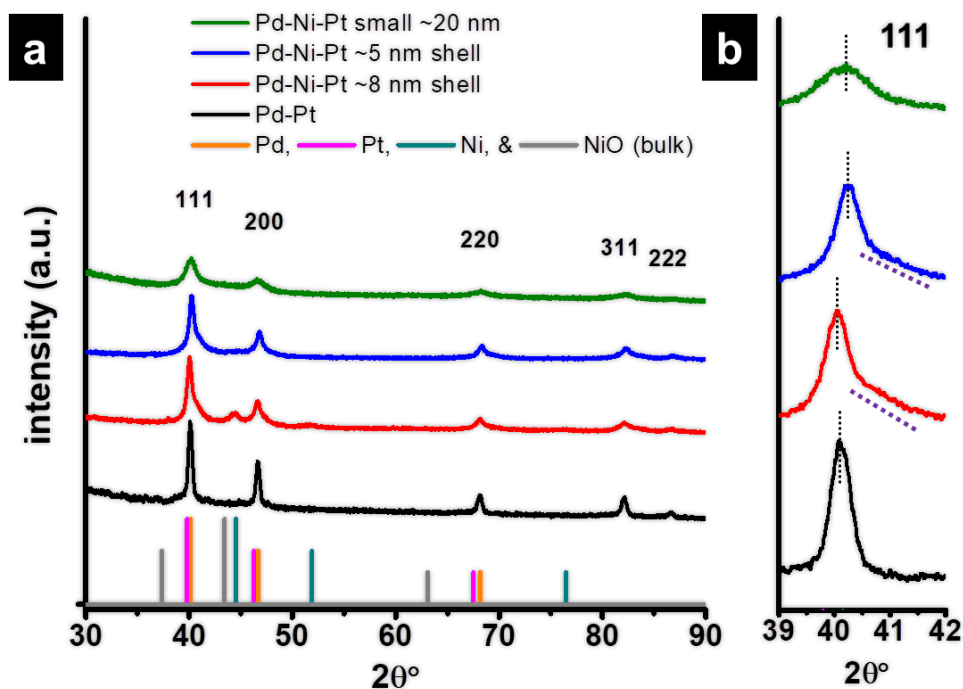


Figure 3.4: (a) Powder XRD spectra of the different Pd-Ni-Pt and Pd-Pt NPs with peak positions of bulk Pd, Ni, Pt, and NiO for reference. Plot (b) magnifies the 111 region to show the peak shift and tailing of the Pd-Ni-Pt NPs as compared to the Pd-Pt NPs.

3.4.4 Electrocatalysis by Pd-Ni-Pt Sandwich Nanoparticles

The catalytic properties of the cubic Pd-Ni-Pt NPs of different sizes and shell thicknesses were studied in the electrooxidation of methanol and formic acid. It is generally believed that both of these catalytic reactions readily occur on more open (100) and (110) surfaces of Pt as opposed to the close-packed (111) facets.³⁷ Significant improvements have been made to Pd and Pt MOR catalysts by addition of a transition metal to the structure, including alloyed and core-shell structures.⁵³⁻⁵⁸ In our work, different shell thicknesses and sizes of Pd-Ni-Pt NPs are compared alongside the Pd-Pt

core-shell NP control. Cyclic voltammetric (CV) and chronoamperometric curves (CA) were obtained for the catalysts of different sizes and Ni thicknesses to show both activity and stability. Typical blank scans in acidic and alkaline electrolyte solutions are shown in Figure 3.5a,b. Integration of the current collected from the hydrogen desorption peak was used to determine the electrochemical surface area of the different catalysts. This surface area was then used to normalize the catalytic activity for the electrooxidation reactions. The CV plots of initial activity, bar plot summaries, and CA curves for alkaline MOR, and for MOR and FOR in acidic conditions, are shown in Figures 3.6 and 3.7, respectively.

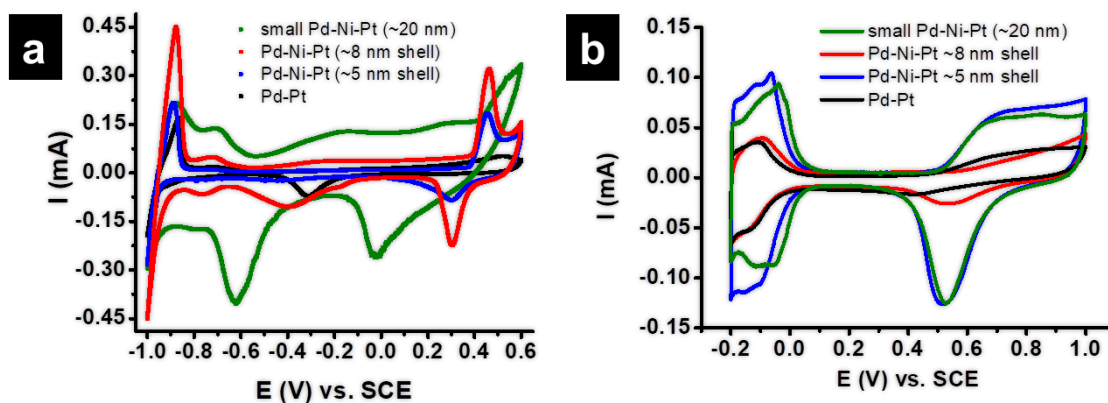


Figure 3.5: Typical a. acidic and b. alkaline blank scans for each catalyst. The Hydrogen sorption peak was utilized to determine the electrochemically active surface in order to normalize the activity.

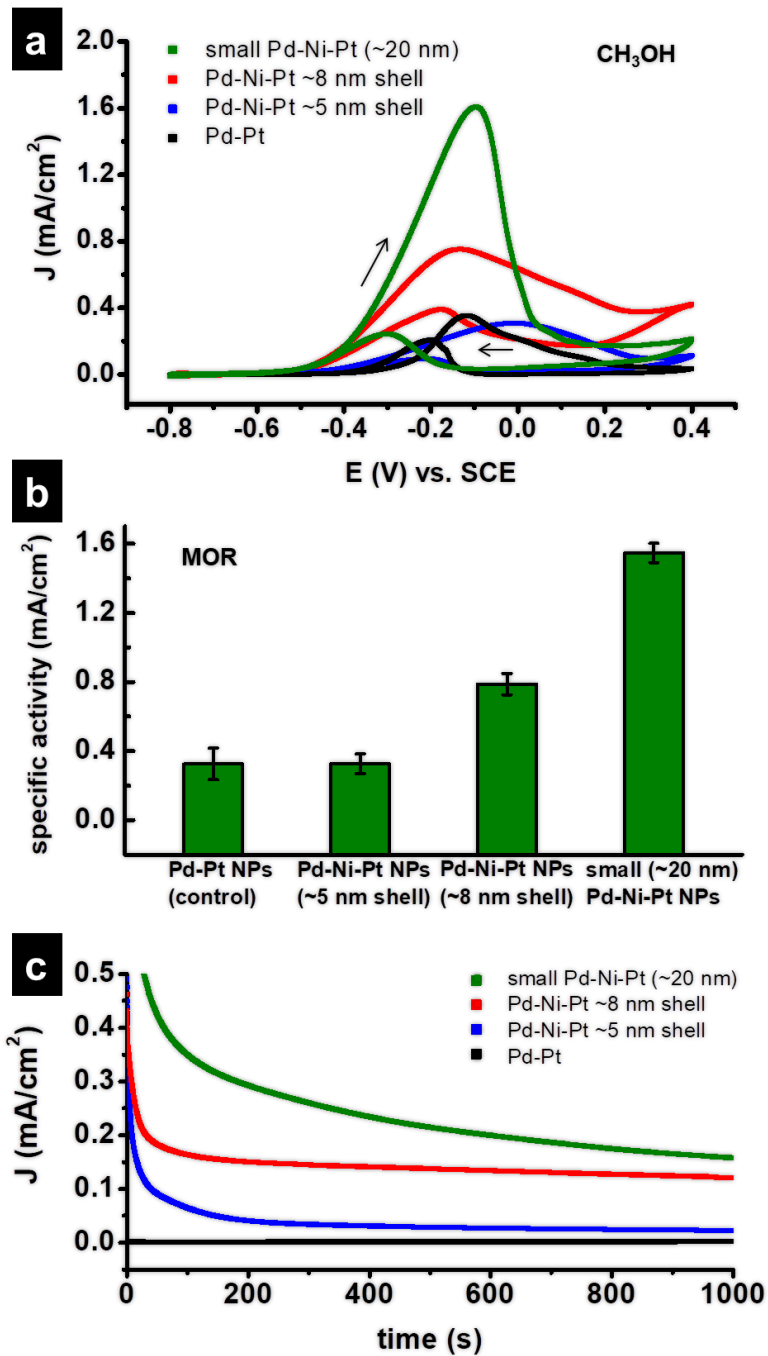


Figure 3.6: Cyclic voltammetry and chronoamperometry of multilayered Ni nanoparticles showing the catalytic activity for methanol electrooxidation in alkaline conditions. (a) CV cycles obtained in solutions which were 0.1 M in KOH and 0.05 M in CH_3OH , and (b) bar graph of trends in catalyst specific activity showing the average peak current densities

for multiple batches of each catalyst. (c) CA curves for the different NP catalysts for MOR at -0.1 V vs SCE to show the transient current density.

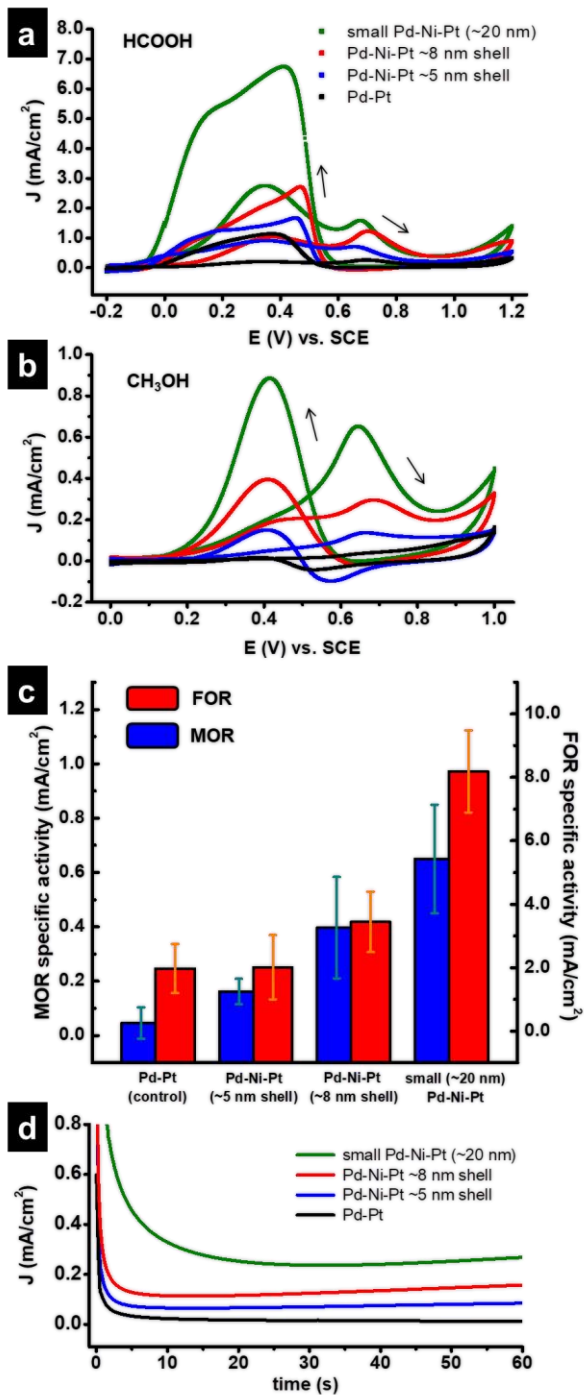


Figure 3.7: Cyclic voltammetry and chronoamperometry of multilayered Ni nanoparticles showing the catalytic activity for electro-oxidations in acidic conditions. (a) CV cycles obtained in solutions which were 0.5 M in both HCOOH and HClO₄, (b) CV curves obtained in solutions which were 0.5 M in both CH₃OH and H₂SO₄, and (c) bar graph of trends in specific activity for each reaction. Multiple batches of each catalyst were synthesized and their peak current densities averaged. (d) CA curves for the different NP catalysts for FOR at 0.4 V vs SCE.

FOR and MOR on Pt surfaces proceed by formation of intermediates, which are oxidized and removed on the forward and reverse scans.³⁷ We use the forward and reverse scan peak current densities to discuss the initial activity of the various catalysts for FOR and MOR in acidic and basic solutions. It has been reasoned that a sandwich layer consisting of a single atomic monolayer of mismatching nonprecious metal would impart little to no strain to a Pt monolayer surface in Pt-M-Pt structures; therefore, any changes in catalytic behavior are predicted to arise primarily through ligand effects.¹¹ In contrast, for the case of multiple sandwich layers and more than one monolayer of Pt surface atoms (the case here), ligand effects are expected to be minimalized, and the influence of lattice strain is expected to be the major contributor to catalysis, assuming restructuring due to dealloying or leaching of the nonprecious component does not occur to a significant extent because of the relatively thick Pt surface layer.¹⁸ As the Ni layer thickness increases for the Pd-Ni-Pt NPs, we would expect the influence of the mismatch to become greater, and so the perturbation to Pt surface atoms may be increased, resulting in changes to catalytic activity.

3.4.5 Electrocatalytic Oxidation of Methanol in Alkaline Electrolyte

To test the hypothesis of a strain influence on catalysis, CV scans were carried out for MOR in alkaline solutions shown in Figure 3.6a. It was observed that the larger, thicker Ni-layered NPs showed current density at $\sim 0.8 \text{ mA/cm}^2$. The catalysts with thinner Ni layers and the Pd-Pt control showed similar peak activities around $\sim 0.4 \text{ mA/cm}^2$, at best, roughly half the activity of the Pd-Ni-Pt NPs with thicker shells. This confirms a diminished strain effect for thin Ni sandwich layers and increasing strain from larger Ni amounts. In addition, the ratio of the forward to reverse scan peak currents is much higher with the sandwich catalysts compared to the control, which shows more efficient oxidation and CO-tolerance for these catalysts.^{54,59} A bar plot summary in Figure 3.6b for MOR in base demonstrates the average activity across different catalyst batches to be consistent. Smaller Pd-Ni-Pt NPs had a much higher current density compared to the other catalysts at $\sim 1.6 \text{ mA/cm}^2$, showing that the design could be extended down to size ranges that are more relevant for industrial applications. Figure 3.6c gives CA curves for MOR in alkaline solution generated by holding the voltage at -0.1 V vs SCE . This value was chosen because it overlapped with the position of the forward oxidation peak. These transient current density curves follow similar trends in activity, as for the CV experiments, with the Ni-sandwiched catalysts holding the highest activity over time.

3.4.6 Electrocatalytic Oxidation of Formic Acid and Methanol in Acidic

Electrolyte

Improvement of FOR and MOR electrocatalysis in acidic conditions was also observed. For FOR catalysis shown in Figure 3.7a, it can be seen that the larger Pd-Ni-Pt NPs again outperform the Pd-Pt control. Catalysts with thicker Ni layers show higher current densities (nearly double) compared to the thinner-shelled NPs. The low forward scan peak for each of the catalysts is indicative of the Pt indirect pathway,³⁷ confirming the surface composition. The smaller sized Pd-Ni-Pt NPs have the highest specific activity at $\sim 7 \text{ mA/cm}^2$. These trends follow suit in MOR in acidic electrolyte shown in Figure 3.7b, with the large Pd-Ni-Pt NPs with thicker Ni layers achieving $\sim 0.4 \text{ mA/cm}^2$. Again the smaller sized Pd-Ni-Pt cubic NPs attained the highest activity at $\sim 0.8 \text{ mA/cm}^2$. The similar trends in reactivity observed between the different catalytic oxidations could be expected based on the similarity of the reaction pathways on Pt, following direct oxidation to CO_2 , and indirect oxidation through adsorbed carbonaceous intermediates, such as CO and formate.³⁷ In fact, all of the Pd-Ni-Pt ternary metal NP structures outperform the Pd-Pt control. A summary of the specific activities for both reactions in acid electrolyte is given in the bar plot in Figure 3.7c, where initial activity for different batches of each of the four catalysts were again averaged to show the consistency. We note the higher activity for MOR catalysis in base is generally ascribed to adsorbed hydroxyls assisting in the oxidation reaction.⁵⁸

The CA studies given in Figure 3.7d show the catalyst durability for FOR at constant 0.4 V; chosen due to the location of the oxidation peak. The catalysts retain their

activity trends following Ni amounts in the sandwich layer and size of the Pd-Ni-Pt NPs. Recent reports show that larger sized particles are more sensitive toward nonprecious metal leaching in acidic conditions, making them unstable and less active over time.⁶⁰ Since the particle size here is above the limit proposed, we would expect to see activity changes over time due to this effect. Figure 3.8 shows the transient current density plot over an extended time frame. An increase in the activity is observed for the Ni-containing catalysts after the initial drop from 0 s, where they rise to reach a plateau before they finally begin to decay. Markovic et al. have discussed a similar feature for Pt-Ru alloy surfaces as being due to poisoning and removal of CO adsorbed after an initial period of time by Ru sites, however this feature on the Pd-Ni-Pt catalysts is unexpected given the conformal Pt-coating, unless dealloying is occurring.⁵⁸ The reason for this and the variation in activity for reaction in acidic media would become clear upon examination of the catalyst structure after electrochemical experiments.

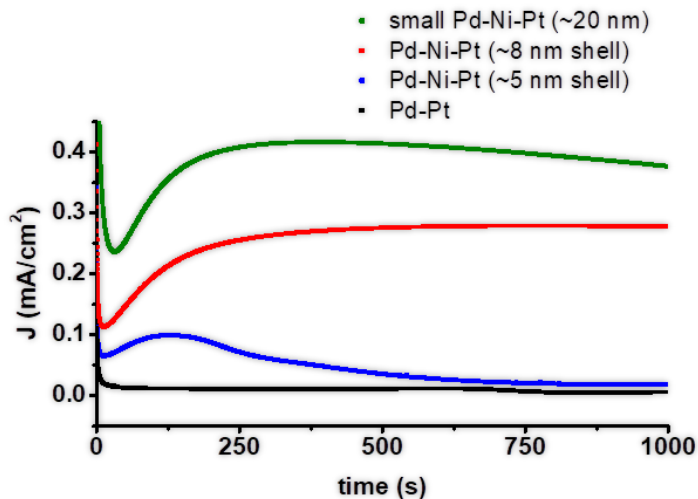


Figure 3.8: Transient current density plots over extended time frame. After the initial drop in activity, the Ni containing samples show a marked increase in activity prior to

reaching a plateau. The same trend in activity still remains, however the likely increase is due to either surface poisoning followed by removal or metal leaching/dealloying.

3.4.7 Re-examination of Pd-Ni-Pt Sandwich Nanoparticles after Electrocatalysis

Experiments

We initially assumed that the improved performance of the small Pd-Ni-Pt catalysts and the difference in activity for higher Ni amounts in the sandwich layer were lattice strain-related based on the catalytic trends, XRD peak shifts and tailing, and HRTEM of the catalysts before the reactions; however, this assumes the NP surfaces underwent no changes during the potential cycling in acid and base electrolyte. The catalysts were re-examined in TEM after the electrochemical experiments were carried out to confirm whether or not the layered NP structure remained intact. The images of the highest-performing catalysts (small and large Pd-Ni-Pt NPs with the thickest Ni layer) on the carbon support after CA experiments in acidic FOR and basic MOR are shown in Figure 3.9. A stark difference is apparent in the NP catalysts after reaction in acidic conditions in Figure 3.9e-h), whereas after reaction in base in Figure 3.9a-d, the structure resembles that before electrochemistry is carried out. For FOR in perchloric acid and blank scans in sulfuric acid, the core of the Pd-Ni-Pt NPs appears void, despite the Pt coating. The Pd and Ni signals remaining in EDX of the sample indicate the metals are not completely removed, however, and this suggests Pd and Ni sites remain in the frameworks.

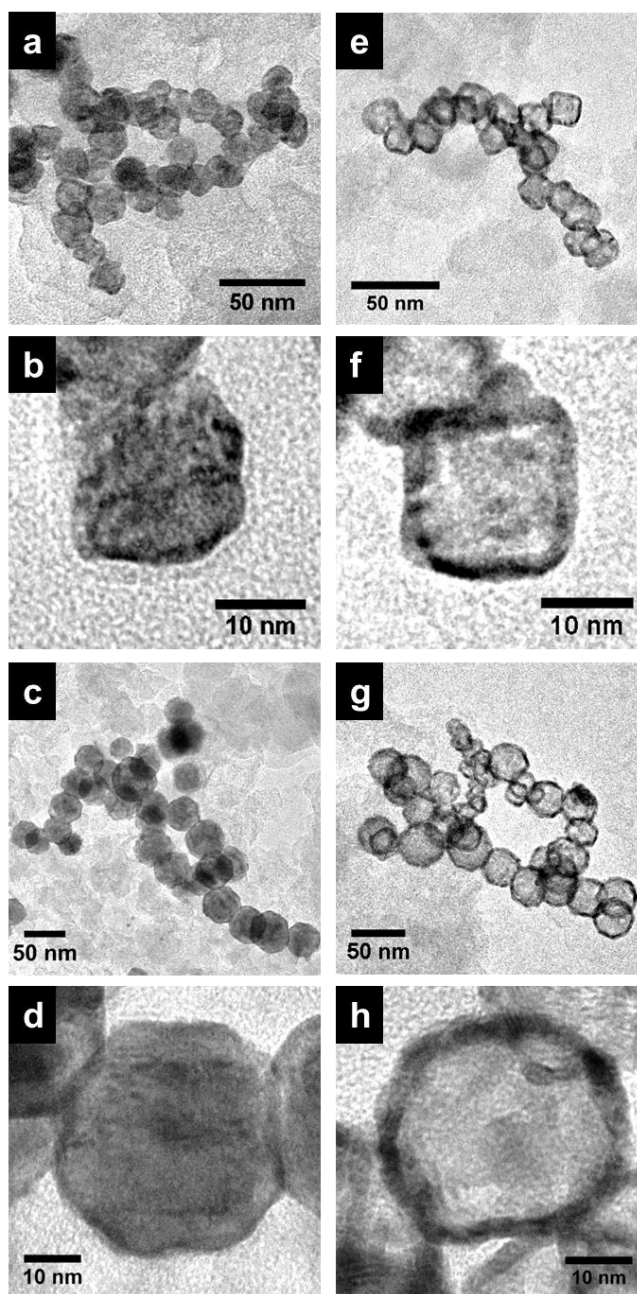


Figure 3.9: TEM images of cubic Pd-Ni-Pt NPs on the carbon support after the electrochemical experiments in acid and base electrolyte. Images of small Pd-Ni-Pt NPs are given after reaction in basic conditions in (a and b) and acidic conditions in (e and f). (c, d) and (g,h) The large Pd-Ni-Pt NPs after reaction in basic and acidic media, respectively.

Following from the TEM results, the case of MOR in KOH solution where catalyst stability is higher, strain governs reactivity, whereas in acidic FOR and MOR conditions, the NPs restructure so that a combination of strain, ligand, and ensemble effects govern the reactivity trends. Before reaction, we believe the compressive strain on the Pt surface may be highest in the small Pd-Ni-Pt NPs, due to the combined strain effects from Ni sandwich layers and smaller size, followed by the larger NPs with ~4.1 nm Ni, the NPs with ~2.5 nm Ni, and the Pd-Pt control NPs. This would explain the enhanced catalytic performance in basic MOR. The higher activity with increasing amounts of Ni and decreasing overall NP size for both FOR and MOR in acidic conditions is more likely a result of a combination of this effect and composition changes from dealloying and restructuring. Notably, the hollow structures observed after cycling in acid resemble recent displays of electrocatalysts with stable porous M-Pt nanosheets and nanoframeworks,^{61,62} although formed by a different route. The Pt-Ni nanoframeworks produced by C. Chen, Y. Kang et al. were formed from oxidative aging of the particles in solution after the synthesis and still showed considerable enhancement and stability for oxygen reduction catalysis. These examples support the finding of increased activity of the catalysts after leaching of Pd and Ni. The post-cycling TEM also suggests that even Pd in a core-shell configuration is susceptible to leaching effects from potential cycling in acid, and examination of such Pd-containing electrocatalysts after reaction should not be excluded from future studies.

3.4.8 Synthesis of Quaternary, Multi-shelled Au-Pd-Ni-Pt Nanoparticles and Pd-Ni-Pt Sandwich Nanooctahedra

Lastly, we demonstrate the synthesis affords differently shaped and more sophisticated layered nanostructures. It was found that the Ni and Pt overgrowth could be replicated on ~30 nm Pd octahedra and on cubic Au-Pd core-shell substrates. This was accomplished by replacing the Pd nanocubes with Pd octahedra or Au-Pd core-shell nanocubes in the growth solution. The resulting NP TEM images are shown in Figure 8. The octahedral ternary metal NPs appear in Figure 3.10a-d and the cubic quaternary metal NPs appear in Figure 3.10e-h. The octahedral Pd-Ni-Pt NPs are expected to be the subject of future work as promising candidates for oxygen reduction catalysis (ORR) for fuel cell cathodes. In the high magnification TEM image in Figure 3.10g, the four metal phases in one of the quaternary cubic NPs can be resolved. A gold cubooctahedral seed is established in the core as the darkest contrast, with a slightly brighter, distinct cubic Pd shell encasing it. As before with the cubic ternary metal NPs, a thin layer of lighter contrast Ni phase surrounds the Au-Pd cube followed by a thin, dark band of Pt at the surface. This shows our method could be used to create NPs with as many as four different and distinguishable metal layers while holding the particle size at or below ~20 nm. The shaped multi-shelled metal NPs displayed in this work are rare in the literature, to our knowledge, though there is an excellent example of hollow ternary layered noble metal NPs from González et al.⁶³ A recolored TEM image of the Au-Pd-Ni-Pt NP is given in Figure 3.11 to more clearly show the four metal phases along with EDX data to confirm the metal composition in the NPs.

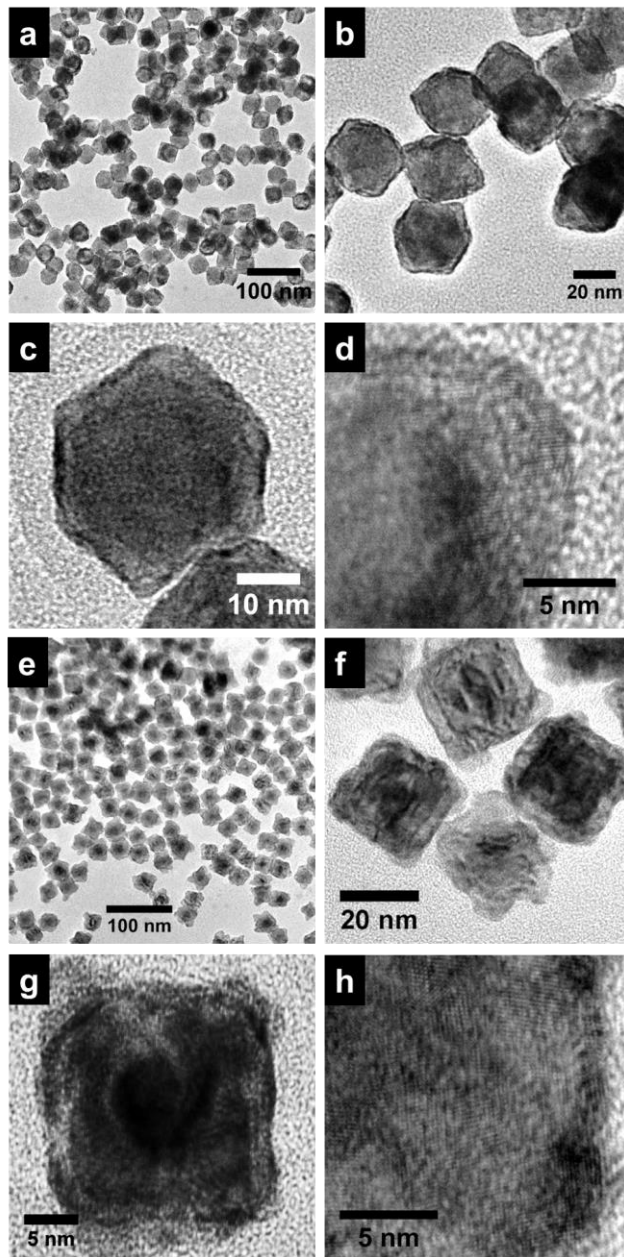


Figure 3.10: (a-d) TEM and HRTEM images of ~ 30 nm Pd-Ni-Pt nanooctahedra; (e-h) images of cubic multishelled Au-Pd-Ni-Pt quaternary metal NPs. (c and g) TEM images of single particles are shown where each of the multiple metal phases can be resolved by contrast, and HRTEM images of the respective NPs are given in (d and h).

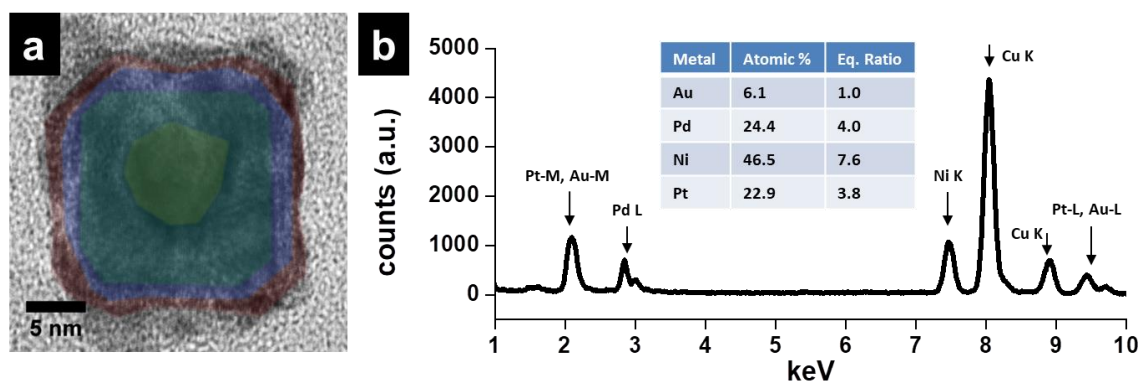


Figure 3.11: Respectively, a and b, show TEM image with colored overlay to more clearly show the metal boundaries; Au (yellow), Pd (green), Ni (blue), and Pt (red) as well as the EDX data confirming the metal composition within the nanoparticle

3.5 Conclusion

Shaped Pd-Ni-Pt core-sandwich-shell NPs are synthesized using cubic and octahedral Pd substrates in the aqueous phase at low temperature with cationic surfactant and hydrazine as the reducing agent. It has been demonstrated that the method produces ternary and quaternary multilayered metal nanoparticles comprising Ni with control of shape, size, and Ni layer thickness. Importantly, the one-pot, layer-by-layer overgrowth strategy allows for “trapping” of the pristine, metallic Ni layer before surface oxidation occurs. The novel NP structures are characterized and served as a platform to study the activity of the catalysts in the electrocatalytic oxidation of methanol and formic acid. Their stability is also assessed *via* chronoamperometry. The improved performance of the Pd-Ni-Pt particles over the Pd-Pt control results from increased compressive strain on the Pt surface. It was found that the smaller sized particles and larger Ni sandwich layers are more active and stable over a longer period of time, suggesting a potentially effective

catalyst design in future work. Further investigations are aimed at a systematic study of the impact of different shapes and different Ni and Pt layer thicknesses on electrocatalysis by the multishelled structures; in particular, the tuning of the Ni and Pt shell thickness of octahedral Pd-Ni-Pt NPs to obtain a better-performing ORR catalyst.

3.6 References

- [1.] Mayrhofer, K. J. J.; Arenz, M. Fuel Cells: Log on for New Catalysts. *Nat. Chem.* **2009**, *1*, 518–519.
- [2.] Debe, M.K. Electrocatalyst Approaches and Challenges for Automotive Fuel Cells. *Nature.* **2012**, *486*, 43–51.
- [3.] Stephens, I.E.L.; Bondarenko, A.S.; Gronbjerg, U.; Rossmeisl, J.; Chorkendorff, I. Understanding the Electrocatalysis of Oxygen Reduction on Platinum and its Alloys. *Energy Environ. Sci.* **2012**, *5*, 6744–6762.
- [4.] Norskov, J. K.; Bligaard, T.; Rossmeisl, J.; Christensen, C. H. Towards the Computational Design of Solid Catalysts. *Nat. Chem.* **2009**, *1*, 37–46.
- [5.] Long, N. V.; Thi, C. M.; Yong, Y.; Nogami, M.; Ohtaki, M. Platinum and Palladium Nano-Structured Catalysts for Polymer Electrolyte Fuel Cells and Direct Methanol Fuel Cells. *J. Nanosci. Nanotechnol.* **2013**, *13*, 4799–4824.
- [6.] Singh, A. K.; Xu, Q. Synergistic Catalysis over Bimetallic Alloy Nanoparticles. *ChemCatChem* **2013**, *5*, 652–676.
- [7.] Guo, S.; Zhang, S.; Sun, S. Tuning Nanoparticle Catalysis for the Oxygen Reduction Reaction. *Angew. Chem., Int. Ed.* **2013**, *52*, 8526–8544.
- [8.] Bandarenka, A.S.; Koper, M.T.M. Structural and Electronic Effects in Heterogeneous Electrocatalysis: Toward a Rational Design of Electrocatalysts. *J. Catal.* **2013**, *308*, 11–24.
- [9.] Wu, B. H.; Zheng, N. F. Surface and Interface Control of Noble Metal Nanocrystals for Catalytic and Electrocatalytic applications. *Nano Today* **2013**, *8*, 168–197.
- [10.] Oezaslan, M.; Hasché, F.; Strasser, P. Pt-Based Core-Shell Catalyst Architectures for Oxygen Fuel Cell Electrodes. *J. Phys. Chem. Lett.* **2013**, *4*, 3273–3291.

- [11.] Kaya, S.; Friebel, D.; Ogasawara, H.; Anniyev, T.; Nilsson, A. Electronic Structure Effects in Catalysis Probed by X-ray and Electron Spectroscopy. *J. Electron Spectrosc. Relat. Phenom.* **2013**, *190* (Part A), 113–124.
- [12.] Zhang, X.; Lu, G. Computational Design of Core/Shell Nanoparticles for Oxygen Reduction Reactions. *J. Phys. Chem. Lett.* **2013**, *5*, 292–297.
- [13.] Wang, G.; Van Hove, M. A.; Ross, P. N.; Baskes, M. I. Monte Carlo Simulations of Segregation in Pt-Ni Catalyst Nanoparticles. *J. Chem. Phys.* **2005**, *122*, 024706.
- [14.] Menning, C. A.; Hwu, H. H.; Chen, J. G. Experimental and Theoretical Investigation of the Stability of Pt-3d-Pt(111) Bimetallic Surfaces under Oxygen Environment. *J. Phys. Chem. B* **2006**, *110*, 15471–15477.
- [15.] Wang, C.; Chi, M.; Li, D.; Strmcnik, D.; van der Vliet, D.; Wang, G.; Komanicky, V.; Chang, K.-C.; Paulikas, A.P.; Tripkovic, D.; *et al.* Design and Synthesis of Bimetallic Electrocatalyst with Multilayered Pt-Skin Surfaces. *J. Am. Chem. Soc.* **2011**, *133*, 14396–14403.
- [16.] Porosoff, M. D.; Yu, W.; Chen, J. G. Challenges and Opportunities in Correlating Bimetallic Model Surfaces and Supported Catalysts. *J. Catal.* **2013**, *308*, 2–10.
- [17.] Cui, C.; Gan, L.; Heggen, M.; Rudi, S.; Strasser, P. Compositional Segregation in Shaped Pt Alloy Nanoparticles and Their Structural Behaviour During Electrocatalysis. *Nat. Mater.* **2013**, *12*, 765–771.
- [18.] Strasser, P.; Koh, S.; Anniyev, T.; Greeley, J.; More, K.; Yu, C.; Liu, Z.; Kaya, S.; Nordlund, D.; Ogasawara, H.; *et al.* Lattice Strain Control of the Activity in Dealloyed Core-Shell Fuel Cell Catalysts. *Nat. Chem.* **2010**, *2*, 454–460.
- [19.] Cui, C.; Gan, L.; Li, H.-H.; Yu, S.-H.; Heggen, M.; Strasser, P. Octahedral PtNi Nanoparticle Catalysts: Exceptional Oxygen Reduction Activity by Tuning the Alloy Particle Surface Composition. *Nano Lett.* **2012**, *12*, 5885–5889.
- [20.] Choi, S.-I.; Xie, S.; Shao, M.; Odell, J. H.; Lu, N.; Peng, H.-C.; Protsailo, L.; Guerrero, S.; Park, J.; Xia, X.; *et al.* Synthesis and Characterization of 9 nm Pt-Ni Octahedra with a Record High Activity of 3.3 A/mgPt for the Oxygen Reduction Reaction. *Nano Lett.* **2013**, *13*, 3420–3425.
- [21.] Wu, J.; Gross, A.; Yang, H. Shape and Composition Controlled Platinum Alloy Nanocrystals Using Carbon Monoxide as Reducing Agent. *Nano Lett.* **2011**, *11*, 798 – 802.

- [22.] Porter, N. S.; Wu, H.; Quan, Z.; Fang, J. Shape-Control and Electrocatalytic Activity-Enhancement of Pt-Based Bimetallic Nanocrystals. *Acc. Chem. Res.* **2013**, *46*, 1867–1877.
- [23.] Wu, Y.; Cai, S.; Wang, D.; He, W.; Li, Y. Syntheses of Water Soluble Octahedral, Truncated Octahedral, and Cubic Pt-Ni Nanocrystals and Their Structure-Activity Study in Model Hydrogenation Reactions. *J. Am. Chem. Soc.* **2012**, *134*, 8975–8981.
- [24.] Jin, M.; Zhang, H.; Wang, J.; Zhong, X.; Lu, N.; Li, Z.; Xie, Z.; Kim, M. J.; Xia, Y. Copper Can Still Be Epitaxially Deposited on Palladium Nanocrystals To Generate Core-Shell Nanocubes Despite Their Large Lattice Mismatch. *ACS Nano* **2012**, *6*, 2566–2573.
- [25.] Ping, H.; Chen, Y.; Guo, H.; Wang, Z.; Zeng, D.; Wang, L.; Peng, D.-L. A Facile Solution Approach for the Preparation of Ag@Ni Core-Shell Nanocubes. *Mater. Lett.* **2014**, *116*, 239–242.
- [26.] Sau, T. K.; Murphy, C. J. Room Temperature, High-yield Synthesis of Multiple Shapes of Gold Nanoparticles in Aqueous Solution. *J. Am. Chem. Soc.* **2004**, *126*, 8648–8649.
- [27.] Kuo, C.-H.; Lamontagne, L. K.; Brodsky, C. N.; Chou, L.-Y.; Zhuang, J.; Sneed, B. T.; Sheehan, M. K.; Tsung, C.-K. The Effect of Lattice Strain on the Catalytic Properties of Pd Nanocrystals. *ChemSusChem*. **2013**, *6*, 1993–2000.
- [28.] Sneed, B. T.; Kuo, C.-H.; Brodsky, C. N.; Tsung, C.-K. Iodide Mediated Control of Rhodium Epitaxial Growth on Well-Defined Noble Metal Nanocrystals: Synthesis, Characterization, and Structure-Dependent Catalytic Properties. *J. Am. Chem. Soc.* **2012**, *134*, 18417–18426.
- [29.] Sneed, B. T.; Brodsky, C. N.; Kuo, C.-H.; Lamontagne, L. K.; Jiang, Y.; Wang, Y.; Tao, F.; Huang, W.; Tsung, C.-K. Nanoscale-Phase-Separated PdRh Boxes Synthesized via Metal Migration: An Archetype for Studying Lattice Strain and Composition Effects in Electrocatalysis. *J. Am. Chem. Soc.* **2013**, *135*, 14691–14700.
- [30.] Habas, S.E.; Lee, H.; Radmilovic, V.; Somorjai, G.A.; Yang, P. Shaping Binary Metal Nanocrystals Through Epitaxial Seeded Growth. *Nat. Mater.* **2007**, *6*, 692–697.
- [31.] DeSantis, C.J.; Sue, A.C.; Bower, M.M.; Skrabalak, S.E. Seed Mediated Co-reduction: A Versatile Route to Architecturally Controlled Bimetallic Nanostructures. *ACS Nano* **2012**, *6*, 2617–2628.
- [32.] Kuo, C.H.; Hua, T.E.; Huang, M.H. Au Nanocrystal-Directed Growth of Au-Cu₂O Core-Shell Heterostructures with Precise Morphological Control. *J. Am. Chem. Soc.* **2009**, *131*, 17871–17878.

- [33.] Wang, J. X.; Inada, H.; Wu, L.; Zhu, Y.; Choi, Y.; Liu, P.; Zhou, W.-P.; Adzic, R. R. Oxygen Reduction on Well-Defined Core-Shell Nanocatalysts: Particle Size, Facet, and Pt Shell Thickness Effects. *J. Am. Chem. Soc.* **2009**, *131*, 17298–17302.
- [34.] Hwang, S.J.; Kim, S.-K.; Lee, J.-G.; Lee, S.-C.; Jang, J.H.; Kim, P.; Lim, T.-H.; Sung, Y.-E.; Yoo, S. J. Role of Electronic Perturbation in Stability and Activity of Pt-Based Alloy Nanocatalysts for Oxygen Reduction. *J. Am. Chem. Soc.* **2012**, *134*, 19508–19511.
- [35.] Xin, H.; Linic, S. Communications: Exceptions to the d-band Model of Chemisorption on Metal Surfaces: The Dominant Role of Repulsion Between Adsorbate States and Metal d-states. *J. Chem. Phys.* **2010**, *132*, 221101.
- [36.] Yu, T. H.; Hofmann, T.; Sha, Y.; Merinov, B. V.; Myers, D. J.; Heske, C.; Goddard, W. A. Finding Correlations of the Oxygen Reduction Reaction Activity of Transition Metal Catalysts with Parameters Obtained from Quantum Mechanics. *J. Phys. Chem. C* **2013**, *117*, 26598–26607.
- [37.] Koper, M. T.M. Structure Sensitivity and Nanoscale Effects in Electrocatalysis. *Nanoscale* **2011**, *3*, 2054–2073.
- [38.] Grzelczak, M.; Pérez-Juste, J.; Rodríguez-González, B.; Spasova, M.; Barsukov, I.; Farle, M.; Liz-Marzán, L. M. Pt-Catalyzed Growth of Ni Nanoparticles in Aqueous CTAB Solution. *Chem. Mater.* **2008**, *20*, 5399–5405.
- [39.] Sanles-Sobrido, M.; Banobre-Lopez, M.; Salgueirino, V.; Correa-Duarte, M. A.; Rodriguez-Gonzalez, B.; Rivas, J.; Liz-Marzan, L. M. Tailoring the Magnetic Properties of Nickel Nanoshells Through Controlled Chemical Growth. *J. Mater. Chem.* **2010**, *20*, 7360–7365.
- [40.] Grzelczak, M.; Rodríguez-González, B.; Pérez-Juste, J.; Liz-Marzán, L. M. Quasi-Epitaxial Growth of Ni Nanoshells on Au Nanorods. *Adv. Mater.* **2007**, *19*, 2262–2266.
- [41.] Sánchez-Iglesias, A.; Grzelczak, M.; Rodríguez-González, B.; Guardia-Girós, P.; Pastoriza-Santos, I.; Pérez-Juste, J.; Prato, M.; Liz-Marzán, L. M. Synthesis of Multifunctional Composite Microgels *via in-Situ* Ni Growth on pNIPAM-Coated Au Nanoparticles. *ACS Nano* **2009**, *3*, 3184–3190.
- [42.] Wu, Z. G.; Munoz, M.; Montero, O. The Synthesis of Nickel Nanoparticles by Hydrazine Reduction. *Adv. Powder Technol.* **2010**, *21*, 165–168.
- [43.] Sarkar, S.; Sinha, A.K.; Pradhan, M.; Basu, M.; Negishi, Y.; Pal, T. Redox Transmetalation of Prickly Nickel Nanowires for Morphology Controlled Hierarchical Synthesis of Nickel/ Gold Nanostructures for Enhanced Catalytic Activity and SERS Responsive Functional Material. *J. Phys. Chem. C* **2010**, *115*, 1659–1673.

- [44.] Senapati, S.; Srivastava, S.K.; Singh, S.B.; Biswas, K. Capping Agent Assisted and Ag-Catalyzed Growth of Ni Nanoflowers. *Cryst. Growth Des.* **2010**, *10*, 4068–4075.
- [45.] Nelson, N. C.; Ruberu, T. P. A.; Reichert, M. D.; Vela, J. Templated Synthesis and Chemical Behavior of Nickel Nanoparticles within High Aspect Ratio Silica Capsules. *J. Phys. Chem. C* **2013**, *117*, 25826–25836.
- [46.] Jana, S.; Chang, J. W.; Rioux, R. M. Synthesis and Modeling of Hollow Intermetallic Ni-Zn Nanoparticles Formed by the Kirkendall Effect. *Nano Lett.* **2013**, *13*, 3618–3625.
- [47.] Zhang, W.-B.; Chen, C.; Zhang, S.-Y. Equilibrium Crystal Shape of Ni from First Principles. *J. Phys. Chem. C* **2013**, *117*, 21274–21280.
- [48.] Ming, T.; Feng, W.; Tang, Q.; Wang, F.; Sun, L.D.; Wang, J.F.; Yan, C. H. Growth of Tetrahedral Gold Nanocrystals with High-index Facets. *J. Am. Chem. Soc.* **2009**, *131*, 16350–1.
- [49.] Wu, H.L.; Kuo, C.H.; Huang, M.H. Seed-Mediated Synthesis of Gold Nanocrystals with Systematic Shape Evolution from Cubic to Trisoctahedral and Rhombic Dodecahedral Structures. *Langmuir* **2010**, *26*, 12307–12313.
- [50.] Kuo, C.-H.; Tang, Y.; Chou, L.-Y.; Sneed, B. T.; Brodsky, C. N.; Zhao, Z.; Tsung, C.-K. Yolk-Shell Nanocrystal@ZIF-8 Nanostructures for Gas-Phase Heterogeneous Catalysis with Selectivity Control. *J. Am. Chem. Soc.* **2012**, *134*, 14345–14348.
- [51.] Zhang, B.; Wu, J.; Li, X.; Liu, H.; Yadian, B.; Ramanujan, R. V.; Zhou, K.; Wu, R.; Hao, S.; Huang, Y. Passivation of Nickel Nanoneedles in Aqueous Solutions. *J. Phys. Chem. C* **2014**, *118*, 9073–9077.
- [52.] Lim, B.; Jiang, M.; Camargo, P. H. C.; Cho, E. C.; Tao, J.; Lu, X.; Zhu, Y.; Xia, Y. Pd-Pt Bimetallic Nanodendrites with High Activity for Oxygen Reduction. *Science* **2009**, *324*, 1302–1305.
- [53.] Liu, X.-J.; Cui, C.-H.; Gong, M.; Li, H.-H.; Xue, Y.; Fan, F.-J.; Yu, S.-H. Pt-Ni Alloyed Nanocrystals with Controlled Architectures for Enhanced Methanol Oxidation. *Chem. Commun.* **2013**, *49*, 8704–8706.
- [54.] Kang, Y.; Pyo, J. B.; Ye, X.; Gordon, T. R.; Murray, C. B. Synthesis, Shape Control, and Methanol Electro-oxidation Properties of Pt-Zn Alloy and Pt₃Zn Intermetallic Nanocrystals. *ACS Nano* **2012**, *6*, 5642–5647.
- [55.] Deivaraj, T. C.; Chen, W.; Lee, J. Y. Preparation of PtNi Nanoparticles for the Electrocatalytic Oxidation of Methanol. *J. Mater. Chem.* **2003**, *13*, 2555–2560.

- [56.] Wang, L.; Liu, P.; Guan, P.; Yang, M.; Sun, J.; Cheng, Y.; Hirata, A.; Zhang, Z.; Ma, E.; Chen, M.; *et al.* *In Situ* Atomic Scale Observation of Continuous and Reversible Lattice Deformation Beyond the Elastic Limit. *Nat. Commun.* **2013**, *4*, 1–7.
- [57.] Abdel Rahim, M. A.; Hassan, H. B.; Abdel Hameed, R. M. Graphite Electrodes Modified with Platinum-Nickel NanoParticles for Methanol Oxidation. *Fuel Cells* **2007**, *7*, 298–305.
- [58.] Tripković, A. V.; Popović, K. D.; Grgur, B. N.; Blizanac, B.; Ross, P. N.; Marković, N. M. Methanol Electrooxidation on Supported Pt and PtRu Catalysts in Acid and Alkaline Solutions. *Electrochim. Acta* **2002**, *47*, 3707–3714.
- [59.] Prabhuram, J.; Manoharan, R. Investigation of Methanol Oxidation on Unsupported Platinum Electrodes in Strong Alkali and Strong Acid. *J. Power Sources* **1998**, *74*, 54–61.
- [60.] Gan, L.; Heggen, M.; O'Malley, R.; Theobald, B.; Strasser, P. Understanding and Controlling Nanoporosity Formation for Improving the Stability of Bimetallic Fuel Cell Catalysts. *Nano Lett.* **2013**, *13*, 1131–1138.
- [61.] Jia, Y.; Jiang, Y.; Zhang, J.; Zhang, L.; Chen, Q.; Xie, Z.; Zheng, L. Unique Excavated Rhombic Dodecahedral PtCu₃ Alloy Nanocrystals Constructed with Ultrathin Nanosheets of High-Energy {110} Facets. *J. Am. Chem. Soc.* **2014**, *136*, 3748–3751.
- [62.] Chen, C.; Kang, Y.; Huo, Z.; Zhu, Z.; Huang, W.; Xin, H. L.; Snyder, J. D.; Li, D.; Herron, J. A.; Mavrikakis, M.; *et al.* Highly Crystalline Multimetallic Nanoframes with Three-Dimensional Electrocatalytic Surfaces. *Science* **2014**, *343*, 1339–1343.
- [63.] González, E.; Arbiol, J.; Puntès, V. F. Carving at the Nanoscale: Sequential Galvanic Exchange and Kirkendall Growth at Room Temperature. *Science* **2011**, *334*, 1377–1380.

4.0 Synthesis of Shaped Ni₃Pt Nanoframes through the Low-Temperature Annealing of Pd-Ni-Pt Core-Sandwich-Shell Nanoparticles

4.1 Abstract

Intermetallic nanoparticles (NPs) have recently received great attention due to the precise tunability of their geometric and electronic surface structure; however, achieving morphological control of intermetallic NPs is challenging due to the high temperature required during synthesis to achieve the stable intermetallic structure. Here, we present a synthetic strategy for the formation of shape-controlled intermetallic nanoframes (NFs) using multilayered core-sandwich-shell NPs as precursors. Our precursor structure consists of a cubic Pd core coated with alternating Ni and Pt layers of varying thickness and number. The required annealing temperature to form the intermetallic NF depends on a variety of factors. Thin, four-layered particles achieve mixing at a lower temperature than their thick, two-layered counterparts due to higher defect concentrations, shorter diffusion lengths, and higher interfacial energies. Using transmission electron microscopy (TEM), a series of lattice measurements, and x-ray diffraction (XRD), the crystal structure of the intermetallic NFs is studied. To probe the NF electronic structure, a series of electrochemical small molecule oxidations is performed. The platform and insights presented herein represent an important step toward the realization of shape-controlled intermetallic NPs tailored to each potential application.

4.2 Introduction

As demand grows for renewable and carbon neutral energy sources, nanomaterial design has increasingly focused on developing highly active and stable catalysts for chemical transformations¹⁻⁶. Platinum group metals are particularly active for a diverse set of reactions, but they are expensive and susceptible to surface poisoning, limiting their applicability in new technologies like fuel cells. By incorporating nonprecious metals in an alloyed or core-shell fashion, catalyst cost can be lowered and activity can be increased⁷⁻¹², but many alloyed and core-shell structures are unstable in acidic media or other harsh environments. Nonprecious incorporation strategies have thus recently shifted attention to their intermetallic counterparts^{2, 13}. Intermetallic compounds (IMCs) are crystalline alloys composed of two or more metallic/metalloid elements with specific stoichiometry and long-range atomic order. More robust and resilient to etching¹⁴, these atomically ordered structures offer unique properties, e.g. shape memory¹⁵, hydrogen storage¹⁶, and superconductivity¹⁷. Further, their tunable surface electronic structures¹⁸⁻¹⁹ allow their sorption and desorption properties to be tailored to specific chemical reactions.

In previous works, bulk IMCs have been extensively studied. More recent studies have focused on IMC nanoparticles (NPs) for their tailorable geometries, electronic surface structures and molecular adsorption properties²⁰⁻²³. IMC NPs are typically synthesized via three approaches. In the top-down approach, bulk phase IMCs are synthesized by annealing mixed powders of metallic elements and then crushing the bulk material to form IMC NPs²⁴. The size and shape of NPs synthesized by this top-down

method cannot be well-controlled. In the bottom-up approach, IMC NPs are directly synthesized by wet-chemistry methods. Shaped IMC NPs have been generated by using this method²⁵⁻²⁶; however, the need to precisely and simultaneously control the deposition rates of the chosen metals makes the understanding of formation kinetics challenging. Alternatively, a third approach has been proposed in which alloy NPs or heterostructured bimetallic NPs (e.g., core-shell or dimer) are synthesized via wet-chemistry, and these precursor NPs are converted into the IMC phase through metallic intermixing triggered by thermal annealing²⁷.

Many of these direct synthesis methods have generated a variety of intermetallic nanoparticles with unique properties and diverse crystal structures and compositions, but the combination of ill-defined metal NP precursors and high annealing temperatures has made precise morphological control difficult²⁷. The resulting indistinct particle shapes can convolute catalytic results due to inconsistencies in size, shape/faceting, and surface composition, making the fundamental study of the catalyst surface or active sites difficult. In this work, we aim to optimize this third approach because we believe that intermixing, taking place in well-controlled nanoscale geometries, offers the best opportunity to understand the shape-dependent formation kinetics of IMC phases, leading to a general synthesis scheme for shaped IMC NPs.

Since the greatest contributor to the need for high annealing temperatures is the solid-solid interdiffusion of metal atoms²⁸⁻³⁰, we focus on lowering the diffusion barriers through the use of strained metallic layers of variable thickness. Previously, our group developed defined overgrowth methods for well controlled core-shell NPs using mild aqueous phase systems^{9-10, 31}. During these syntheses, such things as substrate size and

shape, layer thickness and compositions, and layer number could be controlled. Notably, our Pd-Ni-Pt system¹⁰ stands out as an interesting candidate for the study of intermetallic formation, as the incorporation of Ni into Pt NPs has been shown to increase catalytic activity towards small molecule redox reactions^{7-8, 14, 27}. This well studied platform serves as an ideal arena in which to study intermetallic formation, specifically the formation of intermetallic PtNi NFs. Here in, we focus on the PtNi₃ system as it has the highest loading of the non-precious metal, Ni, relative to the precious metal, Pt. To maintain a bimetallic and more easily studied system, the core particle used to direct the shape of the NPs must be inert to the layer above it. For this reason, the Pd core was chosen; Pd and Ni are not known to mix below extreme temperatures far above our annealing temperatures. By using defined, core-sandwich-shell structures as precursors to intermetallic NFs, we can begin to construct a set of design parameters to be extended to other IMC NP structures of various shapes and compositions.

4.3 Experimental Methods

4.3.1 Chemicals

Nickel (II) Chloride hexahydrate (NiCl₂·6H₂O), potassium tetrachloroplatinate (II) (K₂PtCl₄), palladium (II) chloride (PdCl₂), L-ascorbic acid (AA, (C₆H₈O₆), 99%), sodium iodide (NaI, 99.5%), and potassium hydroxide (KOH) were all obtained from Sigma-Aldrich Co., LLC. Hydrazine monohydrate (N₂H₄·H₂O, 98%) was purchased from Alfa Aesar. Cetyltrimethylammonium bromide (CTAB, 99%) was bought from Calbiochem, and methanol (CH₃OH, 99.8%) was purchased through Acros Organics.

Nanopure deionized water (DI water, 18.2 M Ω) was utilized in all experiments. Nitrogen gas (N₂, UHP300) was obtained from Airgas. All reagents were used as received unless otherwise stated.

4.3.2 Synthesis of cubic two layered Pd-Ni-Pt core-sandwich-shell nanoparticles

Cubic Pd substrates (~30 nm) were prepared according to our previous work.^{1–3} 0.05 g of CTAB was dissolved in 10 mL of DI water *via* sonication in a 20 mL glass vial. 500 μ L of a concentrated Pd nanocube solution (containing Pd cubes from eight reactions, re-dispersed in 5 mL of water) was added to the vial, which was gently swirled. 300 μ L of 0.01 M NiCl₂ were added as Ni²⁺ ion source and 500 μ L of 1.0 M hydrazine were added as reducing agent. The vial was swirled, capped, and left unstirred for ~2 hours in an oil bath set to 50 °C. The appearance of small particulates in the reaction solution indicated completed overgrowth. The vial was then removed from the bath and briefly sonicated. 100 μ L of 0.01 M K₂PtCl₄ were added as Pt²⁺ ion source. The solution was returned to the oil bath, still at 50 °C, and left unstirred for ~30 min. The Pd-Ni-Pt nanoparticles were collected *via* centrifugation at 4000 rpm and washed three times with water

4.3.3 Synthesis of Cubic Four Layered Pd-Ni-Pt Core-Sandwich-Shell Nanoparticles

To create the Pd-(Ni-Pt)₂ samples, the initial amount of Ni precursor added was 150 μ L and that of Pt was 50 μ L. Prior to centrifugation, the same procedure was

performed as was used to reduce down the layer of Ni and subsequent layer of Pt. These samples were then collected *via* centrifugation at 4000 rpm and washed three times with water.

4.3.4 Deposition of Nanoparticle Catalysts on Vulcan Carbon Support and Thermal Annealing

3.25 mg of carbon were added to the collected nanoparticles dispersed in ~1 mL of DI water. The carbon and nanoparticle mixture was sonicated for about 5 min. Sonicating for longer induced carbon coverage of the nanoparticle surface, decreasing catalytic surface area. The vial was then capped with a rubber septum and moved to an oil bath at 90 °C. The particles were dried overnight under nitrogen flow and removed from the oil bath. The same method was used to form all both nanoparticle/carbon composites (Pd-Ni-Pt/C and Pd-(Ni-Pt)₂/C).

The dried samples were added to a porcelain boat and calcined in a Lindberg/Blue M TF55030A-1 tube furnace at a ramp rate of 5 °C/min under nitrogen flow. Once to temperature (200-600 °C), the samples were held at the constant temperature for 1 hour then allowed to cool immediately. Once cooled, the samples were ready for electrochemical measurements.

4.3.5 Characterization

For analysis by transmission electron microscopy (TEM), the samples were washed three times in water by centrifugation at 4,000 rotations per minute. Once washed

three times, the samples were concentrated to $\sim 500 \mu\text{L}$. From this solution, $10 \mu\text{L}$ was dropcast directly onto a carbon-coated copper grid (Ted Pella Inc., Formvar/Carbon 200 mesh, Cu); for the calcined samples the samples were dropcast onto silicon oxide-coated gold grids (SPI Supplies, holey silicon oxide, Au). TEM characterization was run using a JEOL JEM2010F accompanied with EDX attachment operated at 200 kV. For analysis by x-ray diffraction (XRD), particles were concentrated in $20 \mu\text{L}$ of ink solution then dropped on a thin glass slide and allowed to dry; for the calcined samples, a silicon chip was used as the substrate. A Bruker AXS D2 Phaser diffractometer was used for the XRD characterization.

4.3.6 ICP-OES

Analysis by inductively coupled plasma-optical emission spectroscopy (ICP-OES) measurements were performed by the following. Multi-element standard solutions for ICP-OES of $100 \mu\text{g/mL}$ of Pt and Pd were purchased from Inorganic Ventures. Trace metal grade 37 % (w/w) hydrochloric acid. ICP-OES data were acquired using an Agilent 5100 VDV spectrometer equipped with an HF-resistant sample introduction system. Concentrations were determined by external calibration with three points for ca. 1, 10, and $100 \mu\text{g/mL}$ of each element. Multi-element standard solutions of $100 \mu\text{g/mL}$ of Pt, Pd, and other elements in a 4.3 % (w/w) HCl matrix were used to prepare the 10 and $1 \mu\text{g/mL}$ standards volumetrically by dilution with identical matrices.

4.3.7 Electrochemical Measurements

The Pd-Ni-Pt and Pd-(Ni-Pt)₂ nanoparticle catalysts were loaded onto carbon black (Vulcan XC-72) by adding ~ 3.25 mg directly to the nanoparticle ink solution, sonicated briefly and then dried overnight. The nanoparticle on carbon samples were then calcined at the appropriate temperature to be used for electrochemical measurements. For the as synthesized samples, they were loaded on carbon and dried, then used. The carbon black with nanoparticle loading was added to a vial and diluted to ~500 μL and 5 μL dropped directly onto a glassy carbon working electrode (CH Instruments) allowed to dry followed by a second 5 μL drop for cyclic voltammetry. The cyclic voltammetry (CV) was performed using a BioLogic VSP potentiostat in a typical three electrode system; a saturated calomel electrode was used as the reference electrode and a platinum wire as the counter electrode (both also obtained from CH Instruments). Blank scans were run in 0.1 M KOH which was purged with nitrogen. The CV cycle was scanned from -1.0 to 0.6 V at a scan rate of 50 mV/s until stabilization of the hydrogen sorption/desorption peak was reached, usually after ~20 cycles. The electrochemically active surface area was determined by the total charge collected from the hydrogen peak divided by the charge per area required to remove a layer of hydrogen from the Pt surface (210 $\mu\text{C}/\text{cm}^2$). For the alkaline electrooxidation of methanol, a 0.5M solution of methanol in 0.1M KOH was purged with nitrogen. This solution was cycled from -0.8 to 0.6 V at a scan rate of 50 mV/s until a decrease in activity was observed. Electrochemical measurements on the Pd-(Ni-Pt)₂/C catalysts were performed in the same manner.

4.4 Results and Discussion

4.4.1 Pd-Ni-Pt Layer Number and Thickness Control Study of Precursor

Nanoparticle Catalysts

To probe the intermetallic NF formation in the systems, a variety of characterization techniques are utilized. To track the level of intermixing, TEM, powder x-ray diffraction (PXRD), and lattice spacing measurements are used. To probe the catalytic surface, small molecule electro-oxidations are performed. Once the stable phase is reached, catalytic activity and stability should peak due to the highly active intermetallic surface. By promoting the intermetallic formation at lower temperatures, the non-equilibrium NP structure can be maintained. Representative transmission electron microscopy (TEM) images can be seen in Figure 1 Pd-Ni-Pt (Figure 4.1a and c) and the Pd-(Ni-Pt)₂ (Figure 4.1b and d) core-sandwich-shell NP precursors. Each layer shows epitaxial overgrowth, even with the high interfacial energy and strain associated with the metal boundary between the highly mismatched (~10%) lattices of Ni and Pt. This induced strain should contribute to a lower diffusion barrier and easier metal-metal migration, particularly through the open (100) facet (which dominates the surface of our cubic NPs), to the more stable intermetallic phase. Calculations for the expected thickness of the metallic layers were performed based on atomic ratios obtained through ICP-OES, and nanoparticle volume. The base cube was assumed to be 30 nm in edge length. The final sandwich structure, either two- or four-layered, was assumed to be 35 nm in edge length, while lattice constants of 352.4 pm and 392.42 pm were used for Ni and Pt, respectively. For the Pd-Ni-Pt particles, layers of 3.6 nm and 1.4 nm were found

respectively for the Ni and Pt (3.52 and 1.43 were measured by TEM). The calculation for the four layered particles further assumed that both shell layers were of equivalent thickness for each metal. Based on this assumption, thicknesses of 1.7 nm and 0.8 nm (1.78 nm and 0.77 nm were measured by TEM) were found for Ni and Pt, respectively. This maintained ratio of metal atoms and the layered effect allows for the thermodynamically favorable intermetallic phase of the PtNi₃ to be reached. By comparing the mixing of these two structures, as seen in scheme 4.1, we will shed light on the mechanism of formation of our IMC NFs.

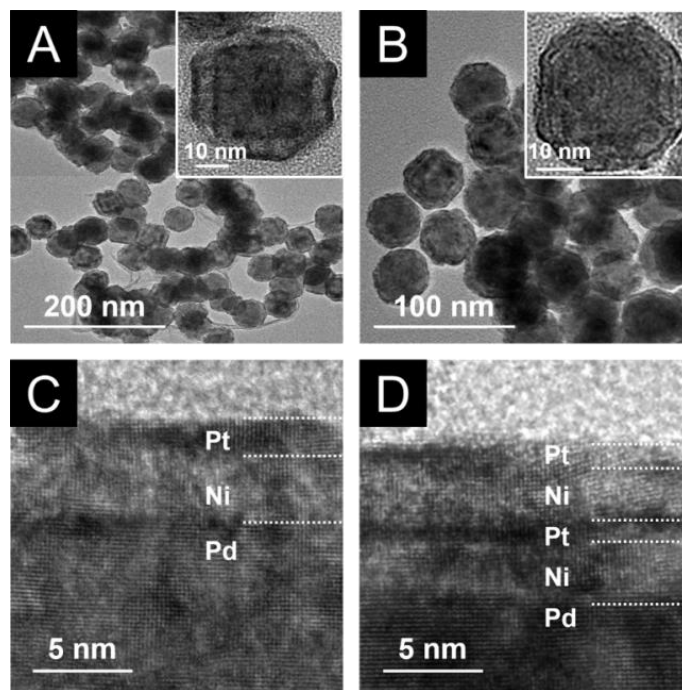
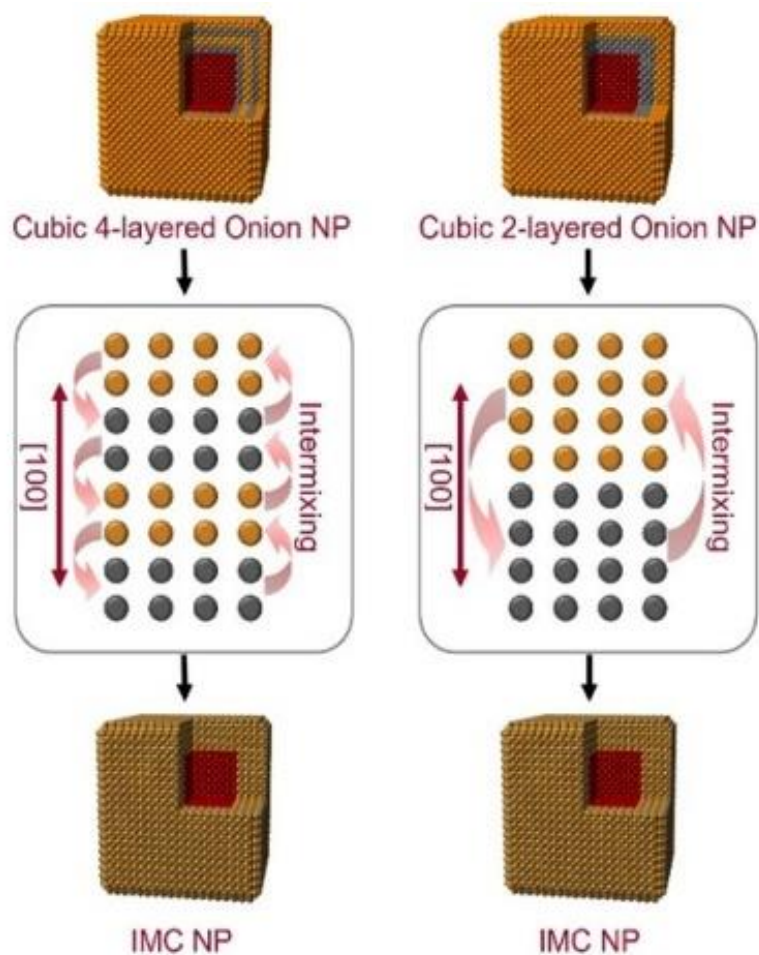


Figure 4.1: TEM images of the as-synthesized (a) Pd-Ni-Pt samples at low magnification with the inset showing a single precursor particle and (b) Pd-(Ni-Pt)₂ samples at low magnification with the inset showing a single precursor particle. (c and d) show high magnification images of the Pd-Ni-Pt and Pd-(Ni-Pt)₂ particles, respectively, with the lighter Ni phase “sandwiched” between the darker Pd and Pt phases.



Scheme 4.1: Schematic representation of the conversion process from shaped Pd-Ni-Pt and Pd-(Ni-Pt)₂ nanoparticle precursors to Pd-Ni₃Pt intermetallic nanoframe structures through atomic diffusion

4.4.2 Nanoframe Synthesis through Thermal Annealing of Precursor Pd-Ni-Pt Nanoparticles

In order to synthesize the initial precursor Pd-Ni-Pt nanoparticles, the same synthesis from previous works was utilized.¹⁰ Pd nanocubes were first synthesized to be used to direct the shape followed by reduction of Ni²⁺ ions onto the surface. Finally, the

Ni layer was capped with a layer of Pt. In order to form the four layered structures, this Ni and Pt reduction step was performed again. During the initial synthesis of the precursor core-sandwich-shell NPs the target ratio was 1:3 for Pt:Ni, matching the stable intermetallic PtNi₃ phase. This ratio was achieved using nominal loading and concentration control. The composition was then confirmed using inductively coupled plasma optical emission spectroscopy (ICP-OES), revealing the ratios to be Pd-Ni_{3.1}-Pt for the two layered samples and Pd-(Ni_{1.3}-Pt_{0.5})₂ for the four layered samples, as can be seen in Table 4.1. These values are close to the expected values from the nominal concentration loading. Each sample was then loaded on Vulcan XC-72 carbon and dried under nitrogen for 24 hours. Once dry, the samples were annealed under a nitrogen atmosphere. The temperature was raised at a ramp rate of 5 °C/min, and the final temperature was held for one hour before immediate cooling. A series of temperatures and holding times were chosen to study the conversion from core-sandwich-shell nanoparticles to fully mixed nanoframes.

Sample	Ni	Pt
Pd-Ni-Pt	3.2	1
Pd-(Ni-Pt) ₂	2.6	1

Table 4.1: ICP-OES analysis data of the different catalyst samples prepared prior to calcinations. The values given are calculated molar ratios. For the Pd-Ni-Pt samples, the Ni and Pt content are for the single layers. For the Pd-(Ni-Pt)₂ samples, the Ni and Pt content are from the altering sandwich layers.

4.4.3 Electrochemical Alkaline Methanol Oxidation Before and After Thermal Annealing

Each sample was tested for the alkaline methanol electro-oxidation reaction (MOR), a typical small molecule oxidation reaction with potential in fuel cell applications. Electrochemical measurements illuminate the surface electronic structure of the catalyst by testing its ability to perform desired transformations. Intermetallic compounds display high activity, through the homogeneity of surface sites, and high stability, through decreased interaction with poisoning species. The performance and durability of MOR catalysts can be negatively impacted by the (often irreversible) adsorption of a CO intermediate, but it has been shown that intermetallic structures are less prone to CO poisoning³². They are also more resistant to etching in acidic media, showcasing higher stability as a result. The electrochemical conversions were performed using a standard three electrode system: Pt wire as the counter electrode, saturated calomel electrode as the reference electrode, and a glassy carbon electrode loaded with 5 μL of the synthesized nanocatalysts supported on Vulcan carbon as the working electrode. From Figure 4.2, a comparison of each sample (two- and four-layered) at the designated temperatures can be seen. At 200 $^{\circ}\text{C}$, the four-layered sample outperforms the two-layered sample due to its increased lattice strain, but both samples perform nominally the same as that of the as-synthesized samples. The same trend is seen at 300 $^{\circ}\text{C}$, where each sample has a slight increase in activity. By 400 $^{\circ}\text{C}$, the four-layered sample has a significant jump in activity. This is thought to be from the complete mixing, as can be seen in the lattice spacing measurements (Figure 4.3), of the Ni and Pt metal

atoms to form the intermetallic NF, yielding a more active surface. However, at the same temperature, the two-layered sample has an activity drastically lower and on par with the four layered sample at 300 °C. At this point, it is hypothesized there is some mixing of the Ni and Pt, but the stable intermetallic phase has not been reached. We thus moved to higher temperatures to see if we could induce the same degree of migration in the two-layered sample as seen in the four-layered. By 500 °C, a larger jump in activity is observed. The four-layered sample, meanwhile, decreases in activity. This deactivation of the four-layered catalyst is attributed to phase segregation or aggregation at such high annealing temperatures. To test whether the two-layered structure would follow suit at higher temperatures, an annealing temperature of 600 °C was used; the same dip in activity was observed. It should be noted that we are not concerned with the mixing of the Pd and Ni atoms due to the extreme temperatures, in excess of 1000 °C, that must be reached for this mixing to occur in the solid state. Each sample and temperature profile was run in triplicate, leading to the errors bars depicted based on standard error. It is worth addressing the larger error bars at higher temperatures. As previously stated, we attribute the decrease in activity to phase segregation of the Ni and Pt metals, as well as potential aggregation, at such high temperatures. These processes are neither homogeneous nor highly repeatable; that is to say, it is not surprising that they would occur to different degrees in different samples, yielding large errors. Moreover, the change in the surface structure also causes breaks in the consistency of the active sites, which would also lead to a higher degree of error.

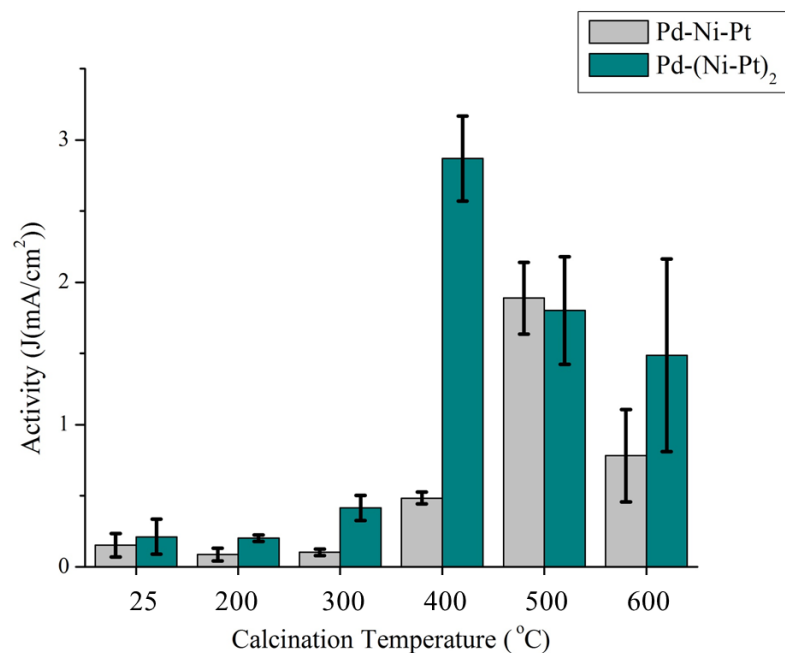


Figure 4.2: Electrochemical activity for methanol oxidation catalyzed by Pd-Ni-Pt and Pd-(Ni-Pt)₂ NPs annealed at various temperatures. Grey bars represent the two-layered Pd-Ni-Pt and teal bars represent the four-layered Pd-(Ni-Pt)₂.

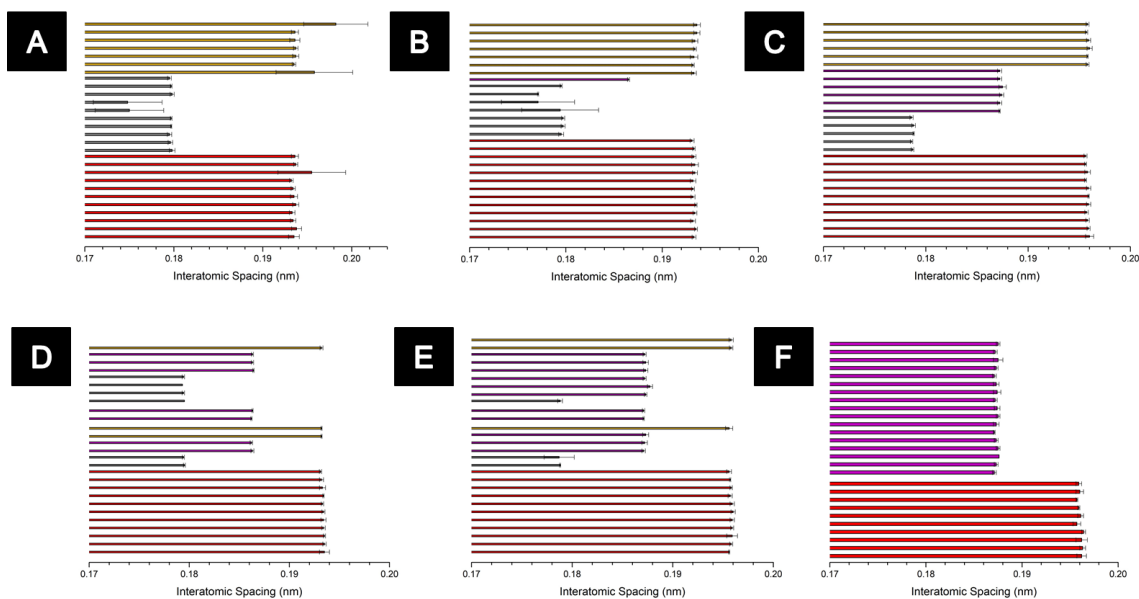


Figure 4.3: Lattice measurements throughout the catalyst (top measurements from the Pt surface down to the Pd core) samples based off of high resolution transmission electron microscopy images. As the samples are calcined, the metal atoms are able to diffuse to their intermetallic structure. The lattice values will change as the atoms mix due to the different lattice parameters of each atom. The lattice tracking of a-c.) Pd-Ni-Pt samples and d-f.) Pd-(Ni-Pt)₂ samples with a,d. at 200 °C; b,e. at 300 °C; and c,f. at 400 °C. Red indicated Pd, grey indicates Ni, yellow indicates Pt, and purple indicates the mixed lattice for Ni and Pt

4.4.4 Electrochemical Alkaline Methanol Oxidation After Thermal Annealing Held for Differing Time Periods

The specifics of the annealing procedure outlined in Figure 4.2 beg two questions: Firstly, is the annealing time of one-hour ideal for the mixing process? Perhaps a longer annealing time at a lower temperature could prevent aggregation and preserve fidelity to the initial cubic NP shape. Secondly, can the Pd-Ni-Pt NPs achieve an activity comparable to the Pd-(Ni-Pt)₂ NPs if given more time to mix? These questions were addressed using extended time studies, annealing the NPs for longer times at each temperature, as shown in Figure 4.4. Annealing for longer than one hour at 200 °C appears to have little effect on the catalytic activity, for both the Pd-Ni-Pt and Pd-(Ni-Pt)₂ NPs, implying that the low annealing temperature is unable to overcome the kinetic barriers associated with mixing, irrespective of the annealing time. This experiment supports the need to increase annealing temperatures in order to induce metallic mixing. The extended annealing at 400 °C shows two distinct effects of the Pd-Ni-Pt and Pd-(Ni-

Pt)₂ NPs. For Pd-(Ni-Pt)₂, extending the annealing time serves to decrease the activity, corroborating our hypothesis that high temperatures lead to phase segregation if the NPs are exposed to them for too long. For Pd-Ni-Pt, activity continues to increase up to a five-hour annealing time. This result suggests that, given enough time, the thicker Ni and Pt layers can achieve mixing similar to the thinner layers in Pd-(Ni-Pt)₂. After more than five hours, the activity decreases, which we again attribute to phase segregation.

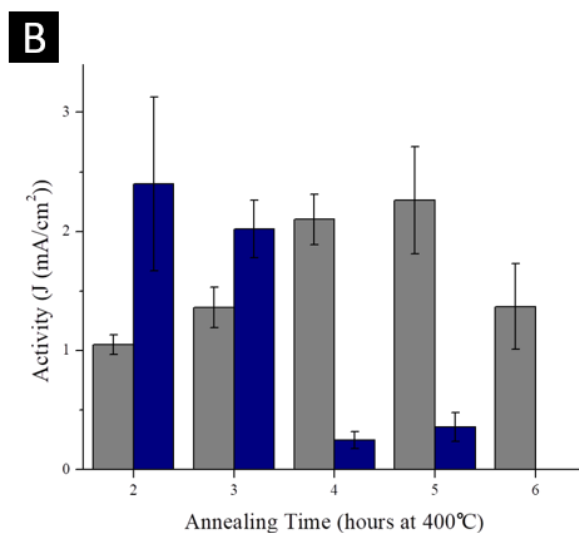
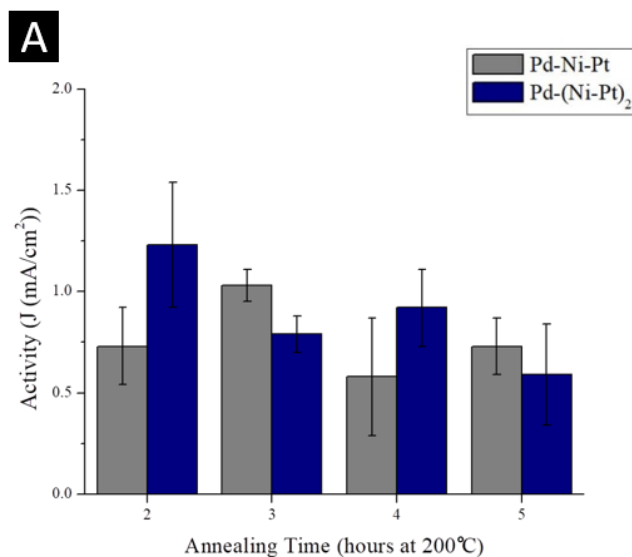


Figure 4.4: Electrochemical activity for methanol oxidation catalyzed by Pd-Ni-Pt and Pd-(Ni-Pt)₂ NPs annealed at (a) 200 °C or (b) 400 °C for various amounts of time. Grey bars represent the two-layered Pd-Ni-Pt and blue bars represent the four-layered Pd-(Ni-Pt)₂.

4.4.5 Pd-Ni₃Pt Formation and TEM Study After Thermal Annealing

A schematic representation of the layered approach can be seen in Scheme 4.1 and is central to understanding why the two- and four-layered core-shell-sandwich NPs behave differently. Using interfacial free-energy calculations, the intermixing barriers between the Ni and Pt layers can be studied for various numbers of metallic layers. Based on these calculations, the formation of the intermetallic phase is easier with more alternating thin layers, and thus much lower annealing temperatures are required to reach the intermetallic state. With multiple Ni and Pt layers, the metal atoms can diffuse in multiple directions, reducing the diffusion length needed for mixing. Moreover, the thinness of the shell layers increases strain, interfacial energies, and defect concentrations. It is thus reasonable that the thicker, two-layered particles would require a higher annealing temperature to undergo the same phase transition as the thinner, four-layered particles. In both cases, the Ni and Pt layers serve as metal atom reservoirs where vacancies allow diffusion and intermixing, but the additional two layers in the four-layered NPs further lower the barrier to mixing. This understanding agrees well with our catalytic results.

TEM was used to study the crystal structures of our NFs after annealing at various temperatures. By comparing a and b to d and e in Figure 4.5, the differing degree to

which the Ni and Pt atoms have intermixed can be noted. At lower temperatures, the two-layered particles in Figure 4.5a and b continue to show a lighter Ni phase contrasted by the darker Pd core and Pt outer shell. From 200 °C to 300 °C the lighter Ni phase thins as the higher temperature begins to overcome the diffusion barrier. In comparison, Figure 4.5d and e represent the four layered particles at the same temperatures. In this case, the distinct Ni and Pt phases cannot readily be identified via Z-contrast differences between the lighter and heavier atoms. This indicates Ni/Pt intercalation at the lower temperatures. At 400 °C (Figure 4.5c and f), both samples have a degree of Pt and Ni intermixing, causing the atomic layers to appear less distinct. To more quantitatively track the degree of mixing for each temperature, high resolution TEM (HRTEM) images were taken to study the lattice parameters and the changes that occur. Figure 4.6 shows representative HRTEM images taken of each sample at three different temperatures in the [200] direction. For pristine Pd, Ni, and Pt, the d-spacing measurements in the [200] direction are 0.1945 nm, 0.1760 nm, 0.1960 nm, respectively. With the migration of the metal atoms, the lattice spacing is expected to change due to the different lattice constants. The larger Pt lattice will compress due to the incorporation of Ni while Ni will expand. Once completely mixed and stable, the lattice measurements throughout the intermetallic shell should be the same (~0.1875 nm). Figure 4.3 showing a graphical representation of the changes in the lattice parameters from the Pt shell down to the Pd core. From the lattice spacing measurements taken, the four-layered sample appears to begin mixing after annealing at 200 °C and is completely mixed after annealing at 400 °C. In comparison, the two-layered particles do not have consistent metal mixing until temperatures above

400 °C. Again, these observations agree well with our MOR results and theoretical understanding.

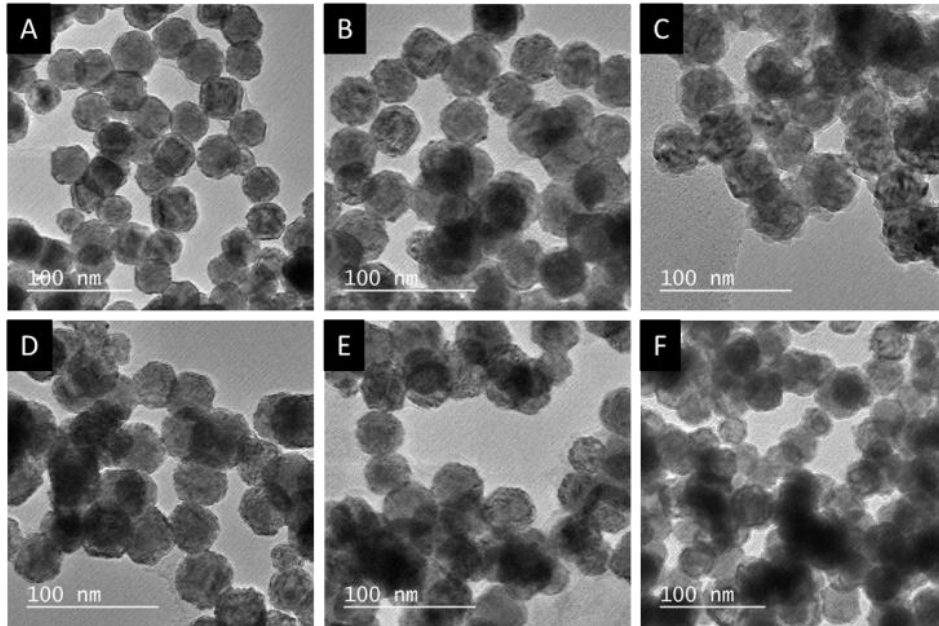


Figure 4.5: TEM images of (a-c) Pd-Ni-Pt and (d-f) Pd-(Ni-Pt)₂ sample annealed at (a,d) 200 °C, (b,e) 300 °C, and (c,f) 400 °C

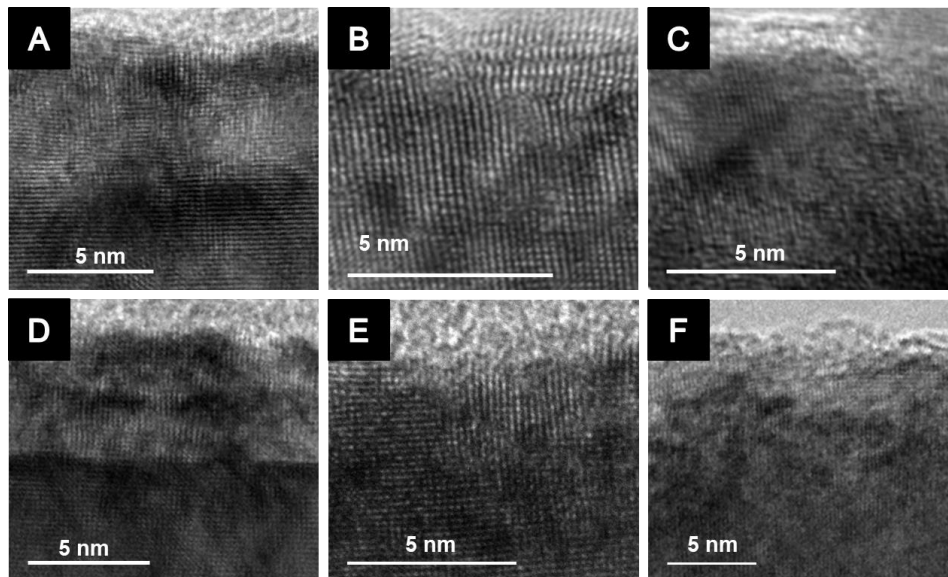


Figure 4.6: TEM images of a-c) Pd-Ni-Pt and d-f) Pd-(Ni-Pt)₂ lattice images after annealing at different temperatures; a,d) 200 °C, b,e) 300 °C, and c,f) 400 °C

4.4.6 X-ray Diffraction Characterization of Pd-Ni-Pt Nanoparticle Catalyst Before and After Thermal Annealing

X-ray diffraction (XRD) was used to investigate long-range order in our NP crystal structure, before and after annealing. In order to perform XRD, NPs from four to five individual syntheses were combined and drop cast on a glass slide for room temperature studies or a silicon chip for the annealed samples. Annealing was performed under nitrogen, with the temperature ramped up at a rate of 5 °C/min and held at the desired point for one hour, then immediately cooled to room temperature. Typically, the x-ray diffraction angles are based off of the d-spacing in the consistent lattice for the metal being studied. With slight differences in d-spacing, the diffraction angle shifts accordingly. For typical face-centered cubic (*fcc*) metals, such as Pd, Ni, and Pt, certain diffraction peaks are characteristic of the metallic species, with the largest peak being that of the (111) plane. With most intermetallic systems currently under study, there is a complete crystal structure change once the nonprecious and precious metal mix. For instance, when Pt and Fe mix, the crystal structure changes from the *fcc* Pt and Fe structures to a completely different, face-centered tetragonal structure. With this transition, XRD becomes a powerful tool to characterize the formation of an intermetallic structure, as relatively large shifts and even new peaks are observed. In our system, however, *fcc* Pt and *fcc* Ni are mixing to form *fcc* Pt₃Ni, limiting the potential differences in our pre- and post-annealing spectra. Since the small crystallite size in our NPs yields broad peaks, the Pt₃Ni peak around 42° lies within the tail of the strong Pd peak at 40°

(Figure 4.7). Post-annealing, the Pd peaks seem to demonstrate greater tailing near 42° , which may be attributed to a broad intermetallic peak.

Despite these challenges, useful information can be found in the XRD results. Between the pre- and post-annealing samples, a key difference can be seen in the metallic Ni peak near 44° . In both the two- and four-layered as-synthesized samples, a distinct Ni peak is observed (Figure 4.7 (b) shows a zoomed in region of the four layered sample where the Ni peak is clearly visible). Post-annealing, this peak is no longer visible. The disappearance of the Ni peak shows that the Ni lattice is being incorporated with the Pt layer, in agreement with our lattice measurements (Figure 4.3).

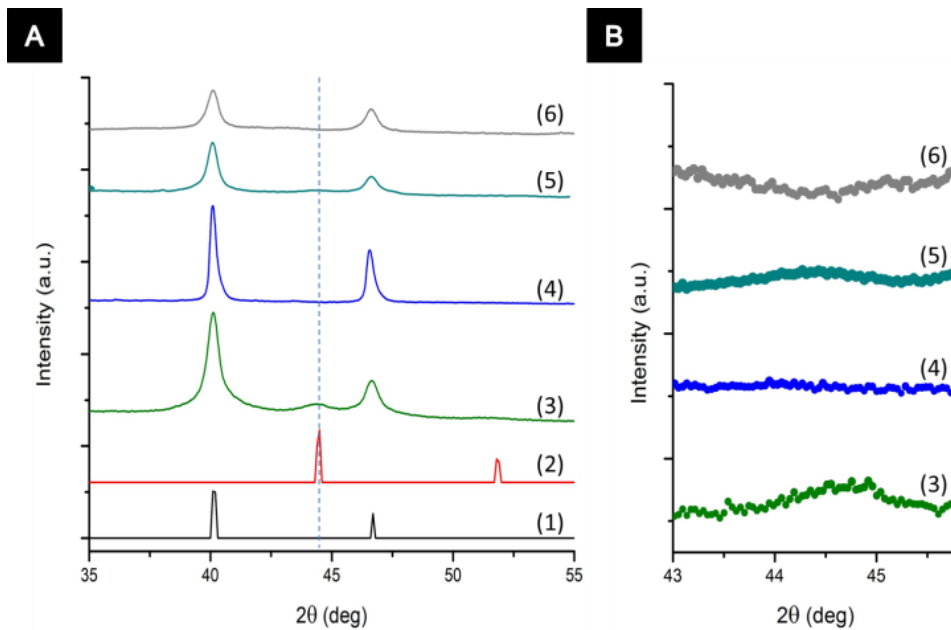


Figure 4.7: Powder X-Ray diffraction spectra of: (a) (1) The Pd simulated spectra (2) the Ni simulated spectra (3) Pd-Ni-Pt as-synthesized; (4) Pd-Ni-Pt annealed at 500°C ; (5) Pd-(Ni-Pt)₂ as-synthesized; (6) Pd-(Ni-Pt)₂ annealed at 400°C . (b) A zoomed in portion of the showing the disappearance of the Ni peak after annealing.

4.5 Conclusion

In conclusion, we have successfully synthesized shape-controlled PtNi₃ intermetallic NFs through low-temperature annealing using a shaped multilayered core-shell platform. By performing a layer-by-layer synthesis with shaped Pd substrates, core-sandwich-shell NPs were produced, with varying shape, layer number, and layer thickness. From TEM, XRD, and electrochemical measurements, the impact of different starting structures on the temperature needed to reach the stable intermetallic phase was found, with results in agreement with previously performed interfacial free energy calculations of diffusion barriers. Electrochemically, the activity was tracked for each annealing temperature, with the highest activity attributed to the 400 °C five layered sample. Our multilayered core-sandwich-shell platform can be extended to the synthesis of other intermetallic structures, with widely varied compositions, simply by changing the metals found in the core and outer layers. The mechanistic insights of our study can be applied as we move toward the tailoring of IMC NPs and NFs to varied applications, particularly in the area of catalysis.

4.6 References

- [1.] Li, L. D.; Zhou, L.; Ould-Chikh, S.; Anjum, D. H.; Kanoun, M. B.; Scaranto, J.; Hedhili, M. N.; Khalid, S.; Laveille, P. V.; D'Souza, L.; Clo, A.; Basset, J. M., Controlled Surface Segregation Leads to Efficient Coke Resistant Nickel/Platinum Bimetallic Catalysts for the Dry Reforming of Methane. *Chemcatchem* **2015**, *7*, 819-829.
- [2.] Li, X.; An, L.; Chen, X.; Zhang, N. L.; Xia, D. G.; Huang, W. F.; Chu, W. S.; Wu, Z. Y., Durability Enhancement of Intermetallics Electrocatalysts *via* N-anchor Effect for Fuel Cells. *Scientific Reports* **2013**, *3*.
- [3.] Xia, T. Y.; Liu, J. L.; Wang, S. G.; Wang, C.; Sun, Y.; Gu, L.; Wang, R. M., Enhanced Catalytic Activities of NiPt Truncated Octahedral Nanoparticles Toward Ethylene Glycol Oxidation and Oxygen Reduction in Alkaline Electrolyte. *ACS. Appl. Mater. Inter.* **2016**, *8*, 10841-10849.
- [4.] Xu, S. C.; Walter, E. D.; Zhao, Z. C.; Hu, M. Y.; Han, X. W.; Hu, J. Z.; Bao, X. H., Dynamic Structural Changes of SiO₂ Supported Pt-Ni Bimetallic Catalysts over Redox Treatments Revealed by NMR and EPR. *J. Phys. Chem. C.* **2015**, *119*, 21219-21226.
- [5.] Zhu, Z. J.; Zhai, Y. L.; Dong, S. J., Facial Synthesis of PtM (M = Fe, Co, Cu, Ni) Bimetallic Alloy Nanosponges and Their Enhanced Catalysis for Oxygen Reduction Reaction. *ACS. Appl. Mater. Inter.* **2014**, *6*, 16721-16726.
- [6.] Zhang, S.; Zhang, X.; Jiang, G. M.; Zhu, H. Y.; Guo, S. J.; Su, D.; Lu, G.; Sun, S. H., Tuning Nanoparticle Structure and Surface Strain for Catalysis Optimization. *J. Am. Chem. Soc.* **2014**, *136*, 7734-7739.
- [7.] Zou, L. F., J; Zhou, Y; Wang, C; Li, J; Zou, Z; Yang, H, Conversion of PtNi Alloy from Disordered to Ordered for Enhanced Activity and Durability of Methanol Tolerant Oxygen Reduction Reaction. *Nano Res.* **2015**, *8*, 2777-2788.
- [8.] Cui, C. G., L; Li, H; Yu, S; Heggen, M; Strasser, P, Octahedral PtNi Nanoparticle Catalysts: Exceptional Oxygen Reduction Activity by Tuning the Alloy Particle Surface Composition. *Nano Letters* **2012**, *12*, 5885-5889.
- [9.] Sneed, B. B., C; Kuo, C.H; Lamontagne, L; Jiang, Y; Wang, Y; Tao, F; Huang, W; Tsung, C.K, Nanoscale-Phase-Separated Pd-Rh Boxes Synthesized *via* Metal Migration: An Archetype for Studying Lattice Strain and Composition Effects in Electrocatalysis. *J. Am. Chem. Soc.* **2013**, *135*, 14691-14700.
- [10.] Sneed, B. Y., A; Jalalpoor, D; Golden, M; Mao, S; Jiang, Y; Wang, Y; Tsung C.K, Shaped Pd-Ni-Pt Core-Sandwich-Shell Nanoparticles: Influence of Ni Sandwich Layers on Catalytic Electrooxidations. *ACS Nano* **2014**, *8*, 7239-7250.

- [11.] Park, K. W. C., J.H; Kwon, B.K; Lee, S.A; Sung, Y.E, Chemical and Electronic Effects of Ni in Pt/Ni and Pt/Ru/Ni Alloy Nanoparticles in Methanol Electrooxidation. *J. Phys. Chem. B* **2002**, *106*, 1869-1877.
- [12.] Yang, H. V., W; Lamy, C; Alonso-Vante, N, Structure and Electrocatalytic Activity of Carbon-Supported Pt-Ni Alloy Nanoparticles Toward the Oxygen Reduction Reaction. *J. Phys. Chem. B* **2004**, *108*, 11024-11034.
- [13.] Wolff, I. M.; Hill, P. J., Platinum Metals Based Intermetallics for High-Temperature Service. *Platinum Met. Rev.* **2000**, *44*, 158-166.
- [14.] Hasché, F. O., M; Strasser, P, Activity, Structure and Degradation of Dealloyed PtNi₃ Nanoparticle Electrocatalyst for the Oxygen Reduction Reaction in PEMFC. *J. Electrochemical Soc.* **2012**, *159*, B24-B33.
- [15.] Dikshtein, I.; Koledov, V.; Shavrov, V.; Tulaikova, A.; Cherechukin, A.; Buchelnikov, V.; Khovailo, V.; Matsumoto, M.; Takagi, T.; Tani, J., Phase Transitions in Intermetallic Compounds Ni-Mn-Ga with Shape Memory Effect. *IEEE Trans. Mag.* **1999**, *35*, 3811-3813.
- [16.] Evans, M. J.; Wu, Y.; Kranak, V. F.; Newman, N.; Reller, A.; Garcia-Garcia, F. J.; Haeussermann, U., Structural Properties and Superconductivity in the Ternary Intermetallic Compounds MAB (M=Ca, Sr, Ba; A=Al, Ga, In; B=Si, Ge, Sn). *Phys. Rev. B* **2009**, *80*, 064514.
- [17.] Fernandez, J. F.; Cuevas, F.; Leardini, F.; Bodega, J.; Ares, J. R.; Garces, G.; Perez, P.; Sanchez, C., A New Pseudo-Binary Mg(6)Ni(0.5)Pd(0.5) Intermetallic Compound Stabilized by Pd for Hydrogen Storage. *J. Alloys and Compounds* **2010**, *495*, 663-666.
- [18.] Zhao, Y.; Yu, J. K.; Wu, L. L.; Wan, B.; Zhang, Y. K.; Gao, R.; Zhang, J. W.; Gou, H. Y., Mechanical Properties and Electronic Structures of Diverse Pt-Al Intermetallics: First-Principles Calculations. *Comp. Mater. Sci.* **2016**, *124*, 273281.
- [19.] Furukawa, S.; Ehara, K.; Ozawa, K.; Komatsu, T., A Study on the Hydrogen Activation Properties of Ni-Based Intermetallics: A Relationship Between Reactivity and the Electronic State. *Phys. Chem. Chem. Phys.* **2014**, *16*, 19828-19831.
- [20.] Besenbacher, F.; Chorkendorff, I.; Clausen, B. S.; Hammer, B.; Molenbroek, A. M.; Norskov, J. K.; Stensgaard, I., Design of A Surface Alloy Catalyst for Steam Reforming. *Science* **1998**, *279*, 1913-1915.

- [21.] Studt, F.; Abild-Pedersen, F.; Bligaard, T.; Sorensen, R. Z.; Christensen, C. H.; Norskov, J. K., Identification of Non-Precious Metal Alloy Catalysts for Selective Hydrogenation of Acetylene. *Science* **2008**, *320*, 1320-1322.
- [22.] Armbruster, M.; Kovnir, K.; Friedrich, M.; Teschner, D.; Wowsnick, G.; Hahne, M.; Gille, P.; Szentmiklósi, L.; Feuerbacher, M.; Heggen, M.; Girgsdies, F.; Rosenthal, D.; Schlogl, R.; Grin, Y., Al₁₃Fe₄ as a Low-Cost Alternative for Palladium in Heterogeneous Hydrogenation. *Nat. Mater.* **2012**, *11*, 690-693.
- [23.] Yan, Y.; Du, J. S.; Gilroy, K. D.; Yang, D.; Xia, Y.; Zhang, H., Intermetallic Nanocrystals: Syntheses and Catalytic Applications. *Adv. Mater.* **2017**, *29*, 1605997.
- [24.] Enayati, M. H.; Salehi, M., Formation Mechanism of Fe₃Al and FeAl Intermetallic Compounds During Mechanical Alloying. *J. Mater. Sci.* **2005**, *40*, 3933-3938.
- [25.] Schaefer, Z. L.; Vaughn II, D. D.; Schaak, R. E., Solution Chemistry Synthesis, Morphology Studies, and Optical Properties of Distinct Nanocrystalline Au-Zn Intermetallic Compounds. *J. Alloy Compd.* **2010**, *490*, 98-102.
- [26.] Maksimuk, S.; Yang, S.; Peng, Z.; Yang, H., Synthesis and Characterization of Ordered Intermetallic PtPb Nanorods. *J. Am. Chem. Soc.* **2007**, *129*, 8684-8685.
- [27.] Leonard, B. M.; Zhou, Q.; Wu, D.; DiSalvo, F. J., Facile Synthesis of PtNi Intermetallic Nanoparticles: Influence of Reducing Agent and Precursors on Electrocatalytic Activity. *Chem. Mater.* **2011**, *23*, 1136-1146.
- [28.] Wang, D. S.; Peng, Q.; Li, Y. D., Nanocrystalline Intermetallics and Alloys. *Nano Res.* **2010**, *3*, 574-580.
- [29.] Belova, I. V.; Murch, G. E., Interdiffusion in Intermetallics. *Metall. Mater. Trans. A* **2013**, *44A*, 4417-4421.
- [30.] Mehrer, H., Diffusion in Intermetallics. *Mater. T. Jim.* **1996**, *37*, 1259-1280.
- [31.] Brodsky, C. Y., A; Ng, K; Kuo, C.H.; Tsung, C.K., Electrochemically Induced Surface Metal Migration in Well-Defined Core-Shell Nanoparticles and Its General Influence on Electrocatalytic Reactions. *ACS Nano* **2014**, *8*, 9368-9378.
- [32.] Qi, Z.; Xiao, C.; Liu, C.; Goh, T. W.; Zhou, L.; Maligal-Ganesh, R.; Pei, Y.; Li, X.; Curtiss, L. A.; Huang, W., Sub-4 nm PtZn Intermetallic Nanoparticles for Enhanced Mass and Specific Activities in Catalytic Electrooxidation Reaction. *J. Am. Chem. Soc.* **2017**, *139*, 4762-4768.

5.0 One-pot Metal Nanoparticle Encapsulation Utilizing Metal Organic Framework as Crystalline Capping Agent for Selective Catalysis

Portions of this chapter may be seen in Lien-Yang Chou's 2016 dissertation titled, "Design and Synthesis of Nanopore-Modulated Heterogeneous Catalysts". I thank him for the use of this material as a co-researcher for this work.

5.1 Abstract

The encapsulation of metal nanoparticles (NPs) within MOF pores serves as a platform for catalytic reactions where the encapsulated NPs are fixed within the MOF, gaining the intrinsic selectivity of the MOF coating. The uniformly sized pores and apertures as well as affinity to particular molecules based on the functionalization of the linking species helps to impart this selectivity. In a typical NP@MOF synthesis, the nanoparticles are either preformed and coated by capping agents or the MOF is preformed and the metal precursors diffuse in and are reduced. In both cases, many challenges need to be addressed such as the ill-defined structure and surface of NPs. In this work, metal NPs are reduced to form colloidal NPs followed by MOF coating to be used as a crystalline capping agent. The complete separation, encapsulation and compositional control of alloyed (Pd/Pt) NPs as well as differently sized NPs are shown by using size exclusion catalysis and ethylene hydrogenation. The catalytic activity of the differing compositions is also compared. The tunable nature and cleaner surface NP encapsulation approach could be applied to other metal-MOF composites for future catalysis and surface studies.

5.2 Introduction

Metal–organic frameworks (MOFs) synthesized *via* metal secondary building units (SBU) and organic linking species, have become new, promising crystalline porous materials¹⁻⁴ for several applications, such as, gas storage⁵, chemical separation⁵⁻⁶, drug delivery⁷⁻⁸, and heterogeneous catalysis⁹⁻¹⁰. The tailorable chemistry of the pores and cavities has made MOFs suitable for the encapsulation of functional guest species for a variety of applications. By altering the sizes of the pores and functionalizing a MOFs' interior cavities and apertures, the composite material can act as a form of molecular sieve, allowing only reactants of a particular size or affinity to pass through to interact with the encapsulated guest¹¹⁻¹³. This approach allows for the exclusion of undesired molecules and protection of the encapsulated guest. In particular, the encapsulation of metal nanoparticles (NPs) in MOFs (NPs@MOF) has attracted a lot of attention due to synergetic physical and chemical properties the NPs@MOF composites possess¹⁴⁻¹⁵. With the encapsulation of NPs, an abundance of new applications becomes available¹¹, including, surface plasmon resonance (SPR)¹⁶⁻¹⁹, biological imaging²⁰, and catalysis¹²⁻¹⁵. In this paper, we focus on NP@MOF composites for catalysis using their activities as a probe to determine the encapsulation capabilities of the as synthesized MOF motif and the properties of the controlled alloyed and sized particles. This composite material gains the advantages of the catalytic properties of the NPs and the selectivity¹¹ and relative stability from aggregation²¹ of the MOF coating. Currently, there are two common approaches to form these materials¹⁴⁻¹⁵: post-synthetic wetness impregnation²²⁻²⁵ and the use of pre-formed colloidal nanoparticles which are then encapsulated^{12,18-19,26-28}. While

both of these routes allow for the formation of novel composite materials, new routes could impart additional benefits such as NP composition and size control, as well as MOF structures which have maintained their crystalline nature and integrity, allowing for the use of their intrinsic selectivity

The first widely used approach involves MOFs serving as a template to provide confined spaces for the reduction of metal salts to form NPs within the pores. The second approach involves the synthesis of monodispersed metal NPs prior to their incorporation into MOF synthesis conditions for encapsulation. While both methods prove useful, in the first, the effective control over the dispersity, size and composition of metal NPs within MOFs, as well as the MOF morphology, and size, due to damages from ion diffusion²⁹ can still present challenges causing a decrease in catalytic selectivity. Great efforts have been made to tackle these drawbacks^{15,29}, yet very few examples are available that can completely confine the NPs within the MOF crystals, without forming NP aggregates on the MOF exterior^{24,30-32}. In the latter method for forming these composites, pre-synthesized NPs formed by traditional colloidal syntheses are used; these require the use of strongly binding organic capping agents, such as surfactants and polymers. For example, polyvinylpyrrolidone (PVP) is a commonly used capping agent on NP surfaces as well as encapsulation agents²⁸. The organic capping agents act as a protective barrier maintaining the separation of the NPs and initiating and attracting MOF growth on their surface. Due to the high binding affinity to the metal surface, catalytic active sites can be blocked, lowering overall catalytic activity³³⁻³⁴. The strong binding affinity also makes their removal to form a cleaner metal surface more difficult. The use of non-traditional, easily removable capping agents to leave a cleaner more open

nanoparticle surface could remedy this. Therefore, a suitable approach of forming tunable (composition and size) metal NPs@MOF composites without the use of such capping agents is desired.

The MOF linker is able to interact with the metal NP surface acting as an anchor, leading to the MOF coating around them. Li and coworkers first synthesized capping agent free Pt NPs coated with ZIF-8³⁵. Recently, a second Li's group, in China, used a one pot method that allows for the NPs to be reduced and capped by the forming MOF *in situ*³⁶⁻³⁷. These afford a great possibility for new methods of forming these NP@MOF motifs with cleaner surfaces, while still opening a challenge for better control over the NP (size and composition) as well as the MOF morphology and defects. By functionalizing the linker used during synthesis with functional groups that are known to show affinity/chelating effects towards metals, such as amines^{33,38} or thiols³⁹⁻⁴⁰, the NP encapsulation and separation may be retained, while instilling them with the intrinsic size selectivity for catalysis. Specifically, the amine group functionalized linkers help to tether the growing MOF to the metal surface, initially acting as a form of capping agent, reducing the NP surface energy. Unlike traditional capping agents, the amine-metal binding is weaker, allowing for the surface to be washed by mild methods. This was shown using IR spectroscopy as seen in Figure S4. The NPs are then able to form within the crystalline MOF, ultimately forming the final capping agent. The use of MOF as a crystalline capping agent can bring about a higher degree of selective catalysis by having a cleaner metal surface, freeing up important active sites and creating a diffusion pathway of reactants to the NP surfaces. Furthermore, the addition of MOF to NPs shows an

increased robustness from aggregation and sintering of the NPs, thus an increased robustness of the catalytic system towards thermal/chemical stability.

Here, we report a one-pot method to synthesize NPs@MOF composites without the aid of organic/polymer capping agents with a more simplified system with no additional reducing agents; the solvent acts as the reducing agent. Specifically we show the introduction of UiO-66-NH₂, a very robust zirconium based MOF with high thermal and chemical stability as the NP capping agent⁴¹. In order to encapsulate capping agent free metal NPs into MOF, a strong interaction with the ability to be removed once formed, and quick MOF coating are required to prevent their aggregation. By using an amine group functionalized MOF linker to tether to the NPs surface, the colloidal NPs are monodispersed and fully encapsulated into the MOF pores. While other methods have shown the encapsulation of NPs within MOFs, the ability to have full encapsulation on the interior rather than the surface is still difficult. This method shows the complete encapsulation of NPs within the MOF rather than on the surface, maintaining the size selectivity of the MOF material.

5.3 Experimental Methods

5.3.1 Chemicals

Zirconium(IV) chloride (ZrCl₄, Aldrich, 99.5%), terephthalic acid (Aldrich, 98%), 2-aminoterephthalic acid (Aldrich, 99%), acetic acid (Sigma-Aldrich, 99.7%), N,N-dimethylformamide (Sigma-Aldrich, 99.8%), palladium(II) 2,4-pentanedione (Pd(acac)₂, Alfa Aesar, Pd 34.7%), platinum(II) acetylacetonate (Pt(acac)₂, STREM CHEMICALS,

98%), Chloroplatinic acid hydrate (H_2PtCl_6 , Sigma-Aldrich, 99.995%), Palladium(II) chloride (PdCl_2 , Aldrich, 99%), ammonium tetrachloroplatinate(II) ($(\text{NH}_4)_2\text{PtCl}_4$, Sigma-Aldrich, 99%), cyclohexene (Sigma-Aldrich, 99%), cis-cyclooctene (Sigma-Aldrich, 95%), sodium hydroxide (NaOH , Sigma-Aldrich, 98%), polyvinylpyrrolidone (PVP, Mw~40,000, Aldrich), tetramethylammonium bromide ($\text{N}^+(\text{CH}_3)_4\text{Br}^-$, Sigma-Aldrich, 99%), ethylene glycol (Sigma-Aldrich, >99%), crotonaldehyde (Sigma-Aldrich, >99%), tetradecene (TCI, >99.0%), deuterated chloroform (Cambridge Isotope Laboratories Inc, D, 99.0%) were purchased from the indicated sources and used without further purification. Hydrogen (Airgas, 99.999%), ethylene (Airgas, 99.995%) and helium (Airgas, 99.999%) were used for heterogeneous gas phase catalysis.

5.3.2 Synthesis of UiO-66 and UiO-66-NH₂

In a typical synthesis reaction for UiO-66, 18.6 mg (0.08 mmol) ZrCl_4 and 13.3 mg (0.08 mmol) terephthalic acid were dissolved in 8.622 mL DMF, then 1.378 mL acetic acid was added into the solution to make the final volume to 10 mL. The solution was transferred into a 20mL scintillation vial and heated for 24 hours in a 120 °C oil bath. After cooling down, the formed UiO-66 was collected by centrifugation. To form the UiO-66-NH₂, the same reaction parameters were followed, just with the use of 14.5 mg (0.08 mmol) 2-aminoterephthalic acid to obtain the functionalized MOF. The isolated samples were washed three times in methanol and dried in a vacuum oven at 150 °C overnight.

5.3.3 Synthesis of NP@UiO-66-NH₂ and NP/UiO-66 Composites

A typical synthesis reaction for Pd@UiO-66-NH₂ or Pt@UiO-66-NH₂ composite follows a similar procedure as the synthesis of UiO-66-NH₂; 8 x 10⁻³ mmol Pd(acac)₂ (for Pt, H₂PtCl₆ was used) was dissolved in the DMF prior to the heating step. The reaction was then run for 24 hours at 120 °C and collected by centrifugation. To form the Pd/UiO-66 composite, the same reaction parameters were followed, just with the use of terephthalic acid instead of 2-aminoterephthalic acid. The isolated samples were washed three times in methanol and dried in a vacuum oven at 150 °C overnight. Similarly, in order to synthesize the PdPt@UiO-66-NH₂ samples, differing nominal loadings of potassium tetrachloropalladate (K₂PdCl₄) or potassium tetrachloroplatinate (K₂PtCl₄) were dissolved in the DMF prior to the heating step. The total metal loading was maintained at 8 x 10⁻³ mmol, while the stoichiometry was changed to form differently alloyed nanoparticle compositions. These reactions were then run for 24 hours at 120 °C. They were collected, centrifuged and dried in the same manner.

5.3.4 Synthesis of Size Controlled Pd@UiO-66-NH₂ and Pt@UiO-66-NH₂ Composites

8 x 10⁻³ mmol Pd(acac)₂ and 14.5 mg (0.08 mmol) 2-aminoterephthalic acid was dissolved in 2 mL DMF as solution A. The solution A was stirred and heated to the desired temperature (90, 120 and 150°C) in an oil bath for 2 hours. In the meantime, 18.6 mg (0.08 mmol) ZrCl₄ was dissolved in 6.622 mL DMF, then 1.378 mL acetic acid was added into the solution to make the final volume to 8 mL as solution B. Solution B was

preheated to 120°C in an oil bath. Solution A was then added into the solution B and heated for 24 hours in a 120 °C oil bath. To form size controlled Pt@UiO-66-NH₂ composite, the same reaction parameters were followed, just with the use of 8 x 10⁻³ mmol H₂PtCl₆ and another 0.5 mL (200 proof) ethanol was added into the solution to make the final volume to 2 mL as solution A. The isolated samples were washed three times in methanol and dried in a vacuum oven at 150 °C overnight.

5.3.5 Synthesis of PVP Capped 5 nm Pt and Pd Nanocrystals and Corresponding PVP Coated 5nm Pt NPs@UiO-66-NH₂ and Pt NPs/UiO-66-NH₂ Composites

A total of 0.025 mmol of Pt ions (NH₄)₂PtCl₄, 0.75 mmol of tetramethylammonium bromide, and 0.5 mmol of poly(vinylpyr-rolidone) (in terms of the repeating unit; Mw 40 000) were dissolved into 5 mL of ethylene glycol in a 25 mL round-bottom flask at room temperature. The mixed solution was stirring and heated to 200°C in an oil bath for 20 minutes. For Pd nanocrystals synthesis, the same reaction parameters were followed, just with the use of Pd ions precursor PdCl₂ instead of Pt ions.⁴⁶ Once synthesized, a similar procedure as the synthesis of UiO-66-NH₂ was followed. 1 mL of 0.25 mg/mL of the DMF solution of PVP capped Pt particles was added the UiO-66-NH₂ synthetic solution to make the final volume to 10 mL. The solution was transferred into a 20 mL scintillation vial and heated for 24 hours in a 120 °C oil bath. The isolated samples were washed three times in methanol and dried in a vacuum oven at 150 °C overnight. For the samples with the Pt NPs coated in PVP on the outer surface of the MOF, pre-synthesized UiO-66-NH₂, was dispersed in DMF while 1

mL of the 0.25 mg/mL of the Pt PVP capped particles was added to the vial, stirred from 24 hours and then centrifuged down, and washed.

5.3.6 Synthesis of Pt@UiO-66-NH₂ through Wetness Impregnation

These samples were synthesized utilizing the same method in the 2014 Huang group ACS Catalysis paper³². UiO-66-NH₂ was first synthesized (200 mg) and soaked in 12 mL of deionized water. 4.3 mg of K₂PtCl₄ in 2 mL was then added dropwise and stirred overnight. The sample was then collected and washed three times, oven dried at 120 °C and then under vacuum for 12 hours. Finally, the embedded Pt salt was reduced under a flow of hydrogen gas at 200 °C for 1 hour. The sample was then collected and used in the aldehyde hydrogenation step.

5.3.7 Catalysts Preparation and Gas Phase Hydrogenation Study

All nanostructures were homogeneously diluted with mesoporous silica (MCF-17) by mixing them together as a solution in ethanol, with stirring and then drying the mixture in the vacuum oven overnight for heterogeneous catalysis. To prepare the samples of Pd nanocrystals deposited directly on the surface of UiO-66-NH₂, the desired amount of solution containing Pd nanocrystals was mixed with UiO-66-NH₂ in DMF (methanol for PVP capped particles) with stirring. After the mixture gradually settled down, the precipitate was collected by centrifugation. The mixture was dried in the vacuum oven overnight. Once prepared, 6.8 mg 0.5 wt% Pd@UiO-66-NH₂, 10.2 mg 0.5 wt% Pd/UiO-66, and 6.4 mg 0.5 wt% Pd (PVP) on UiO-66-NH₂ samples were diluted

with low surface area quartz and loaded into glass reactors for size selective alkene hydrogenations. 10 mg metal@UiO-66-NH₂ (0.01 wt% Pd, Pt and Pd_xPt₁ alloy) samples were diluted with low surface area quartz and loaded into glass reactors for ethylene hydrogenations activity measurement. Temperature was controlled by a furnace (Carbolite) and PID controller (Digi-Sense) with a type-K thermocouple. Gas flows, including helium, hydrogen gas and ethylene were regulated using calibrated mass flow controllers. The desired partial pressure of cyclohexene and *cis*-cyclooctene were achieved by bubbling helium through the liquid and assuming saturation.³⁴ For all reactions, gas composition was analyzed with a mass spectroscope (MKS special V2000P). The turnover frequency of ethylene hydrogenation is normalized by using the percentage of surface atoms following the palladium cluster diameter.⁴⁷ Liquid phase catalytic hydrogenation of crotonaldehyde

5.0 mg of 0.7-0.8wt% samples of Pt@UiO-66-NH₂, Pt(PVP)@UiO-66-NH₂, Pt(PVP)/UiO-66-NH₂, and Pt(wetness)@UiO-66-NH₂ were placed in 20 mL glass scintillation vials. Isopropanol (1.0 mL) was added to each followed by 30 seconds of sonication. Each sample was then pipetted into its own individual glass 3 mL ampule. An additional 1.0 mL of isopropanol was added to each scintillation vial, sonicated 30 seconds and added to the appropriate ampule. Similarly, 0.1 mL of crotonaldehyde and 0.1 mL of tetradecene (a standard) was added followed by 0.3 mL of isopropanol; for a total volume in each ampule of 2.5 mL. The ampules were placed in a small parr reactor, sealed and flushed with hydrogen before pressurizing to 30 barr at 30 °C and allowed to react for 18 hours. After 18 hours, the pressure was slowly released and from each

sample and aliquot of the supernatant was tested under ^1H nuclear magnetic resonance spectroscopy (NMR)

5.3.8 ^1H NMR Characterization of Crotonaldehyde Hydrogenation Products

NMR measurements were performed on the supernatant from the crotonaldehyde reactions. Sample was added to deuterated chloroform in an NMR tube and run using a Varian NMR Inc 600 MHz instrument. The peaks were then analyzed and integrated; crotonaldehyde at 9.42-9.48 ppm, butyraldehyde at 9.72 ppm, butanol at 3.58-3.6 ppm, and 2-butene-1-ol at 6.81-6.88 ppm to determine the conversion and selectivity.

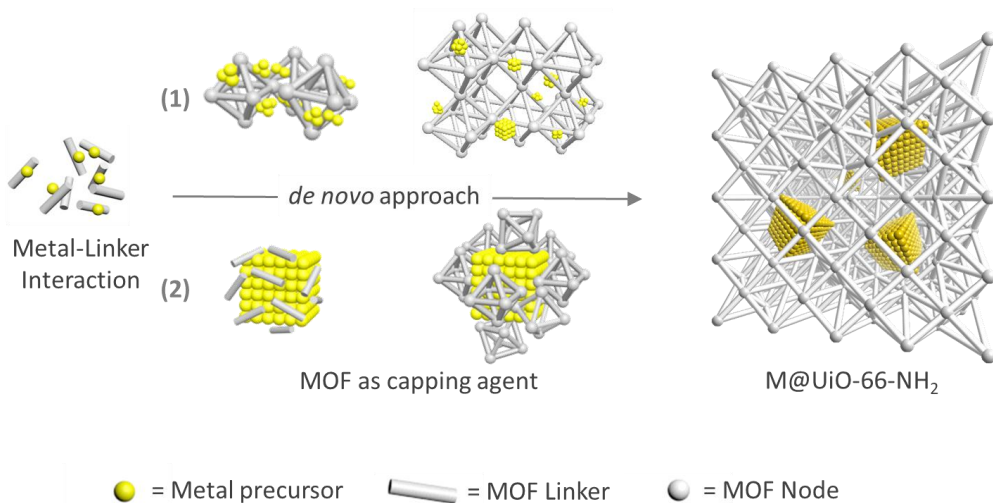
5.3.9 Characterization

Transmission electron microscope (TEM) images were obtained on JEOL JEM2010F operated at 200 kV. Scanning transmission electron microscope (STEM) and Energy-dispersive X-ray spectroscopy (EDX) mapping experiments were performed on a FEI Probe Cs corrected Titan operating at 200 kV. Scanning electron microscope (SEM) images were obtained on a JEOL JSM6340F. The powder x-ray diffraction patterns (pXRD) were collected on a Bruker AXS diffractometer with Cu $K\alpha$ radiation ($\lambda = 1.5418 \text{ \AA}$). The infrared spectrum (IR) data were collected on a Bruker Alpha ATR FT-IR Spectrometer. The nuclear magnetic resonance spectrums (^1H -NMR) were obtained on a Varian NMR Inc. 600 MHz.

5.4 Results and Discussion

5.4.1 One-pot Synthesis of Pd and Pt Nanoparticles in UiO-66-NH₂

In typical experimental conditions, a one-pot method was utilized by directly mixing metal precursor salts of Pd(acac)₂ and the MOF precursors zirconium tetrachloride, Zr(Cl)₄, and 2-aminoterephthalic acid, BDC-NH₂, with acetic acid in an N,N-dimethylformamide (DMF) solvent system. The system is kept at 120 °C for 24 hours without stirring (Scheme 5.1). It was found that Pd NPs formed within the first 15 minutes of heating followed by the formation of UiO-66-NH₂; this was tracked *via* a time study of the NP and UiO-66-NH₂ growth solution with TEM monitoring (Figure 5.1). The UiO-66-NH₂ formed at the surface of Pd NPs due to the amino group interaction. The initial encapsulation resulted in the stopped growth of the Pd NPs. Finally the uniformly sized, crystalline Pd@UiO-66NH₂ nanocrystals was produced (Figure 5.2 a, b and d).



Scheme 5.1: Schematic representation of the *de novo* encapsulation approach (1) compared to the utilization of UiO-66-NH₂ as the nanoparticle capping agent (2)

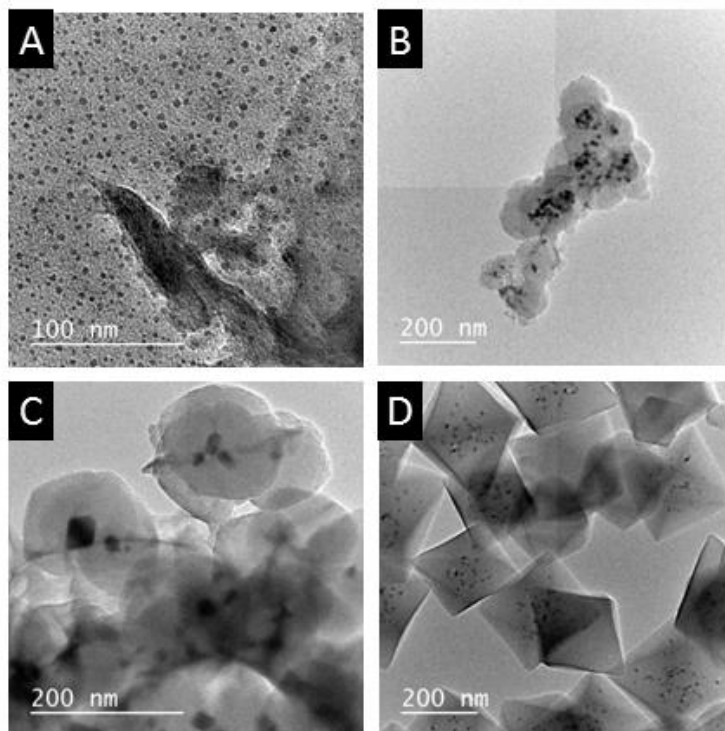


Figure 5.1: Time study of UiO-66-NH₂ capping of palladium nanoparticles: (a) time at 0.25 hours, (b) time at 0.75 hours, (c) time at 1.25 hours, and (d) time at 6.5 hours.

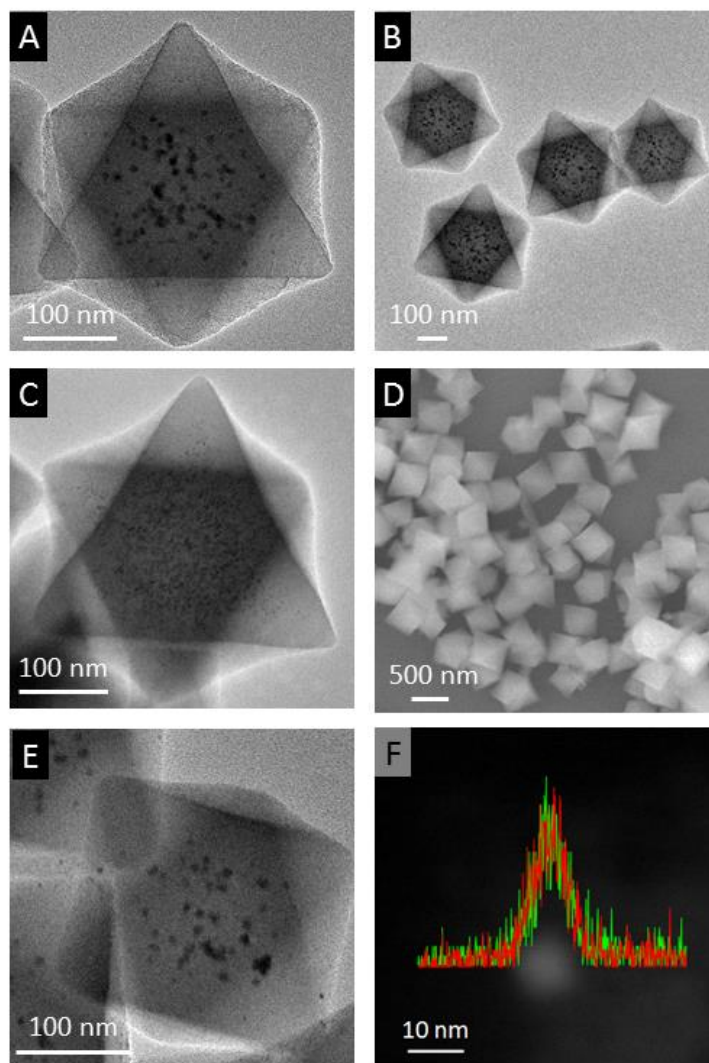


Figure 5.2: TEM images of Pd and UiO-66-NH₂ composites (a-b) Pd@UiO-66-NH₂ using the amine functionalized BDC linker showing encapsulation (c) Pt@UiO-66-NH₂ (d) SEM image of Pd@UiO-66-NH₂ uniformity (e) TEM images of Pd_{0.7}Pt₁@UiO-66-NH₂. (f)STEM/EDX line mapping of Pd_{0.7}Pt₁@UiO-66-NH₂. Green trace corresponds to Pd and red trace corresponds to Pt

To provide evidence of the mechanism of encapsulation *via* the interaction of the amine group functionalized MOF linker with the surface of the metal NPs, a control

experiment was performed using terephthalic acid (BDC) in the same experimental conditions rather than the BDC-NH₂ as the MOF linker (Figure 5.3a-d and Figure 5.4). Depending on the metal salt precursor used, both Pd and Pt formed a series of aggregates outside of the MOF crystal, implying that the absence of the amine group on the non-functionalized UiO-66 causes a lack of chelating interactions so the particles cannot be fully encapsulated. Fourier transform infrared spectroscopy (FTIR) was performed to demonstrate the surface interaction (Figure 5.3e and 5.5).

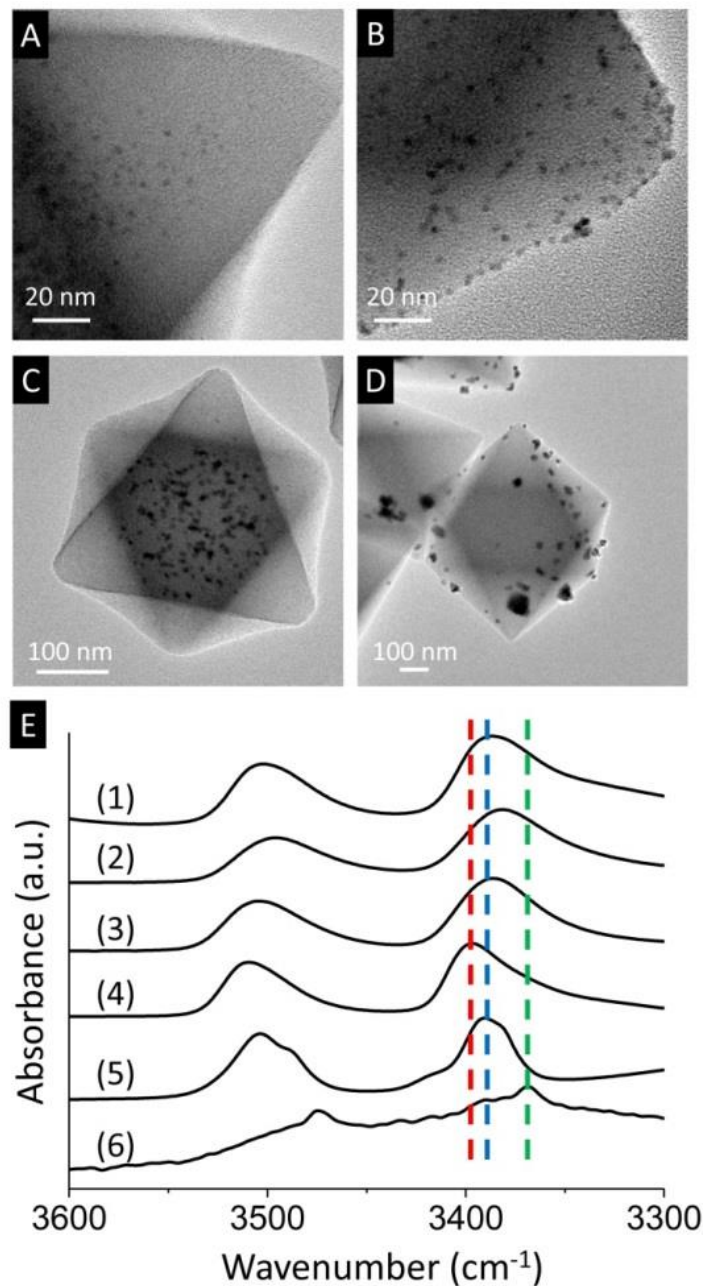


Figure 5.3: TEM images and FTIR spectra of NP and UiO-66-NH₂ composites (A) Pt@UiO-66-NH₂ using the amine functionalized BDC linker showing encapsulation (B) Pt/UiO-66 composite using the normal BDC linker showing lack of encapsulation. (C) Pd@UiO-66-NH₂ using the amine functionalized BDC linker showing encapsulation. (D) Pd/UiO-66 composite using the normal BDC linker showing lack of encapsulation. (E)

FTIR spectra of (1) Pd@UiO-66-NH₂ Rinsed with DMF (2) Pd@UiO-66-NH₂ Rinsed with MeOH (3) as-synthesized Pd@UiO-66-NH₂ (4) UiO-66-NH₂ (5) BDC-NH₂ (6) Pd-BDC-NH₂. Red, blue and green dash line represent peak positions of sample (4), (5) and (6).

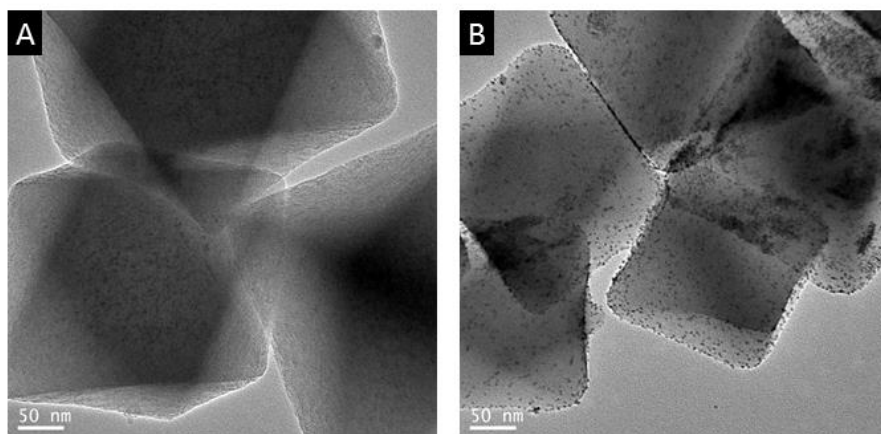


Figure 5.4 : TEM images of NP and UiO-66-NH₂ composites (a) Pt@UiO-66-NH₂ using the amine functionalized BDC linker showing encapsulation (b) Pt/UiO-66 composite using the normal BDC linker showing lack of encapsulation.

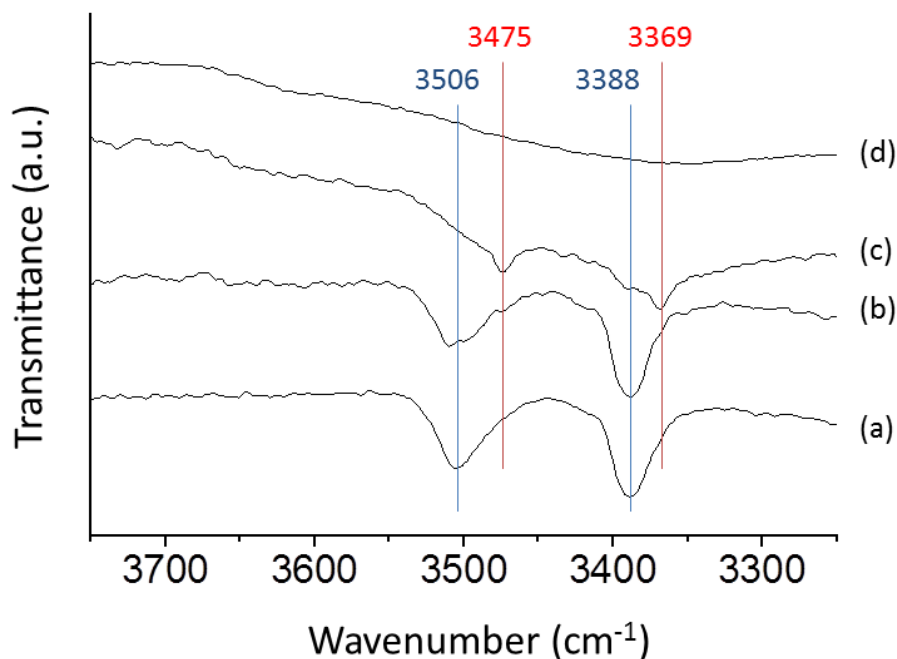


Figure 5.5: IR data showing the surface interaction of BDC-NH₂ with the nanoparticle metal surface. (a) amines stretches of BDC-NH₂ (b) Physical mixture of solid BDC-NH₂ with Pd nanoparticle (c) amines stretches of BDC-NH₂ interaction with Pd (d) the sample (c) after 3 times methanol washing.

5.4.2 Probing the NP@UiO-66-NH₂ Surface through Fourier-transform Infrared Spectroscopy (FTIR)

FTIR was used to measure the N-H stretching mode of BDC-NH₂ (Figure 5.3e), the linker of UiO-66-NH₂. N-H stretching peaks (anti-symmetric and symmetric stretching) are shifted to different positions due to the local chemical environment changes. We hypothesize that there are four possible chemical environments after Pd encapsulation; the N-H stretching mode of (a) free BDC-NH₂ (b) BDC-NH₂ in MOF with the carboxyl group bound to Zr metal centers (c) free BDC-NH₂ interacting with Pd

within the MOF cavities and (d) BDC-NH₂ in MOF with the NH₂ group interacting with Pd and the carboxyl group bound to the Zr metal centers. The N-H stretching of Pd@UiO-66-NH₂ may be the combination of these four aforementioned chemical environments. In the study, BDC-NH₂ (Figure 5.3e-5) was used as a control to represent the peak positions of free linker environment (a) N-H stretching of BDC-NH₂; While UiO-66-NH₂ (Figure 5.3e-4) was used to represent peak positions of the linker in the MOF environment (b) N-H stretching of BDC-NH₂ in MOF. Environments (c) and (d) may be more difficult to de-convolute the stretching peaks and hard to see the difference by FTIR. However, bound Pd-BDC-NH₂ (Figure 5.3e-6) was used as a representative peak positions for N-H stretching of BDC-NH₂ interacting with Pd NPs. The difference of environment (c) and (d) could be indirectly differentiated by detecting the decrease of peak intensity after washing procedures.

Three separate control samples are used so that each sample only contains one possible chemical environment. Comparing FTIR spectra of the three control samples, we observed various symmetric stretching peak positions of pure UiO-66-NH₂ (~3397 cm⁻¹, red dashed line), BDC-NH₂ (~3390 cm⁻¹, blue dashed line), and Pd-BDC-NH₂ (~3368 cm⁻¹, green dashed line) (Figure 5.3e). As-synthesized Pd@UiO-66-NH₂ (Figure 5.3e-3 and 5.5-3) may contain a combination of NH₂ group stretching environments, including free BDC-NH₂ as well as NH₂ peaks from incorporated linkers within MOF, but not bound to Pd particles. It is possible the peak contains three peaks when de-convoluted, (4) UiO-66-NH₂, (5) BDC-NH₂ and (6) N-H interacting with Pd. After MeOH washing (Figure 5.3e-2 and 5.5-2), free BDC-NH₂ was removed causing the peak shift to right. After DMF washing (Figure 5.3e-1 and 5.5-1), the Pd surface bound BDC-NH₂ was

washed so the peak shifted back to left. The results demonstrate that the interaction between the Pd surface and amine group of the linker can be reduced by using DMF washing steps to create a cleaner Pd surface. Ethylene hydrogenation was performed to compare activities of sample (1)-(3). The higher activity after DMF washing implies cleaner surfaces of Pd NPs which are consistent with the observation of FTIR results.

5.4.3 Composition and Size Control of the NP@UiO-66-NH₂ Composites using a One-pot and Two-pot Method

The formation of NP aggregates outside the MOF crystal isn't the only challenge involved with wetness impregnation; control of the metal NP composition and size is also a complication. In our method however, metal NPs reduce down first so the composition and size of the NPs is tunable. In addition to single metal NP@UiO-66-NH₂, we have shown our one-pot approach can also be applied to alloyed systems. In many previous reports⁴²⁻⁴⁵, alloyed systems have shown an increase in catalytic activity due to a synergetic relationship between the types of metal atoms present. The alteration of their d-bands due to lattice mis-match and the metal/metal bonds formed, changes their sorption and desorption properties from the altered electronic properties, helping to maximize their catalytic activity. The two commonly used methods for forming these types of composites, as stated, have the drawback of a lack in composition control of the encapsulated NPs. By being able to reduce the NPs *in situ* while simultaneously encapsulating them, we are able to co-reduce the two metals salts to form alloys maintain the cleaner surface. In a typical synthesis for the alloyed NPs@UiO-66-NH₂, the metal concentration was maintained at the same ratio as the monometallic composites. To form

alloys of different compositions (Pt and Pd), precursor amounts of each metal was varied by nominal loading. By altering the ratio of Pd to Pt metal precursor, several different PdPt alloys were formed (three different alloys along with the two monometallic forms, Table 5.1), and encapsulated using the same one-pot synthesis method. To help verify the formation of alloyed particles, the samples were synthesized in the one-pot method, followed by the digestion of the UiO-66-NH₂ coating in strong base, allowing for the use of scanning transmission electron microscopy combined with energy dispersive spectroscopy (STEM/EDX) (Figure 5.6). The elemental mapping from the STEM/EDX results show both Pd and Pt in the NP sample in an alloyed fashion, by showing an equal distribution of both metals throughout the particle (Figure 5.1 and 5.6). The transmission electron microscopy (TEM) images of Pt, Pd, and Pd_{1.3}Pt₁@UiO-66-NH₂ composites (Figure 5.1 a, c, and e), show the versatility of this approach. The morphology of NPs@MOF composites show high similarity to pure UiO-66-NH₂ nanocrystals indicating the metal precursors and encapsulation process does not affect the MOF synthesis.

Sample	Pd (ppm)	Pt (ppm)	Mole ratio (Pd:Pt)
Pd	2.36	0.002	--
Pd _{3.2} Pt ₁	1.61	0.92	3.22
Pd _{1.3} Pt ₁	1.29	1.77	1.34
Pd _{0.7} Pt ₁	0.58	1.47	0.72
Pt	0.027	2.23	--

Table 5.1: Summary of ICP data of UiO-66-NH₂ with various compositions of Pd and Pt

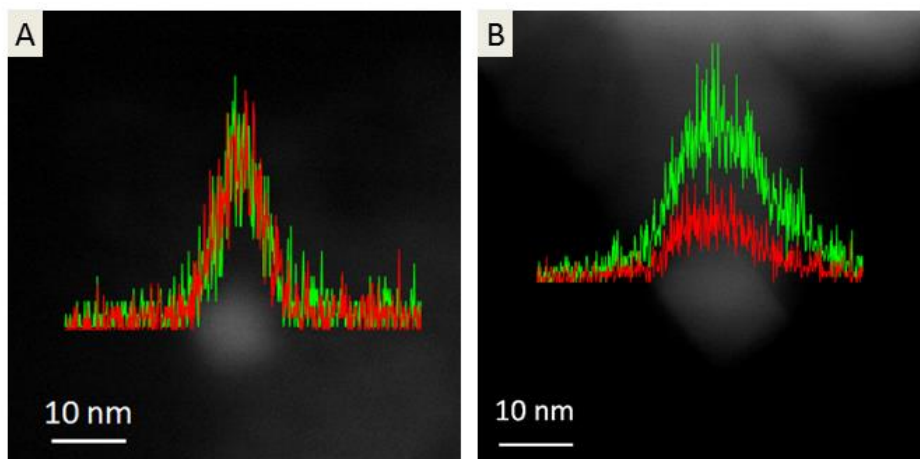


Figure 5.6: STEM/EDX line mapping of (a) Pd_{0.7}Pt₁@UiO-66-NH₂ (b) Pd_{3.2}Pt@UiO-66-NH₂. Green color represents Pd and red color represents Pt.

Comparing the synthesized NP@MOF composites with the native MOF powder x-ray diffraction (pXRD) patterns, there does not appear to be a loss in structural integrity, as the long range order peaks remain (Figure 5.7). During the synthesis conditions, there is the possibility of NP etching occurring due to the use of acetic acid and the chloride ions present in the precursor salts. A control experiment was run using the same synthesis conditions with all components except for the zirconium precursor and incorporating NaCl to reach the same chloride ion concentration as in the typical synthesis. This was then heated and stirred for 24 hours and the particles were viewed under TEM to see if any visible etching occurred; none was observed. Similarly, the process was repeated using PVP capped NPs and no etching was observed (Figure 5.8 c, d).

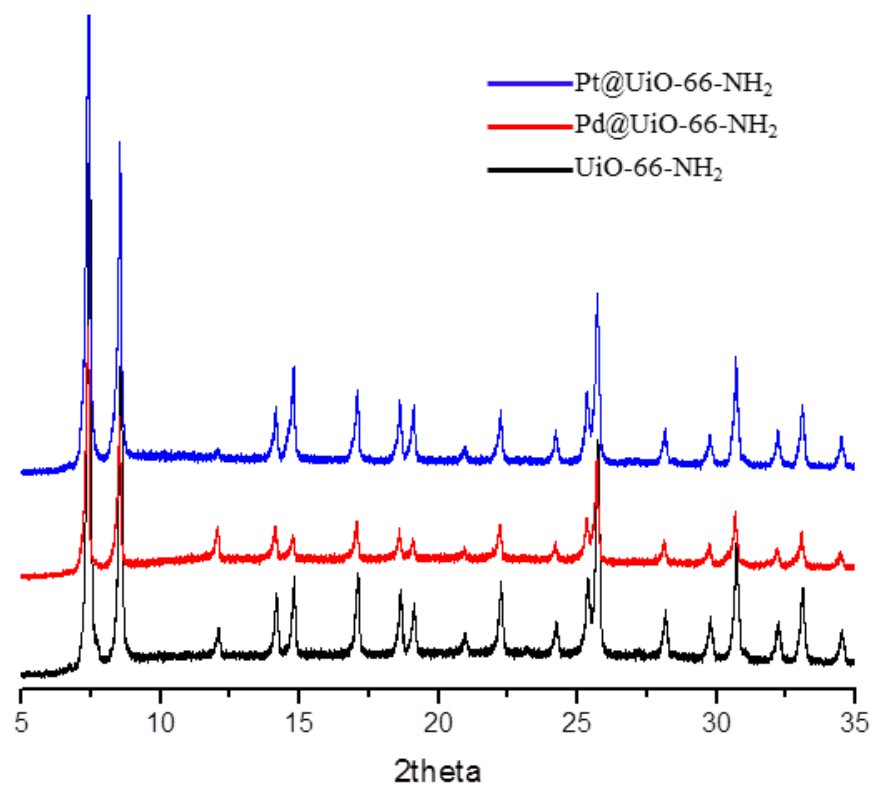


Figure 5.7: pXRD patterns of UiO-66-NH₂ for pure, palladium nanoparticles capped with UiO-66-NH₂ and platinum nanoparticles capped with UiO-66-NH₂.

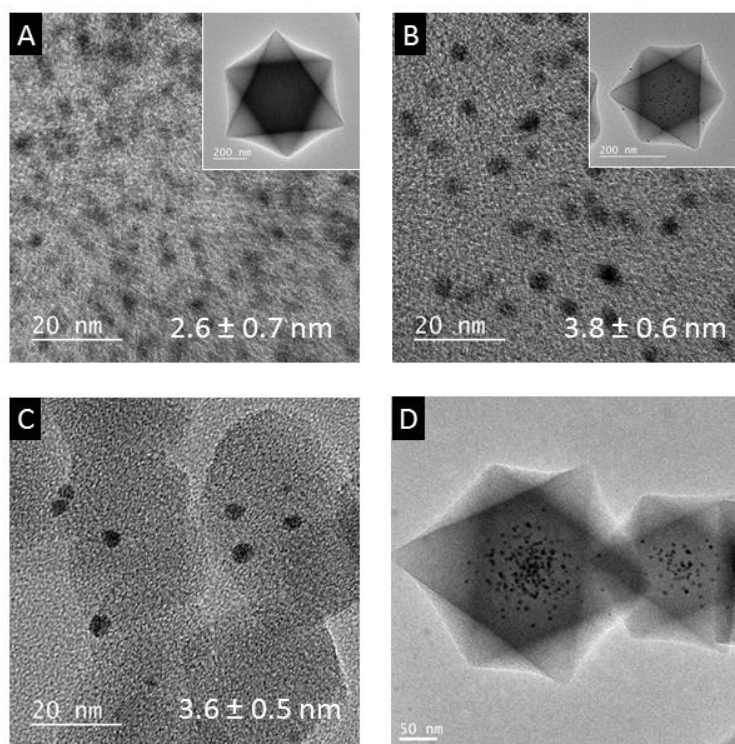


Figure 5.8: TEM of Pt@UiO-66-NH₂ synthesized at (a) 120 °C, (b) 90 °C with presence of EtOH, (c) Pt NPs loaded on support in DMF with 2.4 M acetic acid and 3.2 mM sodium chloride at 120 °C for 24 hrs, (d) PVP coated 5nm Pt NPs@UiO-66-NH₂ synthesized with 2.4 M acetic acid at 120 °C.

In a similar fashion, the one pot method can be used to allow for control of the size of NP *via* temperature alterations. In wetness impregnation, the size control of the encapsulated NPs is very difficult to control due to the diffusion barrier causing a lack in mono-dispersity. In order to control particle size within the MOF, we adjust the synthesis temperatures of the metal NPs prior to MOF coating, altering the nucleation and growth rates of the nanoparticles. At higher temperatures, the nucleation rate is high, so more nuclei are formed. With more nuclei, the particles size is smaller, while with lower temperatures larger sizes are formed. Figure 5.9 shows a smaller average size of Pd NPs

corresponding to higher temperatures. The size distribution derived from the TEM image by counting ca. 80–100 NPs is plotted in Fig. 5.9d-f. Pd NP sizes can be tuned from 3.6 ± 1.0 nm to 9.9 ± 1.8 nm by simply decreasing the synthesis temperatures from 150 °C to 90 °C (Figure 5.9). Similar results are found when using Pt precursors to form the Pt NP motif.

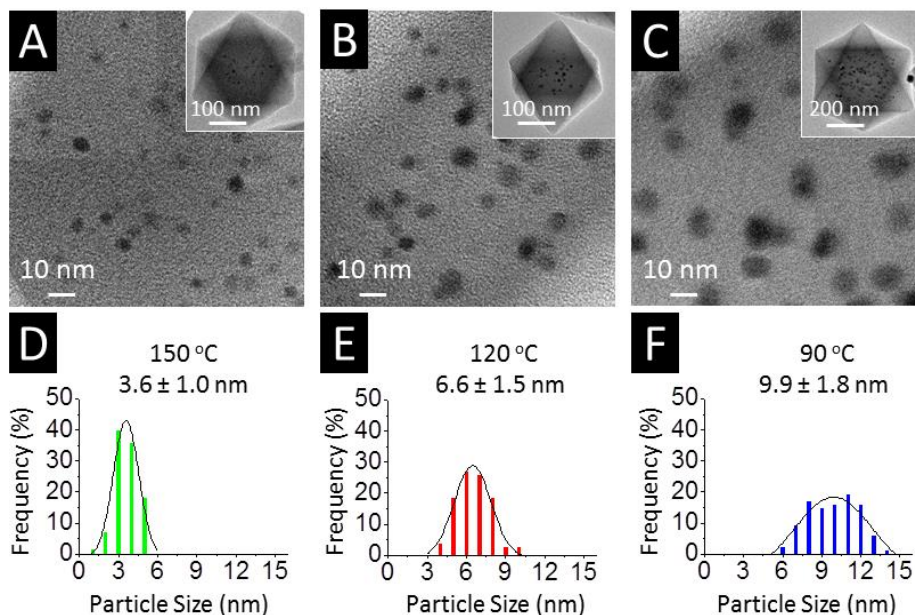


Figure 5.9: TEM images of Pd@UiO-66-NH₂ synthesized at (a) 150 °C, (b) 120 °C and (c) 90 °C. (d-f) size distribution of Pd NPs at various synthetic temperatures.

5.4.4 Size Selective Alkene Hydrogenations Over Encapsulated NP@UiO-66-NH₂

Scanning electron microscopy (SEM) images (Figure 5.1c and 5.10) and TEM images of Pt and Pd@UiO-66-NH₂ show well dispersed metal NPs encapsulated into uniform octahedral UiO-66-NH₂ nanocrystals. Each nanocrystal contains multiple metal NPs fully encapsulated and separated. Size selective hydrogenations of alkenes were

carried out to confirm that the metal NPs were fully encapsulated within the MOF nanocrystals. The Pd@UiO-66-NH₂ composites were compared with a control sample containing the same metal loading of Pd NPs deposited on the external surface of UiO-66-NH₂ crystals (Figure 5.11a). Both samples show activity in ethylene and cyclohexene hydrogenations; both ethylene and cyclohexene molecules have small enough diameters to diffuse through the pore aperture of UiO-66-NH₂ (5 Å), while little to no activity was observed for cyclooctene hydrogenation over the Pd@UiO-66-NH₂; yet appreciable activity was observed over the control sample. The size of the cyclooctene molecules is larger compared to the aperture size of UiO-66-NH₂, thus showing the size selectivity the MOF coating provides to the encapsulated catalysts. The selective hydrogenation results suggest that the metal nanocrystals are fully encapsulated within MOF nanocrystals and that no fractures or fragmentations exist in the single crystalline UiO-66-NH₂ shell. Similar experiments were performed to Pd/MOF composites synthesized from BDC as a MOF ligand (Figure 5.3d). Appreciable activity of cyclooctene hydrogenation was observed over the sample with confirmed aggregated and poly-dispersed Pd NPs formed outside the MOF crystal (Figure 5.12).

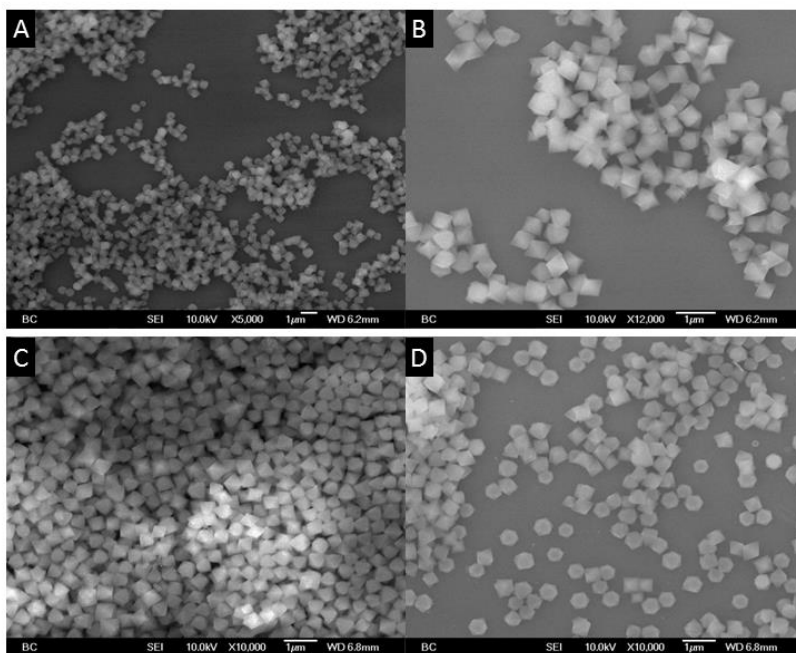


Figure 5.10: SEM image of (a-b) Pd@UiO-66-NH₂ and (c-d) pure UiO-66-NH₂.

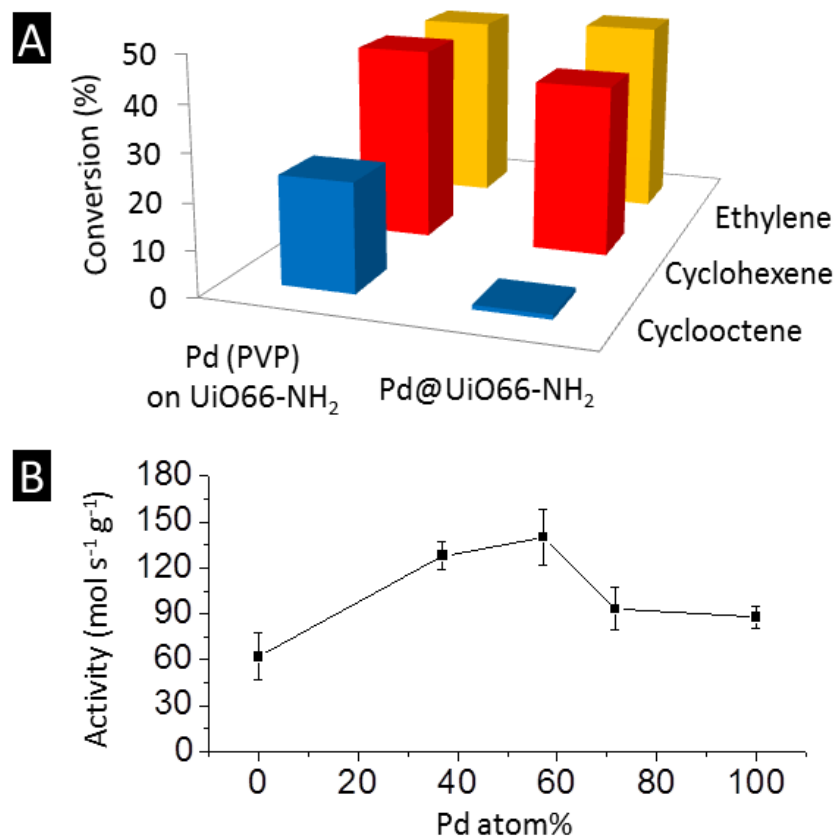


Figure 5.11: Alkene hydrogenation catalysis (a) Size selective alkene hydrogenation over Pd@UiO-66-NH₂ and Pd (PVP) on UiO-66-NH₂. Ethylene hydrogenation is performed at 0 °C, Cyclohexene

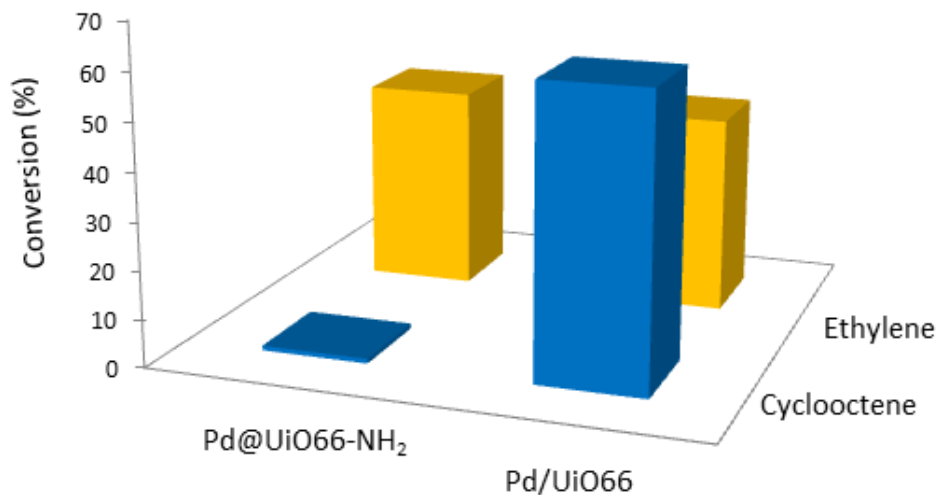


Figure 5.12: Size selective alkene hydrogenation over Pd@UiO-66-NH₂ and Pd/UiO-66 composite. Ethylene hydrogenation is run at 0 °C and Cyclooctene hydrogenation is run at 40 °C.

5.4.5 Composition Effect on Ethylene Hydrogenation Activity

Along with selectivity controls to confirm the incorporation of NPs solely within the UiO-66-NH₂, ethylene hydrogenation was run for each of the prepared alloyed samples to compare their activities. It was expected that the alloyed compositions would cause an increase in the catalytic activity toward ethylene hydrogenations compared to the pure Pt and Pd counterparts. This is due to interactions of the Pt and Pd atoms altering the d-band of the metals in turn changing their de/sorption properties of reactant and product molecules. By forming a series of differently alloyed compositions, a volcano curve, following the Sabatier principle, where there is a specific ratio of the Pd/Pt

composition for the highest activity, was expected. In order to prevent the interference of particle size effects, the activities are normalized by surface atoms, and ICP measurements were taken to normalize by the exact Pd to Pt ratio for catalysis. It was found after performing the hydrogenations over each sample the highest activity was for the alloyed sample containing a molar ratio of Pd_{1.3}Pt₁ and a decay in activity was seen with both increased Pt and Pd content (Figure 5.11b). Control experiments were performed by using a mixture of pure Pt and Pd catalyst showing no such synergistic effects (Figure 5.13). Furthermore, the ethylene hydrogenation activities can be further used to confirm a cleaner metal surface than traditional capping agent. PVP capped NPs were encapsulated in UiO-66-NH₂ for a fair comparison (Figure 5.14). The Pt NPs synthesized by our one pot method show more than double the activity (Figure 5.14) implying a higher active site surface than the PVP capped NP.

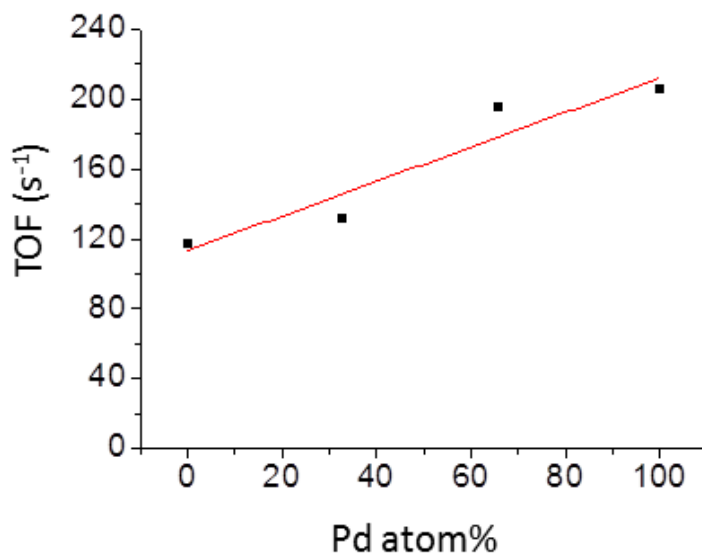


Figure 5.13: Ethylene hydrogenation catalysis with the various mixtures of Pd and Pt NPs

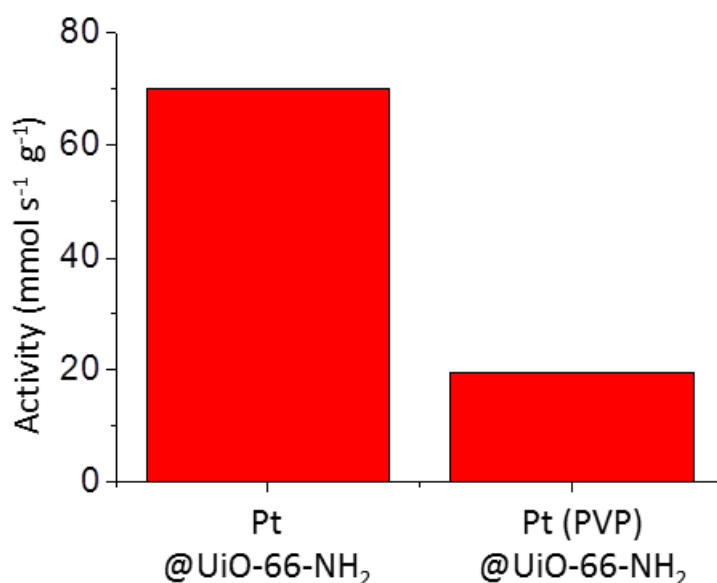
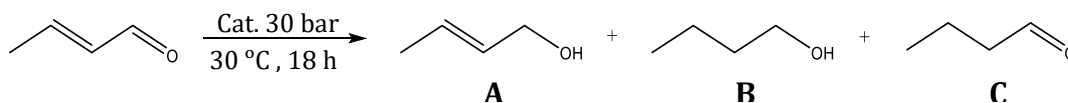


Figure 5.14: Ethylene hydrogenation catalysis with Pt@UiO-66-NH₂ and Pt (PVP)@UiO-66-NH₂

5.4.6 Liquid Phase Hydrogenation of Crotonaldehyde

Additionally, hydrogenation of crotonaldehyde was performed in order to further study the effects of PVP on the NP surface compared to that of the cleaner, surfactant free, sample. During the hydrogenation of crotonaldehyde, the structure can give rise to multiple different hydrogenated products: butanol, butryaldehyde, or 2-buten-1-ol. To test the hypothesis that the one pot encapsulated NPs coated in MOF have a cleaner surface than particles that are capped in polymer (PVP) or other surfactants, the selectivity of the hydrogenated products are compared in Table 5.2. Three separate samples are synthesized in order to directly compare the MOF coated samples; the one-pot Pt NP MOF coated sample, the PVP coated NPs encapsulated in MOF, and the PVP coated NPs on the MOF surface.

Both samples that contained PVP as a capping agent, the PVP capped Pt NPs within UiO-66-NH₂ and those on the surface of the MOF material, showed selectivity different compared to the sample not containing PVP. The crotonaldehyde hydrogenation when performed using both samples containing PVP produce a mixture of butyraldehyde and butanol with no conversion to 2-buten-1-ol (unsaturated alcohol product) seen under ¹H NMR. In comparison, the same hydrogenation reaction was performed using the samples synthesized by the one-pot Pt NP encapsulation method produces a mixture of all three potential products with a higher selectivity towards the desired unsaturated alcohol. The cleaner surface particles as synthesized by our one pot encapsulation method are able to produce the more desirable unsaturated alcohol product. From these reactions, it can be observed that the surface of the Pt NP plays a key role in the selectivity of the products formed due to the altered interaction of the incoming reactants with the Pt active surface. For polymer coated samples, the distribution of products is different when compared to the cleaner particle surface. We attribute the distribution of all three potential products to the small size of crotonaldehyde and the flexibility of the MOF structure.



Conversion (%)	Crotonaldehyde (Reactant)	Unsaturated Alcohol (Target product)	butyraldehyde	butanol
Pt@UiO	55.2	18.9±3.3	15.8±6.6	10.1±0.2
Pt(PVP)@UiO	73.3	0	14.5±4.3	12.2±0.6
Pt(PVP) on UiO	60.5	0	28.7±10.8	10.7±3.5

Table 5.2: Summary of crotonaldehyde hydrogenation products over various nanoparticle and MOF composite materials utilizing different metal catalyst surfaces

5.5 Conclusion

In summary, we were able to use a one-pot synthesis method to encapsulate metal nanoparticles using crystalline UiO-66-NH₂ as a capping agent. The use of MOF allowed for a higher relative stability of the nanoparticles due to the more robust nature of the MOF material when compared to traditional capping agents. Using the one-pot method of the *in situ* production of NPs followed by encapsulation, a broader control over the composition, differently alloyed *via* nominal loading, and the size, by changing the reduction parameters (temperature), was seen. Size exclusion catalysis was performed to ensure the complete encapsulation while ethylene hydrogenation was used as a tool to determine the effect of the alloyed particles compared to the pure counterparts. A volcano type curve was seen with the introduction of the bimetallic systems with a heightened activity with the Pd_{1.3}Pt₁ particle composite.

5.6 References

- [1.] Li, M.; Li, D.; O'Keeffe, M.; Yaghi, O. M., Topological Analysis of Metal-Organic Frameworks with Polytropic Linkers and/or Multiple Building Units and the Minimal Transitivity Principle, *Chem. Rev.* **2014**, *114*, 1343-1370.
- [2.] Li, H.; Eddaoudi, M.; O'Keeffe, M.; Yaghi, O. M., Design and Synthesis of an Exceptionally Stable and Highly Porous Metal-Organic Framework, *Nature* **1999**, *402*, 276-279.
- [3.] Farha, O. K.; Hupp, J. T., Rational Design, Synthesis, Purification, and Activation of Metal-Organic Framework Materials, *Acc. Chem. Res.* **2010**, *43*, 1166-1175.
- [4.] Eddaoudi, M.; Moler, D. B.; Li, H.; Chen, B.; Reineke, T. M.; O'Keeffe, M.; Yaghi, O. M., Modular Chemistry: Secondary Building Units as a Basis for the Design of Highly Porous and Robust Metal-Organic Carboxylate Frameworks, *Acc. Chem. Res.* **2001**, *34*, 319-330.
- [5.] Li, J. R.; Kuppler, R. J.; Zhou, H. C., Selective Gas Adsorption and Separation in Metal-Organic Frameworks *Chem. Soc. Rev.* **2009**, *38*, 1477-1504.
- [6.] Chaemchuen, S.; Kabir, N. A.; Zhou, K.; Verpoort, F., Metal-Organic Frameworks for Upgrading Biogas *via* CO₂ Adsorption to Biogas Green Energy, *Chem. Soc. Rev.* **2013**, *42*, 9304-9332.
- [7.] Horcajada, P.; Gref, R.; Baati, T.; Allan, P. K.; Maurin, G.; Couvreur, P.; Ferey, G.; Morris, R. E.; Serre, C., Metal-Organic Frameworks in Biomedicine, *Chem. Rev.* **2012**, *112*, 1232-1268.
- [8.] Zhuang, J.; Kuo, C.-H.; Chou, L.-Y.; Liu, D.-Y.; Weerapana, E.; Tsung, C.K., Optimized Metal-Organic Framework Nanospheres for Drug Delivery: Evaluation of Small-Molecule Encapsulation, *ACS Nano* **2014**, *8*, 2812-2819.
- [9.] Farrusseng, D.; Aguado, S.; Pinel, C., Metal-Organic Frameworks: Opportunities for Catalysis, *Angew. Chem. Int. Ed. Engl.* **2009**, *48*, 7502-7513.
- [10.] Lee, J.; Farha, O. K.; Roberts, J.; Scheidt, K. A.; Nguyen, S. T.; Hupp, J. T., Metal-Organic Framework Materials as Catalysts, *Chem. Soc. Rev.* **2009**, *38*, 1450-1459.
- [11.] Doherty, C. M.; Buso, D.; Hill, A. J.; Furukawa, S.; Kitagawa, S.; Falcaro, P., Using Functional Nano- and Microparticles for the Preparation of Metal-Organic Framework Composites with Novel Properties, *Acc. Chem. Res.* **2014**, *47*, 396-405.

- [12.] Zhao, M.; Deng, K.; He, L.; Liu, Y.; Li, G.; Zhao, H.; Tang, Z., Core-shell Palladium Nanoparticle@Metal-Organic Frameworks as Multifunctional Catalysts for Cascade Reactions, *J. Am. Chem. Soc.* **2014**, *136*, 1738-1741.
- [13.] Kuo, C. H.; Tang, Y.; Chou, L. Y.; Sneed, B. T.; Brodsky, C. N.; Zhao, Z.; Tsung, C. K., Yolk-shell Nanocrystal@ZIF-8 Nanostructures for Gas-Phase Heterogeneous Catalysis with Selectivity Control, *J. Am. Chem. Soc.* **2012**, *134*, 14345-14348.
- [14.] Zhu, Q. L.; Xu, Q., Metal-Organic Framework Composites, *Chem. Soc. Rev.* **2014**, *43*, 5468-5512.
- [15.] Hu, P.; Morabito, J. V.; Tsung, C.-K., Core-Shell Catalysts of Metal Nanoparticle Core and Metal-Organic Framework Shell, *ACS Catal.* **2014**, *4*, 4409-4419.
- [16.] Motl, N. E.; Smith, A. F.; DeSantis, C. J.; Skrabalak, S. E., Engineering Plasmonic Metal Colloids through Composition and Structural Design, *Chem. Soc. Rev.* **2014**, *43*, 3823-3834.
- [17.] Li, J. F.; Huang, Y. F.; Ding, Y.; Yang, Z. L.; Li, S. B.; Zhou, X. S.; Fan, F. R.; Zhang, W.; Zhou, Z. Y.; WuDe, Y.; Ren, B.; Wang, Z. L.; Tian, Z.Q., Shell-Isolated Nanoparticle-Enhanced Raman Spectroscopy, *Nature* **2010**, *464*, 392-395.
- [18.] Hu, P.; Zhuang, J.; Chou, L. Y.; Lee, H. K.; Ling, X. Y.; Chuang, Y. C.; Tsung, C. K., Surfactant-Directed Atomic to Mesoscale Alignment: Metal Nanocrystals Encased Individually in Single-Crystalline Porous Nanostructures, *J. Am. Chem. Soc.* **2014**, *136*, 10561-10564.
- [19.] Sugikawa, K.; Furukawa, Y.; Sada, K., SERS-Active Metal-Organic Frameworks Embedding Gold Nanorods, *Chem. Mater.* **2011**, *23*, 3132-3134.
- [20.] Lohse, S. E.; Murphy, C. J., Applications of Colloidal Inorganic Nanoparticles: From Medicine to Energy, *J. Am. Chem. Soc.* **2012**, *134*, 15607-15620.
- [21.] White, R. J.; Luque, R.; Budarin, V. L.; Clark, J. H.; Macquarrie, D. J., Supported Metal Nanoparticles on Porous Materials. Methods and Applications *Chem. Soc. Rev.* **2009**, *38*, 481-494.
- [22.] Jiang, H.-L.; Liu, B.; Akita, T.; Haruta, M.; Sakurai, H.; Xu, Q., Au@ZIF-8: CO Oxidation over Gold Nanoparticles Deposited to Metal-Organic Framework, *J. Am. Chem. Soc.* **2009**, *131*, 11302-11303.
- [23.] Gu, X.; Lu, Z. H.; Jiang, H. L.; Akita, T.; Xu, Q., Synergistic Catalysis of Metal-Organic Framework-Immobilized Au-Pd Nanoparticles in Dehydrogenation of Formic Acid for Chemical Hydrogen Storage, *J. Am. Chem. Soc.* **2011**, *133*, 11822-11825.

- [24.] Aijaz, A.; Karkamkar, A.; Choi, Y. J.; Tsumori, N.; Ronnebro, E.; Autrey, T.; Shioyama, H.; Xu, Q., Immobilizing Highly Catalytically Active Pt Nanoparticles inside the Pores of Metal-Organic Framework: A Double Solvents Approach, *J. Am. Chem. Soc.* **2012**, *134*, 13926-13929.
- [25.] Zhu, Q. L.; Li, J.; Xu, Q., Immobilizing Metal Nanoparticles to Metal-Organic Frameworks with Size and Location Control for Optimizing Catalytic Performance, *J. Am. Chem. Soc.* **2013**, *135*, 10210-10213.
- [26.] Tsuruoka, T.; Kawasaki, H.; Nawafune, H.; Akamatsu, K., Controlled Self-Assembly of Metal-Organic Frameworks on Metal Nanoparticles for Efficient Synthesis of Hybrid Nanostructures, *ACS Appl. Mater. Interfaces* **2011**, *3*, 3788-3791.
- [27.] He, L.; Liu, Y.; Liu, J.; Xiong, Y.; Zheng, J.; Tang, Z., Core-Shell Noble-Metal@Metal-Organic-Framework Nanoparticles with Highly Selective Sensing Property, *Angew. Chem. Int. Ed. Engl.* **2013**, *52*, 3741-3745.
- [28.] Lu, G.; Li, S.; Guo, Z.; Farha, O. K.; Hauser, B. G.; Qi, X.; Wang, Y.; Wang, X.; Han, S.; Liu, X.; DuChene, J. S.; Zhang, H.; Zhang, Q.; Chen, X.; Ma, J.; Loo, S. C. J.; Wei, W. D.; Yang, Y.; Hupp, J. T.; Huo, F., Imparting Functionality to a Metal-Organic Framework Material by Controlled Nanoparticle Encapsulation, *Nat. Chem.* **2012**, *4*, 310-316.
- [29.] Meilikhov, M.; Yusenko, K.; Esken, D.; Turner, S.; Van Tendeloo, G.; Fischer, R. A., Metals@MOFs – Loading MOFs with Metal Nanoparticles for Hybrid Functions, *Eur. J. Inorg. Chem.* **2010**, *2010*, 3701-3714.
- [30.] Esken, D.; Turner, S.; Lebedev, O. I.; Van Tendeloo, G.; Fischer, R. A., Au@ZIFs: Stabilization and Encapsulation of Cavity-Size Matching Gold Clusters inside Functionalized Zeolite Imidazolate Frameworks, ZIFs, *Chem. Mater.* **2010**, *22*, 6393-6401.
- [31.] Chen, Y.-Z.; Zhou, Y.-X.; Wang, H.; Lu, J.; Uchida, T.; Xu, Q.; Yu, S.-H.; Jiang, H.-L., Multifunctional PdAg@MIL-101 for One-Pot Cascade Reactions: Combination of Host-Guest Cooperation and Bimetallic Synergy in Catalysis, *ACS Catal.* **2015**, *5*, 2062-2069.
- [32.] Guo, Z.; Xiao, C.; Maligal-Ganesh, R. V.; Zhou, L.; Goh, T. W.; Li, X.; Tesfagaber, D.; Thiel, A.; Huang, W., Pt nanoclusters Confined within Metal-Organic Framework Cavities for Chemoselective Cinnamaldehyde Hydrogenation, *ACS Catal.* **2014**, *4*, 1340-1348.
- [33.] Chen, M.; Wu, B.; Yang, J.; Zheng, N., Small Adsorbate-Assisted Shape Control of Pd and Pt Nanocrystals, *Adv. Mater.* **2012**, *24*, 862-879.

- [34.] Kuhn, J. N.; Tsung, C.-K.; Huang, W.; Somorjai, G. A., Effect of Organic Capping Layers over Monodisperse Platinum Nanoparticles upon Activity for Ethylene Hydrogenation and Carbon Monoxide Oxidation, *J. Catal.* **2009**, *265*, 209-215.
- [35.] Wang, P.; Zhao, J.; Li, X.; Yang, Y.; Yang, Q.; Li, C., Assembly of ZIF Nanostructures Around Free Pt Nanoparticles: Efficient Size-Selective Catalysts for Hydrogenation of Alkenes Under Mild Conditions, *Chem Commun (Camb)* **2013**, *49*, 3330-3332.
- [36.] Chen, L.; Chen, H.; Li, Y., One-Pot Synthesis of Pd@MOF Composites without the Addition of Stabilizing Agents, *Chem. Comm.* **2014**, *50*, 14752-14755.
- [37.] Liu, H.; Chang, L.; Chen, L.; Li, Y. J., *In Site* One-Step Synthesis of Metal-Organic Framework Encapsulated Naked Pt Nanoparticles without Additional Reductants, *Mater. Chem. A* **2015**, *3*, 8028-8033.
- [38.] Souza, G. R.; Levin, C. S.; Hajitou, A.; Pasqualini, R.; Arap, W.; Miller, J. H., *In vivo* Detection of Gold-Imidazole Self-Assembly Complexes: NIR-SERS Signal Reporters, *Anal. Chem.* **2006**, *78*, 6232-6237.
- [39.] Hakkinen, H., The Gold-Sulfur Interface at the Nanoscale, *Nat. Chem.* **2012**, *4*, 443-455.
- [40.] Jadzinsky, P. D.; Calero, G.; Ackerson, C. J.; Bushnell, D. A.; Kornberg, R. D., Structure of a Thiol Monolayer-Protected Gold Nanoparticle at 1.1 Å Resolution, *Science* **2007**, *318*, 430-433.
- [41.] Kim, M.; Cohen, S. M., Discovery, Development, and Functionalization of Zr(IV)-based Metal-Organic Frameworks, *CrystEngComm.* **2012**, *14*, 4096-4104.
- [42.] Singh, A. K.; Xu, Q., Synergistic Catalysis over Bimetallic Alloy Nanoparticles, *ChemCatChem* **2013**, *5*, 652-676.
- [43.] Yu, W.; Porosoff, M. D.; Chen, J. G., Review of Pt-Based Bimetallic Catalysis: From Model Surfaces to Supported Catalysts, *Chem. Rev.* **2012**, *112*, 5780-5817.
- [44.] Wang, D.; Li, Y., Bimetallic Nanocrystals: Liquid-Phase Synthesis and Catalytic Applications, *Adv. Mater.* **2011**, *23*, 1044-1060.
- [45.] Stamenkovic, V. R.; Mun, B. S.; Arenz, M.; Mayrhofer, K. J.; Lucas, C. A.; Wang, G.; Ross, P. N.; Markovic, N. M., Trends in Electrocatalysis on Extended and Nanoscale Pt-Bimetallic Alloy Surfaces, *Nat. Mater.* **2007**, *6*, 241-247.

[46.] Tsung, C.K.; Kuhn, J.N.; Huang, W.; Aliaga, C.; Hung, L.I.; Somorjai, G.A.; Yang, P., Sub-10 nm Platinum Nanocrystals with Size and Shape Control: Catalytic Study for Ethylene and Pyrrole Hydrogenation, *J. Am. Chem. Soc.* **2009**, *131*, 5816-5822.

[47.] Nützenadel, C.; Züttel, A.; Chartouni, D.; Schmid, G.; Schlapbach, L., Critical Size and Surface Effect of the Hydrogen Interaction of Palladium Clusters, *Eur. Phys. J. D.* **2000**, *8*, 245-250.

6.0 Hybrid Pt/CNT@uio-66 Electrocatalyst for Increased Stability in the Oxygen Reduction Reaction

6.1 Abstract

Proton exchange membrane fuel cells (PEMFCs) along with solar cells have made several advances in recent years due to the impending energy crisis. PEMFCs are of particular interest due to the input fuels, hydrogen and oxygen, and the byproduct, water, being earth abundant and clean. The use of Nafion in such fuel cells is common practice in order to promote and enhance the proton conductivity to help increase reaction kinetics, though with its introduction, certain limitations arise: high Pt loading, poor stability during working conditions, and subsequent poisoning due to sulfonate groups present in Nafion. This work demonstrates the use metal-organic frameworks (MOFs), in particular UiO-66, as a protector barrier for the Pt catalysts to help prevent the deactivation. A hybrid system is synthesized in which Pt nanoparticles are deposited on carbon nanotubes followed by the selective growth of UiO-66 on the Pt particles; forming the final Pt/CNT@UiO-66 hybrid material. Size selective alkene hydrogenations were run as well as electrochemical measurements to demonstrated the full coverage of Pt particles with UiO-66 while maintaining catalytic activity. Finally, the hybrid materials were utilized to perform the oxygen reduction reaction (ORR) to simulate the catalyst stability for the sluggish cathodic side of the PEMFC reaction. . The Pt/CNT@UiO-66 showed a better stability under ORR condition when compared to Pt/CNT (i.e. without coating) as well as decreased poisoning during the accelerated aging process suggesting

the MOF coating is a promising and efficient means to protect the Pt catalysts from deactivation and aggregation.

6.2 Introduction

With the looming energy crisis, there has been a large push for research and development into more renewable resources such as solar and fuel cells¹⁻³. In particular, proton exchange membrane fuel cells (PEMFC) have been studied for years for the main application in transportation needs due to key advantages of lower working temperatures and pressures⁴. PEMFC utilize more earth abundant reactants, H₂ and O₂, to undergo electrochemical transformations with the by-product being water. As the push to reduce carbon emissions has increased over the past several years, new, more stable PEMFC catalysts are needed. In a typical PEMFC cell, two Pt-based catalysts, for the anodic and cathodic reactions, are separated by a proton permeable/exchange membrane (PEM)⁵. Starting with the anodic process, H₂ is oxidized to form two protons which then cross the membrane to interact with the O₂ on the cathodic side, forming water. Though the process seems ideal, there are disadvantages that have hindered the greater use of PEMFCs. First, the catalyst for both sides of the reaction is Pt, driving the cost up⁶. Similarly, a large quantity is needed in order to be used in vehicles and other industrial applications⁶. Second, though Pt is an active catalyst for both reactions, the surface can easily be poisoned through the sulfonate groups off of Nafion⁷, a sulfonated tetrafluoroethylene polymer, used in the PEM layer to help with proton transfer, as well as poisoned by thiols within feed gas^{8,9}. Sulfonate groups are able to coordinate and bind tightly with the Pt surface, in turn deactivating the catalyst⁸. Finally, although the

working temperatures and pressures are lower in PEMFCs than other fuel cells, the conditions are still harsh for Pt nanoparticles; they will either leach into solution through the course of the reaction or aggregate together decreasing the active surface area^{10,11}.

To address these issues, several approaches have been taken. A common method taken is incorporating less expensive, transition metal catalysts to replace Pt¹²⁻¹⁵. For instance, in Li's group, they synthesized single atom Fe and Co catalysts on N-doped carbon NPs to replace the Pt/C used for the cathodic oxygen reduction¹². With the incorporation of less-precious transition metals, there are benefits in price reduction, but they also have their own limitations with activity and stability^{16,17}. Other attempts have been made at reducing or completely eliminating the need for Nafion within the PEM layer^{18,19}. Sun *et al* used a mixture of SO₃H functionalized UiO-66 and graphene oxide to promote proton conductivity¹⁸. By eliminating the potential poisons, the Pt catalysts will maintain their activity rather than undergoing surface deactivation. Although, completely eliminating the need for Nafion would be ideal, it is still necessary within the PEM layer due to its superior proton conduction²⁰. An additional approach is to protect the surface of the Pt catalyst by a barrier²¹⁻²³. For this to work, the barrier must be porous in order to allow reactants and products to move freely to and from the catalyst surface, but also be able to block the poisoning sulfonate groups from interacting with the surface.

Metal-organic frameworks (MOFs) are crystalline solids formed from the three dimensional coordination of metal nodes (formed from metal ions or clusters) and bridging organic linkers²⁴⁻²⁷. MOF features a permanent microporosity upon the removal of solvent²⁸. MOFs have record surface areas up to few thousand m²/g and high molecular selectivity, which make them attractive and promising materials for gas storage^{29,30}, drug delivery^{31,32}, sensors³³,

catalysis³⁴⁻³⁷ and particularly separation^{29,38}. The highly selective behavior of a MOF is a function of its pore aperture structure and the chemical environment due to the functional groups off of the linkers. MOF material are also highly tunable by changing the metal in the nodes of the linkers and their functional groups making them ideal candidates for highly selective reactions and separation³⁸. The mild synthetic conditions of MOFs allow for their integration with other inorganic nanomaterials possible. From these hybrid MOF materials, the MOF is able to impart their unique functions to the other incorporated materials generating potential solutions for many current technology issues in regards to separation, i.e. the separation of poisoning species from the catalyst surface.

Here in, we report a new methodology for the prevention of Pt/C poisoning by the sulfonate groups off of Nafion; without using a different or secondary proton conducting material. Similarly, the prevention of aggregation and Pt leaching during working conditions is addressed. We propose to utilize a hybrid material incorporating the traditional Pt/C, in the version of carbon nanotubes, coated by a thin layer of MOF material. Although MOF have many advantages, several versions are not stable in harsh environments (high temperature, highly acidic or basic environments) and most are not inherently conductive. During PEMFC reactions, highly acid electrolytes, HClO₄ or H₂SO₄, are used. In order for the Pt/CNT coated in MOF to be stable in the working conditions, a stable and robust MOF with a small aperture is needed. For this, we have chosen the robust, zirconium based MOF, UiO-66 which is stable at low pH and relatively high temperatures, and has shown some conductive behavior^{39,40}. In order to increase the conductivity of the MOF, the CNTs must remain uncoated and in contact with the Pt particle to ensure the transport of electrons through the catalyst.

Pt nanoparticles are first deposited on carbon nanotubes (CNTs) to create decorated CNTs with small, 3.7 nm Pt nanoparticles, even distributed along the CNT. The Pt/CNT material is then used in three separate MOF coating methods to achieve the

most even UiO-66 coating; a pre-hydrolysis method, an aqueous method, and a traditional organic solvent method. The Pt/CNT@UiO-66 catalysts were then characterized through transmission electron microscopy and x-ray diffraction as well as gas phase hydrogenation of alkenes to ensure most Pt particles were covered. Finally, the samples were used to conduct electrochemical oxygen reduction reaction as a demonstration of the UiO-66 ability to protect the Pt particles from aggregation as well as increase their stability towards surface poisoning.

6.3 Experimental Methods

6.3.1 Chemicals

Zirconyl chloride octahydrate ($\text{ZrOCl}_2 \cdot 8\text{H}_2\text{O}$, Acros, 98+%), zirconium (IV) propoxide ($\text{Zr}(\text{OCH}(\text{CH}_3)_2)_4$, 70 wt% in 1-propanol) terephthalic acid (Aldrich, 98%), tetrafluoroterephthalic acid (Aldrich, 97%), acetic acid (Sigma-Aldrich, 99.7%), N,N-dimethylformamide (Sigma-Aldrich, 99.8), potassium tetrachloroplatinate (K_2PtCl_4 , Acros, 40% Pt), ethylene glycol ($\text{C}_2\text{H}_6\text{O}_2$, Fisher), carbon nanotubes (C, Nanolab), hydrochloric acid (HCl, Fisher), perchloric acid (HClO_4 , GFS, 70% veritas double distilled), cis-cyclooctene (Sigma-Aldrich, 95%), were purchased from the indicated sources and used without further purification. Hydrogen (Airgas, 99.999%), ethylene (Airgas, 99.995%) and helium (Airgas, 99.999%), oxygen (Airgas, UHP), and nitrogen (Airgas, UHP) were used for heterogeneous gas phase catalysis and electrochemical measurement purging. Nanopure deionized water (DI water, 18.2 M Ω) from a Milli-Q system was utilized.

6.3.2 Synthesis of Pt/CNT *via* Pt Deposition

11.5 mg (0.027 mmol) of Potassium tetrachloroplatinate and 3 mL of ethylene glycol is added to a 20 mL scintillation vial and sonicated until the metal salt is dissolved. During this time, 25 mg of the carbon nanotubes and 64 mL of ethylene glycol are added to a 100 mL single-necked round bottom flask followed by 20 minutes of sonication on ice. After sonication, the 3 mL of Pt containing ethylene glycol is added and sealed with a rubber stopper.

The resultant solution is stirred (500 rpm) in while submerged in a preheated 50°C oil-bath for 20 minutes. After 20 min, the temperature of oil-bath is increased to 145°C while containing the round bottom flask and held at 145°C while stirring for 30 minutes. After 30 minutes, the solution is removed and cooled back to room temperature followed by vacuum filtration through a nylon membrane (0.45 µm). A total of 1 liter of deionized water is used to wash the as-synthesized Pt/CNT material. The Pt/CNT is then suspended in an additional 200 mL of deionized water and allowed to soak overnight. The following day, the water is vacuum filtered and an additional 1 liter is again used to finish washing the Pt/CNT material. The Pt/CNT is then allowed to dry under mild heat (70°C in an oven) to be used for further experiments.

6.3.3 Synthesis of Pt/CNT@UiO-66: Traditional Method

15 mg of the as synthesized Pt/CNT sample and 4 mL of DMF is added a glass vial and sonicated on ice for 1 minute followed by vigorous stirring for an additional 10 minutes. In a second glass vial, 10.6 mg of terephthalic acid and 10.2 mg of zirconyl

chloride octahydrate are added in addition to a 3.5 mL solution of DMF containing 20.55 μL of concentrated HCl. Once dissolved, the above solution is quickly added to the vigorous stirred Pt/CNT solution, sealed and stirred for 16 hours in a 150°C. The resulting Pt/CNT@UiO-66 solid is collected by centrifugation at 3300 rpm, washed twice with water and dried under mild heat, 70°C in an oven.

6.3.4 Synthesis of Pt/CNT@UiO-66: Pre-hydrolysis Method

In a crimp top vial, 73.94 (0.158 mmol) of zirconium (IV) propoxide, 7 mL of DMF and 4 mL of glacial acetic acid are added. The vial is then capped with the rubber septa and crimp top, gently shaken for 10 seconds, and placed in a pre-heated 140°C oven for 1 hour. After one hour, the solution will change from clear to yellow, indicating the formation of the UiO-66 zirconium nodes to be used in the following coating steps. These nodes may be used for up to one week before having to synthesize a new batch.

As the nodes form, a terephthalic acid solution is prepared by adding 265.81 mg terephthalic acid (0.160 mM) and 10 mL of DMF to a glass vial and sonicating until dissolved. Once the nodes are formed and cooled, the coating process can occur. In a 1 mL Teflon beaker, 5 mg of the as-synthesized Pt/CNT is added, followed by 0.518 mL of DMF. The beaker is then carefully sonicated for 2 minutes on ice until the Pt/CNT are dispersed. Once sonicated, 0.167 mL of the node solution (ZrOPr/OAc/DMF) is added, being sure to wash any material from the beaker sides. Immediately after, 0.150 mL of the stock terephthalic solution is directly added to the center of the beaker followed by 10 seconds of gently swirling. The beaker is then set undisturbed overnight.

After 24 hours, the Pt/CNT@UiO-66 are washed by carefully pipetting the solution and leaving behind the Pt/CNT material stuck to the walls above the solution line, using additional DMF as needed to transfer all of the coated material. The Pt/CNT@UiO-66 is then washed with 5 mL of DMF and centrifuged down at 3300 rpm for 10 minutes. Two additional washes using DI water is also performed. The sample is then allowed to dry under mild heat (70°C) in an oven overnight.

6.3.5 Synthesis of Pt/CNT@UiO-66-4F: Aqueous Method

349.14 mg (0.122 mmol) of zirconyl chloride octahydrate and 3 mL of 3 M acetic acid is added to a 20 mL scintillation vial. In a second glass vial, 261.56 mg (0.110 mmol) of tetrafluoroterephthalic acid and 3 mL of 3 M acetic acid is added. Both two vials are stirred and heated in a 50°C oil-bath for 20 minutes; until the solids dissolve. In a third glass vial, 5 mg of the as-synthesized Pt/CNT and 1 mL of 3 M acetic acid is added followed by sonication on ice for 20 minutes. Immediately following the 20 minutes of sonication, the Pt/CNT solution is vigorously stirred (1000 rpm) for 1 hour at room temperature.

A fourth vial is then pre-heated in the 50°C oil bath. Into this vial, 0.5 mL of the tetrafluoroterephthalic acid solutions and 0.5 mL of the zirconium contain solution is added and stirred at 500 rpm for 1 minute. A resultant white slurry is formed after 1 minutes at 50°C; the seed solution for the following steps. To the Pt/CNT solute, 0.1 mL of the seed solution and is added and stirred for an additional 5 minutes before the final addition of 0.9 mL of 3 M acetic acid is added. The final solution is stirred for 5 minutes

at 500 rpm at room temperature and then left for an additional 3 hours at room temperature, without stirring.

After 3 hours, the Pt/CNT@UiO-66-4F is then washed in a similar fashion as the pre-hydrolyzed sample with the exception that all three washes are performed with water. This sample is then allowed to dry under mild heat (70°C in an oven) to then be used for further experiments.

6.3.6 Characterization

The morphology and coating capabilities were viewed using Transmission electron microscopy (TEM) and scanning electron microscopy (SEM). TEM images were obtained on a JEOL JEM2010F operated at 200 kV. SEM images were obtained on a JEOL JSM6340F. The pore size of all samples were measured by N₂-sorption isotherms on a Micromeritics ASAP 2020. The calculations were based on non-linear density functional theory (NLDFT), Barrett-Joyner-Halenda theory (BJH) and Brunauer-Emmett-Teller theory (BET). The powder x-ray diffraction patterns (pXRD) were collected on a Bruker AXS diffractometer with Cu K α radiation ($\lambda = 1.5418 \text{ \AA}$) in order to test the crystallinity. The content of platinum in samples was measured by inductively coupled plasma- optical emission spectroscopy (ICP-OES, Agilent 7700e). The gas phase reaction was analyzed through mass spectroscopy (MS) using a MKS special V2000P. Electrochemical measurements were performed using a BioLogic VSP potentiostat and ALS, Co. RRDE-3A rotating disk electrode system.

6.3.7 Size-selective Alkene Hydrogenation

The size selective alkene hydrogenations were conducted in a gas phase reactor. Following ICP-OES, several mg of the Pt/CNT and Pt/CNT@UiO-66 synthesized through the traditional method were mixed with ~1 gram of sand to achieve a loading of 1% Pt. This mixture was then carefully transferred to the U-shape reactor with quartz frit. The gas phase system was purged with pure He gas at 100°C for 30 minutes for pretreatment to ensure absorbed water would be driven off. Two alkenes with different sizes were used for reaction in order to determine the capability of the MOF to protect and guard the Pt nanoparticle catalysts. Ethylene was diluted with H₂ gas and He gas; a volume ratio of 1.2 : 12 : 77 ethylene : H₂ : He. This was then used to purge the system and reach and equilibrium as data was collected on the output gas composition and analyzed *via* mass spectroscopy (MS). Data was recorded at both 22 °C and 40 °C with the temperature being controlled by a Carbolite furnace with PID controller (Digi-Sense). The conversion was the percentage of ethylene present at 22°C divided by that at 40°C. Cyclooctene was then bubbled using He gas in order to aerosolize the cyclooctene to then be carried by the gas mixture into the U-tube to undergo reaction. The gas volume ratio was 10 : 10 : 10 of cyclooctene : H₂ : He. The higher flow of He into the cyclooctene was needed due to the general lower activity of cyclooctene hydrogenation and also the fact that it was necessary to bubble the solution to saturate the carrier gas. Temperatures of 50°C and 60°C were used with the output gas composition being analyzed in the same fashion.

6.3.8 ICP-OES

In order to run electrochemical oxygen reduction (ORR), the Pt content of the samples must be known. First, 5 mg of the Pt/CNT sample is massed out in a crucible. This weight is considered the “wet” weight prior to all of the water being driven off. The crucible is then placed in a tube furnace (Lindberg/Blue M TF55030A-1) with the temperature raised to 120 °C at a rate of 5 °C/minute and held at the final temperature for 1 hour. During this process a constant flow of N₂ is run through the tube (2-3 psi). After the hour, the sample is allowed to cool under N₂ flow and then reweighed to obtain the “dry” weight after the complete removal of water. After the weight is obtained, the crucible is placed back in the tube furnace and raised up to 850 °C at a ramp rate of 1 °C/minute and held at 850 °C for 2 hours under a constant flow of air (2-3 psi) in order to dry ash the CNTs.

Once dry ashed, the sample is allowed to cool and be prepped for ICP analysis. 0.3 mL of concentrated hydrochloric acid (HCl) and 0.1 mL concentrate nitric acid (HNO₃) are pipetted into the crucible followed by the slow addition of 0.3 mL 40% hydrogen peroxide (H₂O₂) ensuring the sample does not bubble over during the addition. After the addition, the crucible is placed in a sand bath and heated on medium-low heat until the solution turns orange carefully monitoring the sample to ensure it does not bubble over. The heating was continued until all liquid was evaporated from the crucible. After, 0.976 mL of 6.2 M HCl is added to the crucible and gently heated until all solid dissolves. This liquid is then transferred to a 10 mL volumetric flask. The crucible is then rinsed with additional aliquots of DI water (at least three times) with each aliquot added

to the 10 mL volumetric. Once the crucible has been rinsed three times, the volumetric flask is brought to the correct volume with the DI water to then be used for ICP-OES analysis of the Pt content. All ICP standards were obtained from Inorganic Ventures.

6.3.9 Electrochemical Measurements

The oxygen reduction reaction (ORR) was conducted over Pt/CNT and Pt/CNT@UiO-66 on a rotating disk electrode (RDE) in HClO₄ electrolyte. A three electrode system was used: the working electrode was a glass carbon rotating disk electrode (diameter of 5 mm and a surface area of 0.19635 cm²) with catalyst ink, the counter electrode was a graphite rod, and the reference electrode was a standard hydrogen electrode. To prep the working electrode, it was first polished with 0.5 μm alumina powder followed by rinsing with DI water.

To form the catalyst ink, the Pt content was first found using ICP-OES with the ink preparation all based on the loading of Pt in order to obtain a loading of 3.92649 μg Pt / 10 μL of ink solution. The proper amount of sample was added to a vial followed by a solution ratio of 8 : 3.16 : 0.05 of DI water : isopropanol : Nafion followed by sonication for 30 seconds and vigorous stirring for two days.

Once the ink solution was made (used within one week), 10 μL of the ink was drop casted on a clean RDE and rotated at 500 r.p.m. for 5 minutes to initiate drying followed by an increase in a rotation rate of 200 r.p.m. every 2 minutes until a speed of 1500 r.p.m was reached. As an activation step, the dried ink was then dropped with 10 μL of methanol-containing water (50%) followed by rotation at 1500 r.p.m to ensure electrolyte penetration during cycling.

The RDE was then immersed in 0.1 M HClO₄ and continuously purged with N₂ for 20 minutes through a fritted adapter. The following electrochemical experiments were conducted in O₂ (or N₂) saturated HClO₄ electrolyte with a constant flow of O₂ (or N₂). The working electrode was first stabilized by cyclic voltammetry (CV) at a scan rate of 500 mV/s from 1.2 V to 0.0 V for 150 cycles with a rotation speed of 2500 r.p.m. Followed by a second set of CV scans (without rotation) at a rate of 20 mV/s from 1.0V to 0.015V for 3 cycles under N₂. These scans were used as blank scans to achieve the electrochemically active surface area (ECSA). After obtaining the ECSA, linear sweep voltammetry (LSV) was performed scanning 10 mV/s from 1.0V to 0.0V (rotation of 1600 r.p.m. under a N₂ atmosphere) to measure the baseline limiting current density of the sample.

After the measurement of ECSA and baseline limiting current density under a N₂ saturated environment, the electrolyte was purged with O₂ for 20 minutes, followed by stabilization at a scan rate of 50 mV/s from 1.2 V to 0.05 V for 10 cycles at a rotation speed of 1600 r.p.m. LSV scans were then performed at a scan rate of 10 mV/s from 1.0 V to 0.0 V to measure the limiting current density at the same 1600 r.p.m.

For extended stabilization test, an accelerated aging process was utilized; CV scans, in a narrowed scan window of 0.6 V to 1.0 V at a scan rate of 100 mV/s were performed for 5000 cycles under a N₂ atmosphere with no rotation. After the accelerated aging process, all procedures mentioned above were conducted again under their same conditions.

The ECSA, specific activity surface area (SA), mass activity surface area (MA), limiting current density and half-wave potentials were calculated from the above results.

The calculation of ECSA was done by integration of the area belonging to adsorption of H₂ and further transformation with following equation:

$$\text{ECSA (cm}^2\text{g}^{-1}\text{)} = Q_{int} \div 0.21, Q_{int}(\text{mC}) = \text{Area} \div 0.02\text{Vs}^{-1}$$

Where the area is the integration. MA is calculated based on the LSV using the following equation:

$$\frac{1}{j} = \frac{1}{j_k} + \frac{1}{j_d}$$

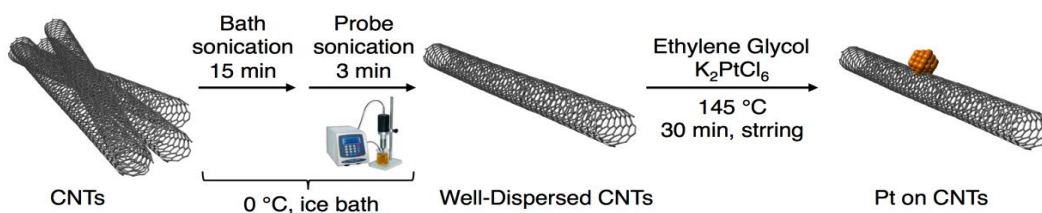
Where j is the current density at 0.9 V, j_k is the kinetic current density and j_d is limiting current density. SA is calculated by dividing MA with ECSA. The half-wave potential is the potential at which the current decreases to half of limit current density.

6.4 Results and Discussion

6.4.1 Synthesis and TEM Characterization of Pt Nanoparticles Deposited on Carbon Nanotubes

To produce the Pt decorated carbon nanotubes (CNTs), an ethylene glycol synthesis was used. Carbon nanotubes were distributed in a solution of ethylene glycol through sonication. Potassium tetrachloroplatinate, the Pt²⁺ precursor, were reduced into small Pt nanoparticles that were deposited on the carbon nanotubes in a uniform fashion, as shown in Scheme 6.1. During the synthesis, the ethylene glycol acted as both solvent and reducing agent during the heating process. Figure 6.1a shows representative

transmission electron microscopy (TEM) images showing the small uniform Pt nanoparticles (small dark dots) deposited on the CNTs (lighter, tubed material). To study the uniformity of the synthesis method, a size distribution count of the Pt/CNT nanoparticle size was taken. The average particle size, as seen in Figure 6.1b, was 3.7 nm (100 separate nanoparticles were measured) and the size distribution showed the uniformity of Pt nanoparticles reduced by ethylene glycol on the length of the CNTs rather than clusters.



Scheme 6.1: General schematic representation of the Pt/CNT synthesis method

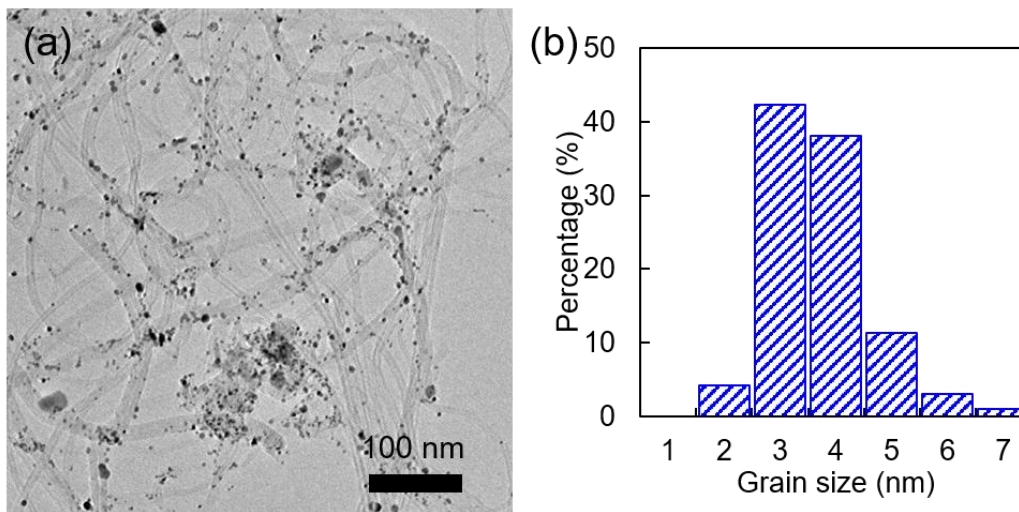
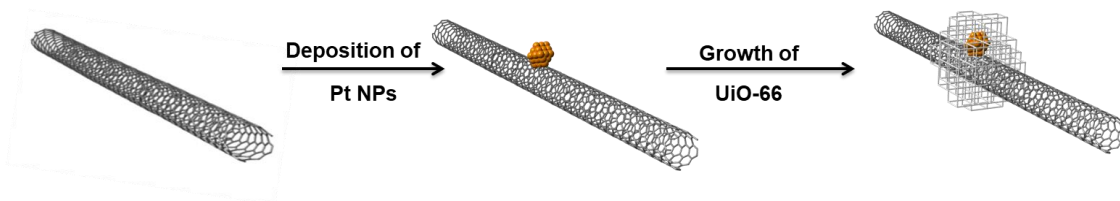


Figure 6.1: (a) Transmission electron microscopy images of the as-synthesized Pt/CNTs and (b) the corresponding size count and distribution showing an average grain size of 3.7 nm with a tight size dispersity.

6.4.2 Synthesis and Characterization of UiO-66 Coated Pt Nanoparticles Deposited on Carbon Nanotubes

With successful formation of dispersed Pt/CNT samples, three different UiO-66 coating methods were used to for the Pt/CNT@UiO-66 composite: first, a pre-hydrolysis method which mitigated the need for strong acids, second, a water-phase method which produced the MOF quickly to coat the exposed Pt particles, and third, a traditional method with high selectivity of MOF formation on just the Pt particle surface. Each method produced different materials with their own advantages and drawbacks. A general synthesis scheme can be seen in Scheme 6.2 where each coating method produces the end caged structure.



Scheme 6.2: General schematic representation of the composite Pt/CNT@UiO-66 material

First, the pre-hydrolysis method was used. In this method, the zirconium node MOF building block was pre-synthesized prior to use in the coating step. By pre-forming the nodes, a weaker acid (acetic acid) could be used as well as a much lower synthesis temperature. During MOF formation, the hindering step that requires the higher synthesis temperatures is the node formation, not the node and organic linker coordination. During this synthesis, the nodes were pre-formed at 140 °C in a solution containing acetic acid,

DMF, and zirconium propoxide. The additional benefit of this method is by no longer needing strong acids (HCl) there was also a reduction in the Cl^- concentration in the Pt/CNT and MOF growth solution. Cl^- ions are known to easily stabilize Pt when in solution which can cause problems with Pt leaching from the NP surface and thus a reduction in the Pt content pre and post MOF coating. With this method, because the nodes are pre-synthesized, during the coating method both room temperature and $50\text{ }^\circ\text{C}$ were used. With room temperature, the MOF forms more slowly and has a tendency to aggregate together rather than coat the NP surface, as seen in Figure 6.2a. Similarly, the process was run at $50\text{ }^\circ\text{C}$ where the MOF grew more rapidly and coated the particle surfaces more evenly (Figure 6.2b). Unfortunately with this method, due to the modulator free environment, the MOF material was less crystalline and ordered and grew rapidly adhering to both the nanoparticle surface as well as the CNTs with free MOF in the solution

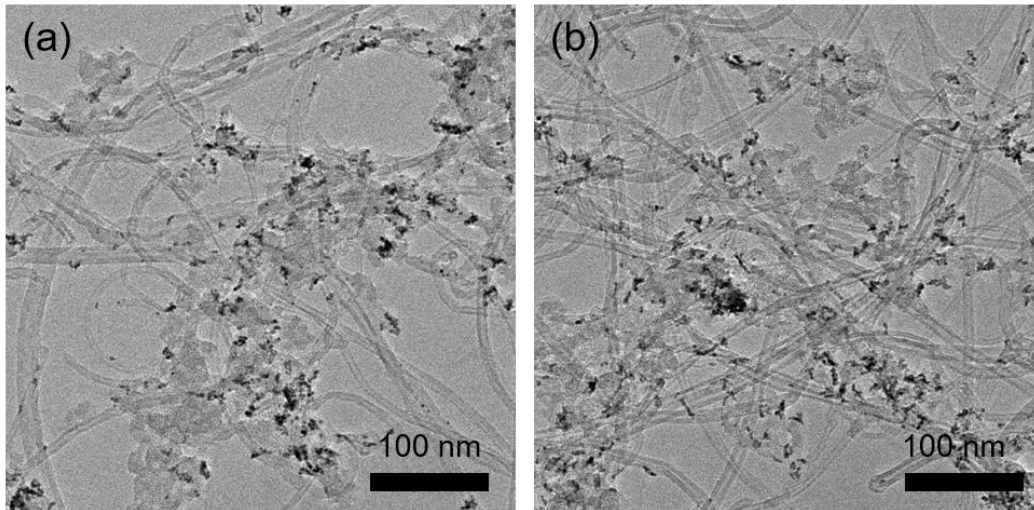


Figure 6.2: TEM images of the Pt/CNT@UiO-66 formed through the pre-hydrolysis method at (a) room temperature and (b) 50 °C with the MOF material being the lighter disorganized material

To try and obtain a better more selective UiO-66 coating on the Pt surface, an aqueous synthesis route was performed. For this method, switching from DMF, also a known stabilizer of Pt, to acetic acid, the hope was to be able to perform the coating with more selectivity due to the use of modulator in the solvent as well as reduce the interaction between the Pt and a stabilizer that allowed for it to leach. During this synthesis, tetrafluoroterephthalic acid replaced the non-functionalized terephthalic acid from the previous synthesis. The metal precursor and ligands were both added to acetic acid solutions followed by addition into the Pt/CNT material. During this synthesis, the acetic acid in solution acts a growth modulator and slows down the formation of the UiO-66-4F. TEM images of the sample as synthesise can be seen in Figure 6.3a-d.

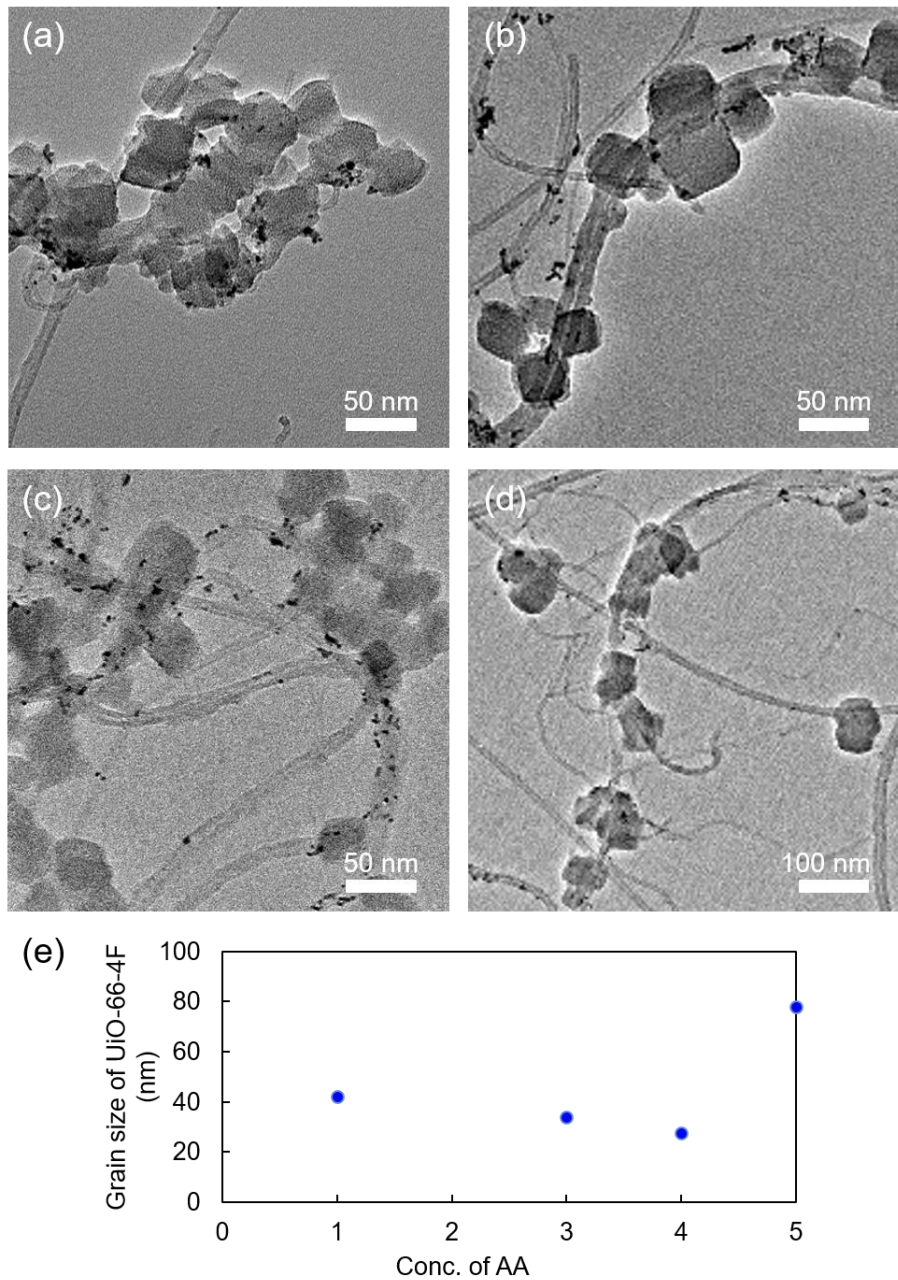


Figure 6.3: TEM images of Pt/CNT@UiO-66-4F synthesized using acetic acid solutions of different concentrations (a) 1 M, (b) 3 M, (c) 4 M, (d) 5 M. The higher the concentration the slower the UiO-66-4F forms and larger the grain size (e).

During the synthesis, different concentrations of acetic acid solutions were used to alter the growth kinetics of the MOF. The lower the concentration of acetic acid, the quicker the MOF can form; the higher the acetic acid concentration the slower the MOF forms. This can be seen in Figure 6.3e when looking at the average grain size of the UiO-66-4F particles after coating. During this synthesis, though we had more control over thickness and growth rate, the TEM images clearly show that there is still a relative lack in selectivity and also several areas that are not coated in UiO-66-4F and that several of the Pt NPs detached from the CNTs, most likely due to the high concentration of acetic acid used. Out of all of the samples, the 3 M acetic acid solution showed the most promise and was carried forward.

Finally, a more traditional UiO-66 coating method was chosen (i.e. HCl modulator and DMF organic solvent). During this method, the Pt/CNT was incorporated into a traditional UiO-66 synthesis with zirconium precursor and terephthalic acid with DMF solvent and HCl modulator at 150 °C. Initially, there was concern with using both HCl and DMF which both stabilize Pt as well as using such a high temperature during synthesis which could increase the chance of detachment and aggregation of the Pt particles. From Figure 6.4 however, the TEM images show high coverage of the Pt NPs and selective growth on the NPs compared to the CNT. We attribute this selectivity due to the difference in the Pt and CNT surface; Pt is relatively hydrophilic due to the adsorbed hydroxyl groups which attract and stabilize the Zr promoting growth on the particle surface, whereas the CNT is very hydrophobic and does not.

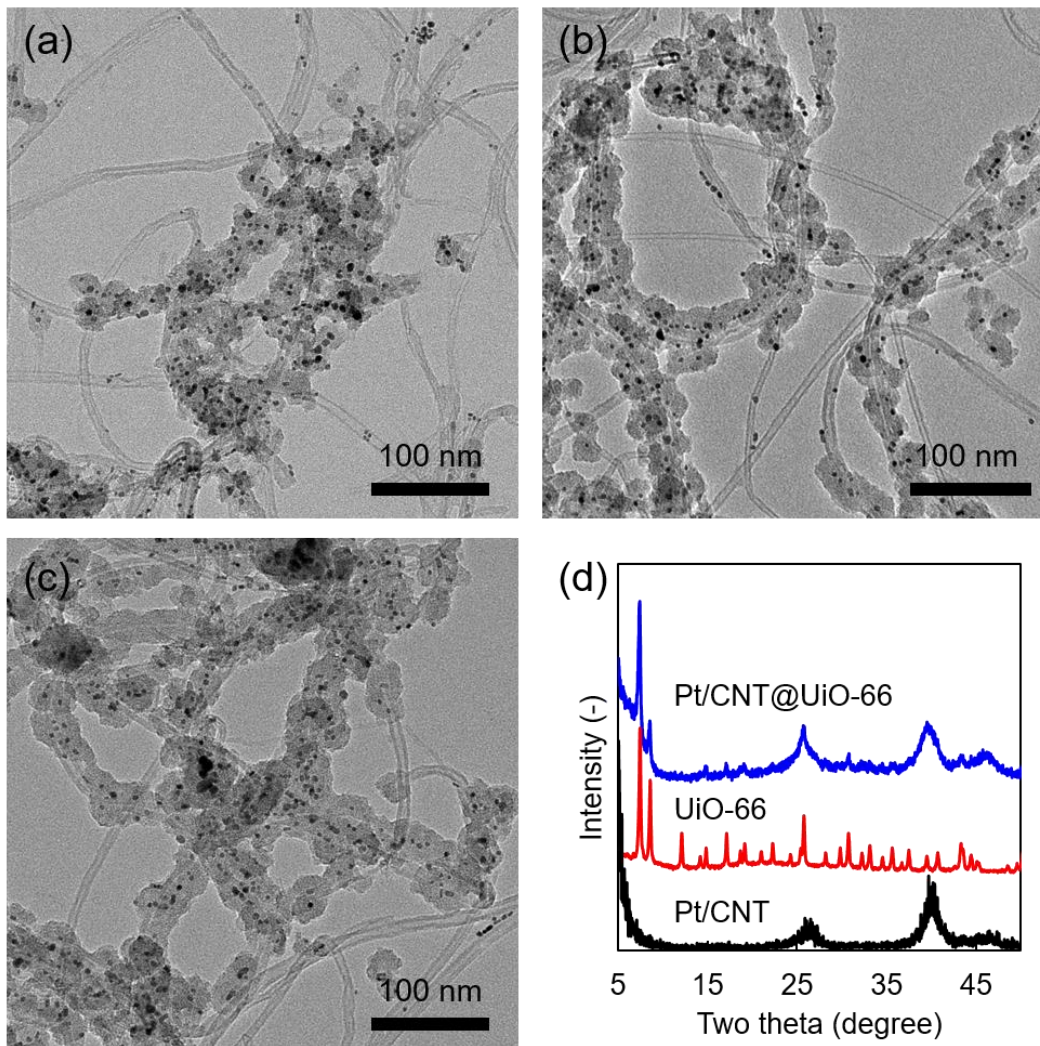


Figure 6.4: TEM images of the Pt/CNT@UiO-66 composite using the traditional synthesis method with differing concentrations of MOF precursors (a) 40 μmol , (b) 65 μmol , and (c) 95 μmol of terephthalic acid and ZrOCl_2 were used for synthesis. (d) x-ray diffraction pattern of Pt/CNT as-synthesized, pristine UiO-66, and the 65 μmol synthesized Pt/CNT@UiO-66 sample

For the traditional synthesis, the precursor concentration was changed in order to see the effect on Pt coverage. In Figure 6.4a, with the lowest concentration of precursors, several of the Pt particles detached from the CNTs due to the stabilizing species in the

bulk solution and the slow growth rate of the UiO-66. In Figure 6.4b 65 μmol of precursors was used. Better coverage was seen with less Pt NP detachment, but Figure 6.4c shows the fullest coverage, including areas that do not have Pt NPs deposited on them. Powder x-ray diffraction was run on the 65 μmol precursor sample (Figure 6.4d) where the diffraction peak at 26.74° is attributed to the (002) phase of CNT and that at 39.8° to the (111) phase of Pt nanoparticles. The two sharp diffraction peaks located in the lower angle region (below 10°) indicated the crystallized UiO-66 on Pt/CNT.

During the coating process, Pt leaching and detachment is a concern (Figure 6.5). During the synthesis, if Pt leaches into the solution, the precious metal is lost and is no longer available for catalysis. Similarly, Pt detachment from the CNT surface is also detrimental. During electrochemical measurements, if the Pt catalyst particle is not in contact with the conductive support, the activity will decrease (the MOF is not conductive). During the synthesis conditions, the goal is to decrease Pt percentage loss. To study the amount lost due to leaching, inductively coupled plasma-optical emission spectroscopy (ICP-OES) is performed before and after coating on the same batch of Pt/CNT particles as used to coat. From this, we are able to determine the amount of Pt lost during the synthesis conditions due to leaching and etching. Results of the ICP-OES, after the dry ashing method, can be seen in Table 6.1 from all coating methods. Generally, leaching can range from 9% loss to 55% loss depending on the synthesis method chosen and how hard the synthesis conditions were. From Table 6.1, the traditional coating method garners the best results for the least amount of Pt lost. It is also easy to see that with the addition on higher concentration of the precursors for UiO-66 the amount of MOF present also increases. This was done by looking at the Zr present in

the ICP-OES result, and converting to determine the number of Zr nodes present (since the nodes are formed from metal-oxide Zr_6 species).

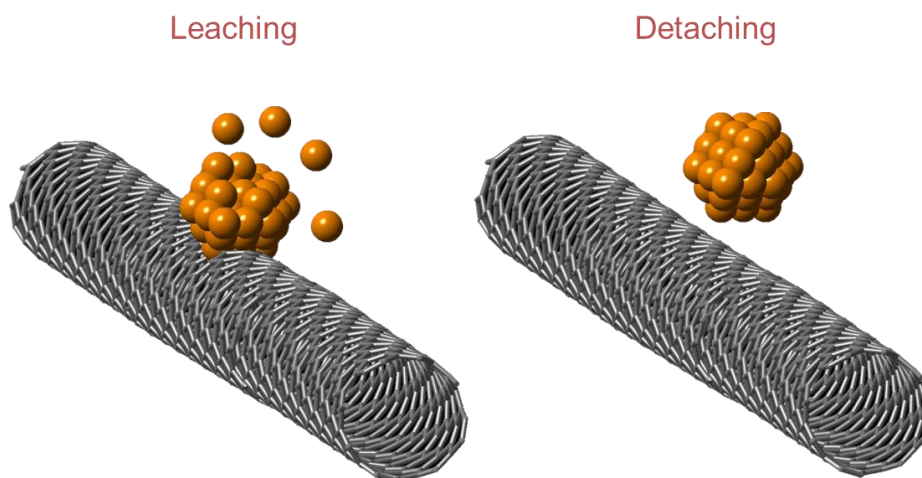


Figure 6.5: Representation of Pt NP (orange) leaching into solution or detachment from the CNT (black).

Coating Process		Content (%)			Pt loss (%)	
		CNT	Pt	UiO-66		
Pre-hydrolysis		67.6	10	22.4	22	
Water-phase		42.42	3.12	54.46	56	
Traditional	Precursor (μmol)	40	61.8	9.6	28.6	20
		65	50.8	9.4	39.8	8
		95	46.3	9	44.7	4

Table 6.1: ICP-OES results showing the extent of Pt loss due to leaching and etching during the different MOF coating methods

6.4.3 Size Selective Alkene Hydrogenations of Ethylene and Cyclooctene

With several tested coating methods analyzed through TEM, XRD, and ICP-OES, size selective alkene hydrogenations were used to determine the UiO-66 ability to fully/mostly encapsulate the Pt NPs decorated on the CNTs. This was run in order to determine whether the MOF material would be able to protect the Pt surface from large or bulky species that can poison and deactivate the NP surface during reactions, in particular, protect the Pt surface from the sulfonate groups used in Nafion polymer. If the surfaces are not protected, show a high degree of activity for both small (ethylene) and large (cyclooctene) alkenes, then the Pt surface is able to interact and deactivate from the sulfonate contact. If there is high ethylene conversion, but very low to no cyclooctene conversion, the particle surface is protected but still available to perform catalysis.

For this reaction, ethylene (kinetic diameter of 2.5 Å) and cyclooctene (kinetic diameter of 5.5 Å) are used due to the aperture size of UiO-66 (5.0 Å) being larger than the size of ethylene yet smaller than that of cyclooctene. Due to the differences in size and aperture size, the ethylene should be able to pass through the Pt/CNT@UiO-66 and interact with the Pt NPs to produce ethane. In comparison, the cyclooctene, if the UiO-66 is indeed covering the Pt NPs, is too large to pass through to interact with the Pt surface therefore not producing cyclooctane. The selective hydrogenations were run to determine the conversion over Pt/CNT as a control (would be able to hydrogenate both the ethylene and cyclooctene) as well as the Pt/CNT@UiO-66 using the traditional coating method. The conversions can be seen in Figure 6.6 and Table 6.2. From the data, the hydrogenation conversion of ethylene to ethane is comparable over both samples

demonstrating the ability of the coated Pt particles to still be highly active catalysts. When looking at the conversion of cyclooctene however, a difference in their activities is observed. For the Pt/CNT sample, the cyclooctene is freely able to come in contact with the catalyst surface in turn producing cyclooctane. For the Pt/CNT@UiO-66 sample, a size selective sieving effect is observed; the UiO-66 shelters the Pt surface. With the sheltering effect, the Pt particle is completely separated from coming into contact with the larger species showing the UiO-66 ability to keep harmful species from deactivating the surface.

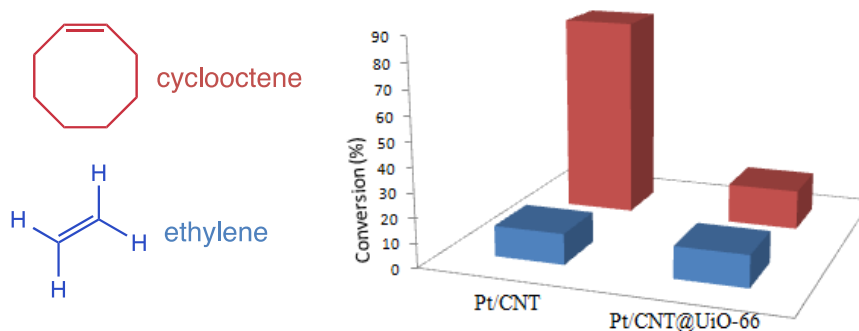


Figure 6.6: Size selective hydrogenation of the Pt/CNT and Pt/CNT@UiO-66 samples for ethylene and cyclooctane hydrogenation. Ethylene runs at 22 °C while cyclooctene is run at 50 °C. The lack in conversion for the Pt/CNT@UiO-66 is due to the size difference between the aperture of UiO-66 and cyclooctene

Conversion (%)	Ethylene (22 °C)	Cyclooctene (50 °C)
Pt/CNT	12.6	82.7
Pt/CNT@UiO-66	13.0	16.4

Table 6.2: Size selective hydrogenation data showing conversion percentage of ethylene to ethane and cyclooctene to cyclooctane over Pt/CNT and Pt/CNT@UiO-66 to show the selective protection of the MOF coating.

6.4.4 Electrochemically Active Surface Area Measurement for Pt Detachment

As mention previously, two major issues with the Pt/CNT@UiO-66 samples are the leaching of Pt species before and after MOF coating, solved by determining the best coating method that provides the least leaching, and that of Pt NP detachment from the conductive CNT support (Figure 6.5). With the size selective hydrogenations, we are able to determine that the Pt surface is an active catalyst even with the MOF coating and is able to selectively keep out larger species, however the issue of detachment is not probed. For these catalyst to be further used in electrochemical measurements, the NP needs to remain in contact with the conductive support, otherwise due to the non-conductive nature of UiO-66, the reaction will not proceed due to lack in electron transfer.

To probe the interaction of the Pt NP with the CNT support before and after UiO-66 coating, measurements of the electrochemically active surface area (ECSA) were performed. The adsorption of hydrogen was used to determine the ECSA in samples with differing amounts of UiO-66 precursors added, following the traditional coating method, and compared to the Pt/CNT (considered 0 μmol of UiO-66). In Figure 6.7, the plotted

data of the ECSA can be seen. From the chart, there is not a large difference in the ECSA for the Pt/CNT and the Pt/CNT@UiO-66 samples. This indicates that the coating method used does not generate significant particle detachment from the CNT surface and the electron transfer from CNT to Pt occurs and there is not a significant deactivation of the catalyst after MOF coating.

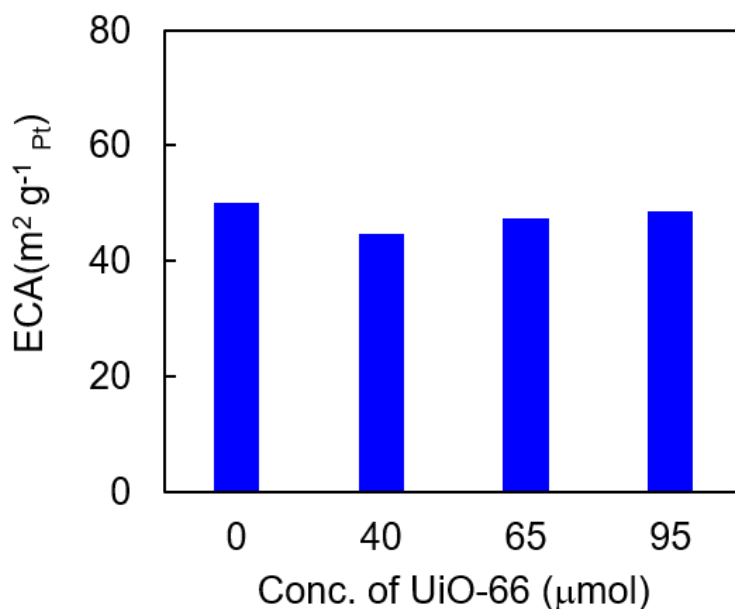


Figure 6.7: Summary of the electrochemically active surface areas (ECSA) for the Pt/CNT sample with no added UiO-66 precursors and increasing amounts of added MOF precursors.

6.4.5 Electrochemical Oxygen Reduction Reaction using a Rotating Ring Electrode System

Having decreased the loss of Pt after coating, determining the selectivity of the majority of the Pt NPs deposited on the CNTs being covered by the UiO-66 and the

relatively low loss in ECSA, electrochemically oxygen reduction was performed using a rotating disk electrode (RDE). For several types of fuel cells, PEMFCs included, the sluggish cathodic ORR is an area in need of improvement. Due to the use of Nafion in several fuel cells, the Pt catalyst can easily be poisoned from the sulfonate functional groups off of the ionomer. Below, in Figure 6.8, the overall catalyst is modeled.

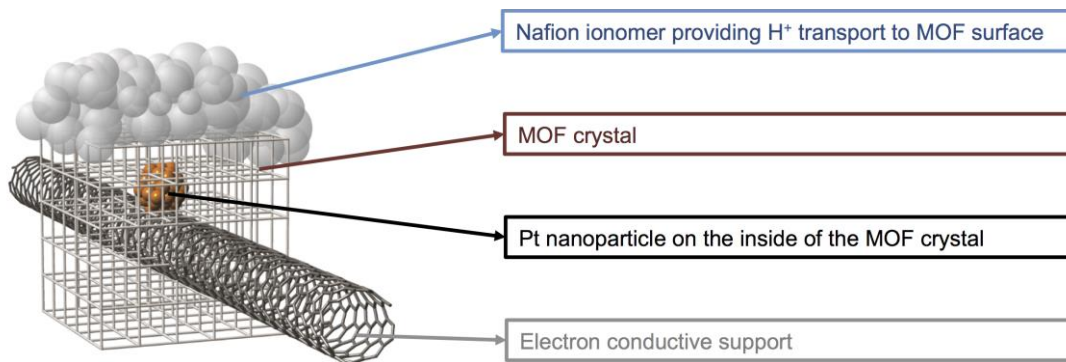


Figure 6.8: Model of the ORR catalyst formed from the Pt/CNT@UiO-66 samples and their corresponding roles. CNTs for electron conductivity to the Pt NPs catalyst, which are then coated in the protective MOF crystal and capped in the common fuel cell ionomer to promote proton transport, Nafion.

We applied both the Pt/CNT and Pt/CNT@UiO-66 catalysts to perform ORR in a three electrode system as seen in Figure 6.9, to demonstrate the protective capabilities of UiO-66 to the Pt NPs to avoid poisoning from the Nafion ionomer. The ECSA, mass active surface area (MA), specific surface area (SA), limiting current density (LC), and the half-wave potential ($E_{1/2}$) were all determined and compared before and after an accelerated aging process (5000 cycles) used to represent working fuel cell conditions. The loss in each was then calculated to determine catalyst stability and effect of the UiO-66 coating. Figure 6.10 represents the results obtained from the ORR experiments before

and after aging and how each value changed over time. With Table 6.3 summarizing the initial and end of life (EOL) values for each area studied, along with the percentage of lost activity.

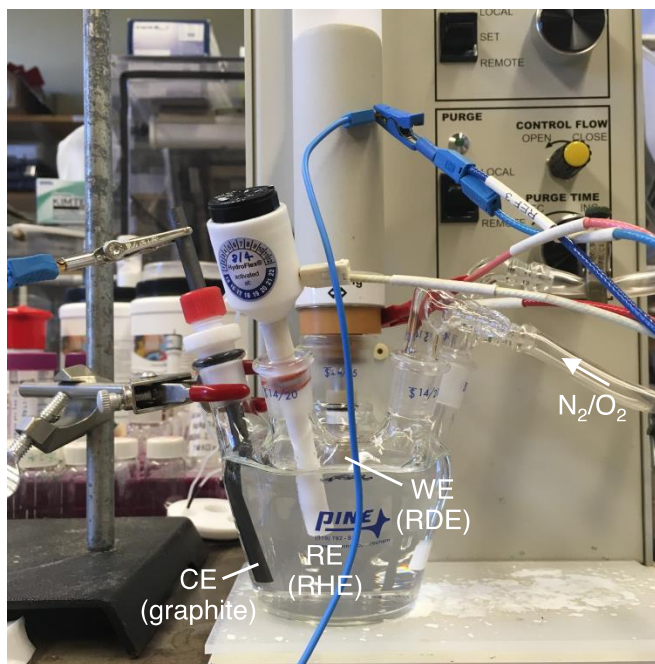


Figure 6.9: ORR three electrode electrochemical cell system. Counter electrode of a graphite rod, the working electrode is a glassy carbon rotating disk electrode, and the reference electrode is a standard hydrogen electrode. Also noted in the photograph is the inlet for the N_2 and O_2 purging and constant bubbling through a porous frit.

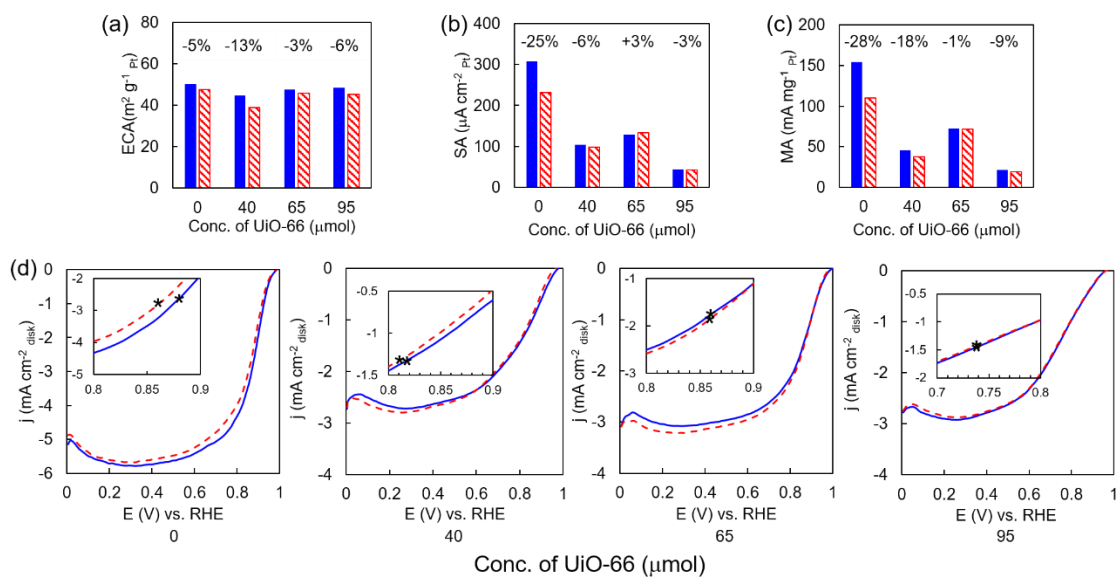


Figure 6.10: Summary and comparison the ORR results for the Pt/CNT and Pt/CNT@UiO-66 samples of various precursor concentrations before and after aging: (a) ECSA values, (b) SA values, (c) MA values, (d) the LC and $E_{1/2}$. All initial values are represented in blue and after accelerated aging in red (represent the end of life (EOL)) values. The black star indicates the $E_{1/2}$ values.

		ECA (m ² g ⁻¹)	SA (mA cm ⁻²)	MA (mA mg ⁻¹)	LC (mA cm ⁻²)	E _{1/2} (V)
Pt/CNT	Initial	50.1	307.3	154.1	-5.85	0.875
	Aging	47.6	231.1	110.0	-5.73	0.862
	% Lost	-5.0	-24.8	-28.5	-2.1	-1.5
PT/CNT@UiO-66 (40 μmol)	Initial	44.6	103.3	46.1	-2.77	0.819
	Aging	38.8	97.4	37.8	-2.85	0.810
	% Lost	-13.0	-5.7	-17.9	+3.0	-1.1
PT/CNT@UiO-66 (65 μmol)	Initial	47.4	129.4	72.2	-3.12	0.860
	Aging	45.8	132.9	71.6	-3.26	0.858
	% Lost	-3.3	+2.6	-0.8	+4.4	-0.2
PT/CNT@UiO-66 (95 μmol)	Initial	48.5	43.7	21.2	-2.97	0.740
	Aging	45.4	42.5	19.3	-2.91	0.740
	% Lost	-6.2	-2.9	-8.9	-1.9	0

Table 6.3: Summary of the ORR data initially and after end of life (EOL) aging

From the data in Figure 6.9 and that in Table 6.3, an increased stability and protection from deactivation in the samples containing a coating of UiO-66 observed; however, though there is an increased stability observed, the overall performance was hindered due to the incorporation of non-conductive UiO-66. Looking at the ECSA value, those with the MOF coating remain similar to the un-coated Pt/CNTs indicating a good connection between the Pt and the CNT with the traditional method used. These ECSA values also help in determining the lowered activity when compared to Pt/CNT comes from the non-conductive nature of the UiO-66, not detachment. For the SA, MA, LC and E_{1/2} values, the % lost after end of life studies was drastically lower. Similarly, ORR studies were performed on the samples synthesized through the pre-hydrolysis and aqueous methods, however due to a large drop in the ECSA before and after MOF

coating, these samples were deemed not suitable because of the disadvantage of Pt NP detachment.

With the initial and EOL studies, a very important value is the half-wave potential, $E_{1/2}$, when determining the stability. In an ideal situation, the $E_{1/2}$ value would remain consistent from beginning to end. For the Pt/CNT non coated samples, there was a shift of -20 mV throughout the reaction showing a decrease stability. In comparison, the samples coated in the differing concentration of UiO-66 had a shift of -14 mV for the lowest concentration to 0 mV for the highest concentration (though this sample also showed the lowed SA and MA from the thick MOF layer). These results indicate a much higher catalyst stability primarily due to a separation of the Nafion ionomer from the Pt surface and further helped by a decrease in Pt NP aggregation by being immobilized by the MOF coating (Figure 6.11a Pt/CNT and b Pt/CNT@UiO-66 after reaction).

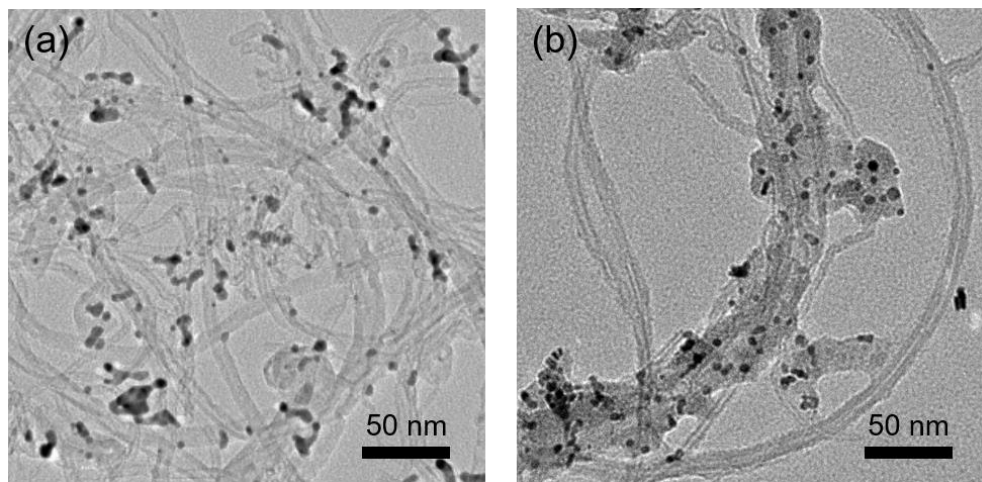


Figure 6.11: TEM images of (a) Pt/CNT and (b) Pt/CNT@UiO-66 with (65 μmol) after the EOL accelerated aging process

6.5 Conclusion

We have demonstrated the ability to deposit Pt NPs of 3.7 nm evenly over CNTs followed by the directed growth of MOF, in particular UiO-66, selectively on the Pt particles. Three different coating methods were realized; a pre-hydrolysis of the Zr nodes method, an aqueous phase synthesis in acetic acid solvent, and a more traditional organic phase synthesis method. From these methods, that of the traditional organic synthesis showed a more selective growth and covering of the Pt NPs while maintaining a clean CNT surface. The samples were then tested through ICP-OES to see how much Pt was lost before and after coating. The traditional method was deemed the most successful and carried through size-selective alkene hydrogenations to ensure full Pt coverage. Similarly, ECSA values were obtained to ensure NP detachment would not be a major problem with the electrochemical studies and electron transport would still be successful. Electrochemical ORR studies were performed to study the stability before and after accelerated aging (representative of working fuel cell conditions). The Pt/CNT showed poor stability through poisoning from Nafion sulfonate groups as well as aggregation of the Pt particles whereas the UiO-66 coated sample had increased stability, indicating the MOFs ability to protect the Pt particles and effectively improve the cathodic reaction stability. The ECSA, MA, SA, LC, and $E_{1/2}$ values were all considered.

6.6 References

- [1.] Wang, Y.; Chen, C.S.; Mishler, J.; Cho, S.C.; Adroher, X.C., A Review of Polymer Electrolyte Membrane Fuel Cells: Technology, Applications, and Needs on Fundamental Research, *Appl. Energy*, **2011**, *88*, 981-1007
- [2.] Sharma, S.; Pollet, B.G., Support Materials for PEMFC and DMFC Electrocatalysts – A Review, *J. Power Sources*, **2012**, *208*, 96-119
- [3.] Kamat, P.V., Meeting the Clean Energy Demand: Nanostructure Architectures for Solar Energy Conversion, *J. Phys. Chem. C.*, **2007**, *111*, 2834-2860
- [4.] Mehta, V.; Cooper, J.S, Review and Analysis of PEM Fuel Cell Design and Manufacturing, *J. Power Sources*, **2003**, *114*, 32-53
- [5.] Kreuer, K.D., On the Development of Proton Conducting Polymer Membranes for Hydrogen and Methanol Fuel Cells, *J. Memb. Sci.*, **2001**, *185*, 29-39
- [6.] Lipman, T.E.; Edwards, J.L.; Kammen, D.M., Fuel Cell System Economics: Comparing the Costs of Generating Power with Stationary and Motor Vehicle PEM Fuel Cell Systems, *Energy Policy*, **2004**, *32*, 101-125
- [7.] Subbaraman, R.; Strmcnik, D.; Paulikas, A.P.; Stamenkovic, V.R.; Markovic, N.M., Oxygen Reduction Reaction at Three-Phase Interfaces, *ChemPhysChem*, **2010**, *11*, 2825
- [8.] Shi, W.; Yi, B.; Hou, M.; Jing, F.; Ming, P., Hydrogen Sulfide Poisoning and Recovery of PEMFC Pt-Anodes, *J. Power Sources*, **2007**, *165*, 814-818
- [9.] Postole, G.; Auroux, A., The Poisoning Level of Pt/C Catalysts used in PEM Fuel Cells by the Hydrogen Feed Gas Impurities: The Bonding Strength, *Int. J. Hydrog. Energy*, **2011**, *36*, 6817-6825
- [10.] Yu, X.; Ye, S., Recent Advances in Activity and Durability Enhancement of Pt/C Catalytic Cathode in PEMFC Part II: Degradation Mechanism and Durability Enhancement of Carbon Supported Platinum Catalyst, *J. Power Sources*, **2007**, *172*, 145-154
- [11.] Gruver, G.A.; Pascoe, R.F.; Kunz, H.R., Surface Area Loss of Platinum Supported on Carbon in Phosphoric Acid Electrolyte, *J. Electrochem. Soc.* **1980**, *127*, 1219-1224
- [12.] Chen, Y.; Ji, S.; Wang, Y.; Dong, J.; Chen, W.; Li, Z.; Shen, R.; Zheng, L.; Zhuang, Z.; Wang, D.; Li, Y., Single Iron Atom Anchored on N-Doped Porous Carbon as an Electrocatalyst for the Oxygen Reduction Reaction, *Angew. Chem. Int. Ed. Engl.*, **2017**, *56*, 6937-6941

- [13.] Yin, P.; Yao, T.; Wu, Y.; Zheng, L.; Lin, Y.; Liu, W.; Ju, H.; Zhu, J.; Hong, X.; Deng, Z.; Zhou, G.; Wei, S.; Li, Y., Single Cobalt Atoms with Precise N-Coordination as Superior Oxygen Reduction Reaction Catalysts, *Angew. Chem. Int. Ed. Engl.*, **2016**, *55*, 10800-10805
- [14.] Stamenkovic, V.R.; Fowler, B.; Mun, B.S.; Wang, G.; Ross, P.N.; Lucas, C.A.; Markovic, N.M., Activity on Pt₃Ni(111) via Increased Surface Site Availability, *Science*, **2007**, *315*, 493-497
- [15.] Prabhudev, S.; Bugnet, M.; Bock, C.; Botton, G., Strained Lattice with Persistent Atomic Order in Pt₃Fe₂ Intermetallic Core-Shell Nanocatalysts, *ACS Nano*, **2013**, *7*, 6103-6110
- [16.] Banham, D.; Ye, S.; Pei, K.; Ozaki, J.; Kishimoto, T.; Imashiro, Y., A Review of the Stability and Durability of Non-Precious Metal Catalysts for the Oxygen Reduction Reaction in Proton Exchange Membrane Fuel Cells, *J. Power Sources*, **2015**, *285*, 334-348
- [17.] Chen, Z.; Higgins, D.; Yu, A.; Zhang, L.; Zhang, J., A Review on Non-Precious Metal Electrocatalysts for PEM Fuel Cells, *Energy Environ. Sci.*, **2011**, *4*, 3167-3192
- [18.] Sun, H.Z.; Tang, B.B.; Wu, P.Y., Rational Design of S-Uio-66@GO Hybrid Nanosheets for Proton Exchange Membranes with Significantly Enhanced Transport Performance, *ACS Appl. Mater. Inter.*, **2017**, *9*, 26077-26087
- [19.] Kraysberg, A.; Ein-Eli, Y., Review of Advanced Materials for Proton Exchange Membrane Fuel Cells, *Energy Fuels*, **2014**, *28*, 7303-7330
- [20.] Lui, L.; Chen, W.; Li, Y., An Overview of the Proton Conductivity of Nafion Membranes through a Statistical Analysis, *J. Memb. Sci.*, **2016**, *504*, 1-9
- [21.] Curnick, O.J.; Mendes, P.M.; Pollet, B.G., Enhanced Durability of a Pt/C Electrocatalyst Derived from Nafion-Stabilized Colloidal Platinum Nanoparticles, *Electrochem. Commun.* **2010**, *12*, 1017-1020
- [22.] Zhang, Q.; Lee, I.; Ge, J.; Zaera, F.; Yin, Y., Surface-Protected Etching of Mesoporous Oxide Shells for the Stabilization of Metal Nanocrystals, *Adv. Funct. Mater.* **2010**, *20*, 2201-2214
- [23.] Luo, Y.; Calvillo, L.; Daignebonne, C.; Daletou, M.K.; Granozzi, G.; Alonso-Vante, N., A Highly Efficient and Stable Oxygen Reduction Reaction on Pt/CeO_x/C Electrocatalyst Obtained via a Sacrificial Precursor Based on a Metal-Organic Framework, *Appl. Catal. B. Environ.*, **2016**, *189*, 39-50

- [24.] Furukawa, H.; Cordova, K.E.; O’Keeffe, M.; Yaghi, O.M., The Chemistry and Applications of Metal-Organic Frameworks, *Science*, **2013**, *341*, 974, 1230444-1 – 1230444-12
- [25.] Tranchemontagne, D.J.; Mendoza-Cortes, J.L.; O’Keeffe M.; Yaghi, O.M., Secondary Building Units, Nets, and Bonding in the Chemistry of Metal-Organic Frameworks, *Chem. Soc. Rev.*, **2009**, *38*, 1257-1283
- [26.] Eddaoudi, M.; Moler, D. B.; Li, H.; Chen, B.; Reineke, T. M.; O’Keeffe, M.; Yaghi, O. M., Modular Chemistry: Secondary Building Units as a Basis for the Design of Highly Porous and Robust Metal-Organic Carboxylate Frameworks, *Acc. Chem. Res.* **2001**, *34*, 319-330
- [27.] Li, H.; Eddaoudi, M.; O’Keeffe, M.; Yaghi, O. M., Design and Synthesis of an Exceptionally Stable and Highly Porous Metal-Organic Framework, *Nature* **1999**, *402*, 276-279
- [28.] Furukawa, H.; Ko, N.; Go, Y.B.; Aratani, N.; Choi, S.B.; Choi, E.; Yazaydin, A.O.; Snurr, R.Q.; O’Keeffe, M.; Kim, J.; Yaghi, O.M.; Ultrahigh Porosity in Metal-Organic Frameworks, *Science*, **2010**, *329*, 424-428
- [29.] Li, J. R.; Kuppler, R. J.; Zhou, H. C., Selective Gas Adsorption and Separation in Metal-Organic Frameworks *Chem. Soc. Rev.* **2009**, *38*, 1477-1504
- [30.] Li, B.; Wen, H.M.; Zhou, W.; Chen, B., Porous Metal-Organic Frameworks for Gas Storage and Separation: What, How, and Why?, *J. Phys. Chem. Lett.*, **2014**, *5*, 3468-3479
- [31.] Horcajada, P.; Gref, R.; Baati, T.; Allan, P. K.; Maurin, G.; Couvreur, P.; Ferey, G.; Morris, R. E.; Serre, C., Metal-Organic Frameworks in Biomedicine, *Chem. Rev.* **2012**, *112*, 1232-1268
- [32.] Zhuang, J.; Kuo, C.-H.; Chou, L.-Y.; Liu, D.-Y.; Weerapana, E.; Tsung, C.K., Optimized Metal-Organic Framework Nanospheres for Drug Delivery: Evaluation of Small-Molecule Encapsulation, *ACS Nano* **2014**, *8*, 2812-2819
- [33.] Kreno, L.E.; Leong, K.; Farha, O.K.; Allendorf, M.; Van Duyne, R.P.; Hupp, J.T., Metal-Organic Framework Materials as Chemical Sensors, *Chem. Rev.*, **2012**, *112*, 1105-1125
- [34.] Guo, Z.; Xiao, C.; Maligal-Ganesh, R.V.; Zhou, L.; Goh, T.W.; Li, X.; Tesfagaber, D.; Thiel, A.; Huang, W., Pt Nanoclusters Confined within Metal-Organic Framework Cavities for Chemoselective Cinnamaldehyde Hydrogenation, *ACS Catal.*, **2014**, *4*, 1340-1348

- [35.] Farrusseng, D.; Aguado, S.; Pinel, C., Metal-Organic Frameworks: Opportunities for Catalysis, *Angew. Chem. Int. Ed. Engl.* **2009**, *48*, 7502-7513.
- [36.] Lee, J.; Farha, O. K.; Roberts, J.; Scheidt, K. A.; Nguyen, S. T.; Hupp, J. T., Metal-Organic Framework Materials as Catalysts, *Chem. Soc. Rev.* **2009**, *38*, 1450-1459
- [37.] Rosler, C.; Fischer, R., Metal-Organic Frameworks as Hosts for Nanoparticles, *CrystEngComm.*, **2015**, *17*, 199-217
- [38.] Chaemchuen, S.; Kabir, N. A.; Zhou, K.; Verpoort, F., Metal-Organic Frameworks for Upgrading Biogas via CO₂ Adsorption to Biogas Green Energy, *Chem. Soc. Rev.* **2013**, *42*, 9304-9332
- [39.] Cavka, J. H.; Jakobsen, S.; Olsbye, U.; Guillou, N.; Lamberti, C.; Bordiga, S.; Lillerud, K. P. A New Zirconium Inorganic Building Brick Forming Metal Organic Frameworks with Exceptional Stability. *J. Am. Chem. Soc.* **2008**, *130*, 13850–13851
- [40.] Borges, D. D.; Devautour-Vinot, S.; Jolic, H.; Ollivier, J.; Nouar, F.; Semino, R.; Devic, T.; Serre, C.; Paesani, F.; Maurin, G. Proton Transport in a Highly Conductive Porous Zirconium-Based Metal–Organic Framework: Molecular Insight. *Angew. Chem. Int. Ed.* **2016**, *55*, 3919–3924

7.0 Conclusion

In the past several decades, advancements in nanoparticle synthesis and control as well as porous materials, in particular metal-organic frameworks, have made significant progress. With nanoparticle synthesis improvements, shaped particles as well as composition control in simple structures were two areas involved in the largest area of growth. Now, libraries of particles can be synthesized to perform different reactions as well as for biological applications. In this work, the electronic structure and surface catalysis of nanoparticle heterogeneous catalyst were studied. First, by the formation of Au-Pd core-shell structures and studying the migration of atoms throughout electrochemical conversions. This basic knowledge and understanding of catalyst restructuring led to alloyed surfaces with improved electrochemical oxidation due to straining of the surface atoms and the changing of their electronic band structure, as well as from synergistic effects due to the alloyed surface. Similarly, the knowledge gained from the migration of the Au core to the Pd shell allowed for more complex motifs with the aid of understanding a metal's preferential location based on their differing energies.

With the migration of the Au-Pd particles, the strain effect on catalytic activity was convoluted with the synergetic effect of alloying, so the Pd-Ni-Pt core-sandwich-shell particles, one of the first of its kind, were synthesized to probe just the strain effect. With the use of the shape directing Pd core, the Ni layer for enhanced lattice strain, and the catalytically active Pt shell, electrochemical methanol oxidation was run. To truly study the strain effect, differing thickness of Ni was deposited to engineer a higher degree of strain in the Pt surface (the thicker Ni layer retained the smaller lattice once far enough

removed from the influence of the Pd core). With the generated 11% lattice mismatch, and further strain induced by smaller particles, the increase in electrochemical methanol oxidation was realized in alkaline conditions. A similar trend was observed for electrochemical methanol and formic acid oxidation under acidic conditions, however, the non-precious metal leached causing the activity to increase due, originally to strain effects transitioning to compositional effects. With this work, the need to characterize the catalyst before and after reaction conditions was recognized and helped to promote that idea for future works.

Finally, for the below the surface approach, the same Pd-Ni-Pt particles were taken a step further. More recently, groups have become focused on intermetallic structures because of their unique properties, including higher stability, however, the control of shaped particles is lacking because of the high temperatures needed. Using the Pd core as a shape directing substrate, Pd-Ni₃Pt nanoframes were synthesized for electrochemical methanol oxidation. With the higher incorporation of Ni, the catalyst cost decreases, but can also still reach the stable PtNi₃ structure. Using thin, alternating layer of Ni to Pt, the synthesis temperatures from external annealing were reduced and allowed for the overall cubic shape to be maintained. This approach allows for new compositions with shaped facets to be obtained.

With the increased interest in nanoparticle synthesis and controlling heterogeneous catalysis by altering compositions from alloying, core-shell, core-sandwich-shell, or intermetallic structures of the catalyst surface from electronic effects, a secondary approach can be taken. For this method the use of metal-organic frameworks becomes viable. Nanoparticles encapsulated in metal-organic frameworks adapt the

surface chemistry and catalysis due to gating effect of the encapsulating MOFs. Here, we were able to show the unique interaction between the amine group of UiO-66-NH₂ promoting the encapsulation of capping agent free nanoparticles. Differing from other approaches, pre-synthesis of the nanoparticle followed by encapsulation or wetness impregnation, the *in situ* produced and coating nanoparticles have shape and size control, are fully encapsulated as shown through size selective alkene hydrogenations, don't damage the MOF structure and maintain the crystallinity and have cleaner particle surfaces due to the capping by the MOF rather than use of traditional colloidal capping agents. The cleaner surface was probed by FTIR as well as selective aldehyde hydrogenations.

Finally, with the result of the NP within UiO-66 and their increased selectivity and activity, a more complex composite material was synthesized for use in PEMFC technologies. The Pt on carbon nanotubes was first used for electrochemical oxygen reduction, but showed a lack in stability due to particle aggregation and leaching. The Pt/CNT samples were then coated in thin layer of UiO-66 using three approaches to try and induce stability while decreasing Pt loss. Ultimately, an organic phase synthesis was chosen. The UiO-66 selectively coated the Pt particles, with little loss or detachment of Pt during synthesis, and then used to perform electrochemical oxygen reduction. An increased stability was observed over the Pt/CNT samples after accelerated aging.